Title

Regulation of mTORC1 Signaling in Subcellular Compartments

Author

Zhong, Yanghao

Publication Date

2022

UNIVERSITY OF CALIFORNIA SAN DIEGO

Regulation of mTORC1 Signaling in Subcellular Compartments

A dissertation submitted in partial satisfaction
of the requirements for the degree Doctor of Philosophy

in

Biomedical Sciences

by

Yanghao Zhong

Committee in charge:

Professor Jin Zhang, Chair
Professor Gen-Sheng Feng
Professor Kun-Liang Guan
Professor Alexandra Newton
Professor Alan Saltiel

2022

The Dissertation of Yanghao Zhong is approved, and it is acceptable in quality and form for publication on microfilm and electronically.

University of California San Diego

2022

DEDICATION

In dedication to my advisor Dr. Jin Zhang.

EPIGRAPH

“Two roads diverged in a wood, and I—
I took the one less traveled by,
And that has made all the difference.”

Robert Frost, *The Road Not Taken*

TABLE OF CONTENTS

LIST OF FIGURES

ACKNOWLEDGEMENT

I would like to thank Dr. Jin Zhang for giving me the opportunity to join her lab to do such exciting research, for her greatest support and mentorship along my journey to obtain my Ph.D. degree, for her excellent insight and guidance that make me grow scientifically, and for her charisma that impacts me to dedicate my lifetime to research.

I would like to thank Dr. Xin Zhou for her endless hours of mentorship in both experiments and scientific writing, for establishing solid research projects which I could pick up and continue working on, and for all the invaluable suggestions she gave me in my graduate life.

I would like to thank Qiang Ni for his always-perfect support on reagent requests, equipment maintenance and supply arrangement, which provided me an environment free of worries to work in.

I would like to thank the Zhang lab alumni: Dr. Eric Greenwald, Dr. Terri Clister, Dr. Simin Li, Dr. Brian Tenner, Dr. Gary Mo, Dr. Jason Zhang, Dr. Brian Ross, Dr. Tengqian Sun, Dr. Jeremiah Keyes, Dr. Fabian Hertel and Eric Xu, for sharing experience with me that improves my research.

I would like to thank all the current Zhang lab members: Dr. Sohum Mehta, Ayse Sahan, Dr. Wei Lin, Dr. Danielle Schmitt, Dr. Yonghoon Kwon, Dr. Skott Lee, Dr. Qi Su, Shawn Chen, Jinfan Zhang, Clara Posner, Julia Hardy, Ryan Weeks, Emily Pool, Anne Lyons, Michelle Frei, who inspired great questions and discussions during lab meeting which evoked my critical thinking of my results.

I would like to thank my thesis committee members: Dr. Alexandra Newton, Dr. Alan Saltiel, Dr. Gen-Sheng Feng and Dr. Kun-Liang Guan, who provided insightful suggestions and encouragement that kept me focused.

I would like to thank my collaborators Dr. Silvio Gutkind and Dr. Zhiyong Wang in the Gutkind lab for their expertise on head and neck cancer cells.

I would like to thank my friends Eric Wang, Natalie Hollingsworth, Jacey Liu, Ian Mathew, Nina Gao and Doug Zuill, for their friendship, emotional support and making graduate life fun.

Last but not least, I want to thank my parents, who always love me no matter when I am up or down.

Introduction, in full, is currently being prepared for submission of publication of the material. Zhong, Y., Mehta, S., Zhang, J. Scalpels at hand: genetically encoded biosensors to dissect PI3K-Akt-mTOR signaling pathway. The dissertation author was the primary investigator and author of this work.

Chapter 1, in full, is a reformatted reprint of the material as it appears in Zhou, X., Zhong, Y., Molinar-Inglis, O., Kunkel, M.T., Chen, M., Sun, T., Zhang, J., Shyy, J.Y.-J., Trejo, J., Newton, A.C., Zhang, J. (2020). Location-specific inhibition of Akt reveals regulation of mTORC1 activity in the nucleus. *Nat Commun* 11, 6088. The dissertation author was the primary investigator and author of this work.

Chapter 2, in full, has been accepted for publication of the material as it will appear in Zhong, Y., Zhou, X., Guan, KL., Zhang, J. Rheb Regulates Nuclear mTORC1 Activity Independent of Farnesylation. *Cell Chemical Biology*. The dissertation author was the primary investigator and author of this work.

Chapter 3, in full, is currently being prepared for submission for publication of the material. Zhong, Y., Zhou, X., Sahan A., Gutkind, JS., Zhang, J. Genetically targetable mTORC1 inhibitor reveals differential transcriptional control by subcellular mTORC1. The dissertation author was the primary investigator and author of this work.

VITA

EDUCATION

2022	Doctor of Philosophy, University of California San Diego
2015	Bachelor of Science, University of Science and Technology of China

PUBLICATIONS

Published:

- **Zhong, Y**., Zhou, X., Guan, KL., Zhang, J. Rheb Regulates Nuclear mTORC1 Activity Independent of Farnesylation. *Cell Chemical Biology (accepted)*
- Chen, M., Sun, T., **Zhong, Y**., Zhou, X., Zhang J. A highly sensitive fluorescent Akt biosensor reveals lysosome-selective regulation of lipid second messengers and kinase activity. *ACS Central Science (accepted)*
- Zhou, X., **Zhong, Y**., and Zhang, J. (2021). Regulation of nuclear mTORC1. Mol Cell Oncol *8*, 1896348.
- Zhou, X., **Zhong, Y**., Molinar-Inglis, O., Kunkel, M.T., Chen, M., Sun, T., Zhang, J., Shyy, J.Y.-J., Trejo, J., Newton, A.C., Zhang, J. (2020). Location-specific inhibition of Akt reveals regulation of mTORC1 activity in the nucleus. Nat Commun *11*, 6088.

In preparation:

- **Zhong, Y**., Zhou, X., Sahan A., Gutkind, JS., Zhang, J. Genetically targetable mTORC1 inhibitor reveals differential transcriptional control by subcellular mTORC1.
- **Zhong, Y.,** Mehta, S., Zhang, J. Scalpels at hand: genetically encoded biosensors to dissect PI3K-Akt-mTOR signaling pathway.
- Lee, HN., **Zhong, Y.,** Lin, W., Zhang, J. Nanoclustering of an anchoring protein fine tunes cAMP signaling output.
- Kwon Y., Clark, M., Walters, G., **Zhong, Y**., Mehta, S., Sunahara, R., Zhang, J. Noncanonical β-adrenergic activation of ERK at endosomes.

PRESENTATIONS

- Poster presentation, "The Regulation of mTORC1 Activity in The Plasma Membrane", Experimental Biology meeting, San Diego, 2018
- Poster presentation, "Constitutively Active Rheb Regulates Nuclear mTORC1 Activity and Functions", FASEB meeting, Palm Spring, 2019

FELLOWSHIPS

- CTSBB Predoctoral fellowship (Center for Trans-scale Structural Biology and Biophysics, UCSD, 2019)

ABSTRACT OF THE DISSERTATION

Regulation of mTORC1 Signaling in Subcellular Compartments

by

Yanghao Zhong

Doctor of Philosophy in Biomedical Sciences

University of California San Diego, 2022

Professor Jin Zhang, Chair

The mechanistic target of rapamycin complex 1 (mTORC1) is a signaling hub that senses numerous upstream signals including growth factors and regulates a broad range of cellular functions. Dysregulation of mTORC1 signaling pathway has been implicated in various pathological conditions such as cancers and diabetes. To achieve precise regulation and functions, mTORC1 signaling is compartmentalized. Canonical mTORC1 activation on the lysosome has been well established, but mTORC1signaling at other subcellular compartments is undefined. In these studies, using synthetic biology approaches, we developed and applied molecular tools for monitoring and perturbing mTORC1 signaling at subcellular compartments to dissect the mechanisms that regulate subcellular mTORC1 activity and to examine the functions of subcellular mTORC1. Specifically, growth factor-stimulated mTORC1 activity was observed in the nucleus and nuclear mTORC1 was regulated by nuclear Akt and Rheb, two essential positive regulators of mTORC1, through a noncanonical mechanism. By specifically perturbing mTORC1 activity in the nucleus, we found that compared with canonical mTORC1 activity, nuclear mTORC1 played a distinct role in regulating gene transcription in glycolysis, a critical process involved in cancer cell survival. Thus, these studies suggest that precisely tuning subcellular mTORC1 activity rather than targeting it with a sledgehammer approach may provide therapeutic benefits.

Introduction

Cells need to promptly respond and adapt themselves to the changing extracellular and intracellular environment in order to survive, grow and proliferate. A sophisticated network formed by numerous proteins and small molecules is responsible for sensing the environmental cues, propagating the signals and regulating different cellular processes. One of the key signaling pathways within the signal transduction network centers around phosphoinositide 3-kinase (PI3K), Akt, and mechanistic target of rapamycin (mTOR), which regulates almost every aspect of cellular processes, including growth and metabolism. Dysregulation of PI3K-Akt-mTOR pathway has been widely associated with many pathological conditions such as cancers and diabetes, and pharmacologically targeting this pathway has been one of the therapeutic strategies (Bilanges et al., 2019; Manning and Toker, 2017; Saxton and Sabatini, 2017).

In order to precisely control specific biological functions, signaling compartmentalization for PI3K-Akt-mTOR pathway plays an essential role (Mehta and Zhang, 2021). The activation of this pathway is initiated by the stimulation of receptor tyrosine kinases (RTK) or G-protein-coupled receptors (GPCRs), which recruit PI3K to the plasma membrane, generating 3-phosphoinostides including phosphatidylinositol-3,4-bisphosphate ($PI(3,4)P_2$) and phosphatidylinositol-3,4,5-triphosphate (PIP_3) (Bilanges et al., 2019). Inactive Akt is subsequently recruited to the plasma membrane by 3-phosphoinostides, and activated through phosphorylation by upstream kinases. Active Akt can turn on the mTORC1 signaling pathway, including canonical mTORC1 activation on the lysosomal membrane (Jewell and Guan, 2013) and noncanonical mTORC1 activation in the nucleus (Zhou et al., 2020).

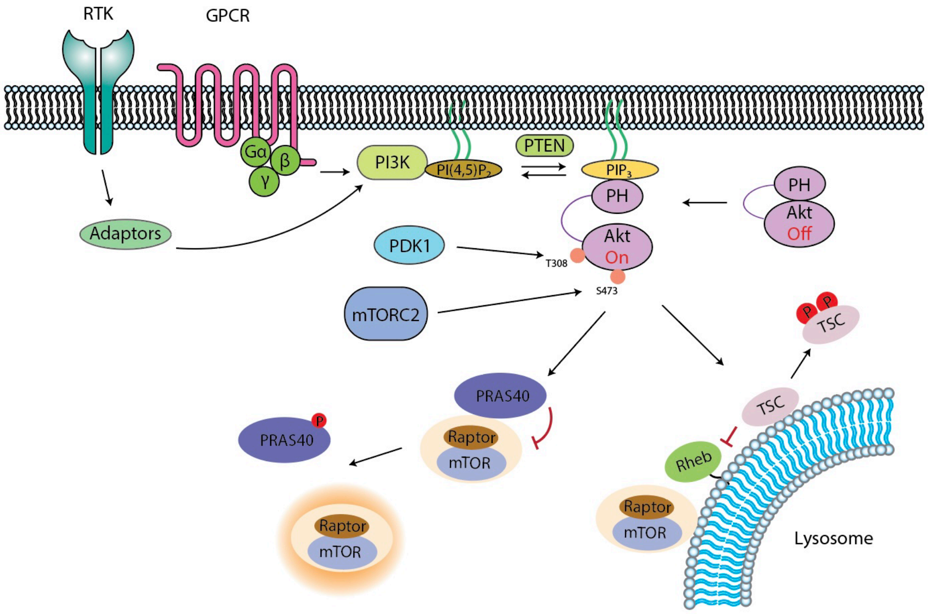

Figure 0.1 Overview of the PI3K-Akt-mTOR signaling pathway.

To study PI3K-Akt-mTOR signaling at subcellular locations, traditional biochemical methods such as subcellular fractionation were used to probe the components of the signaling pathway in different subcellular compartments. Indeed, many regulatory proteins and small molecules of the signaling pathway were found at different subcellular locations (Barlow et al., 2010; Bernardi et al., 2006a; Kantidakis et al., 2010; Martelli et al., 2012; Rosner and Hengstschläger, 2012; Wan et al., 2017), yet debates remained regarding the properties, behaviors and activity of these regulatory proteins and molecules in subcellular compartments (Gozani et al., 2003; Rosner and Hengstschläger, 2012), partly due to the lack of tools that enable direct examination of the biological changes in subcellular compartments. The development of genetically encoded fluorescent biosensors has enabled the visualization of biochemical changes and signaling activities in live cells. In contrast to the traditional biochemical assays which usually provide snapshots of what occur in a population of cells, often without single cell resolution and spatiotemporal precision, genetically encoded biosensors can be introduced into live cells and allow for dynamic examination of the biochemical changes. These biosensors can also be targeted to specific cellular compartments, unraveling unique regulation of spatially compartmentalized signaling (Mehta and Zhang, 2021).

General design strategies of genetically encoded biosensors

Owing to the extensive efforts of the research community, many different ways have been invented to construct biosensors to probe the dynamics of signaling pathways, including PI3K-Akt-mTOR pathway (Greenwald et al., 2018). In general, many genetically encoded fluorescent biosensors share a modular design containing a sensing unit that detects a biochemical change induced by a specific signaling process, and a reporting unit that transforms the biochemical change into optical readout. The sensing unit often functions as a “molecular switch” that undergoes a conformational change triggered by a binding or post-translational modification event when a specific signaling activity is turned on. Such conformational changes are rapidly transmitted to the reporting unit, which is physically linked to the sensing unit, generating a measurable optical signal that reveal real-time dynamics of the signaling pathway. Components of the molecular switch are often derived from native cellular proteins or protein domains whose specific property determines the biochemical event that a sensor can detect. For example, biosensors containing domains that undergo a conformational change upon small molecules binding often serve as “indicators” of the signaling molecules. Likewise, a full-length signaling protein can also be used as a molecular switch whose conformation changes between “active” and “inactive” states, constituting an “activation” sensor. In an “activity” sensor, the molecular switch functions as a surrogate substrate for the enzyme of interest and undergoes a conformational change in response to the catalytic activity of the enzyme, such as a post-translational modification. All these types of biosensors have been used to monitor signaling dynamics of the PI3K-Akt-mTOR pathway (Greenwald et al., 2018).

The reporting unit usually consists of one or more fluorescent proteins (FP) that change their spectral properties in response to the conformational change rising from the molecular switch, and the readout from the reporting unit serves as a dynamic and quantitative representation of the signaling event. Depending on how the reporting unit is constructed, there are two classes of commonly used biosensors: fluorescence resonance energy transfer (FRET) -based and single fluorescent protein-based biosensors. FRET is a quantum-mechanical process in which a “donor” fluorophore that initially absorbs energy and reaches its electronic exited state, transfers part of the energy to a neighboring “acceptor” fluorophore through nonradiative dipole-dipole

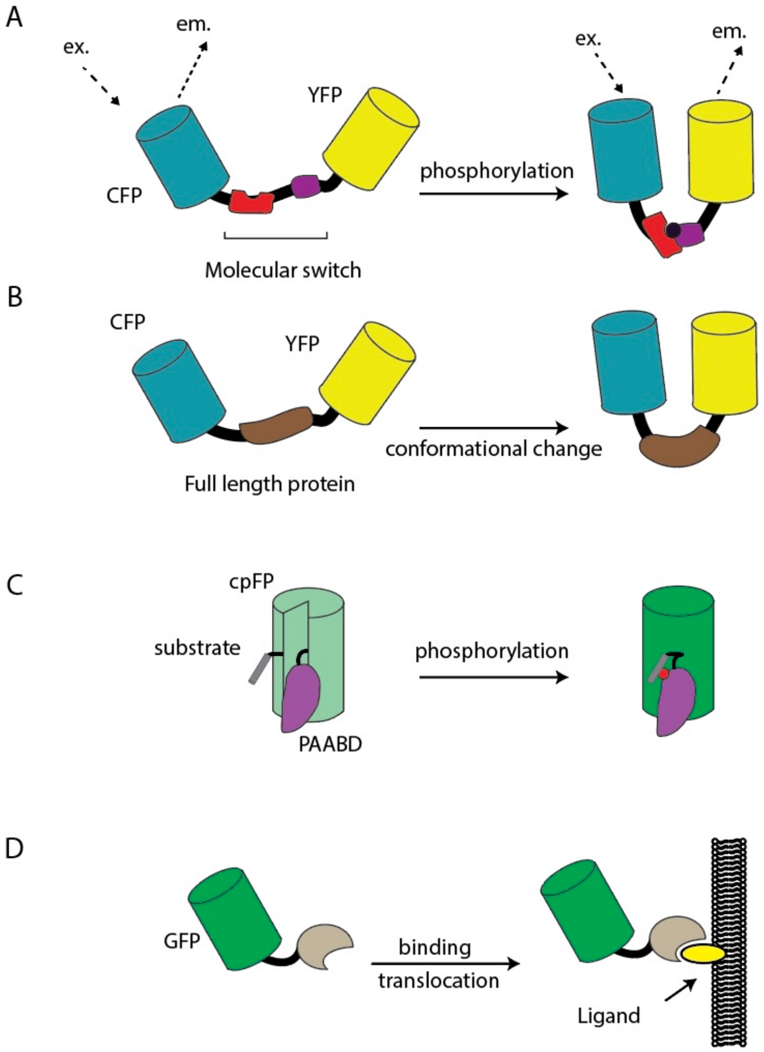

Figure 0.2 General strategies for designing fluorescent biosensors. (A). FRET-based biosensor design. When a biological event such as phosphorylation induces a conformational change to the molecular switch, the efficiency FRET between the fluorescent proteins changes, reflecting the biological event. (B). Activation biosensor design. Full length signaling protein acts as a molecular switch. Once the conformation of the signaling protein changes, the FRET efficiency between the FRET pair also changes accordingly. (C). Single FP-based biosensor design. Circularly permuted FP is sandwiched by a substrate and a phosphoamino acid binding domain (PAABD). Upon phosphorylation, intramolecular binding between the substrate and PAABD induces a conformational change of the cpFP, which changes the intensity of cpFP. (D). Translocation/localization-based biosensor design. GFP is directly linked to a ligand binding domain that specifically recognizes signaling molecules localized to different subcellular compartments, giving spatial information of the ligand.

coupling. Therefore, when FRET occurs, donor fluorescence is reduced and the acceptor fluorophore is "excited" by the nonradiative energy transfer, whose efficiency mainly depends on the distance, orientation and spectral overlap of the donor and acceptor (Bajar et al., 2016; Periasamy et al., 2015). In a FRET-based biosensor, the molecular switch is typically sandwiched by a pair of FPs between which FRET can occur. Upon detecting the specific cellular signaling event of interest, the molecular switch will undergo a conformational change that will alter the relative distance and orientation between the attached FPs, resulting in changes in FRET efficiency, which can be measured by the ratio between the donor fluorescence and sensitized emission from the acceptor or by monitoring changes in the fluorescence lifetime of the donor FP using fluorescence lifetime imaging microscopy (FLIM) (Calleja et al., 2003). In contrast to FRET-based biosensors, which rely on an FP pair, an alternative design involves directly linking the molecular switch into a single FP. These single-FP biosensors utilize conformational changes in the molecular switch to modulate fluorescence (Mehta et al., 2018; Nakai et al., 2001). Single-FP biosensors occupy less spectral space than FRET-based biosensor, and are thus more conveniently applied to multiplexed imaging, which utilizes color variants of different biosensors to study dynamic signaling propagation and crosstalk in living cells.

Unlike the indicator that relies on changes in FRET or FP fluorescence, a class of indicators utilize subcellular redistribution of fluorescence, or translocation, as the readout. These biosensors often contain a protein domain that interacts with a target lipid molecule and a FP. The interacting domain can bind to target lipids and direct the FP to the specific locations where the molecules are enriched. A suite of fluorescent biosensors have been developed, based on these general designs, to probe the spatial regulation of the PI3K-Akt-mTOR pathway (Greenwald et al., 2018).

Probing phosphoinositides

PtdIns lipids in the membrane can be phosphorylated to form phosphatidylinositol phosphate, or phosphoinositides. The phosphorylation can happen on the three, four and five hydroxyl groups in seven combinations by a variety of lipid kinases, including PI3Ks. There are three classes of PI3Ks: class I PI3Ks act downstream of RTKs and GPCRs in the plasma membrane, while class II and class III PI3Ks mainly control membrane trafficking and indirectly regulate cell signaling (Bilanges et al., 2019). Catalytically, all three classes of PI3Ks can phosphorylate the 3' position of the inositol group of phosphatidylinositol (PtdIns) lipids, which serve as regulators of a broad range of proteins and are crucial to the signaling pathway. For example, 3-phosphoinositides, such as PtdIns(3,4,5)P_3 (PIP_3) stimulate the activation of downstream Akt signaling (Manning and Toker, 2017). On the other hand, cellular levels of phosphoinositides are balanced by phosphatases (Dempke et al., 2018; Malek et al., 2017), preventing over-activation of the oncogenic pathway. PIP_3 can be dephosphorylated by 5-phosphatases SHIP1 and/or SHIP2, producing PtdIns(3,4)P_2 (PI(3,4)P_2), and by 3-phosphatase PTEN to generate PtdIns(4,5)P_2 (PI(4,5)P_2). PTEN is also a key regulator of cellular PtdIns(3,4)P_2, converting it to PtdIns(4)P (PI(4)P).

Phosphoinositide levels are often dynamically regulated, and biosensors can be designed to examine the spatiotemporal dynamics of these lipid molecules.

FP translocation/localization -based phosphoinositide indicators

Searching from the effector proteins downstream of the phosphoinositide signaling, a panel of proteins have been identified to directly bind to phosphoinositides with high selectivity. Specific binding proteins have been identified for all seven phosphoinositides. In general, phosphoinositide indicators can be generated by fusing a fluorescent protein with the phosphoinositide-binding

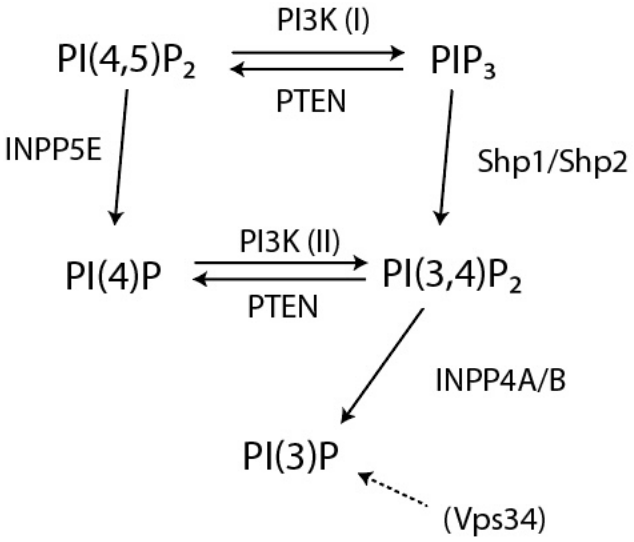

Figure 0.3 The conversion between phosphoinositides by kinases and phosphatases. Class I PI3K phosphorylates PI(4,5)P_2 to generate PIP_3, and class II PI3K phosphorylates PI(4)P to generate PI(3,4)P_2. Class III PI3K Vps34 is believed to produce PI(3)P, but the process is not clearly understood. 3-phosphotase PTEN can dephosphorylate PIP_3 and PI(3,4) to generate PI(4,5)P_2 and PI(4)P, respectively. 5-phosphotase INPP5E dephosphorylates PI(4,5)P_2, Shp1/Shp2 dephosphorylate PIP_3, and INPP4A/B dephosphorylate PI(3,4)P_2.

protein or domain derived from the protein to examine the localization of a specific phosphoinositide.

PtdIns(3)P (PI(3)P) generated by VPS34, the primordial class III PI3K conserved from yeast to human (Balla, 2013; Herman and Emr, 1990), was found to bind to FYVE domain of human early endosome antigen (EEA1) (Burd and Emr, 1998) and PX domain of the p40phox subunit of the NADPH oxidase (Ellson et al., 2001; Kanai et al., 2001). Green fluorescent protein (GFP) tagged FYVE domain was found to predominantly localize to endocytic membranes compartments and the localization requires VPS34 activity (Burd and Emr, 1998). GFP-PX was also showed to colocalize with EEA1 and transiently accumulate around the entire phagosome, suggesting PI(3)P was a candidate for controlling the phagosomal maturation. PI(4)P generated by 3-phosphatase PTEN can bind to P4M domain of the secreted effector protein SidM from bacteria. The indicator, GFP-P4M, showed a wider cellular distribution of PI(4)P, including plasma membrane and Rab7-positive late endosomes/lysosomes (LEL) as well as previously reported Golgi membranes (Hammond et al., 2014). Another PI(4)P indicator using oxysterol-binding protein-related protein 5 (ORP5) or ORP8 revealed plasma membrane PI(4)P is required for tethering ORP5 and ORP8 (Chung et al., 2015). These findings suggest PI(4)P may have wide distribution across the cellular membrane compartments. Interestingly, the 5-phosphoinositide, PtdIns(5)P (PI(5)P) is less studied but an indicator based on the homeodomain (PHD) finger of the inhibitor of growth protein 2 (ING2) found PI(5)P might function as ligands of nuclear proteins to modulate broad nuclear processes (Gozani et al., 2003).

3-phosphoinositides including PIP_3 and $PI(3,4)P_2$ interact with lipid-binding pleckstrin homology (PH) domain in a variety of effector proteins to modulate their localization and/or activity. Quantitative analysis has shown that PH domains from Bruton tyrosine kinase (Btk) and general receptor for phosphoinositides-1 (GRP1) and tandem-PH domain containing protein-1 (TAPP1) bind to PIP_3 and $PI(3,4)P_2$, respectively, whereas other PH domains, including those from Akt, and ADP-ribosylation factor nucleotide-binding site opener (ARNO), bind to both PIP_3 and $PI(3,4)P_2$ (Dowler et al., 2000; Manna et al., 2007). This might explain why two 3-phosphoinosite indicators, PH(Akt)-GFP and PH(GRP1)-GFP, behaved differently in earlier studies. Only PH(Akt)-GFP, but not PH(GRP1)-GFP, was localized at the plasma membrane after 30 min of hydrogen peroxide treatment following growth factor stimulation in NIH3T3 cells (Gray et al., 1999). These results obtained from fluorescent indicators further emphasized the overlapping but distinct roles of 3-phosphoinositides. To specifically examine the spatiotemporal dynamics and signaling roles of $PI(3,4)P_2$, Goulden *et al* constructed a indicator for $PI(3,4)P_2$ by fusing three tandem copies of PH domains from TAPP1 with enhanced GFP (EGFP). Combining a synthetic biology approach and live cell imaging, they found the overwhelming majority of $PI(3,4)P_2$ accumulates through degradation of class I PI3K-produced PIP_3 and $PI(3,4)P_2$ is subject to hydrolysis by tumor suppressor protein PTEN.

$PI(4,5)P_2$ is the major phosphoinositide at the inner leaflet of the plasma membrane (Hammond and Balla, 2015). Upon growth factor stimulation, $PI(4,5)P_2$ is metabolized to some of the most important messenger molecules, such as inositol (1,4,5) -trisphosphate (IP_3) and diacylglycerol (DAG) by phospholipase C (PLC), and PIP_3 by PI3K (Nishioka et al., 2008). Due to the importance of this molecule, much more efforts have been invested in developing fluorescent indicators for $PI(4,5)P_2$. Earlier studies identified PH domain from PLC-δ1 and Tubby protein interact with $PI(4,5)P_2$ and GFP-PH (PLC-δ1) and GFP-Tubby showed plasma membrane localization but rapidly redistributed to cytosol when PLC is activated by ionophores or receptor stimulation (Santagata et al., 2001; Stauffer et al., 1998; Várnai and Balla, 1998). PH (PLC-δ1) also has high affinity to cytosolic IP_3 produced from $PI(4,5)P_2$ via PLCβ and Tubby protein does not faithfully report PLCβ-dependent PI(4,5)P2 dynamics (Leitner et al., 2019); thus, alternative indicators were made using PH (PLC-δ4), or modified Tubby versions (Lee et al., 2004; Quinn et al., 2008). Recent improvement was made by utilizing the ENTH domain from mammalian epsin 1 protein (Itoh et al., 2001) which selectively binds to $PI(4,5)P_2$ but not IP3 and does not compete with endogenous signals (Leitner et al., 2019).

Comparing with other 3-phosphoinositides, $PtdIns(3,5)P_2$ ($PI(3,5)P_2$) is less studied. An indicator has been made by fusing GFP to two repeats of MLN1, the lipid-binding domain of transient receptor potential Mucolipin 1 (TRPML1) (Li et al., 2013). GFP-MLN1 potently and specifically binds to $PI(3,5)P_2$ in the endosome and lysosome. Live cell imaging using GFP-MLN1 revealed that $PI(3,5)P_2$ undergoes rapid changes immediately before fusion of LELs, but future investigation is needed to understand $PI(3,5)P_2$ dynamics in signaling transduction and membrane trafficking.

FRET-based phosphoinositide indicators

Fluorescent protein-fused phosphoinositide binding domains from different proteins have proved to be an invaluable tool to examine the dynamics of cellular phosphoinositides, though some drawbacks are obvious. First, when translocation or fluorescence redistribution is visualized by fluorescence microscopy, even minor focal drift or cell morphology change can make the quantification unreliable (van der Wal et al., 2001). Second, translocation is difficult to be captured in very flat cells (van der Wal et al., 2001) or in regions with high surface-to-volume ratio (SVR) (Nishioka et al., 2008). Third, those FP-based translocation/localization sensors cannot be targeted to specific subcellular compartments to monitor the local changes of phosphoinositides (Ananthanarayanan et al., 2005). Researchers have thus developed FRET-based phosphoinositide indicators using the same phosphoinositide binding domains as in the translocation/localization-based indicators.

The very first FRET-based PI(4,5)P_2 indicator adapted bimolecular design, in which two PH domain from PLC-δ1 was separately fused with a cyan FP (CFP) and a yellow FP (YFP), between which FRET can occur. PLC activation triggers similar translocation of the sensor from plasma membrane to the cytosol, where lower effective concentration of the sensor is expected, resulting in lower intermolecular FRET. Quantification of FRET signal changes to various GPCR agonists revealed heterogeneous PLC activation kinetics (van der Wal et al., 2001). The bimolecular design requires similar expression levels of two PH domains, which always needs optimization. Unimolecular design should solve this problem. A unimolecular indicator CYPHR for PI(4,5)P_2 was developed by sandwiching PH (PLC-δ1) domain between CFP and YFP. Similarly to the bimolecular design, PLC activation induced intramolecular FRET change (Violin et al., 2003).

Translocation-based biosensors are difficult to target to subcellular compartments. Another set of biosensors were developed based on lipid-binding induced conformational changes. CAY utilized a sequence from the surface protein ActA, which undergoes a conformational change upon phosphoinositide binding, though the specificity is lacking (Cicchetti et al., 2004). Another indicator FLLIP designed to monitor membrane PIP_3 contains a membrane targeting motif, a PH(GRP1) domain, a CFP and a YFP, connected by engineered α-helical linkers, one of which contains a diglycine-based hinge. PH(GRP1) domain binds to membrane PIP_3 resulting in a FRET change, presumably through an engineered conformational change induced by biosensor binding to the membrane lipids (Sato et al., 2003). Comparing the platelet-derived growth factor (PDGF) stimulated FRET changes between plasma membrane targeted FLLIP-pm and endomembrane targeted FLLIP-em revealed that endomembrane PIP_3 increased after plasma membrane PIP_3, suggesting these lipids are present in endomembrane (Sato et al., 2003). Using a similar design for FLLIP, a series of Pippi biosensors have been developed, including Pippi-PI(3,4)P_2, a PI(3,4)P_2 indicator using PH(TAPP1), a PI(4,5)P_2 indicator using PH(PLC-δ1) and a PI(4)P indicator using PH domain from FAPP1 (Nishioka et al., 2008; Yoshizaki et al., 2006). Ananthanarayanan *et al* used a different strategy based on competition between a negatively charged pseudo-ligand and endogenous phosphoinositides for binding to the PH(Akt) domain, and constructed the PI(3,4,5)P_3 and PI(3,4)P_2 dual indicator named InPAkt. Nuclearly targeted InPAkt showed no FRET change upon PDGF stimulation in NIH3T3 cells, suggesting there is no appreciable amounts of accessible PI(3,4,5)P3 and PI(3,4)P2 in the nucleus upon growth factor stimulation (Ananthanarayanan et al., 2005). Following a similar design for InPAkt, an indicator for PI(4,5)P2, PIcR, was also developed essentially by replacing PH(Akt) domain in InPAkt with PH(PLC-δ1) domain, which binds to PI(4,5)P_2 (Hertel et al., 2020).

Besides the widely used phosphoinositide indicators, some unique indicators were developed to suit a specific application. For example, the donor of the FRET pair can be switched to luciferase to generate bioluminescence resonance energy transfer (BRET)-based phosphoinositide indicators (Pierre-Eugene et al., 2012). BRET-based indicators are particularly suitable for high-throughput screening using plate-reading. Single FP-based InPAkt using the FP exchange (FPX) design was developed to simultaneously monitor phosphoinositide dynamics and other signaling events in multiplexed imaging (Ding et al., 2015; Hertel et al., 2020). The versatile biosensor toolkit for phosphoinositides will provide invaluable tools to untangle the complex regulation of PI3K signaling.

Probing Akt activation and activity

The Ser/Thr kinase Akt, also known as protein kinase B (PKB), is one of the most important effector proteins of PI(3,4,5)P_3 generated by PI3K (Manning and Toker, 2017). The canonical pathway to activate Akt is initiated by stimulating receptor tyrosine kinases (RTKs) or G-protein coupled receptors (GPCRs), which leads to the recruitment of class I PI3K to the plasma membrane, producing PIP_3. Akt is subsequently recruited to the plasma membrane via its PH domain that can bind to PIP_3 and PI(3,4)P_2, the latter being produced by converting PI(3,4,5)P_3 by SHIP1 and/or SHIP2 or synthesized by class II PI3K using PI(4)P (Bilanges et al., 2019; Manning and Toker, 2017). The 3-phosphatase PTEN can dephosphorylate PIP_3 and PI(3,4)P_2, serving as a negative regulator of Akt activation (Malek et al., 2017). Akt is activated via phosphorylation: T308 (residue number based on human Akt1 sequence) of the activation loop in the catalytic kinase core by phosphoinositide-dependent protein kinase 1 (PDK1) and S473 in the C-terminal hydrophobic motif by mTOR complex 2 (mTORC2) or Akt itself (Baffi et al., 2021). Phosphorylation of both residues is required for the maximum activation of Akt (Alessi et al., 1996). Active Akt can directly phosphorylate proteins from numerous functional classes, including kinases, transcription factors, regulators of small GTPases, metabolic enzymes and many others, most of which contain the minimal consensus phosphorylation motif (Manning and Toker, 2017). Akt substrates localize to various compartments such as endomembrane and nucleus, suggesting that compartmentation of Akt activity serves to ensure the specificity and fidelity in substrate selection, as well as spatial regulation of specific downstream signaling.

Akt activation and its activity are both fine-tuned so that understanding every detail of the process would help us understand the delicate regulation of Akt signaling pathway. Fluorescent biosensors with their ability to detect signaling changes in intact cells under physiological conditions serve as ideal tools to dissect the molecular mechanism regulating Akt signaling. There are mainly two categories of Akt biosensors: activation biosensor to understand the molecular mechanisms and kinetics of enzyme activation and activity biosensor to probe and monitor kinase activity in substrate phosphorylation.

FRET-based Akt activation biosensor

Activation of Akt is an exquisite multi-step process involving membrane recruitment, phosphorylation and membrane detachment (Ananthanarayanan et al., 2007). Conformational changes in Akt can be utilized to construct Akt activation biosensor, in which full length Akt is sandwiched by a FRET pair. Any conformational changes, even subtle ones, in Akt may result in a FRET change. The very first demonstration of such an Akt activation biosensor was accomplished by Calleja *et al* (Calleja et al., 2003), and was improved by changing the FRET pair from GFP/YFP to GFP/RFP (Calleja et al., 2007). Using the Akt activation biosensor GFP-PKB-RFP, the authors showed Akt undergoes phosphoinositide-dependent conformational change. Under basal state, Akt exhibits an autoinhibited "PH-in" conformation where PH domain interacts with catalytic domain. Upon agonist stimulation, Akt is recruited to the plasma membrane through the binding of phosphoinositides via PH domain, switching to an active "PH-out" conformation, which can be accessed by PDK1 for phosphorylation (Calleja et al., 2007).

Many details have been elucidated as for how Akt is recruited and phosphorylated, but the mechanism by which active Akt dissociates from the plasma membrane is unclear. To elucidate the mechanism, using the same design as GFP-PKB-RFP, Ananthanarayanan *et al* independently constructed Akt activation biosensor, ReAction, which showed FRET change in the plasma membrane. Importantly, the conformational change is dependent on T308 phosphorylation. Further mutagenesis of the key regulatory residues of Akt revealed that phosphorylation of T308 increased the interaction between PH domain and catalytic domain and reduced the Akt membrane association, providing a model of Akt dissociation from the plasma membrane (Ananthanarayanan et al., 2007).

There are different ways to constructe an Akt activation biosensor. For example, by inserting the YFP between PH domain and catalytic domain and tagging CFP to the C-terminus, Akind was constructed. This biosensor showed Akt activation predominantly happens in the lamellipodia and peripheral membrane ruffles, correlating with the increase in PI(3,4)P_2 rather than PIP_3 (Yoshizaki et al., 2006). This correlation could be further investigated using multiplexed imaging of both Akt activation and phosphoinositide biosensor.

Akt activity biosensors

Active Akt phosphorylates a wide range of downstream substrates, including glycogen synthase kinase 3β (GSK3β), Tuberous Sclerosis Complex component TSC2 and forkhead box protein O1 (FOXO1) (Manning and Toker, 2017). FRET-based Akt activity reporters utilize the minimum phosphorylation sequence in the substrates as a substrate surrogate, which can be phosphorylated by active Akt and bind to phosphoamino acid binding domain (PAABD), inducing a conformational change within the biosensor to cause change in FRET efficiency. An Akt activity biosensor, Aktus, containing an Akt substrate consensus sequence and a PAABD, 14-3-3 protein that binds to phosphorylated consensus sequence, sandwiched between a FRET pair, showed FRET change only when exogenously expressed Akt was colocalized with Aktus, suggesting active Akt can be localized to subcellular compartments (Sasaki et al., 2003). 14-3-3 is a strong PAABD, so Aktus was presumably irreversible (Zhang et al., 2005). Using forkhead associated domain 2 (FHA2), a relatively weaker PAABD, Kunkel *et al* developed PKB kinase (Akt is also known as PKB) activity reporter (BKAR), whose response can be reversed by PI3K inhibitors;

thus BKAR monitors the balanced effect of Akt and phosphatases towards Akt substrates. Subcellularly targeted BKAR revealed the nucleus showed sustained responses more than the plasma membrane, suggesting the presence of differentially regulated phosphatase activity in the two compartments (Kunkel et al., 2005). The early efforts to develop Akt activity reporter were successful, but the dynamic range of these reporters was low, limiting their wider applications. In this case, many attempts to improve the dynamic range of the biosensor were carried out. By changing the substrate sequence, the PAABD and linkers between the two, the dynamic range of Akt biosensors were substantially improved (Belal et al., 2014; Gao and Zhang, 2008; Komatsu et al., 2011; Miura et al., 2014). Changing the FP to a brighter version also helps to increase the dynamic range (Zhou et al., 2015). Using more sensitive Akt activity reporters, it was found that the kinetics and magnitude of Akt activity were different between raft and non-raft regions of the plasma membrane in a cell type dependent manner (Gao and Zhang, 2008; Miura et al., 2014). Recently, the dynamic range of Akt activity reporter was further significantly improved using a newly developed strategy, where a circularly permuted FP (cpFP) is flanked by Akt substrate sequence and FHA1(Mehta et al., 2018, Chen et al., 2021). While the FRET-based Akt activity biosensor could achieve multiplexed imaging by taking advantages of the newly developed spectrum-compatible FPs (Mo et al., 2020), single FP-based "ExRai" series biosensors should be a more accessible tool in co-imaging of different signaling pathways.

Probing subcellular mTORC1 activity

The Ser/Thr kinase mTOR forms two complexes in cells, mTORC1 and mTORC2. While mTORC2 acts upstream of Akt to regulate its activation, mTORC1 serves as an evolutionarily conserved downstream component of the PI3K and Akt pathway (Manning and Toker, 2017).

mTORC1 is a master signaling hub in cells that can sense a wide range of cues including amino acids, growth factors as well as oxygen level, and exert broad impacts on different cellular progresses, ranging from macromolecule synthesis, cellular metabolism, cell growth to proliferation (Laplante and Sabatini, 2012). Akt can stimulate mTORC1 in two ways: Akt phosphorylates multiple residues of TSC2 component of the TSC complex on the lysosomal membrane, leading to the dissociation of TSC from the membrane and releasing its inhibition on Rheb, which is an essential activator for mTORC1 (Menon et al., 2014); Akt can also phosphorylate T246 of proline-rich Akt substrate of 40 kDa (PRAS40), an mTORC1 interacting and inhibitory protein, resulting in the dissociation of PRAS40 and activation of mTORC1 (Sancak et al., 2007). Although mTORC1 components have been found in different subcellular compartments (Bernardi et al., 2006b; Kantidakis et al., 2010; Rosner and Hengstschläger, 2012; Wan et al., 2017; Yang et al., 2008), the presence of intact mTORC1 complex and activity in subcellular compartments was under debate (Rosner and Hengstschläger, 2012). To examine the subcellular mTORC1 activity, several mTORC1 reporters were developed (Ahmed et al., 2019; Bouquier et al., 2020; Oki et al., 2021; Zhou et al., 2015). The first mTORC1 activity reporter (TORCAR) was constructed by sandwiching the full length mTORC1 substrate, 4EBP1, with a FRET pair. Phosphorylation on 4EBP1 by endogenous mTORC1 resulted in conformational changes that lead to changes of FRET signal (Zhou et al., 2015). TORCARs targeted to subcellular compartments revealed signal- and location- specific activation of mTORC in NIH3T3 cells. Specifically, growth factor PDGF can stimulate mTORC1 activity in the plasma membrane, however, amino acid cannot activate plasma membrane mTORC1 activity. Both growth factor and amino acid can stimulate mTORC1 activity in the lysosomal membrane, cytosol and nucleus (Zhou et al., 2015). The results obtained by TORCAR suggest a crucial role of compartmentation in regulating mTORC1 signaling. A similar design using another mTORC1 substrate S6K1 was reported (Ahmed et al., 2019). In addition, a BRET-based mTORC1 activity reporter called AIMTOR was used for monitoring mTORC1 activity during muscle cell differentiation and in neurons from mouse models with neuronal disorder (Bouquier et al., 2020). However, nearly all current mTORC1 reporters suffer from its low dynamic range, thus future optimization or new designs are needed to further the study of compartmentalized mTORC1 signaling.

One examples of studying PI3K-Akt-mTOR signaling using fluorescent reporters

To showcase how fluorescent biosensors can be used to examine PI3K-Akt-mTOR signaling pathway at subcellular levels, here we present one of the most recently published work (Chen et al., 2021), in which biosensors for phosphoinositides, Akt and mTORC1 were applied to dissect the molecular mechanisms regulating PI3K-Akt-mTOR signaling in the lysosomal membrane.

Chen and Sun *et al* developed a new Akt activity biosensor by introducing mutations to the linker regions flanking the cpGFP in ExRai-AktAR (Mehta et al., 2018), which has the largest dynamic range hitherto, and screening for the improved version of the sensor. A variant, named ExRai-AktAR2, was able to robustly report PDGF induced Akt activity at different subcellular compartments, including the lysosomal membrane. The specific spatial organization of Akt activity and the underlying mechanisms, particularly those controlling Akt activity at the lysosome, are not clearly understood. Using expansion microscopy, the authors found Akt could localize to lysosomes after growth factor stimulation, which correlates with the increased Akt activity at the lysosome. To test the hypothesis that 3-phosphoinositides could mediate the lysosomal localization, authors used lysosomally targeted PIP_3 and $PI(3,4)P_2$ indicator, InPAkt, and found that in response to growth factor stimulation, 3-phosphoinositides accumulates on the lysosomal membrane, in an endocytosis-dependent manner, as inhibition of endocytosis via overexpression of a dominant negative form of dynamin or via dynamin inhibitor completely abolished lysosomal InPAkt response. Since lysosome is the activation site for canonical mTORC1 by Akt, the authors probed both Akt and mTORC1 activity at lysosomes using lysosomally targeted ExRai-AktAR2 and TORCAR. It was shown that endocytosis inhibition also abolished both lysosomal Akt activity and mTORC1 activity. Similar results were observed when lipid phosphatase PTEN or INPP4B, which could destroy PIP_3 and $PI(3,4)P_2$ respectively, were exogenously expressed on the lysosome. The study found an important role of 3-phosphoinositides, which are usually thought to localize to plasma membrane, to accumulate on the lysosomal membrane and regulate multi-faceted kinase Akt to organize lysosome-specific signaling.

Conclusions and perspectives

While we appreciate the unique advantages of using genetically encoded fluorescent biosensors to understand the spatiotemporal regulation of PI3K-Akt-mTOR signaling and its important functions in biological processes, there are still a number of challenges that need to be overcome in order to push this field forward. For example, some of the phosphoinositide indicators are not specific enough to accurately assign signal changes to a specific phosphoinositide. Future screening for biosensor variants with enhanced specificity via directed evolution might be a solution. The dynamic range of mTORC1 biosensors is low, which in some extent limited the progress in understanding the mTORC1 signaling in different contexts. The Cryo-EM structures of both mTORC1 and mTORC2 are resolved (Chen et al., 2018; Yang et al., 2017), which may provide clues to engineer mTORC1 reporter with improved dynamic range and sensitivity.

PI3K-Akt-mTOR pathway regulates many aspects of cellular processes through its various downstream effector proteins. Thanks to the development and application of various biosensors in different cellular contexts, not only can we dissect the exquisite spatiotemporal mechanisms underlying physiological signaling, but we are also able to reveal the crucial roles of the regulatory proteins in pathological conditions, including neurodegenerative disease, diabetes and cancers. In recent decades, genetically encoded fluorescent biosensors have emerged as major tools for the study of cell signaling events due to their specificity, sensitivity and versatile designs. Given the importance of the fluorescent biosensor toolbox in probing the spatiotemporal regulation of cell signaling, many efforts are continually being dedicated to developing newer and better biosensors. With the advancement of chemical biology, synthetic biology, optical imaging and gene editing techniques, the future of genetically encoded fluorescent biosensors to study PI3K-Akt-mTOR signaling is bright.

Summary of chapters

Taking advantage of genetically encoded biosensors and combining a variety of different approaches, I set out to understand the regulation and functions of subcellular mTORC1, which is the focus of this dissertation. **Chapter 1** describes the development of a molecular tool, AktSTOPS, to specifically inhibit nuclear Akt activity and the elucidation of a noncanonical nuclear Akt-dependent mechanism that regulates nuclear mTORC1. **Chapter 2** further examines the role of a small GTPase, Rheb, in regulating nuclear mTORC1 activity, which has led to the discovery of a differential requirement of Rheb farnesylation in subcellular mTORC1 activation. To examine the functions of subcellular mTORC1, **Chapter 3** documents the development and characterization of a genetically targetable mTORC1 inhibitor to specifically suppress nuclear mTORC1 activity, by which a distinct role of nuclear mTORC1 in gene transcription is revealed.

Introduction, in full, is currently being prepared for submission of publication of the material. Zhong, Y., Mehta, S., Zhang, J. Scalpels at hand: genetically encoded biosensors to dissect PI3K-Akt-mTOR signaling pathway. The dissertation author was the primary investigator and author of this work.

References

Ahmed, A.R., Owens, R.J., Stubbs, C.D., Parker, A.W., Hitchman, R., Yadav, R.B., Dumoux, M., Hawes, C., Botchway, S.W., 2019. Direct imaging of the recruitment and phosphorylation of S6K1 in the mTORC1 pathway in living cells. Sci. Rep. 9, 3408.

Alessi, D.R., Andjelkovic, M., Caudwell, B., Cron, P., Morrice, N., Cohen, P., Hemmings, B.A., 1996. Mechanism of activation of protein kinase B by insulin and IGF-1. EMBO J. 15, 6541–6551.

Ananthanarayanan, B., Fosbrink, M., Rahdar, M., Zhang, J., 2007. Live-cell molecular analysis of Akt activation reveals roles for activation loop phosphorylation. J. Biol. Chem. 282, 36634–36641.

Ananthanarayanan, B., Ni, Q., Zhang, J., 2005. Signal propagation from membrane messengers to nuclear effectors revealed by reporters of phosphoinositide dynamics and Akt activity. Proc. Natl. Acad. Sci. USA 102, 15081–15086.

Bajar, B.T., Wang, E.S., Zhang, S., Lin, M.Z., Chu, J., 2016. A guide to fluorescent protein FRET pairs. Sensors (Basel) 16.

Balla, T., 2013. Phosphoinositides: tiny lipids with giant impact on cell regulation. Physiol. Rev. 93, 1019–1137.

Barlow, C.A., Laishram, R.S., Anderson, R.A., 2010. Nuclear phosphoinositides: a signaling enigma wrapped in a compartmental conundrum. Trends Cell Biol. 20, 25–35.

Belal, A.S.F., Sell, B.R., Hoi, H., Davidson, M.W., Campbell, R.E., 2014. Optimization of a genetically encoded biosensor for cyclin B1-cyclin dependent kinase 1. Mol. Biosyst. 10, 191–195.

Bernardi, R, Guernah, I., Jin, D., Grisendi, S., Alimonti, A., 2006. PML inhibits HIF-1α translation and neoangiogenesis through repression of mTOR. Nature.

Bernardi, Rosa, Guernah, I., Jin, D., Grisendi, S., Alimonti, A., Teruya-Feldstein, J., Cordon-Cardo, C., Simon, M.C., Rafii, S., Pandolfi, P.P., 2006. PML inhibits HIF-1alpha translation and neoangiogenesis through repression of mTOR. Nature 442, 779–785.

Bilanges, B., Posor, Y., Vanhaesebroeck, B., 2019. PI3K isoforms in cell signalling and vesicle trafficking. Nat. Rev. Mol. Cell Biol. 20, 515–534.

Bouquier, N., Moutin, E., Tintignac, L.A., Reverbel, A., Jublanc, E., Sinnreich, M., Chastagnier, Y., Averous, J., Fafournoux, P., Verpelli, C., Boeckers, T., Carnac, G., Perroy, J., Ollendorff, V., 2020. AIMTOR, a BRET biosensor for live imaging, reveals subcellular mTOR signaling and dysfunctions. BMC Biol. 18, 81.

Burd, C.G., Emr, S.D., 1998. Phosphatidylinositol(3)-phosphate signaling mediated by specific binding to RING FYVE domains. Mol. Cell 2, 157–162.

Calleja, V., Alcor, D., Laguerre, M., Park, J., Vojnovic, B., Hemmings, B.A., Downward, J., Parker, P.J., Larijani, B., 2007. Intramolecular and intermolecular interactions of protein kinase B define its activation in vivo. PLoS Biol. 5, e95.

Calleja, V., Ameer-Beg, S.M., Vojnovic, B., Woscholski, R., Downward, J., Larijani, B., 2003. Monitoring conformational changes of proteins in cells by fluorescence lifetime imaging microscopy. Biochem. J. 372, 33–40.

Chen, M., Sun, T., Zhong, Y., Zhou, X., Zhang, J., 2021. A Highly Sensitive Fluorescent Akt Biosensor Reveals Lysosome-Selective Regulation of Lipid Second Messengers and Kinase Activity. ACS Cent. Sci.

Chen, X., Liu, M., Tian, Y., Li, J., Qi, Y., Zhao, D., Wu, Z., Huang, M., Wong, C.C.L., Wang, H.-W., Wang, J., Yang, H., Xu, Y., 2018. Cryo-EM structure of human mTOR complex 2. Cell Res. 28, 518–528.

Chung, J., Torta, F., Masai, K., Lucast, L., Czapla, H., Tanner, L.B., Narayanaswamy, P., Wenk, M.R., Nakatsu, F., De Camilli, P., 2015. INTRACELLULAR TRANSPORT. PI4P/phosphatidylserine countertransport at ORP5- and ORP8-mediated ER-plasma membrane contacts. Science 349, 428–432.

Cicchetti, G., Biernacki, M., Farquharson, J., Allen, P.G., 2004. A ratiometric expressible FRET sensor for phosphoinositides displays a signal change in highly dynamic membrane structures in fibroblasts. Biochemistry 43, 1939–1949.

Dempke, W.C.M., Uciechowski, P., Fenchel, K., Chevassut, T., 2018. Targeting SHP-1, 2 and SHIP Pathways: A Novel Strategy for Cancer Treatment? Oncology 1–13.

Ding, Y., Li, J., Enterina, J.R., Shen, Y., Zhang, I., Tewson, P.H., Mo, G.C.H., Zhang, J., Quinn, A.M., Hughes, T.E., Maysinger, D., Alford, S.C., Zhang, Y., Campbell, R.E., 2015. Ratiometric biosensors based on dimerization-dependent fluorescent protein exchange. Nat. Methods 12, 195–198.

Dowler, S., Currie, R.A., Campbell, D.G., Deak, M., Kular, G., Downes, C.P., Alessi, D.R., 2000. Identification of pleckstrin-homology-domain-containing proteins with novel phosphoinositide-binding specificities. Biochem. J. 351, 19–31.

Ellson, C.D., Anderson, K.E., Morgan, G., Chilvers, E.R., Lipp, P., Stephens, L.R., Hawkins, P.T., 2001. Phosphatidylinositol 3-phosphate is generated in phagosomal membranes. Curr. Biol. 11, 1631–1635.

Gao, X., Zhang, J., 2008. Spatiotemporal analysis of differential Akt regulation in plasma membrane microdomains. Mol. Biol. Cell 19, 4366–4373.

Gozani, O., Karuman, P., Jones, D.R., Ivanov, D., Cha, J., Lugovskoy, A.A., Baird, C.L., Zhu, H., Field, S.J., Lessnick, S.L., Villasenor, J., Mehrotra, B., Chen, J., Rao, V.R., Brugge, J.S., Ferguson, C.G., Payrastre, B., Myszka, D.G., Cantley, L.C., Wagner, G., Divecha, N., Prestwich, G.D., Yuan, J., 2003. The PHD finger of the chromatin-associated protein ING2 functions as a nuclear phosphoinositide receptor. Cell 114, 99–111.

Gray, A., Van Der Kaay, J., Downes, C.P., 1999. The pleckstrin homology domains of protein kinase B and GRP1 (general receptor for phosphoinositides-1) are sensitive and selective probes for the cellular detection of phosphatidylinositol 3,4-bisphosphate and/or phosphatidylinositol 3,4,5-trisphosphate in vivo. Biochem. J. 344 Pt 3, 929–936.

Greenwald, E.C., Mehta, S., Zhang, J., 2018. Genetically encoded fluorescent biosensors illuminate the spatiotemporal regulation of signaling networks. Chem. Rev. 118, 11707–11794.

Hammond, G.R.V., Balla, T., 2015. Polyphosphoinositide binding domains: Key to inositol lipid biology. Biochim. Biophys. Acta 1851, 746–758.

Hammond, G.R.V., Machner, M.P., Balla, T., 2014. A novel probe for phosphatidylinositol 4-phosphate reveals multiple pools beyond the Golgi. J. Cell Biol. 205, 113–126.

Herman, P.K., Emr, S.D., 1990. Characterization of VPS34, a gene required for vacuolar protein sorting and vacuole segregation in Saccharomyces cerevisiae. Mol. Cell. Biol. 10, 6742–6754.

Hertel, F., Li, S., Chen, M., Pott, L., Mehta, S., Zhang, J., 2020. Fluorescent biosensors for multiplexed imaging of phosphoinositide dynamics. ACS Chem. Biol. 15, 33–38.

Hsu, P.P., Kang, S.A., Rameseder, J., Zhang, Y., Ottina, K.A., Lim, D., Peterson, T.R., Choi, Y., Gray, N.S., Yaffe, M.B., Marto, J.A., Sabatini, D.M., 2011. The mTOR-regulated phosphoproteome reveals a mechanism of mTORC1-mediated inhibition of growth factor signaling. Science 332, 1317–1322.

Itoh, T., Koshiba, S., Kigawa, T., Kikuchi, A., Yokoyama, S., Takenawa, T., 2001. Role of the ENTH domain in phosphatidylinositol-4,5-bisphosphate binding and endocytosis. Science 291, 1047–1051.

Jewell, J.L., Guan, K.-L., 2013. Nutrient signaling to mTOR and cell growth. Trends Biochem. Sci. 38, 233–242.

Kanai, F., Liu, H., Field, S.J., Akbary, H., Matsuo, T., Brown, G.E., Cantley, L.C., Yaffe, M.B., 2001. The PX domains of p47phox and p40phox bind to lipid products of PI(3)K. Nat. Cell Biol. 3, 675–678.

Kantidakis, T., Ramsbottom, B.A., Birch, J.L., Dowding, S.N., White, R.J., 2010. mTOR associates with TFIIIC, is found at tRNA and 5S rRNA genes, and targets their repressor Maf1. Proc. Natl. Acad. Sci. USA 107, 11823–11828.

Komatsu, N., Aoki, K., Yamada, M., Yukinaga, H., Fujita, Y., Kamioka, Y., Matsuda, M., 2011. Development of an optimized backbone of FRET biosensors for kinases and GTPases. Mol. Biol. Cell 22, 4647–4656.

Kunkel, M.T., Ni, Q., Tsien, R.Y., Zhang, J., Newton, A.C., 2005. Spatio-temporal dynamics of protein kinase B/Akt signaling revealed by a genetically encoded fluorescent reporter. J. Biol. Chem. 280, 5581–5587.

Laplante, M., Sabatini, D.M., 2012. mTOR signaling in growth control and disease. Cell 149, 274–293.

Lee, S.B., Várnai, P., Balla, A., Jalink, K., Rhee, S.-G., Balla, T., 2004. The pleckstrin homology domain of phosphoinositide-specific phospholipase Cdelta4 is not a critical determinant of the membrane localization of the enzyme. J. Biol. Chem. 279, 24362–24371.

Leitner, M.G., Thallmair, V., Wilke, B.U., Neubert, V., Kronimus, Y., Halaszovich, C.R., Oliver, D., 2019. The N-terminal homology (ENTH) domain of Epsin 1 is a sensitive reporter of physiological PI(4,5)P2 dynamics. Biochim. Biophys. Acta Mol. Cell Biol. Lipids 1864, 433–442.

Li, X., Wang, X., Zhang, X., Zhao, M., Tsang, W.L., Zhang, Y., Yau, R.G.W., Weisman, L.S., Xu, H., 2013. Genetically encoded fluorescent probe to visualize intracellular phosphatidylinositol 3,5-bisphosphate localization and dynamics. Proc. Natl. Acad. Sci. USA 110, 21165–21170.

Malek, M., Kielkowska, A., Chessa, T., Anderson, K.E., Barneda, D., Pir, P., Nakanishi, H., Eguchi, S., Koizumi, A., Sasaki, J., Juvin, V., Kiselev, V.Y., Niewczas, I., Gray, A., Valayer, A., Spensberger, D., Imbert, M., Felisbino, S., Habuchi, T., Beinke, S., Cosulich, S., Le Novère, N., Sasaki, T., Clark, J., Hawkins, P.T., Stephens, L.R., 2017. PTEN regulates PI(3,4)P2 signaling downstream of class I PI3K. Mol. Cell 68, 566–580.e10.

Manna, D., Albanese, A., Park, W.S., Cho, W., 2007. Mechanistic basis of differential cellular responses of phosphatidylinositol 3,4-bisphosphate- and phosphatidylinositol 3,4,5-trisphosphate-binding pleckstrin homology domains. J. Biol. Chem. 282, 32093–32105.

Manning, B.D., Toker, A., 2017. AKT/PKB signaling: navigating the network. Cell 169, 381–405.

Martelli, A.M., Tabellini, G., Bressanin, D., 2012. The emerging multiple roles of nuclear Akt. et Biophysica Acta (BBA.

Mehta, S., Zhang, J., 2021. Biochemical Activity Architectures Visualized-Using Genetically Encoded Fluorescent Biosensors to Map the Spatial Boundaries of Signaling Compartments. Acc. Chem. Res. 54, 2409–2420.

Mehta, S., Zhang, Y., Roth, R.H., Zhang, J.-F., Mo, A., Tenner, B., Huganir, R.L., Zhang, J., 2018. Single-fluorophore biosensors for sensitive and multiplexed detection of signalling activities. Nat. Cell Biol. 20, 1215–1225.

Menon, S., Dibble, C.C., Talbott, G., Hoxhaj, G., Valvezan, A.J., Takahashi, H., Cantley, L.C., Manning, B.D., 2014. Spatial control of the TSC complex integrates insulin and nutrient regulation of mTORC1 at the lysosome. Cell 156, 771–785.

Miura, H., Matsuda, M., Aoki, K., 2014. Development of a FRET biosensor with high specificity for Akt. Cell Struct Funct 39, 9–20.

Mo, G.C.H., Posner, C., Rodriguez, E.A., Sun, T., Zhang, J., 2020. A rationally enhanced red fluorescent protein expands the utility of FRET biosensors. Nat. Commun. 11, 1848.

Nakai, J., Ohkura, M., Imoto, K., 2001. A high signal-to-noise Ca(2+) probe composed of a single green fluorescent protein. Nat. Biotechnol. 19, 137–141.

Nishioka, T., Aoki, K., Hikake, K., Yoshizaki, H., Kiyokawa, E., Matsuda, M., 2008. Rapid turnover rate of phosphoinositides at the front of migrating MDCK cells. Mol. Biol. Cell 19, 4213–4223.

Oki, T., Mercier, F., Kato, H., Jung, Y., McDonald, T.O., Spencer, J.A., Mazzola, M.C., van Gastel, N., Lin, C.P., Michor, F., Kitamura, T., Scadden, D.T., 2021. Imaging dynamic mTORC1 pathway activity in vivo reveals marked shifts that support time-specific inhibitor therapy in AML. Nat. Commun. 12, 245.

Periasamy, A., Mazumder, N., Sun, Y., Christopher, K.G., Day, R.N., 2015. FRET Microscopy: Basics, Issues and Advantages of FLIM-FRET Imaging. In: Becker, W. (Ed.), Advanced Time-Correlated Single Photon Counting Applications, Springer Series in Chemical Physics. Springer International Publishing, Cham, pp. 249–276.

Pierre-Eugene, C., Pagesy, P., Nguyen, T.T., Neuillé, M., Tschank, G., Tennagels, N., Hampe, C., Issad, T., 2012. Effect of insulin analogues on insulin/IGF1 hybrid receptors: increased activation by glargine but not by its metabolites M1 and M2. PLoS One 7, e41992.

Quinn, K.V., Behe, P., Tinker, A., 2008. Monitoring changes in membrane phosphatidylinositol 4,5-bisphosphate in living cells using a domain from the transcription factor tubby. J. Physiol. (Lond.) 586, 2855–2871.

Rosner, M., Hengstschläger, M., 2012. Detection of cytoplasmic and nuclear functions of mTOR by fractionation. Methods Mol. Biol. 821, 105–124.

Sancak, Y., Thoreen, C.C., Peterson, T.R., Lindquist, R.A., Kang, S.A., Spooner, E., Carr, S.A., Sabatini, D.M., 2007. PRAS40 is an insulin-regulated inhibitor of the mTORC1 protein kinase. Mol. Cell 25, 903–915.

Santagata, S., Boggon, T.J., Baird, C.L., Gomez, C.A., Zhao, J., Shan, W.S., Myszka, D.G., Shapiro, L., 2001. G-protein signaling through tubby proteins. Science 292, 2041–2050.

Sasaki, K., Sato, M., Umezawa, Y., 2003. Fluorescent indicators for Akt/protein kinase B and dynamics of Akt activity visualized in living cells. J. Biol. Chem. 278, 30945–30951.

Sato, M., Ueda, Y., Takagi, T., Umezawa, Y., 2003. Production of PtdInsP3 at endomembranes is triggered by receptor endocytosis. Nat. Cell Biol. 5, 1016–1022.

Saxton, R.A., Sabatini, D.M., 2017. mTOR Signaling in Growth, Metabolism, and Disease. Cell 168, 960–976.

Stauffer, T.P., Ahn, S., Meyer, T., 1998. Receptor-induced transient reduction in plasma membrane PtdIns(4,5)P2 concentration monitored in living cells. Curr. Biol. 8, 343–346.

van der Wal, J., Habets, R., Várnai, P., Balla, T., Jalink, K., 2001. Monitoring agonist-induced phospholipase C activation in live cells by fluorescence resonance energy transfer. J. Biol. Chem. 276, 15337–15344.

Várnai, P., Balla, T., 1998. Visualization of phosphoinositides that bind pleckstrin homology domains: calcium- and agonist-induced dynamic changes and relationship to myo-[3H]inositol-labeled phosphoinositide pools. J. Cell Biol. 143, 501–510.

Violin, J.D., Zhang, J., Tsien, R.Y., Newton, A.C., 2003. A genetically encoded fluorescent reporter reveals oscillatory phosphorylation by protein kinase C. J. Cell Biol. 161, 899–909.

Wan, W., You, Z., Xu, Y., Zhou, L., Guan, Z., Peng, C., Wong, C.C.L., Su, H., Zhou, T., Xia, H., Liu, W., 2017. mTORC1 Phosphorylates Acetyltransferase p300 to Regulate Autophagy and Lipogenesis. Mol. Cell 68, 323–335.e6.

Yang, H., Jiang, X., Li, B., Yang, H.J., Miller, M., Yang, A., Dhar, A., Pavletich, N.P., 2017. Mechanisms of mTORC1 activation by RHEB and inhibition by PRAS40. Nature 552, 368–373.

Yang, T.T.C., Yu, R.Y.L., Agadir, A., Gao, G.-J., Campos-Gonzalez, R., Tournier, C., Chow, C.-W., 2008. Integration of protein kinases mTOR and extracellular signal-regulated kinase 5 in regulating nucleocytoplasmic localization of NFATc4. Mol. Cell. Biol. 28, 3489–3501.

Yoshizaki, H., Aoki, K., Nakamura, T., Matsuda, M., 2006. Regulation of RalA GTPase by phosphatidylinositol 3-kinase as visualized by FRET probes. Biochem. Soc. Trans. 34, 851–854.

Zhang, J., Hupfeld, C.J., Taylor, S.S., Olefsky, J.M., Tsien, R.Y., 2005. Insulin disrupts beta-adrenergic signalling to protein kinase A in adipocytes. Nature 437, 569–573.

Zhou, X., Clister, T.L., Lowry, P.R., Seldin, M.M., Wong, G.W., Zhang, J., 2015. Dynamic Visualization of mTORC1 Activity in Living Cells. Cell Rep. 10, 1767–1777.

Zhou, X., Zhong, Y., Molinar-Inglis, O., Kunkel, M.T., Chen, M., Sun, T., Zhang, Jiao, Shyy, J.Y.-J., Trejo, J., Newton, A.C., Zhang, Jin, 2020. Location-specific inhibition of Akt reveals regulation of mTORC1 activity in the nucleus. Nat. Commun. 11, 6088.

Chapter 1

Location-specific inhibition of Akt reveals regulation of mTORC1 activity in the nucleus

Introduction

The mechanistic target of rapamycin complex 1 (mTORC1), which contains the protein kinase mTOR, the key scaffolding protein Raptor, and several additional core components (Hara et al., 2002; Kim et al., 2002; Kim et al., 2003), senses a wide range of intracellular and extracellular cues, including growth factors, amino acids, and cellular energy status (Kim and Guan, 2019). When activated, mTORC1 incorporates these signals to coordinate a number of distinct cellular processes, such as cell growth and metabolism, by promoting the biosynthesis of macromolecules and energy production and suppressing the breakdown of proteins via inhibition of autophagy (Kim and Guan, 2019; Saxton and Sabatini, 2017). Activation of mTORC1 on the lysosomal surface is well-documented in the literature (Demetriades et al., 2014; Menon et al., 2014; Zoncu et al., 2011). Upon growth factor stimulation, protein kinase Akt phosphorylates the catalytic component of the tuberous sclerosis complex (TSC), dissociating it from the lysosomal surface and thereby relieving its negative regulation on Rheb, a direct and potent activator of mTORC1 (Dibble and Cantley, 2015; Inoki et al., 2002; Menon et al., 2014). On the other hand, mTORC1 is also recruited and activated at the lysosome in Rag GTPase-dependent or independent manners in response to amino acid stimulation (Laplante and Sabatini, 2013). However, the regulation of mTORC1 within other subcellular compartments is less clear (Betz and Hall, 2013). For instance, although mTOR and Raptor have been found in the nucleus by nuclear fractionation and immunofluorescence (Bernardi et al., 2006; Havel et al., 2015; Kantidakis et al., 2010; Kazyken et al., 2014; Ramiscal et al., 2015; Rosner and Hengstschlager, 2008, 2011, 2012; Wan et al., 2017; Yang et al., 2008), the presence of active and functional nuclear mTORC1 was debatable (Rosner and Hengstschlager, 2008). To examine nuclear mTORC1 activity, we developed a genetically encoded FRET-based biosensor, TORCAR, to visualize the activity dynamics of mTORC1 in living cells (Zhou et al., 2015a). Briefly, TORCAR was constructed by sandwiching the mTORC1-specific substrate 4EBP1 between a pair of fluorescent proteins that can undergo FRET. Phosphorylation of TORCAR by endogenous mTORC1 induces a conformational change that leads to an increase in the emission ratio of cyan over yellow (C/Y) (Zhou et al., 2015a). Using TORCAR targeted to the nucleus via nuclear localization signal (TORCAR-NLS), we showed that nuclear mTORC1 activity is stimulated by either growth factors or amino acid surrogates in serum- and amino acid-starved NIH3T3 cells (Zhou et al., 2015a), providing initial evidence for active mTORC1 in the nucleus.

In this study, we focus on the regulation of nuclear mTORC1 activity. The serine/threonine kinase Akt is a critical component in the growth factor-stimulated mTORC1 signaling pathway. In the classical model, Akt critically regulates mTORC1 signaling at two different levels: Akt phosphorylates TSC2 within the aforementioned TSC complex and results in the activation of Rheb, a direct and potent activator of mTORC1; on the other hand, Akt phosphorylates PRAS40, an inhibitory component of mTORC1, leading to its dissociation from and activation of mTORC1 (Dibble and Manning, 2013; Jewell and Guan, 2013). Here we report a molecular tool, Akt-STOPS, that specifically suppresses Akt signaling at distinct subcellular localizations. Using Akt-STOPS, we discovered that nuclear mTORC1 activity is specifically dependent on the nuclear Akt activity. We further demonstrate that Akt facilitates nuclear translocation of Raptor, the regulatory component of mTORC1, which contributes to nuclear mTORC1 signaling. Thus, our findings reveal a noncanonical regulatory mechanism that specifically regulates a nuclear pool of mTORC1.

Methods

Constructs

To construct Akt-STOPS, AktAR2 in pcDNA3 (Addgene #64932) was cut with *BamH*I/*EcoR*I to replace the backbone with pRSetB to generate AktAR2 in pRSetB. AktAR2 in pRSetB was then cut with *BamH*I/*Sph*I to replace cerulean3 with mCherry. Then, this backbone was cut with *Sph*I/*Sal*I and ligated with a pair of annealed primers encoding Akt substrate recognition sequence derived from FoxO1 (PRPRSCTWPDPRPEF) with *Sph*I/*Sal*I restriction sites, followed by cutting with *Sac*I/*EcoR*I and ligation with a pair of annealed primers encoding PRPRSCTWPDPRPEF with *Sac*I/*EcoR*I restriction sites to generate the final Akt-STOPS in pRSetB. The construct was verified by sequencing after subcloning into a modified version of the mammalian expression vector pcDNA3'. Scramble peptide sequence was generated by randomizing Akt substrate recognition sequence derived from FoxO1 using peptidenexus.com. To generate mCherry tagged scramble peptide, mChe-SP, a series of primers encoding TPCPSEWPRRPRDPF were used following the above cloning scheme. The nuclear targeted constructs, TORCAR-NLS, AktAR2-NLS, Akt-STOPS-NLS and SP-NLS, were constructed by tagging a nuclear localization signal (NLS) PKKKRKVEDA (Ananthanarayanan et al., 2007) to the C terminus of TORCAR (Zhou et al., 2015a), AktAR2 (Zhou et al., 2015a), Akt-STOPS and mChe-SP, respectively. The cytosolic targeted constructs, TORCAR-NES and AktAR2-NES, were generated by fusing a nuclear excluding signal (NES) (Sample et al., 2012) to the C terminus of TORCAR and AktAR2. The plasma membrane targeted constructs, PM-AktAR2 and PM-Akt-STOPS, were constructed by the addition of the N-terminal portion of the Lyn kinase (GCIKSKRKDKD) to the 5’ end of AktAR2 and Akt-STOPS, respectively (Gao et al., 2011).

H2A-mChe was constructed by subcloning with a *Hind*III/*BamH*I-digested PCR fragment encoding Histone 2A and a *BamH*I/*EcoR*I-digested PCR fragment with stop codon encoding mCherry. H2A-mChe-S6K1 and H2A-mChe-Raptor were generated by subcloning with a *BamH*I/*Sph*I-digested PCR fragment encoding mCherry and *Sph*I/*EcoR*I-digested PCR fragment with stop codon encoding S6K1 or Raptor, respectively. FKBP and FRB constructs were kindly provided by Dr. Takanari Inoue (Johns Hopkins University). PM-FRB was generated by the addition of the N-terminal portion of the Lyn kinase (GCIKSKRKDKD) to the 5' end of FRB. FKBP with a flexible linker was added to the N-terminus of Akt-STOPS (Clister et al., 2019) using *Hind*III and *BamH*I restriction sites.

Reagents

PDGF (P3201), insulin (I-5523), IBMX (I5879) and Gö6983 (G1918) were purchased from Sigma. Nuclear-ID Red (Enzo-52406) was purchased from Enzo Life Sciences. Torin1 was purchased from TOCRIS (#4247). Leucine O-methyl ester was purchased from NovaBiochem. Leptomycin B (LMB, AAJ63784EXG) and Importazole (IPZ, S8446) were purchased from Fisher Scientific. Forskolin (F9929) and rapamycin (R-5000) were purchased from LC Labs. Rapalog (AP21967, #635067) was purchased from Takara Bio. GDC-0068 (RG7440) was purchased from APExBIO. STOPS peptide (PRPRSCTWPDPRPE) was synthesized by Fmoc solid phase peptide synthesis and purified by reverse phase HPLC (95.8% purity) with standard TFA removal by GenScript. Identity and purity were confirmed by HPLC-MS. pLKO mouse shRNA 1 raptor was purchased from Addgene (#21339).

Cell culture, transfection, and starvation

NIH3T3 cells (CRL-1658, ATCC) were cultured in Dulbecco's modified Eagle's medium (11885, Gibco) supplemented with 10% calf serum (30-2030, ATCC) and 1% of penicillin-streptomycin (Sigma-Aldrich) and were routinely tested for mycoplasma contamination and found negative. For live cell imaging, cells were plated onto sterile glass-bottomed 35-mm dishes (D35-14-1.5-N, CellVis) and grown to 40% confluency at 37°C with 5% CO_2. For immunofluorescence and proximity ligation assay, NIH3T3 cells were seeded into 18 mm coverslip at ~30% confluency in 35 mm dishes containing glass coverslips (12-541A, FisherBrand). For transfection, cells were either transfected with Lipofectamine 2000 (Invitrogen) or nucleofected using 4D-Nucleofector System (Core and X-unit, Lonza) with recommended kits. For serum starvation, cells were starved in serum-free DMEM for 24 hr. For serum and amino acid starvation (double starvation, referred as "DS", and cells were double-starved if not otherwise indicated), cells were serum-starved for 24 h (DMEM without serum) followed by 2 h amino acid starvation in modified Hank's balanced salt solution (1×HBSS with 2 g/l glucose, pH 7.4, made from 10× HBSS (14065, GIBCO)) at 37°C.

Differentiation and Nucleofection of 3T3-L1 Adipocytes

3T3-L1 preadipocytes were grown to confluency in 10% calf serum/DMEM and stimulated with induction media (DMEM containing 10% fetal bovine serum, 1 μg/ml insulin, 1 μM dexamethasone, and 0.5 mM 3-isobutyl-1-methylxanthine) at 2 days post-confluency. The medium was changed to insulin medium (1 μg/ml) 2 days after induction. Two days later, the medium was replaced with 10% fetal bovine serum/DMEM and then changed every 2 days. Nucleofection with H2A-TORCAR was carried out 10 days after full differentiation according to the manufacturer's instructions (Lonza).

Lentivirus production and cell transduction

Lentivirus was packaged in HEK293T cells. Specifically, HEK293T cells were co-transfected with lentiviral vector (containing sequences expressing shRNA targeting mouse raptor proteins)(Thoreen et al., 2009) + psPAX2 + pMD2.G using PolyJet transfection reagent (SignaGen Laboratories, MD, USA) according to manufacturer's instructions. After 48 hr the supernatants were collected, and then concentrated using Lenti-X concentrator (Takara Bio USA, Inc.) according to the manufacturer's instructions. The concentrated virus was stored at −80°C. For transduction, NIH3T3 cells were seeded, and concentrated solutions containing lentiviral particles were added into the cell culture medium. After 48 hr, cells were passed in fresh growth medium and were treated with puromycin (2 μg/mL) to select transduced cells. Cells were maintained in selection medium for one week and samples were collected for western blot and immunofluorescence staining(Thoreen et al., 2009).

Immunoblotting

Cells were washed with ice-cold PBS and then lysed in RIPA lysis buffer containing protease inhibitor cocktail, 1 mM PMSF, 1 mM Na_3VO_4, 1 mM NaF, and 25 nM calyculin A. Total cell lysates were incubated on ice for 30 min and then centrifuged at 4°C for 20 min. Total protein was separated via 4-15% SDS-PAGE and transferred to PVDF membranes. The membranes were blocked with TBS containing 0.1% Tween-20 and 5% bovine serum albumin and then incubated with primary antibodies overnight at 4°C. After incubation with the appropriate horseradish peroxidase-conjugated secondary antibodies, the membranes were developed using horseradish peroxidase-based chemiluminescent substrate (34579 and 34076, Thermoscientific). The intensity of the bands was quantified with ImageJ 1.52s software. The following primary antibodies were used for immunoblotting: p-4EBP1 (T37/46) (#2855), 4EBP1 (#9452), p-S6K1 (T389) (#9205), S6K1 (#9202), p-GSK3β (S9) (#9322), p-PRAS40 (T246) (#2997), PRAS40 (#2691), p-NDRG1 (S330) (#3506), NDRG1 (#5196), p-rpS6 (S240/244) (#5364), rpS6 (#2317), p-FoxO1 (S256) (#9461), FoxO1 (#2880), p-RanBP3 (S58) (#9380) and tubulin (#2146) antibodies from Cell Signaling Technology, GSK3β (#610201) antibody from BD Bioscience, RanBP3 (700076) antibody from Invitrogen, Raptor antibody (20984-1-AP) from Proteintech, and RFP antibody (A00682-100) from GenScript. The horseradish peroxidase-labeled goat anti-rabbit (PI31460) or anti-mouse (PI31430) secondary antibodies were purchased from Pierce.

Protein purification

The catalytic domain of Akt3 (residues N118 to E479) was subcloned into p3XFlag-CMV-10 (Sigma) and transfected into 3x15 cm dishes of HEK293T cells using Effectene (QIAGEN). Flag-Akt3 catalytic domain (Akt3-Cat) was purified as described(Miller et al., 2019). Briefly, cells expressing Flag-tagged Akt3-Cat were lysed in 20 mM Tris (pH 7.5), 150 mM NaCl, 1 mM EDTA, 1 mM EGTA, 1% Triton X-100, 2.5 mM sodium pyrophosphate, 1 mM β-glycerophosphate, 1 mM Na_3VO_4, 1 mM DTT, 1 mM PMSF, 10 μg/ml leupeptin, 2 μg/ml pepstatin, 10 μg/ml aprotinin. The soluble cell lysate was incubated with anti-FLAG M2 beads (Sigma) for 1 hour at 4°C. After 4 washes total, Akt3-Cat protein was eluted in 50 mM HEPES, pH 7.4, 100 mM NaCl, 1 mM DTT, 5 mM β-glycerophosphate, 0.1 mM Na_3VO_4, 0.01% NP40 (Igepal CA630), 10% glycerol containing 0.5 mg/mL 3xFLAG Peptide (Sigma) (Miller et al., 2019). Protein was quantified using Coomassie (Bradford) Protein Assay (Thermofisher) and stored at -80°C until use. Human PKCβII was cloned into the pFastBac HT/B vector (ThermoFisher) that was modified with a GST tag. PKCβII protein was purified as described (Callender et al., 2018). Briefly, Sf-21 insect cells expressing GST-PKCβII protein were lysed in 50 mM HEPES, pH 7.5, 1 mM EDTA, 100 mM NaCl, 0.1% Triton X-100, 100 μM PMSF, 1 mM DTT, 2 mM benzamidine, 50 μg/mL leupeptin, and 1 μM microcystin. The soluble cell lysate was incubated with glutathione Sepharose beads for 30 min at 4˚C. After washes, GST-PKCβII was eluted in 50 mM HEPES, pH 7.5, 1 mM EDTA, 100 mM NaCl, 0.1 mg/mL BSA, and 1 mM DTT with 10 mM glutathione. Pure protein was quantified by Coomassie gel using BSA as controls and then stored in 50% glycerol at -20°C until use.

***In vitro* kinase assays**

For Akt3 catalytic domain assays, 50 ng of pure protein was used per time point. 80 μl reactions were carried out in 20 mM HEPES, pH7.5, 2 mM $MgCl_2$, 2 mM DTT, 100 μM ATP, 0.1 mg/ml BSA, ~50 μCi/ml γ-^{32}P-ATP (Perkin Elmer) with 0, 3, 10, 30, 100 and 300 μM Akt-STOPS peptide (GenScript) for 10 minutes at 30°C. Reactions were quenched by addition 25 μl 0.1 M ATP, 0.1 M EDTA, pH 8 and spotted on P81 paper (Whatman), washed 4 times with 500 ml 0.4% phosphoric acid and counted in a scintillation counter (Beckman). 30 μM Crosstide peptide was used to confirm Akt3 catalytic domain activity; from this, the specific activity of the preparation was determined to be 380 nmol/min/mg. For PKCβII kinase assays, 50 ng of pure protein was used per time point. 80 μl reactions were carried out in 20 mM HEPES, pH 7.4, 2 mM DTT, 5 mM $MgCl_2$, 100 μM ATP, ~1 μCi gamma-32P-ATP, 140 μM/3.8 μM phosphatidylserine/diacylglycerol membranes, 100 μM Ca2+. Stocks of Akt-STOPS peptide were prepared for final concentrations of 0, 3, 10, 30, 100 and 300 μM, and the kinase reactions were carried out for 10 minutes at 30°C (Keranen and Newton, 1997). Reactions were quenched by addition 25 μl 0.1 M ATP, 0.1 M EDTA, pH 8 and spotted on P81 paper (Whatman), washed 4 times with 500 ml 0.4% phosphoric acid and counted in a scintillation counter (Beckman). 100 µM of MARCKS peptide was used determine the activity of the PKCβII preparation; from this, the specific activity was determined to be 580 nmol/min/mg.

Nuclear Fractionation

NIH3T3 cells were seeded in a 10 cm dish and grown to 80% confluency. Cells were either left untreated or treated for 30-40 min with 50 ng/ml PDGF. Cells were washed twice with ice cold 1x PBS and harvested in 1x PBS. Following centrifugation for 5 min at 2348 xg at 4°C, cell pellet was resuspended in 150µL of 1x hypotonic lysis buffer (20mM HEPES, pH 7.4, 10 mM NaCl, 3 mM $MgCl_2$, Roche protease cocktail inhibitors, 1 mM PMSF, 1 mM Na_3VO_4, 1 mM NaF, and 25 nM calyculin A), and incubated for 1 hr to allow for cell lysis. Cells were passed through a 27 ½ G needle 15 times to maximize lysis. BCA quantification was performed, and protein levels were normalized to the lowest protein concentration (1-2 mg/ml). To extract nuclear content, the membrane proteins were solubilized by adding NP-40 at a final concentration of 0.5% and incubated for 1 hr on ice. All samples were centrifuged at 2348xg for 10 minutes, nuclear pellets were saved and supernatant was centrifuged a second time to remove any remaining nuclear impurities. Nuclear pellets were washed twice, combined accordingly in 150 µL of hypotonic buffer, sonicated to solubilize pellet. Samples were prepared with Laemmli sample buffer with 0.1 mM DTT. Equal protein amounts within respective fractions were loaded (Mata-Cabana et al., 2018) and assessed via SDS-PAGE on 9% gels or gradient gels. Proteins were transferred to PVDF membranes. Membranes were blocked for 1 hr in 4% BSA in 1x TBST and probed overnight in 4% BSA in 1x TBST for mouse anti-p84 (GTX70220, GeneTex), mouse anti-GAPDH (GTX627408, GeneTex), p-mTOR (S2448) (#2971, Cell Signaling), mTOR (#2972, Cell

Signaling), Raptor (20984-1-AP, Proteintech), p-PRAS40 (T246) (#2997, Cell Signaling), and PRAS40 (#2691, Cell Signaling). Blots were incubated in 5% milk in 1x TBST for 1 hr at room temperature and appropriate HRP-conjugated secondary antibodies. Blots were subjected to chemiluminescence, blots were analyzed by densitometry in Image J. For quantification, levels of target proteins in either cytoplasmic or nuclear fractions were normalized to each respective control (GAPDH for cytoplasmic fractions and p84 for nuclear fractions), and the changes between non-treated and treated samples were compared by setting the non-treated sample as 1. In this protocol, we loaded equal protein amounts for each respective fractions, and normalized the levels of the target proteins within respective fractions to a fraction marker (GAPDH and p84 for cytoplasmic and nuclear fractions, respectively), to cancel out the potential loading error (Benvegnu et al., 2017; Merthan et al., 2019; Torrini et al., 2019). This protocol is suited for comparing protein levels in the nuclear fraction before and after PDGF treatment but not designed to compare protein abundance between the cytoplasmic and nuclear fractions(Mata-Cabana et al., 2018).

Proximity Ligation Assay

PLA experiments were performed using the Duolink *in situ* red starter kit for proximity ligation assays (Sigma Aldrich, DUO92101) following the manufacturer's protocol. Briefly, cells grown on coverslips were fixed and permeabilized as in the immunofluorescence experiments then blocked with blocking buffer supplied with the kit at 37˚C for 1 hr. Cells were incubated with the primary antibody (mouse anti-mTOR, 66888-1-Ig, Proteintech, 1:100, and rabbit anti-Raptor, 20984-1-AP, Proteintech, 1:100) overnight at 4˚C, and then with the provided secondary antibody (conjugated with nucleotides) for 1 h at 37˚C with washes after each step. Ligation of the nucleotides and amplification of the strand occurred sequentially by incubating cells with first ligase and then polymerase and detection solution. PLA experiments with mTOR antibodies from different species (mouse anti-mTOR, 66888-1-Ig from Proteintech, 1:100, rabbit anti-mTOR, #2983 from Cell Signaling, 1:100) were used as positive controls, and experiments with mouse anti-mTOR only or mouse anti-mTOR with normal rabbit IgG (#2729, Cell Signaling) provided our negative controls.

Immunofluorescence

Cells were washed 3 times with PBS and fixed with 4% paraformaldehyde in PBS (15710S, Electron Microscopy Sciences) for 30 min at room temperature. Cells were then washed 3 times with PBS and permeabilized with PBS containing 0.1% Triton X-100 for 15 min at room temperature. Following 1-hr incubation in blocking buffer (PBS containing 0.1% Triton X-100 and 5% BSA) at room temperature, coverslips were incubated for 12 hr at 4ºC in primary antibody diluted in blocking buffer. The following primary antibodies were used for immunofluorescence: Raptor (20984-1-AP, Proteintech, 1:100), mTOR (#2983, Cell Signaling, 1:100), p-PRAS40 (T246) (#2997, Cell Signaling, 1:100), PRAS40 (ThermoFisher, AHO1031, 1:100), RanBP3 (Invitrogen, 700076, 1:100). Following three 5 min washes in PBS, coverslips were incubated for 1 hr at room temperature in the dark in secondary antibody (anti-rabbit Alexa Fluor 488, A11006 (1:1000), anti-mouse Alexa Fluor 568, A11004 (1:1000), Life Technologies/Molecular Probes) diluted in blocking buffer containing 0.1% Triton X-100. Following three 5 min washes with PBS, coverslips were mounted in Prolong Glass antifade Mountant with NucBlue (P36981, Invitrogen).

Microscopy and Image Analysis

For live-cell imaging, cells were washed once with modified Hank's balanced salt solution (1×HBSS with 2 g/l glucose, pH 7.4, made from 10× HBSS (14065, GIBCO)) and imaged in the dark at room temperature. Images were acquired on a Zeiss Axio Observer Z1 microscope equipped with a 40x/1.3NA objective and Photometrics Evolve 512 EMCCD. Dual-emission ratio imaging was performed with a 420DF20 excitation filter, a 495DF10 excitation filter, a 450DRLP dichroic mirror, and two emission filters, 475DF40 and 535DF25 for CFP and YFP, respectively. For RFP, a 568DF55 excitation filter, a 600DRLP dichroic mirror, and a 653DF95 emission filter were used. Exposure times were 50–500 ms, and images were taken every 30 s. Imaging data was analyzed with Metafluor 7.7 software (Molecular Device). Fluorescence images were background-corrected by deducting the background (regions with no cells) from the emission intensities of CFP or YFP. Regions of interest (ROIs) at the plasma membrane were used for analysis for PM-AktAR2. The ratios of emissions (cyan-to-yellow for TORCAR related imaging and yellow-to-cyan for AktAR2 related imaging) were then calculated at different time points. The ratio was normalized to the average ratio of timepoints before addition of drugs.

For PLA, the two-color (red and blue, excitation 405/561nm, emission filter BP420-480 + LP605) confocal images were acquired by a Zeiss LSM880 microscope equipped with a Plan-Apochromat 63X/1.4 oil immersion objective and an airyscan super-resolution detector, using Zen Black Zeiss software for acquisition and processing. The z-stack containing 9 optical slices with a thickness of 0.385 μm for each slice was acquired for both channels. The images were 1000 x 1000 pixels with a pixel size of 137nm. Identical settings were kept constant within a batch of experiments. For each condition, four different fields and 20 to 50 cells were analyzed. For quantitative analyses, the central slice of a z-stack containing 9 slices (0.385 μm each) was used, and the number of dots were counted within the nucleus using CellProfiler 3.0.0 software (Broad Institute) (Carpenter et al., 2006).

For quantifying Raptor translocation, the two-color (green and blue, excitation 405/488nm, emission filter BP420-480 + BP495-550) confocal images were acquired by a Zeiss LSM880 microscope as described above, except the images were 3812 x 3812 pixels with a pixel size of 35nm. Identical settings were kept constant within a batch of experiments. For each condition, three to seven different fields and 20 to 30 cells were analyzed per condition. For measuring Akt-STOPS effects on Raptor translocation, the three-color (green, red and blue) images were acquired by Zeiss Axio Observer Z1 microscope with a 40x/1.3NA objective and Photometrics Evolve 512 EMCCD. For DAPI and mCherry imaging, settings were the same as described above in the live cell time lapse imaging section. For AF488, HQ480/30x excitation filter and HQ535/45m emission filter were used. For each condition, 10-20 different fields and 100-600 cells were analyzed per condition.

The nuclear to cytosol ratio was quantified using CellProfiler (Broad Institute) software(Carpenter et al., 2006). Briefly, images were thresholded in each color channel to determine the nuclear and cytoplasmic areas outside of the nucleus. The mean intensity of nuclear fluorescence was then measured as the average pixel intensity within the nuclear area, and the mean intensity of cytoplasmic fluorescence was determined by the average pixel intensity in the non-nuclear cytoplasmic area. Lastly, the nuclear to cytoplasmic ratio was calculated as the mean intensity of nuclear fluorescence divided by the mean intensity of cytoplasmic fluorescence. For cells transfected with H2A-mChe or H2A-Akt-STOPS, the nuc/cyto ratio of Raptor immunostaining was calculated only for cells showing red fluorescence above threshold. For validation of Raptor antibody, the mean intensity of entire cell including cytosol and nucleus was measured.

Time course curve fitting

Using CFTool (3.4.1) in MatLab 8.3.0.532 (R2014A), the reporter response curves were fitted with an empirical sigmoidal funcation (Equation (1)), where F_0 is the response at the baseline, F_{max} is the response at the plateau of the progress curve, t_0 is the sigmoid's midpoint, and k is an apparent rate (Arosio et al., 2015). The lag time t_{lag} is estimated by extrapolating the tangent at the inflection time point to the initial baseline, and is then calculated by Equation (2).

$$F(t) = \frac{F_{\max}}{1+\nu \mathrm{e}^{-k(t-t_0)}} + F_0 \qquad (1)$$

$$t_{lag} = t_0 + \frac{\ln(\nu)-2}{k} \qquad (2)$$

RT-qPCR Analysis

RNA was extracted from cultured cells by using TRIzol (#15596018, Invitrogen, Carlsbad, CA). Total RNA was reverse-transcribed by using Takara (#RR036A-1, Clontech Laboratories, Mountain View, CA), then underwent quantitative real-time PCR (qPCR) with SYBR Green (#1725120, Bio-Rad, Hercules, CA). The relative level of mRNA was calculated by the ΔΔCq method with β-actin as an internal control.

Statistics and reproducibility

All experiments were independently repeated as noted in the figure legends. All replication attempts were successful. The data were analyzed using GraphPad Prism 6. For Gaussian data, pairwise comparisons were performed using two-sided Student's *t*-test or Welch's unequal variance *t*-test, and comparisons among three or more groups were performed using ordinary one-way ANOVA followed by Dunnett's test or Tukey's test for multiple comparisons. For comparisons in Figure 1.18b, statistical analyses were performed using two-way ANOVA followed by Dunnett's multiple comparisons tests. Statistical significance was set at $P < 0.05$. **** indicates a p-value<0.0001; *** indicates a p-value between 0.0001 to 0.001; ** indicates a p-value between 0.001 to 0.01; * indicates a p-value between 0.01 to 0.05; ns, p>0.05, not significant. n numbers, as indicated in figure legends and the main text, represent number of cells. All data are presented as mean ± s.e.m. and violin plots depict the median and quartiles, as indicated in the figure legends.

Results

Growth factor stimulates nuclear mTORC1 activity

Using a genetically encoded FRET-based mTORC1 activity reporter, TORCAR, we observed growth factor-induced mTORC1 activities across different subcellular locations, including the cytoplasm, lysosome, plasma membrane, and nucleus (Zhou et al., 2015a). In particular, serum- and amino acid-starved ("double-starved") NIH3T3 cells expressing nuclear-targeted TORCAR, TORCAR-NLS (**Figure 1.1a** and **Figure 1.2a**), responded to the growth factor stimulation of PDGF with a 6.9 ± 0.7% increase in the emission ratio of cyan/yellow (C/Y) (**Figure 1.1b**, blue trace, n = 23), showing a clear response despite the limited dynamic range of this first-generation mTORC1 activity reporter. Pretreatment with the mTOR kinase inhibitor Torin1 (**Figure 1.1b**, red trace, 0.9 ± 0.1%, p<0.0001, n = 12) or mTORC1 allosteric inhibitor rapamycin (**Figure 1.1c**, red trace, 1.6 ± 0.8%, p<0.0001, n = 9) inhibited the growth factor-induced response

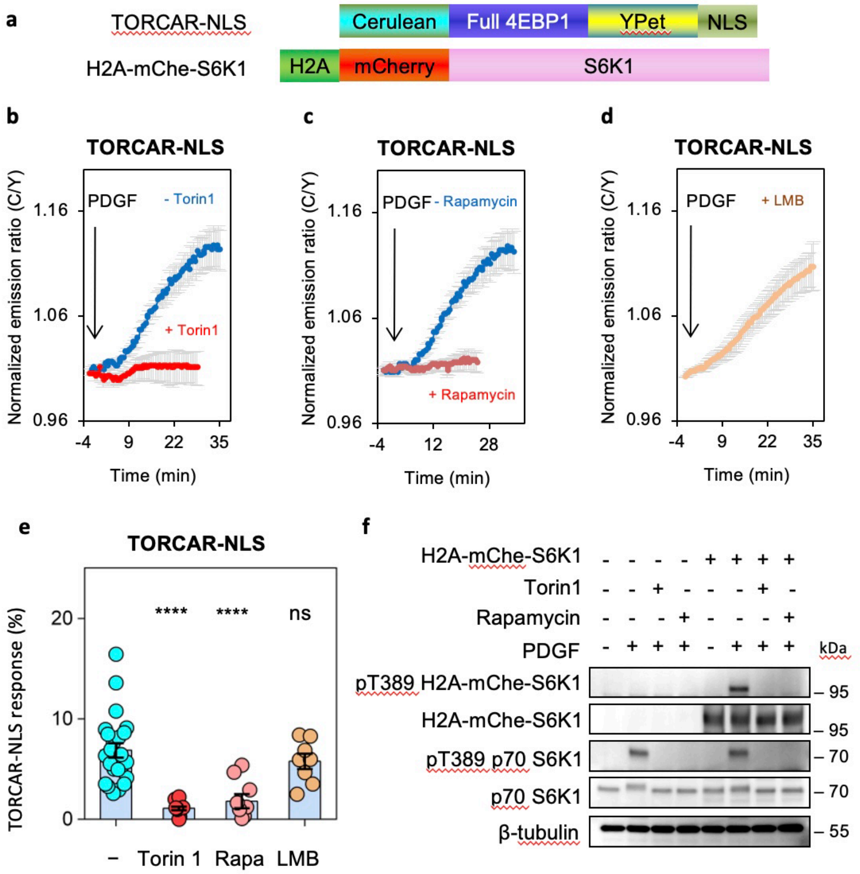

Figure 1.1 Growth factor stimulates mTORC1 activity in the nucleus. **a**. Domain structures of nuclear TORCAR (TORCAR-NLS) and nuclear localized S6K1 (H2A-mChe-S6K1). **b**. Average time courses of normalized emission ratio (Cyan/Yellow) in double-starved NIH3T3 cells expressing nuclear targeted TORCAR (TORCAR-NLS) stimulated with 50 ng/ml of PDGF without (blue trace, n = 23 cells) or with pretreatment with 1 μM of Torin1 for 10 min (red trace, n = 12 cells). Curves are representative of and pooled from 4 and 3 experiments, respectively. **c**. Average time courses of normalized emission ratio (Cyan/Yellow) in double-starved NIH3T3 cells expressing nuclear targeted TORCAR (TORCAR-NLS) stimulated with 50 ng/ml of PDGF without (blue trace, n = 23 cells) or with pretreatment with 50 μM of rapamycin for 10 min (red trace, n = 9 cells). Curves are representative of and pooled from 4 and 5 experiments, respectively. **d**. Average time course of normalized emission ratio (Cyan/Yellow) in double-starved NIH3T3 cells expressing TORCAR-NLS pretreated with 100 nM of leptomycin B (LMB) for 30 min, followed by addition of 50 ng/ml of PDGF. Time course is representative of and pooled from 3 experiments. **e**. Summary of responses of TORCAR-NLS in PDGF-treated double-starved NIH3T3 cells without pretreatment (n = 23), with Torin1 pretreatment (n = 12, ****, p=1 x 10^{-7}), with rapamycin pretreatment (n = 9, ****, p=1 x 10^{-5}), and with LMB pretreatment (n = 8, ns, not significant, p=0.3). All data are individual responses with bar graph showing mean ± s.e.m. Ordinary one-way ANOVA followed by Dunnett's multiple comparisons test. **f**. Western blot analysis of double-starved NIH3T3 cells expressing H2A-mChe-S6K1 treated with Torin (1 μM) or rapamycin (50 μM) for 10 min prior to PDGF (50 ng/ml) stimulation for 30 min. Representative of three independent experiments.

Figure 1.2 Nuclear mTORC1 activity is present. a. Double-starved NIH3T3 cells expressing TORCAR-NLS (YFP) stained with nuclear-ID. Scale bar = 10 µm. Representative of three experiments. **b.** Quantification of Nuc/Cyto ratio of mCherry fluorescence in double-starved NIH3T3 cells expressing mChe-NES without (n = 122 cells) or with treatment of leptomycin B (100 nM, 30 min, n =112 cells). Pooled from three experiments. Boxes indicating interquartile range and mid-points indicating median. Unpaired two-tailed student's t-test. ****, $p=3 \times 10^{-11}$. **c**. Domain structure of nuclear targeted TORCAR (H2A-TORCAR), and its expression in NIH3T3 cells. Scale bar = 10 µm. Representative of three experiments. **d**. Average time courses of normalized emission ratio (Cyan/Yellow) in double-starved NIH3T3 cells expressing H2A-TORCAR stimulated with 50 ng/ml of PDGF without (blue trace, n = 13 cells from 4 experiments) or with pretreatment of Torin1 (1 µM, 10 min) (red trace, n = 16 cells from 3 experiments). **e**. Average time courses of normalized emission ratio (Cyan/Yellow) in double-starved NIH3T3 cells expressing H2A-TORCAR stimulated with 50 ng/ml of PDGF without (blue trace, n = 13 cells from 4 experiments) or with pretreatment of rapamycin (50 µM, 10 min) (red trace, n = 12 cells from 3 experiments). **f.** Summary of responses of H2A-TORCAR in PDGF-treated double-starved NIH3T3 cells without pretreatment, with pretreatment of Torin1 (****, $p=1 \times 10^{-18}$) or rapamycin (****, $p=2 \times 10^{-17}$), as in panel d and e. Error bar represents mean ± s.e.m. One-way ANOVA followed by Dunnett's tests. **g**. Average time courses of normalized emission ratio (Cyan/Yellow) in double-starved 3T3L1 adipocytes expressing H2A-TORCAR stimulated with 400 ng/ml of insulin. n = 3 experiments. Left: 3T3L1 adipocytes expressing H2A-TORCAR were stained with nuclear-ID. Representative of three experiments. Scale bar = 10 µm. **h**. Western blot analysis of double-starved NIH3T3 cells expressing H2A-TORCAR treated with leptomycin B (100 nM, 30 min) prior to PDGF stimulation (50 ng/ml, 30 min). Representative of three independent experiments. **i.** Double-starved NIH3T3 cells expressing H2A-mChe-S6K1 show the nuclear localization. Representative of three experiments. Scale bar = 10 µm.

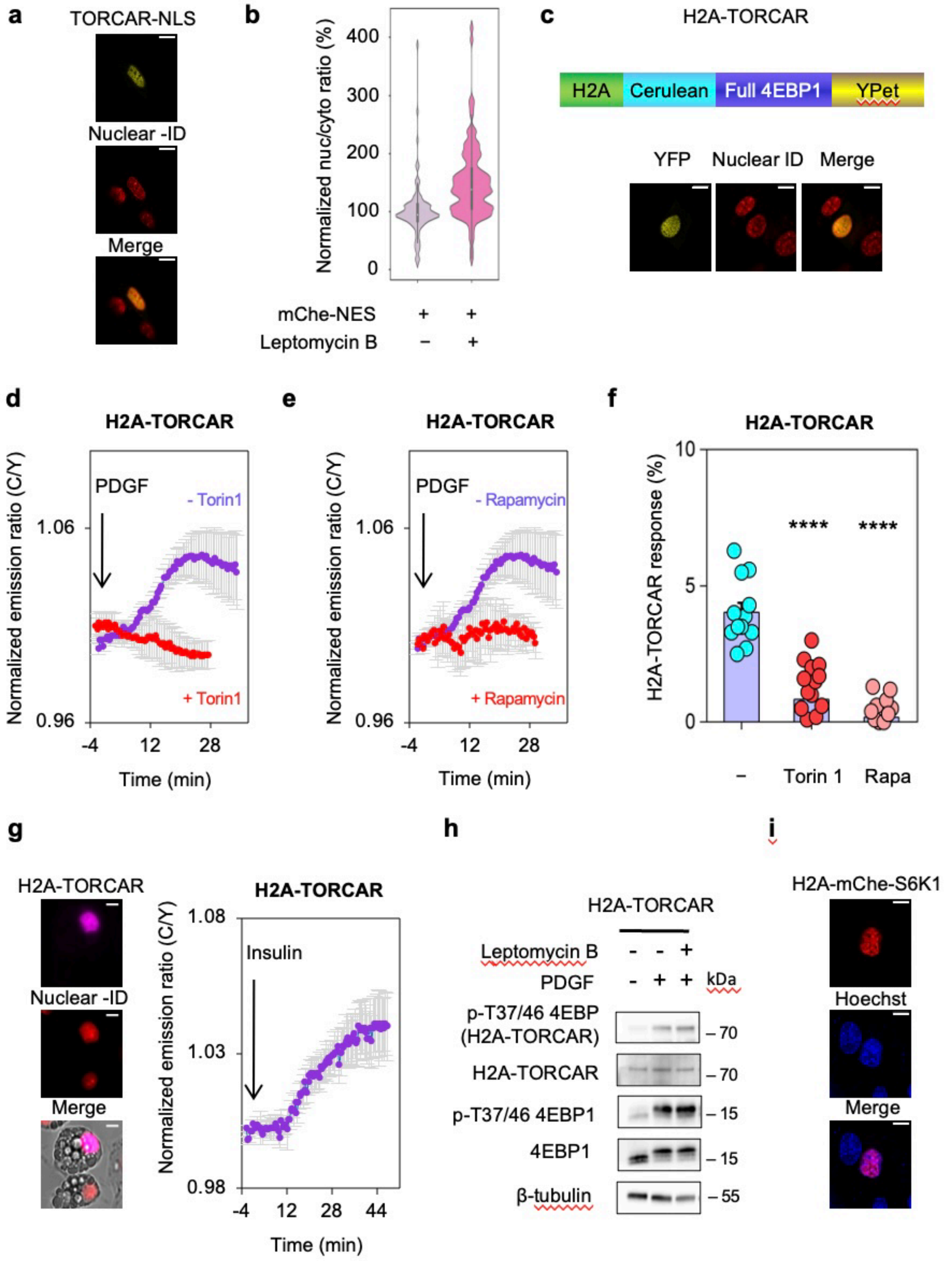
a
TORCAR-NLS
Nuclear -ID
Merge
b
Normalized nuc/cyto ratio (%)
400
300
200
100
0
mChe-NES + +
Leptomycin B − +
c
H2A-TORCAR
H2A
Cerulean
Full 4EBP1
YPet
YFP
Nuclear ID
Merge
d
H2A-TORCAR
Normalized emission ratio (C/Y)
PDGF
- Torin1
+ Torin1
1.06
0.96
-4
12
28
Time (min)
e
H2A-TORCAR
Normalized emission ratio (C/Y)
PDGF
- Rapamycin
+ Rapamycin
1.06
0.96
-4
12
28
Time (min)
f
H2A-TORCAR
H2A-TORCAR response (%)
10
5
0
****
****
–
Torin 1
Rapa
g
H2A-TORCAR
Nuclear -ID
Merge
H2A-TORCAR
Normalized emission ratio (C/Y)
Insulin
1.08
1.03
0.98
-4
12
28
44
Time (min)
h
H2A-TORCAR
Leptomycin B - - +
PDGF - + +
kDa
p-T37/46 4EBP (H2A-TORCAR)
– 70
H2A-TORCAR
– 70
p-T37/46 4EBP1
– 15
4EBP1
– 15
β-tubulin
– 55
i
H2A-mChe-S6K1
Hoechst
Merge

of TORCAR-NLS (**Figure 1.1e**), suggesting the response is mTORC1 specific. Since NLS tagging does not prevent the reporter, TORCAR-NLS, from shuttling between the cytoplasm and the nucleus, we blocked the nuclear export pathway to examine whether the nuclear TORCAR response is reflecting mTORC1 activity exclusively within the nucleus. Treatment of 100 nM of leptomycin B (LMB), a specific inhibitor of the nuclear export receptor Chromosomal Maintenance 1 (CRM1), also known as Exportin 1, for 30 min effectively blocked the export pathway, as shown by nuclear accumulation of mCherry tagged with NES in NIH3T3 cells (**Figure 1.2b**). Under LMB treatment, double-starved NIH3T3 cells expressing TORCAR-NLS showed a response to PDGF with its amplitude on par with the responses of control cells (5.8 ± 0.8%, n = 8, ns) (**Figure 1.1d, e**), suggesting that the nuclear TORCAR response is independent of CRM1-mediated nuclear export pathway and reports nuclear mTORC1 activity exclusively. To corroborate the observed nuclear mTORC1 activity, we anchored TORCAR to the nucleus by tagging histone 2A (H2A) to its N-terminus (H2A-TORCAR) (**Figure 1.2c**). Histone anchoring enhances the nuclear retention of tagged proteins, compared to tagging with NLS (Wagstaff et al., 2012), and therefore allows us to assess the response of TORCAR when it is more stringently confined to the nucleus. Like TORCAR-NLS, H2A-TORCAR is localized exclusively in the nucleus (**Figure 1.2c**) and showed a robust response of (purple trace, 4.0 ± 0.3%, n = 13, **Figure 1.2d, e**) to PDGF stimulation, which was sensitive to pretreatment with Torin1 (red trace, 0.4 ± 0.1%, n = 16, **Figure 1.2d, f**) or rapamycin (red trace, 0.4 ± 0.1%, n = 12, **Figure 1.2e, f**). Furthermore, in double-starved 3T3L1 adipocytes expressing H2A-TORCAR, stimulation with insulin induced a 4 ± 1% increase in C/Y ratio (n = 3, **Figure 1.2g**), suggesting nuclear mTORC1 activity can also be turned on by a metabolic regulator.

Next, we examined the phosphorylation of nuclear TORCAR. The addition of PDGF induced phosphorylation of H2A-TORCAR (at the T37/46 sites within the 4EBP1 portion) by 6.1 ± 0.8 fold (**Figure 1.2h**), whereas leptomycin B pretreatment failed to affect the level of H2A-TORCAR phosphorylation (92 ± 14% relative to no pretreatment, ns, **Figure 1.1h**). As both TORCAR-NLS and H2A-TORCAR utilize full length 4EBP1 as a nuclear substrate surrogate, we further examined nuclear mTORC1 activity towards another established mTORC1-specific substrate, S6K1(Ali and Sabatini, 2005). In cells expressing nuclear targeted S6K1, H2A-mCherry-S6K1 (**Figure 1.1a**, and **Figure 1.2i**), PDGF increased the level of phosphorylation of T398 S6K1 by 34 ± 4 fold (**Figure 1.1f**), and S6K1 phosphorylation was sensitive to pretreatment of either Torin1 or rapamycin (**Figure 1.1f**). The large increases in the phosphorylation of nuclear-confined mTORC1 substrates are indicative of robust nuclear mTORC1 activity. These results provide substantial evidence that mTORC1 is active in the nucleus and its activity can be stimulated by growth factor and insulin signaling pathways.

Development of Akt-STOPS to perturb subcellular Akt signaling

The increase in mTORC1 activity in the nucleus may result from either recruitment of active mTORC1 into the nucleus or from activation of mTORC1 in the nucleus. To distinguish between these possibilities, we compared the kinetics of activity accumulation of mTORC1. We calculated the $t_{1/2}$ of TORCAR responses as the time needed to reach 50% of the maximum amplitude, a metric used in previous studies (Bunemann et al., 2003; Ryu et al., 2015; Wan et al., 2019) (**Figure 1.3a**), and found mTORC1 activity in the nucleus, visualized by nuclear TORCARs, has an apparent $t_{1/2}$ on par with the cytosolic accumulation of mTORC1 activity ($t_{1/2}$ = 13.4 ± 0.9 min, n = 12 for TORCAR-NLS, 13 ± 1 min, n = 12 for H2A-TORCAR, and 12.4 ± 0.8 min, n =

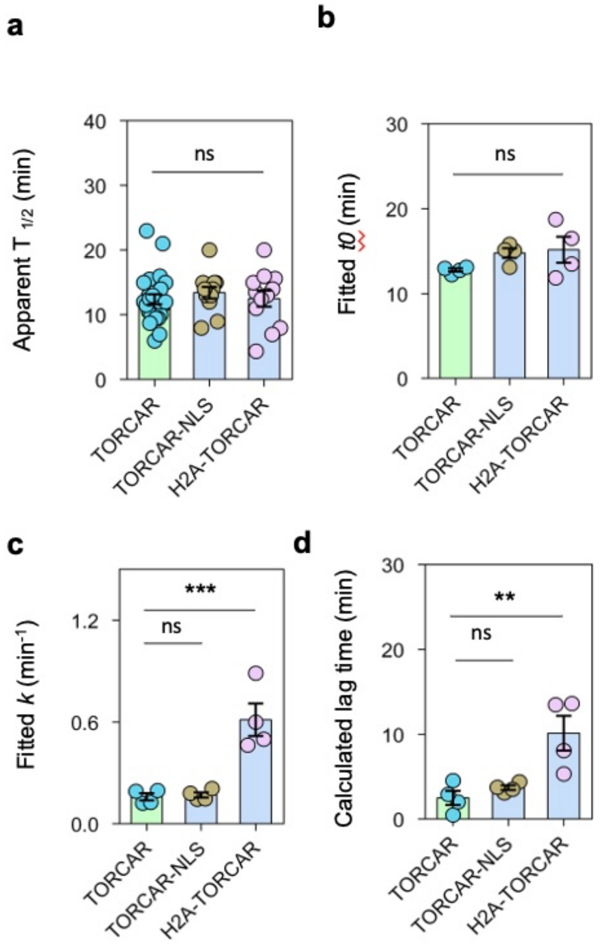

Figure 1.3 Comparison of reporter kinetics. a. Comparison of apparent half-time ($T_{1/2}$) of diffusive TORCAR, and two nuclear TORCARs. n = 25, 12, 12 cells for TORCAR, TORCAR-NLS, and H2A-TORCAR, respectively. All data are mean ± s.e.m. Statistical analyses were performed using ordinary one-way ANOVA followed by Dunnett's multiple comparisons tests. TORCAR vs. TORCAR-NLS, ns, not significant, p=0.3; TORCAR vs. H2A-TORCAR, ns, not significant, p=0.2. **b**. Comparison of fitted parameter, t_0 (see Eq. (1) in Methods). n = 4, 4 and 4 for TORCAR, TORCAR-NLS, H2A-TORCAR, respectively. All data are mean ± s.e.m. Ordinary one-way ANOVA followed by Dunnett's multiple comparisons tests. TORCAR vs. TORCAR-NLS, ns, not significant, p=0.2; TORCAR vs. H2A-TORCAR, ns, not significant, p=0.1. **c**. Comparison of fitted parameter, *k* (see Eq. (1) in Methods). n = 4, 4 and 4 for TORCAR, TORCAR-NLS, H2A-TORCAR, respectively. All data are mean ± s.e.m. Ordinary one-way ANOVA followed by Dunnett's multiple comparisons tests. TORCAR vs. TORCAR-NLS, ns, not significant, p=0.9; TORCAR vs. H2A-TORCAR, ***, p=3 x 10^{-4}. **d**. Comparison of fitted parameter, t_{lag} (see Eq. (2) in Methods). n = 4, 4 and 4 for TORCAR, TORCAR-NLS, H2A-TORCAR, respectively. All data are mean ± s.e.m. Ordinary one-way ANOVA followed by Dunnett's multiple comparisons tests. TORCAR vs. TORCAR-NLS, ns, not significant, p=0.5; TORCAR vs. H2A-TORCAR, ***, p=2 x 10^{-3}.

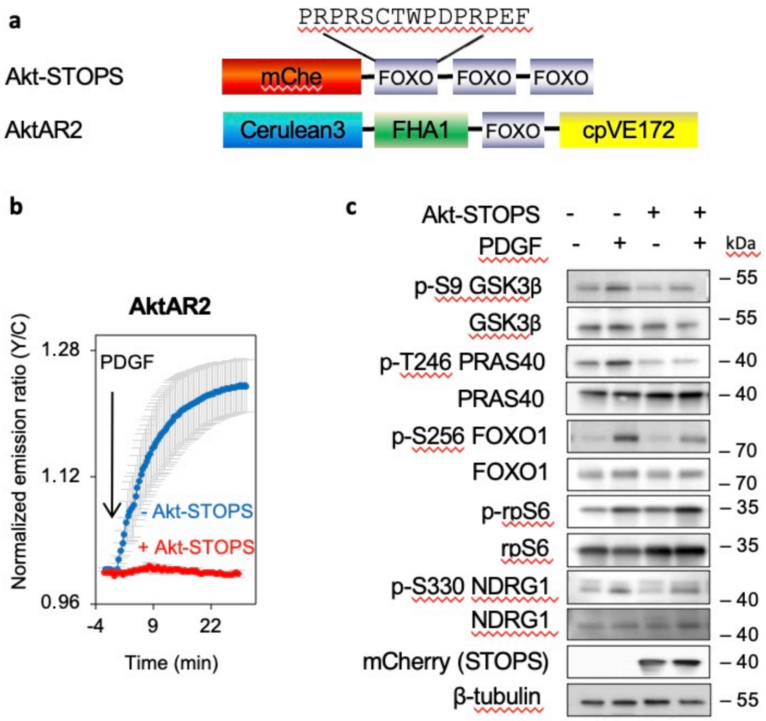

Figure 1.4 Development and characterization of Akt-STOPS. **a**. Domain structures of Akt-STOPS and AktAR2. **b**. Average time courses of normalized emission ratio (Yellow/Cyan) in serum-starved NIH3T3 cells expressing AktAR2 stimulated with 50 ng/ml of PDGF without (blue trace, 12 ± 1%, n = 41 cells) or with expression of Akt-STOPS (red trace, 0.02 ± 0.3%, n = 7 cells, ****, $p=4 \times 10^{-12}$). Error bar represents mean ± s.e.m. Unpaired two-tailed t test with Welch's correction. Curves are representative of and pooled from 4 and 7 experiments, respectively. **c**. Western blot analysis of serum-starved NIH3T3 cells with or without expressing Akt-STOPS treated with 50 ng/ml of PDGF for 30 min. Data were representative of three repeats.

25 for TORCAR; ns) (**Figure 1.3a**). We also performed curve fitting using an empirical sigmoidal function to describe the characteristics of the response curve, with a lag phase and a subsequent increase and found no evidence for faster kinetics for the untargeted TORCAR (**Figure 1.3b-d**). Overall, the comparison of kinetics of mTORC1 activity accumulation inside the nucleus and within cytosol does not allow us to rigorously determine if mTORC1 is activated in the nucleus *in situ* or translocated to the nucleus following activation. Since Akt critically regulates mTORC1 activity at multiple levels, including PRAS40 and TSC2, we reasoned that perturbing Akt signaling exclusively in the nucleus could allow us to examine the dependence of nuclear mTORC1 activity on nuclear Akt signaling. To develop a molecular tool to perturb specific pools of Akt activity based on substrate-based design (Miyamoto et al., 2015), we constructed Akt-STOPS (Akt Substrate-based Tandem Occupancy Peptide Sponge) by attaching three consecutive Akt substrate sequences derived from FoxO1 (**Figure 1.4a**) to the C-terminus of a red fluorescent protein (mCherry). The design strategy was based on high affinity binding between Akt and its substrate sequence, which is typically stronger than a kinase and a pseudosubstrate (Maiuri et al., 2010; Miyamoto et al., 2015). The tandem repeats increase the avidity of the binding and allows the peptide to adopt multiple conformations to facilitate binding to Akt, thus buffering Akt activity. The red fluorescent protein serves both as a scaffold to display the flexible peptides and as a fluorescent tag to mark the location of inhibition. We first characterized Akt phosphorylation of the substrate peptide derived from FoxO1 which was utilized in the Akt-STOPS design. The *in vitro* kinase assay using the synthesized polypeptide (contains only one repeat of Akt substrate sequence) and purified Akt catalytic domain showed an apparent K_m for substrate of 126 ± 9 μM (black trace, **Figure 1.5a**), with undetectable phosphorylation of this substrate by protein kinase C βII (PKCβII) (red trace, **Figure 1.5a**).

We then tested the effects of untargeted Akt-STOPS on Akt activity in live cells by utilizing a FRET-based Akt activity reporter, AktAR2 (Zhou et al., 2015b). Like TORCAR, AktAR2 contains an Akt activity dependent molecular switch and generates a FRET change upon phosphorylation by Akt. While serum-starved NIH3T3 cells expressing AktAR2 showed an increase in Y/C emission ratio upon PDGF stimulation (12 ± 1%, n = 41), suggesting an increase in Akt activity, expression of untargeted Akt-STOPS abolished the PDGF-induced AktAR2 response (0.02 ± 0.3%, n = 7, ****, $p<0.0001$, **Figure 1.4b**). Expression of Akt-STOPS did not affect the cellular activity of protein kinase A (PKA) (21 ± 2%, n = 20), as shown by the unchanged response amplitude of AKAR4 (Depry et al., 2011) (A Protein Kinase Activity Reporter 4) (20 ± 1%, n = 26), a FRET-based PKA activity reporter (**Figure 1.5b**). In addition, expressing mCherry alone (mChe) or mCherry-tagged scramble peptide (mChe-SP) (**Figure 1.5c**) did not reduce the AktAR2 response (**Figure 1.5d**). To further characterize the inhibitory effect of Akt-STOPS, we analyzed the growth factor-stimulated phosphorylation of Akt substrates (GSK3β, PRAS40, and FoxO1), an SGK substrate (NDRG1), and a p70S6K substrate (rpS6) in NIH3T3 cells transiently transfected with Akt-STOPS. Akt-STOPS expression reduced the phosphorylation of GSK3β, PRAS40, and FoxO1, but did not reduce the phosphorylation of NDRG1 and rpS6 (**Figure 1.4c, Figure 1.5e-i**). These results suggest that the cellular Akt activity can be specifically suppressed by Akt-STOPS.

We then tested whether nuclear targeted Akt-STOPS can be used to specifically perturb nuclear Akt activity. Expression of Akt-STOPS-NLS (Figure **1.6a**) decreased the PDGF-induced response of nuclear Akt activity reporter (AktAR2-NLS) (***, $p<0.001$, **Figure 1.6b,c**). Importantly, the nuclear-targeted Akt-STOPS did not significantly change cytosolic Akt activity,

Figure 1.5 Characterization of Akt-STOPS. a. *In vitro* characterization of K_m of Akt-STOPS using Akt3 catalytic domain or PKCβII. K_m of 126 ± 9 μM was derived for Akt3 catalytic domain. **b**. Responses of Hek293T cells expressing AKAR4 with mCherry (19.7 ± 1.1%, n = 26 cells from 4 experiments) or Akt-STOPS (21.2 ± 2.0%, n = 20 cells from 4 experiments) to 50 μM of Forskolin and 100 μM of IBMX. Error bar represents mean ± s.e.m. P value was determined by unpaired two-tailed student's t-test with Welch's correction. **c.** Domain structure of mCherry tagged scramble peptide (mChe-SP). **d**. Summary of responses of PDGF-treated serum-starved NIH3T3 cells expressing AktAR2 without or with co-expression of mCherry, mChe-SP or Akt-STOPS. The responses of AktAR2 alone (-), with expression of mCherry (mChe), with expression of mChe-SP (mChe-SP), and with expression of Akt-STOPS (Akt-STOPS) are 12 ± 1% (n = 41 cells from 4 experiments), 9 ± 1% (n = 12 cells from 3 experiments), 10 ± 1% (n = 19 from 5 experiments), and 0 ± 3% (n = 7 from 7 experiments), respectively. All data are mean ± s.e.m. One-way ANOVA followed by Dunnett's multiple comparisons tests. - vs. mChe, ns, not significant, p=0.1; - vs. mChe-SP, ns, not significant, p=0.2; - vs. Akt-STOPS, ****, $p=9 \times 10^{-6}$. **e-i**. Quantification of relative phosphorylation of GSK3β (**e**, *, p=0.046), PRAS40 (**f**, *, p=0.027), FoxO1 (**g**, *, p=0.016), NDRG1 (**h**, ns, not significant, p=0.63), and rpS6 (**i**, ns, not significant, p=0.046) in western blot experiments described in Figure2c after normalizing to the corresponding unstimulated conditions. Values are means ± s.e.m. Data were representative of 4, 5, 3, 3, 3 experiments for **e-i**, respectively. P value was determined by paired two-tailed student's t-test.

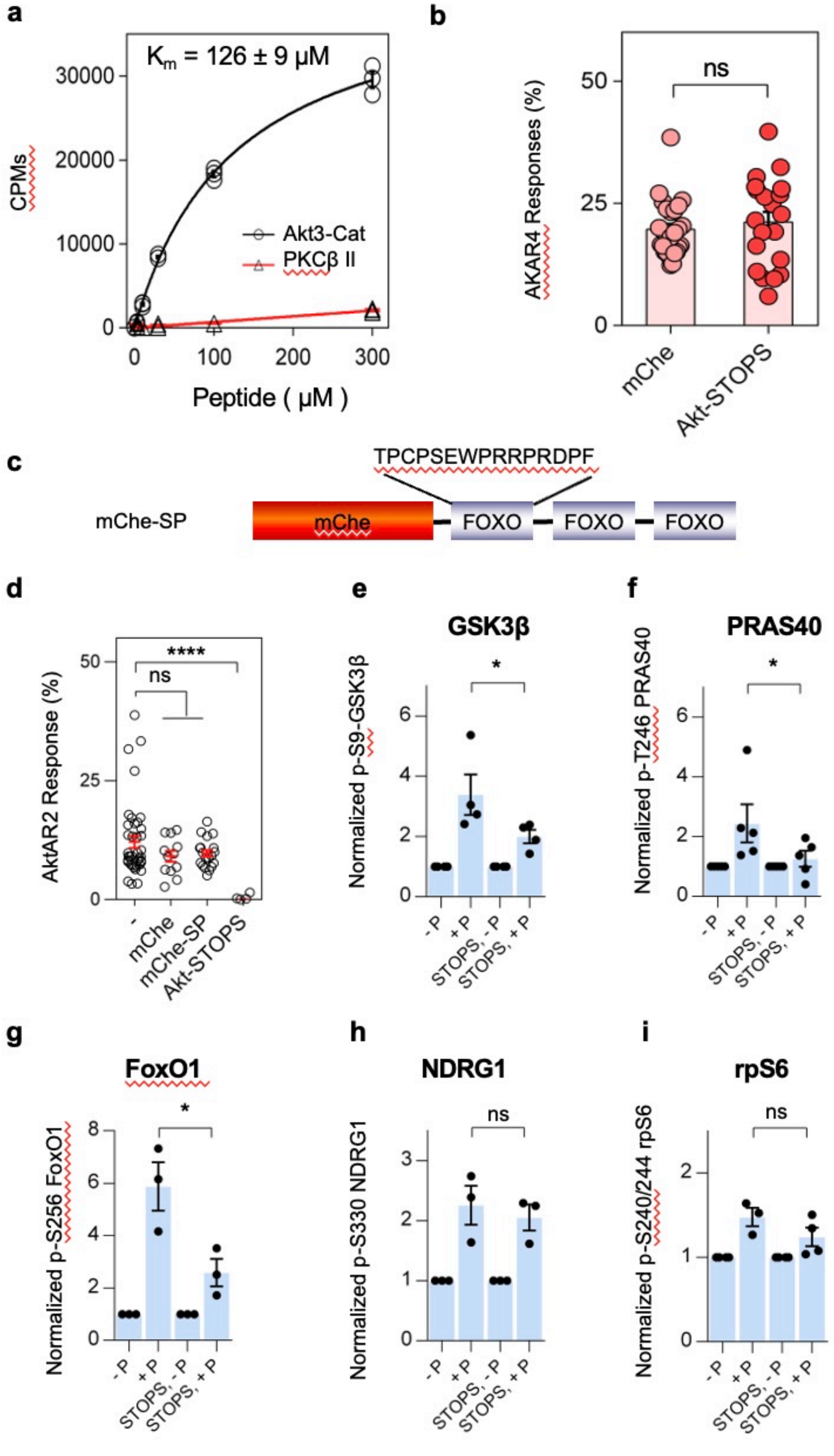
a
K_m = 126 ± 9 μM
CPMs
30000
20000
10000
0
0
100
200
300
Peptide (μM)
Akt3-Cat
PKCβ II
b
AKAR4 Responses (%)
50
25
0
ns
mChe
Akt-STOPS
c
TPCPSEWPRRPRDPF
mChe-SP
mChe
FOXO
FOXO
FOXO
d
AktAR2 Response (%)
50
25
0
****
ns
-
mChe
mChe-SP
Akt-STOPS
e
GSK3β
Normalized p-S9-GSK3β
6
4
2
0
*
- P
+ P
STOPS, - P
STOPS, + P
f
PRAS40
Normalized p-T246 PRAS40
6
4
2
0
*
- P
+ P
STOPS, - P
STOPS, + P
g
FoxO1
Normalized p-S256 FoxO1
8
6
4
2
0
*
- P
+ P
STOPS, - P
STOPS, + P
h
NDRG1
Normalized p-S330 NDRG1
3
2
1
0
ns
- P
+ P
STOPS, - P
STOPS, + P
i
rpS6
Normalized p-S240/244 rpS6
2
1
0
ns
- P
+ P
STOPS, - P
STOPS, + P

Figure 1.6 Akt-STOPS targeted to subcellular localizations perturbs local Akt signaling. a. Domain structures of nuclear Akt-STOPS (Akt-STOPS-NLS), nuclear Akt Activity reporter 2 (AktAR2-NLS), and cytosolic (AktAR2-NES), (AktAR2) and plasma membrane AktAR2 (PM-AktAR2), as well as the Chemical Inducible Dimerization (CID) system using FKBP-rapamycin-FRB (PM-FRB and FKBP-Akt-STOPS). **b.** Average time course of normalized emission ratio (Yellow/Cyan) in serum-starved NIH3T3 cells expressing AktAR2-NLS stimulated with 50 ng/ml of PDGF without (blue trace, n = 11 cells) or with expression of Akt-STOPS-NLS (red trace, n = 15 cells). Error bar represents mean ± s.e.m. Curves are representative of and pooled from 4 and 7 experiments, respectively. **c**. Summary of responses of PDGF-treated serum-starved NIH3T3 cells expressing subcellular targeted AktAR2 with or without co-expression of Akt-STOPS-NLS. Error bar represents mean ± s.e.m. P value was determined by unpaired two-tailed student's t-test. The responses of AktAR2-NLS without and with Akt-STOPS-NLS are 7.0 ± 0.8% (n =11 cells from 4 experiments) and 2.7 ± 0.6% (n = 15 cells from 7 experiments), respectively, ***, $p=2 \times 10^{-4}$; the responses of AktAR2-NES without and with Akt-STOPS-NLS are 16 ± 1% (n = 21) and 13.6 ± 0.8% (n = 16), respectively, ns, p=0.1; the responses of PM-AktAR2 without and with Akt-STOPS-NLS are 18 ± 1% (n = 17) and 15 ± 1% (n = 16), respectively, ns, not significant, p=0.1. **d**. Images of serum-starved NIH3T3 cells expressing the CID system (as shown in **a**). Representative of three independent experiments. Upper panel: pseudocolor images showing the PM-AktAR2 response. Warmer colors indicating higher normalized ratios of Yellow/Cyan for PM-AktAR2. Lower panel: dynamics of FKBP-STOPS. Arrows indicating the addition of PDGF or rapamycin. Scale bar = 10 µm. **e**. Average time course of normalized emission ratio (Yellow/Cyan) in serum-starved NIH3T3 cells expressing PM-AktAR2, PM-FRB, and mCherry-FKBP-STOPS showed a response to PDGF stimulation (50 ng/ml) that was reversed by the addition of rapamycin (100 nM). n = 7. Time course is representative of and pooled from 3 experiments.

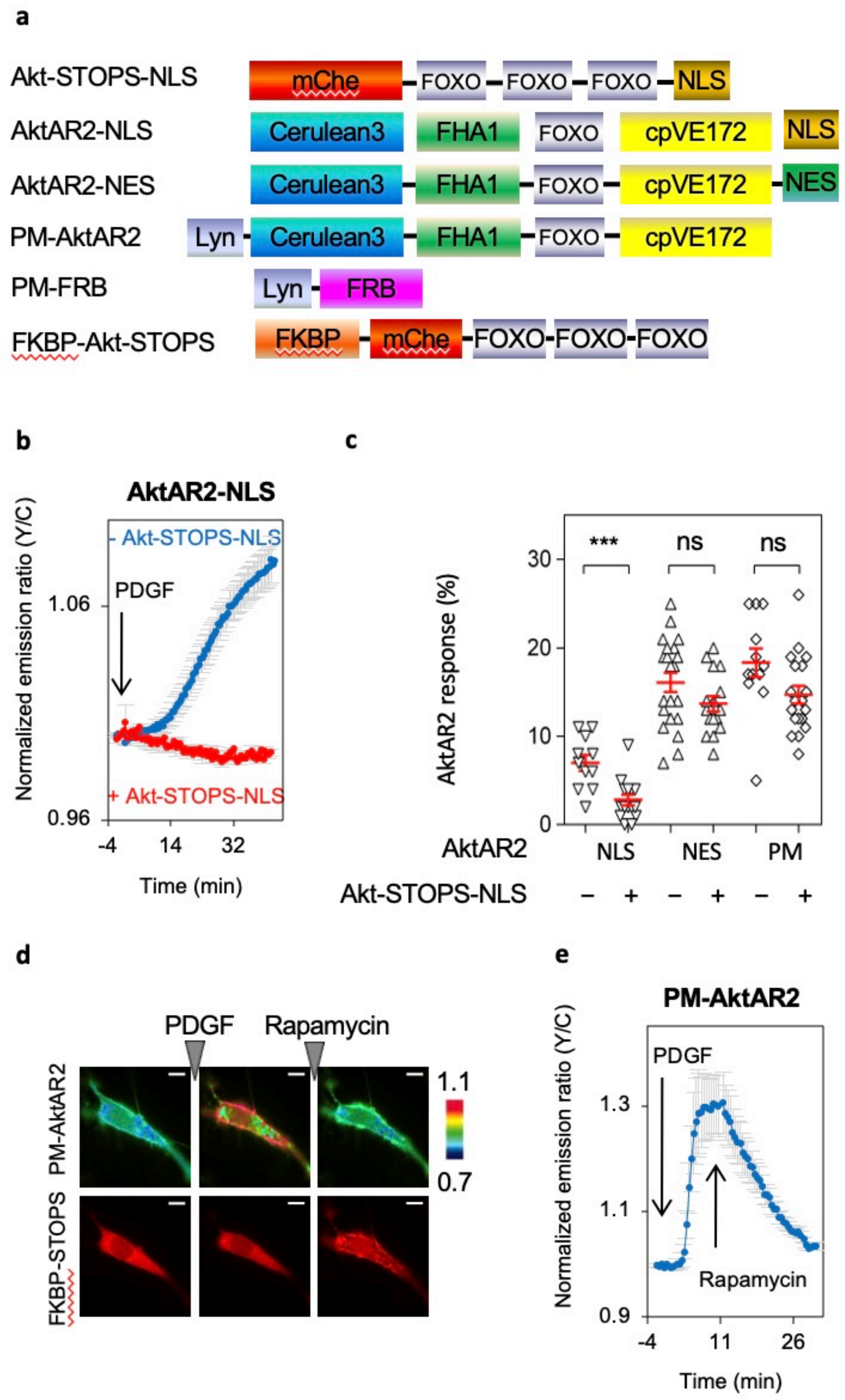
a
Akt-STOPS-NLS
mChe
FOXO
FOXO
FOXO
NLS
AktAR2-NLS
Cerulean3
FHA1
FOXO
cpVE172
NLS
AktAR2-NES
Cerulean3
FHA1
FOXO
cpVE172
NES
PM-AktAR2
Lyn
Cerulean3
FHA1
FOXO
cpVE172
PM-FRB
Lyn
FRB
FKBP-Akt-STOPS
FKBP
mChe
FOXO
FOXO
FOXO
b
AktAR2-NLS
- Akt-STOPS-NLS
PDGF
+ Akt-STOPS-NLS
Normalized emission ratio (Y/C)
1.06
0.96
-4
14
32
Time (min)
c
***
ns
ns
AktAR2 response (%)
30
20
10
0
AktAR2
NLS
NES
PM
Akt-STOPS-NLS
–
+
–
+
–
+
d
PDGF
Rapamycin
PM-AktAR2
FKBP-STOPS
1.1
0.7
e
PM-AktAR2
PDGF
Rapamycin
Normalized emission ratio (Y/C)
1.3
1.1
0.9
-4
11
26
Time (min)

as shown by the response of cytosolic Akt activity reporter (AktAR2-NES) or the plasma membrane Akt activity reporter (PM-AktAR2) (ns, **Figure 1.6c** and **Figure 1.7a**). Expression of Akt-STOPS-NLS also decreased the PDGF-induced phosphorylation of PRAS40 in serum-starved NIH3T3 cells (**Figure 1.7b,c**). These results suggested that Akt-STOPS-NLS selectively suppressed nuclear Akt activity.

We also developed plasma membrane-targeted Akt-STOPS (PM-Akt-STOPS, **Figure 1.8a**) by attaching a lipid modified domain from Lyn to the N-terminus to Akt-STOPS. PM-Akt-STOPS dampened the PDGF-induced responses of plasma membrane Akt activity (****, $p<0.0001$) with little effect on the Akt activity in the cytosol (ns, $p=0.06$) (**Figure 1.8b-d**). Interestingly, nuclear Akt activity was also decreased by expression of plasma membrane Akt-STOPS (***, $p<0.001$) (**Figure 1.8b-d**), suggesting that nuclear Akt activity may have some dependence on plasma membrane Akt activity. To further develop an approach that allows temporal control on the location-specific inhibition of Akt activity, we employed the Chemical Inducible Dimerization (CID) system based on rapamycin induced heterodimerization of FK506-binding proteins (FKBP) and FKBP12-rapamycin Binding (FRB) domain. In these studies, we transiently transfected NIH3T3 cells with FKBP-Akt-STOPS together with a plasma membrane targeted FRB (PM-FRB) (**Figure 1.8a**) and monitored Akt activity at the plasma membrane using PM-AktAR2. Upon addition of the dimerizer rapamycin, a ternary complex of FKBP-rapamycin-FRB is formed, resulting in the recruitment of Akt-STOPS to the plasma membrane (**Figure 1.8d**). As shown in **Figure 1.8d** and **1.8e**, addition of rapamycin following PDGF, led to the rapid reversal of PDGF-stimulated PM-AktAR2 response, suggesting acute recruitment of Akt-STOPS to the plasma membrane inhibits the *in situ* Akt activity. Similarly, the addition of rapalog (Bayle et al., 2006;

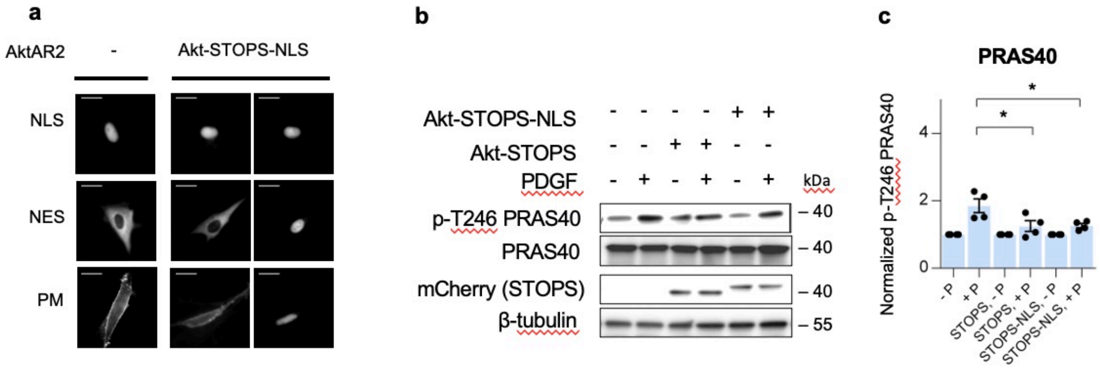

Figure 1.7 Characterization of Akt-STOPS-NLS. a. Representative images showing serum-starved NIH3T3 cells expressing AktAR2-NLS, NES, and PM alone (left) or with co-expression of Akt-STOPS-NLS (right). Scale bar = 10 μm. **b**. Western blot analysis of serum-starved NIH3T3 cells expressing Akt-STOPS or Akt-STOPS-NLS treated with PDGF (50 ng/ml) for 30 min. Representative of four repeats. **c**. Quantification of relative phosphorylation of PRAS40 in western blot experiments described in Figure 1.6b after normalizing to the corresponding unstimulated conditions. Data is representative of 4 independent experiments. Values are means ± s.e.m. P value was determined by paired two-tailed t-test. +P vs. STOPS, +P, *, p=0.027; +P vs. STOPS-NLS, +P, *, p=0.033.

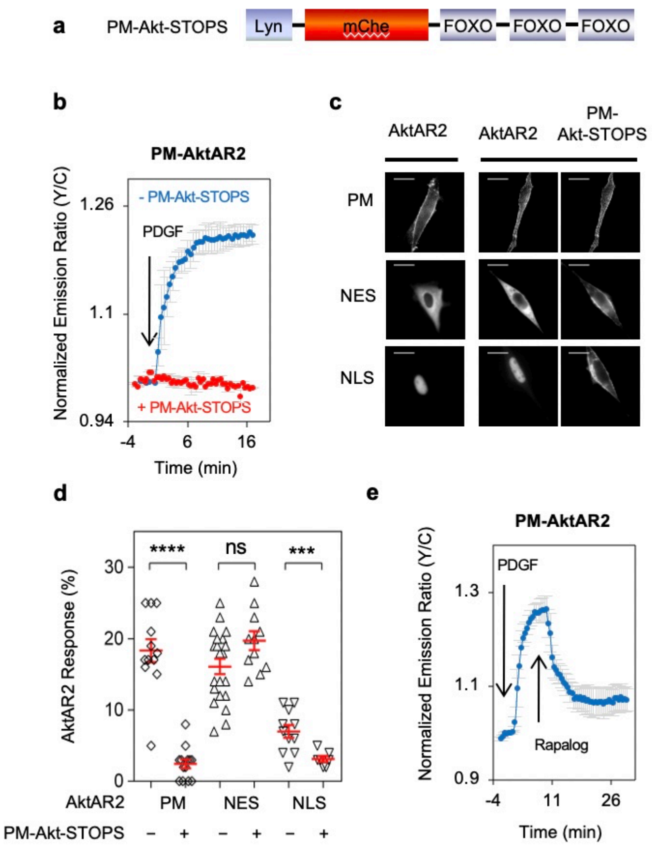

Figure 1.8 Characterization of plasma membrane Akt-STOPS. a. Domain structure of plasma membrane Akt-STOPS (PM-Akt-STOPS). **b**. Average time course of normalized emission ratio (Yellow/Cyan) in serum-starved NIH3T3 cells expressing PM-AktAR2 stimulated with 50 ng/ml of PDGF without (blue trace, n = 17 cells) or with expression of PM-Akt-STOPS (red trace, n =13 cells). Curves are representative of and pooled from 3 and 3 experiments, respectively. **c**. Representative images showing serum-starved NIH3T3 cells expressing PM-AktAR2, AktAR2-NLS and AktAR2-NES alone (left) or with co-expression of PM-Akt-STOPS (right). Scale bar = 10 µm. **d**. Summary of responses of PDGF-treated serum-starved NIH3T3 cells expressing subcellular targeted AktAR2 with or without co-expression of PM-Akt-STOPS. Data are presented as mean ± s.e.m. The responses of PM-AktAR2 without and with PM-Akt-STOPS are 18 ± 1% (n = 17 cells from 3 experiments) and 2.8 ± 0.7% (n = 13 cells from 3 experiments), respectively, unpaired two-tailed student's t-test with Welch's correction, ****, p=7 x 10^{-11}; the responses of AktAR2-NES without and with PM-Akt-STOPS are 16.1 ± 1.1% (n =21 cells from 5 experiments) and 20 ± 1% (n =11 cells from 4 experiments), respectively, unpaired two-tailed student's t-test, ns, not significant, p=0.1; the responses of AktAR2-NLS without and with PM-Akt-STOPS are 7.0 ± 0. 8% (n = 11 cells from 4 experiments) and 3.7 ± 0.4% (n = 19 cells from 4 experiments), respectively, unpaired two-tailed student's t-test, ***, p=3 x 10^{-4}. **e**. Average time course of normalized emission ratio (Yellow/Cyan) in serum-starved NIH3T3 cells expressing PM-AktAR2, PM-FRB, and mCherry-FKBP-STOPS showed a response to PDGF stimulation (50 ng/ml) that was reversed by addition of rapalog (3 µM). n = 5 cells from 3 experiments.

Liberles et al., 1997), which avoids the potential interference via inhibition of mTORC1, also rapidly reversed the PDGF-induced PM-AktAR2 responses (**Figure 1.8e**), suggesting Akt-STOPS is a powerful molecular tool for spatiotemporal suppression of Akt activity in living cells.

Nuclear Akt activity is required for growth factor-induced nuclear mTORC1 activity

The location-selective inhibition by Akt-STOPS-NLS permitted the analysis of whether the nuclear mTORC1 activity is primarily dependent on the nuclear Akt activity. Intriguingly, in double-starved NIH3T3 cells expressing nuclear targeted mTORC1 activity reporter (TORCAR-NLS), the presence of Akt-STOPS-NLS led to a 63 ± 11% inhibition of PDGF-stimulated TORCAR-NLS response (red trace, 2.7 ± 0.7%, n = 14), compared with control cells (blue trace, 6.9 ± 0.7%, n = 23, ***, $p<0.001$) (**Figure 1.9a, b**). In contrast, expression of a nuclear-targeted scramble peptide failed to reduce nuclear TORCAR response (green trace, 9 ± 1%, n = 10, ns, **Figure 1.10a-c**). In addition, the nuclear TORCAR response to PDGF is significantly reduced by pretreatment with Akt inhibitors (GDC-0068 and MK-2206), but not by pretreatment with H89 (PKA inhibitor), Gö6983 (PKC inhibitor), PF-4708671 (p70 S6K inhibitor), LJI308 (p90 RSK inhibitor), or GSK650394 (SGK inhibitor) (**Figure 1.10d-e**), suggesting that growth factor-induced nuclear mTORC1 activity specifically depends on Akt activity. As an additional control, nuclear mTORC1 activity stimulated by an amino acid surrogate leucine O-methyl ester (LeuOMe) was examined and not affected by Akt-STOPS-NLS (8 ± 1% vs 8 ± 1%, n = 11 and 9, ns, **Figure 1.9c-d**), indicating that the amino acid surrogate-induced nuclear mTORC1 activity is independent of nuclear Akt, as expected. Consistent with the TORCAR data, western blot analysis showed that expression of nuclear Akt-STOPS (Akt-STOPS-NLS) abolished the phosphorylation of H2A-

Figure 1.9 Nuclear Akt activity is required for growth factor-induced nuclear mTORC1 activity. a. Average time courses of normalized emission ratio (Cyan/Yellow) in double-starved NIH3T3 cells expressing TORCAR-NLS stimulated with 50 ng/ml of PDGF without (blue trace, n =23 cells from 4 experiments) or with expression of Akt-STOPS-NLS (red trace, n = 14 cells from 3 experiments). Curves are representative of and pooled from 4 and 3 experiments, respectively. **b**. Responses of TORCAR-NLS in PDGF-treated double-starved NIH3T3 cells without (n = 23) or with expression of Akt-STOPS-NLS (n = 14). Error bar represents mean ± s.e.m. P value was determined by unpaired two-tailed student's t-test. ***, $p=4 \times 10^{-4}$. **c**. Average time courses of normalized emission ratio (Cyan/Yellow) in double-starved NIH3T3 cells expressing TORCAR-NLS stimulated with 7.5 mM leucine O-methyl ester (LeuOMe) without (blue trace, n = 11 cells) or with expression of Akt-STOPS-NLS (red trace, n = 9 cells). Curves are representative of and pooled from 5 and 3 experiments, respectively. **d**. Responses of TORCAR-NLS in LeuOMe-treated double-starved NIH3T3 cells without (n = 11 cells from 5 experiments) or with expression of Akt-STOPS-NLS (n = 9 cells from 3 experiments). Error bar represents mean ± s.e.m. Unpaired two-tailed student's t-test. ns, not significant, p=1.0. **e**. Western blot analysis of double-starved NIH3T3 cells expressing H2A-mChe-S6K1 treated with PDGF (50 ng/ml) for 30 min in the absence or presence of STOPS-NLS expression. Representative of three independent experiments.

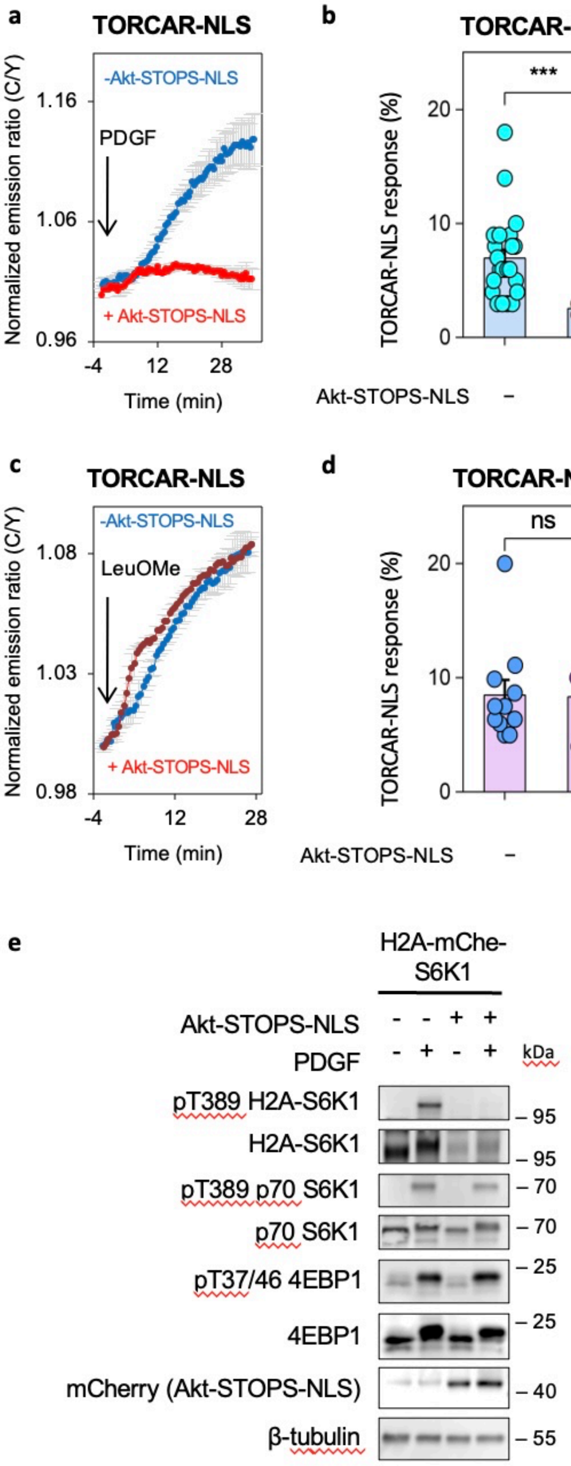
a
TORCAR-NLS
-Akt-STOPS-NLS
PDGF
+ Akt-STOPS-NLS
Normalized emission ratio (C/Y)
1.16
1.06
0.96
-4
12
28
Time (min)
b
TORCAR-NLS
***
TORCAR-NLS response (%)
20
10
0
Akt-STOPS-NLS
–
+
c
TORCAR-NLS
-Akt-STOPS-NLS
LeuOMe
+ Akt-STOPS-NLS
Normalized emission ratio (C/Y)
1.08
1.03
0.98
-4
12
28
Time (min)
d
TORCAR-NLS
ns
TORCAR-NLS response (%)
20
10
0
Akt-STOPS-NLS
–
+
e
H2A-mChe-S6K1
Akt-STOPS-NLS
- - + +
PDGF
- + - +
kDa
pT389 H2A-S6K1
– 95
H2A-S6K1
– 95
pT389 p70 S6K1
– 70
p70 S6K1
– 70
pT37/46 4EBP1
– 25
4EBP1
– 25
mCherry (Akt-STOPS-NLS)
– 40
β-tubulin
– 55

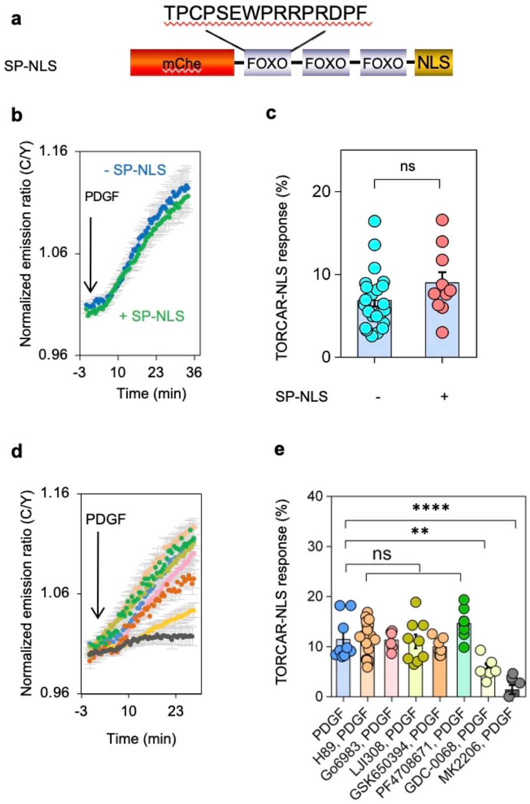

Figure 1.10 Nuclear mTORC1 activity is specifically suppressed by Akt inhibition. a. Domain structure of nuclear targeted scramble peptide (SP-NLS). **b**. Average time course of normalized emission ratio (Cyan/Yellow) in double- starved NIH3T3 cells expressing TORCAR-NLS stimulated with 50 ng/ml of PDGF without (blue trace, n = 23 cells from 4 experiments) or with expression of nuclear targeted scramble peptide (SP-NLS) (green trace, n = 10 cells from 5 experiments). **c**. Summary of responses of PDGF-treated double-starved NIH3T3 cells without or with expressing nuclear targeted scramble peptide (SP-NLS). Data are presented as mean ± s.e.m. P value was determined by unpaired two-tailed student's t-test. ns, not significant, p=0.1. **d**. Average time course of normalized emission ratio (Cyan/Yellow) in double-starved NIH3T3 cells expressing TORCAR-NLS stimulated with 50 ng/ml PDGF without (blue trace) or with 5 min pretreatment of PKA inhibitor H89 (10 µM, light orange), PKC inhibitor Gö 6983 (1 µM, light pink), RSK inhibitor LJI308 (1 µm, lime green), S6K inhibitor PF4708671 (2 µM, green), SGK inhibitor GSK650394(2 µM, orange) , GDC-0068 (1 µM, dark yellow) or Akt inhibitor MK2206 (1 µM, grey). Curves are representative of and pooled from 4, 6, 4, 6, 5, 4, 5 and 4 experiments, respectively. **e**. Summary of responses of TORCAR-NLS in PDGF-treated double-starved NIH3T3 cells without (n = 9 cells from 4 experiments) or with pretreatment of H89 (n = 19 cells from 6 experiments, ns, not significant, p=0.9), Gö 6983 (n = 6 cells from 4 experiments, ns, not significant, p=0.9), LJI308 (n = 9 cells from 6 experiments, ns, not significant, p=0.8), GSK650394 (n = 7 cells from 5 experiments, ns, not significant, p=0.4), PF4708671 (n = 8 cells from 4 experiments, ns, not significant, p=0.1), GDC-0068 (n = 6 cells from 5 experiments, **, p=1 x 10^{-3}), or MK2206 (n = 8 cells from 4 experiments, ****, p=2 x 10^{-8}). Data are presented as mean ± s.e.m. Statistical analyses were performed using ordinary one-way ANOVA followed by Dunnett's multiple comparisons tests.

mChe-S6K1 without affecting the phosphorylation of endogenous S6K1 and 4EBP1, which are primarily localized outside the nucleus (**Figure 1.9e**). Together, these data suggest that nuclear Akt activity is critical for the growth factor-stimulated nuclear mTORC1 activity.

Raptor forms a complex with mTOR in the nucleus

Raptor is the critical and defining component for mTORC1. Within the mTORC1 complex, Raptor binds to the TOR signaling (TOS) motif on mTORC1 substrates to determine substrate specificity and aids the catalysis by mTOR (Ali and Sabatini, 2005; Schalm et al., 2003). To examine whether Raptor potentiates nuclear TORCAR response, we employed shRNA-mediated knockdown to decrease the protein level of Raptor significantly in NIH3T3 cells (**Figure 1.11a**). In these Raptor knockdown NIH3T3 cells, PDGF-stimulated TORCAR-NLS response was significantly decreased (2.0 ± 0.5%, n = 15, ****, p<0.0001, **Figure 1.11b, c**), suggesting Raptor is essential for nuclear mTORC1 activity.

We then examined whether mTOR and Raptor form a complex in the nucleus by proximity ligation assay (PLA). In these experiments, complexes containing mTOR and Raptor were detected in intact, fixed cells. As shown in **Figure 1.11d**, the PLA signal was observed in both the cytoplasm and nucleus. On average, 4.7 ± 0.4 puncta per nucleus (n = 37 cells) were observed for the measurements of mTOR and Raptor interaction in wildtype NIH3T3 cells, which is significantly higher than the background signals observed with either mTOR antibody alone (0.4 ± 0.1 dots per nucleus, n = 50 cells, ****, p<0.0001) or mTOR antibody with normal IgG (2.0 ± 0.3 dots per nucleus, n = 37 cells, ****, p<0.0001). As a control, PLA signals decreased to 2.2 ± 0.3 dots per nucleus in Raptor knockdown NIH3T3 cells (n = 26 cells, ****, p<0.0001) (**Figure**

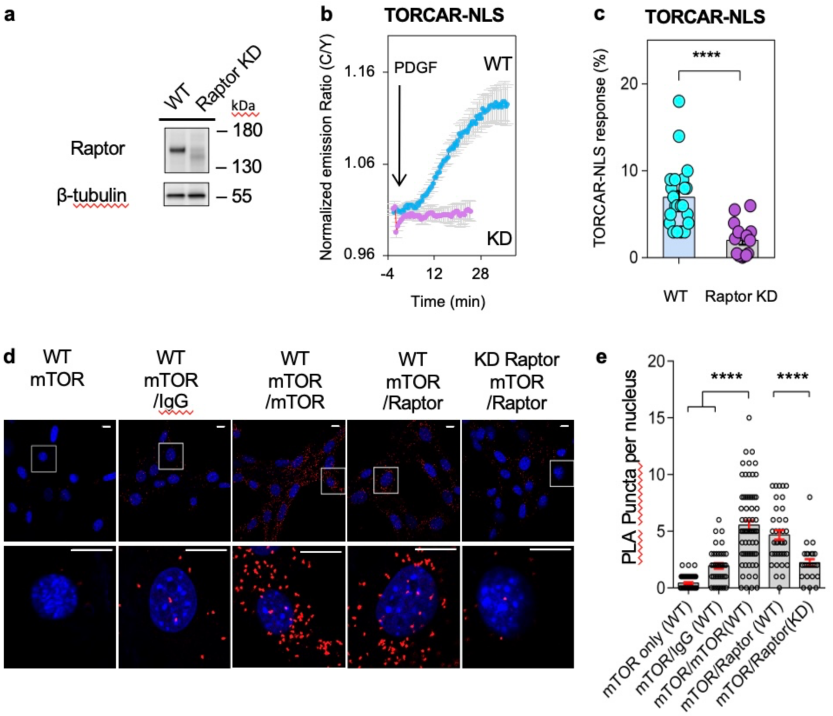

Figure 1.11 Raptor is required for nuclear TORCAR response and forms a complex with mTOR in the nucleus. a. shRNA-mediated knockdown of Raptor in NIH3T3 cells. Western blot analysis showed reduced level in Raptor KD cells. Representative of three independent experiments. Full blots are shown in Supplementary Figure 13. **b**. Average time courses of normalized emission ratio (Cyan/Yellow) in double-starved wildtype (WT, blue trace, n =23 cells) or Raptor knockdown (KD, purple trace, n =15 cells) NIH3T3 cells expressing nuclear targeted TORCAR (TORCAR-NLS) stimulated with 50 ng/ml of PDGF. Time course is representative of and pooled from 4 and 4 experiments, respectively. **c**. Responses of TORCAR-NLS to PDGF in WT (n = 23 cells from 4 experiments) and Raptor KD NIH3T3 cells (n = 15 cells from 4 experiments). Error bar represents mean ± s.e.m. Unpaired two-tailed student's t-test with Welch's correction. ****, p=5 x 10^{-6}. **d**. Representative confocal images of *in situ* proximity ligation assay (PLA) between mTOR and Raptor (red) in wild type NIH3T3 cells (Column 1, 2, 3, 4) or Raptor knockdown NIH3T3 cells (Column 5). Column 1, mouse anti-mTOR only; column 2, mouse anti-mTOR and IgG; column 3, rabbit anti-mTOR antibody and mouse anti-mTOR antibody; column 4 and 5, mouse anti-mTOR and rabbit anti-Raptor antibodies. The middle slices of confocal z-stacks were shown to observe the PLA puncta (red) in the nucleus (blue). Data are representative of two independent experiments. Scale bar = 10 μm. **e**. Quantification of the amount of PLA puncta per nucleus. n = 50, 37, 69, 37 and 26 cells. Error bar represents mean ± s.e.m. Ordinary one-way ANOVA followed by Tukey's multiple comparisons test. mTOR only (WT) vs. mTOR/mTOR (WT), ****, p=5 x 10^{-41}; mTOR/IgG(WT) vs. mTOR/mTOR (WT), ****, p=7 x 10^{-22}; mTOR/Raptor (KD) vs. mTOR/Raptor (WT), ****, p=2 x 10^{-8}.

1.11e). These data suggest that mTOR and Raptor form a complex in the nucleus.

Raptor translocates into the nucleus upon PDGF stimulation

Using an antibody validated for Raptor immunofluorescence (**Figure 1.12a, b**), we examined Raptor localization before and after PDGF stimulation. As shown in **Figure 1.13a** and **1.13b**, PDGF treatment of double-starved NIH3T3 cells resulted in a reproducible increase in nuclear accumulation of endogenous Raptor, with a 49 ± 6% increase in the nuclear/cytosol (Nuc/Cyto) ratio of the immunofluorescence signal of Raptor. To validate Raptor's nuclear localization after PDGF treatment, we utilized whole lysate nuclear extraction to assess the levels of Raptor in control and PDGF treated NIH3T3 cells. Quantifying Raptor levels normalized to a fraction marker (GAPDH and p84 for cytoplasmic and nuclear fractions, respectively), we observed elevated and decreased Raptor protein levels in nuclear and cytosolic fractions, respectively, following growth factor stimulation (**Figure 1.13c**, **Figure 1.14**), although our protocol is not suited for comparing protein abundance between cytosolic and nuclear fractions (see methods). PDGF stimulation also increased the phosphorylation of mTOR at S2448 and PRAS40 at T426 but does not change the total levels of Raptor in whole cell lysates (**Figure 1.13c, Figure 1.14b**). Phosphorylated mTOR at S2448 is a marker for active mTORC1 (Copp et al., 2009), and the observed increased phosphorylation is consistent with increased nuclear mTORC1 activity.

To validate PDGF-induced Raptor nuclear translocation, the nuclear import pathway was blocked using a small molecule inhibitor importazole (IPZ), which inhibits importin β (Soderholm et al., 2011). Treatment of NIH3T3 cells with 100 μM of importazole for 1 hr efficiently blocked

Figure 1.12 Akt facilitates nuclear translocation of Raptor. a. Validation of Raptor antibody. Representative images of Raptor immunostaining in WT or Raptor knockdown NIH3T3 cells. Representative of two independent experiments. Scale bar = 10 µm. **b**. Quantification of mean intensity of Raptor immunostaining per cell in wildtype and Raptor knockdown cells. $p=1.7 \times 10^{-20}$. Boxes indicating interquartile range and mid-points indicating median. n = 137 and 147 cells for WT and Raptor KD from 3 experiments, respectively. **c**. Validation of importazole treatment. Quantification of Nuc/Cyto ratio of mCherry fluorescence in double-starved NIH3T3 cells expressing mChe-NLS without (n = 45 cells) or with importazole (100 µM) treatment for 1 hr (n =59 cells). Data are pooled from three experiments. Boxes indicating interquartile range and mid-points indicating median. P value was determined by unpaired two-tailed student's t-test. ***, $p=6.79 \times 10^{-4}$. **d**. Representative confocal images of immunostaining of endogenous Raptor in double-starved NIH3T3 cells (- P), 30 min following PDGF stimulation (+ P), and pretreatment with 1 µM MK-2206 for 10 min followed by 30 min treatment with PDGF. The middle slices of confocal z-stacks were shown to observe the Raptor staining in the nucleus (Green). Representative of three independent experiments. Scale bar = 10 µm. **e.** Quantification of mean nuclear intensity/mean cytosol intensity ratio (Nuc/Cyto ratio) of Raptor immunostaining per cell. n = 341, 373, 371 cells. All data are mean ± s.e.m. Ordinary one-way ANOVA followed by Dunnett's multiple comparisons tests. - PDGF vs. + PDGF, ****, $p=3 \times 10^{-46}$; + PDGF vs. + MK + PDGF, ****, $p=4 \times 10^{-9}$. **f.** Localization of RanBP3 in the nucleus. Representative confocal images of middle slices of endogenous RanBP3 in double-starved NIH3T3 cells without (- P) or with PDGF (50 ng/ml) treatment for 30 min (+ P) reveals the primary localization of RanBP3 in the nucleus. n = three experiments. Scale bar =10 µm.

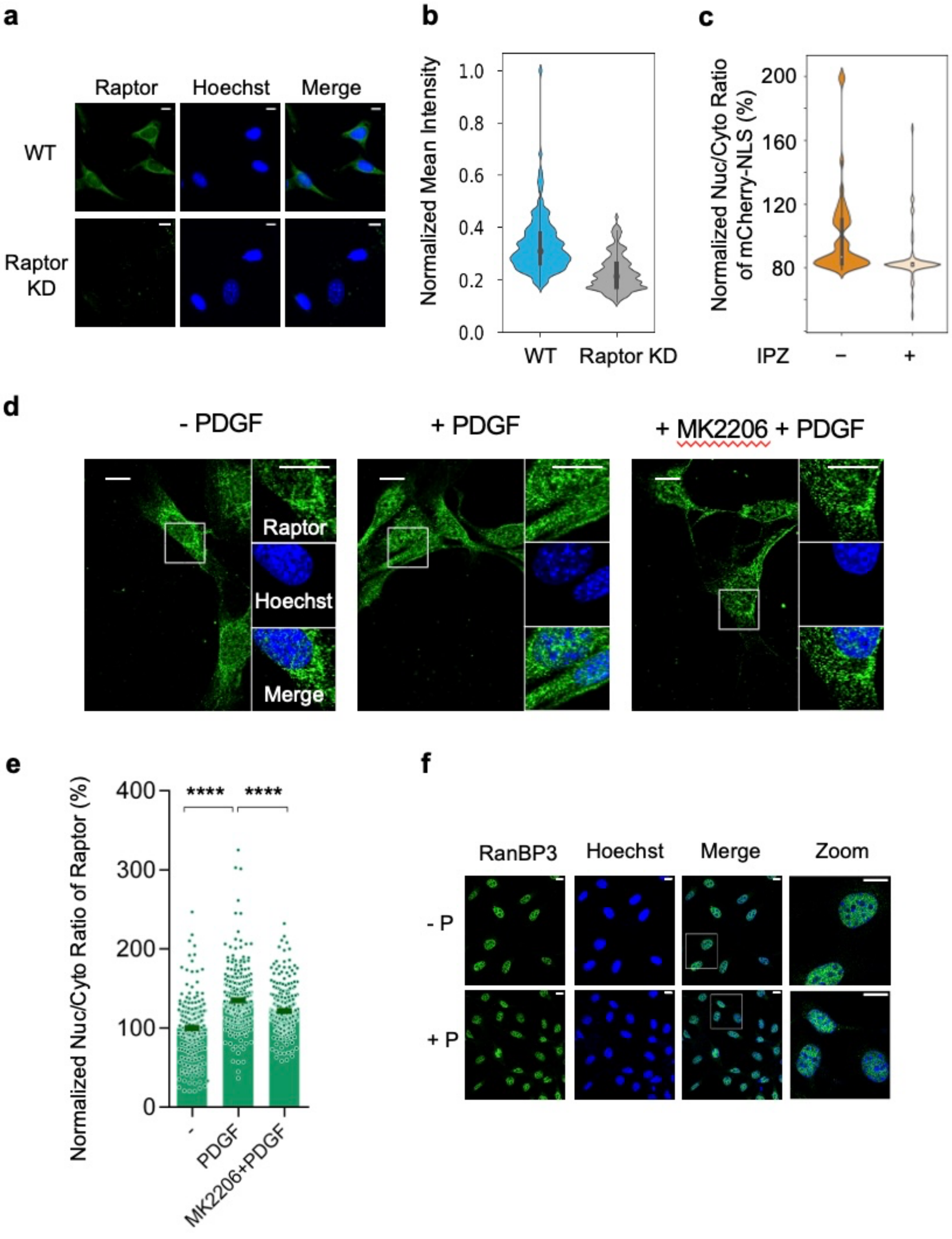
a
Raptor
Hoechst
Merge
WT
Raptor KD
b
Normalized Mean Intensity
1.0
0.8
0.6
0.4
0.2
0.0
WT
Raptor KD
c
Normalized Nuc/Cyto Ratio of mCherry-NLS (%)
200
160
120
80
IPZ
−
+
d
- PDGF
+ PDGF
+ MK2206 + PDGF
Raptor
Hoechst
Merge
e
Normalized Nuc/Cyto Ratio of Raptor (%)
400
300
200
100
0
****
****
-
PDGF
MK2206+PDGF
f
RanBP3
Hoechst
Merge
Zoom
- P
+ P

Figure 1.13 Raptor translocation into the nucleus upon growth factor stimulation is dependent on nuclear Akt activity. a. Confocal images of immunostaining of endogenous Raptor in double-starved NIH3T3 cells (-PDGF), 30 min following PDGF stimulation (+PDGF), and treatment with 100 μM importazole (IPZ) for 1 hr followed by PDGF stimulation for 30 min (+IPZ+PDGF). The middle slices of confocal z-stacks were shown to observe the Raptor staining in the nucleus (Green). Scale bar = 10 μm. n = 3 experiments. **b**. Quantification of mean nuclear intensity/mean cytosol intensity ratio (Nuc/Cyto ratio) of Raptor immunostaining per cell. n = 22, 29, 23 cells from 3 experiments. Error bar represents mean ± s.e.m. One-way ANOVA followed by Tukey's tests. -PDGF vs. +PDGF, ****, $p=6 \times 10^{-10}$; +PDGF vs. +IPZ+PDGF, ****, $p=6 \times 10^{-13}$. **c**. Western blot analysis of cytoplasmic and nuclear fractions from double-starved NIH3T3 cells treated without or with PDGF (50 ng/ml) for 30 min. P84 and GAPDH were used as nuclear and cytoplasmic markers, respectively. Data are representative of three experiments. Full blots are shown in Supplementary Figure 13. **d**. Summary of changes in Nuc/Cyto ratio of Raptor immunostaining in double-starved NIH3T3 cells expressing mCherry (H2A-mChe) or Akt-STOPS in the nucleus (H2A-STOPS) stimulated without or with PDGF (50 ng/ml) for 30 min. n = 49, 78, 82, and 71 cells from 3 experiments. Error bar represents mean ± s.e.m. One-way ANOVA followed by Tukey's tests. H2A-mChe, -PDGF vs. H2A-mChe, +PDGF, **, $p=2 \times 10^{-6}$; H2A-STOPS, -PDGF vs. H2A-STOPS, +PDGF, ns, not significant, p=0.5. **e**. Western blot analysis of phosphorylation of RanBP3 in double-starved NIH3T3 cells with different treatment indicated. Lane 1, no treatment; Lane 2, PDGF (50 ng/ml) treatment for 30 min; Lane 3, cells expressing H2A-STOPS were treated with PDGF (50 ng/ml) for 30 min; Lane 4, pretreatment with GDC-0068 (1 μM) for 10 min followed by PDGF (50 ng/ml) for 30 min. n = three experiments. Full images of blots are shown in Supplementary Figure 13.

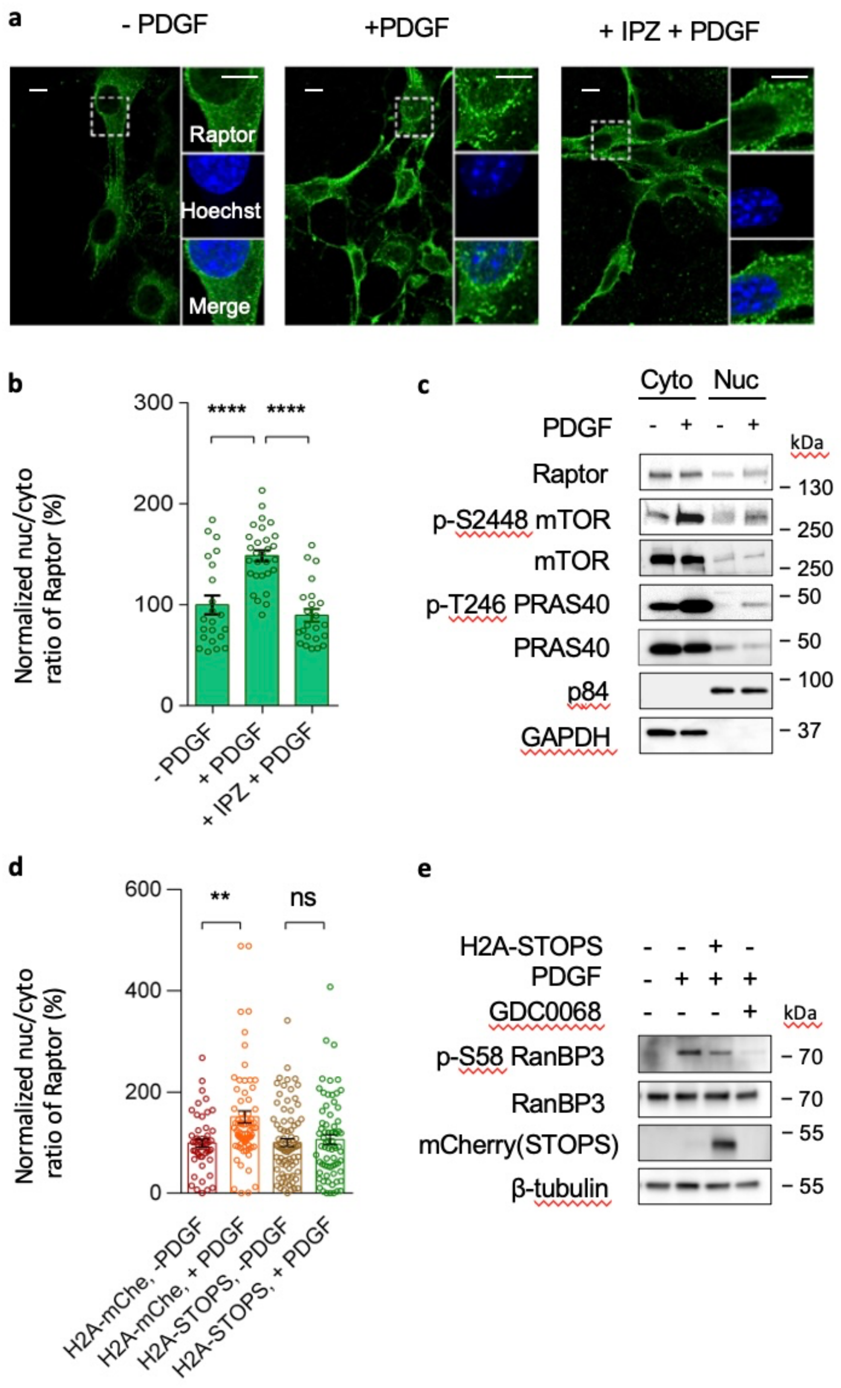
a
- PDGF
+PDGF
+ IPZ + PDGF
Raptor
Hoechst
Merge
b
300
200
100
0
****
****
Normalized nuc/cyto ratio of Raptor (%)
- PDGF
+ PDGF
+ IPZ + PDGF
c
Cyto
Nuc
PDGF
- + - +
kDa
Raptor
p-S2448 mTOR
mTOR
p-T246 PRAS40
PRAS40
p84
GAPDH
130
250
250
50
50
100
37
d
600
400
200
0
**
ns
Normalized nuc/cyto ratio of Raptor (%)
H2A-mChe, -PDGF
H2A-mChe, + PDGF
H2A-STOPS, -PDGF
H2A-STOPS, + PDGF
e
H2A-STOPS
- - + -
PDGF
- + + +
GDC0068
- - - +
kDa
p-S58 RanBP3
RanBP3
mCherry(STOPS)
β-tubulin
70
70
55
55

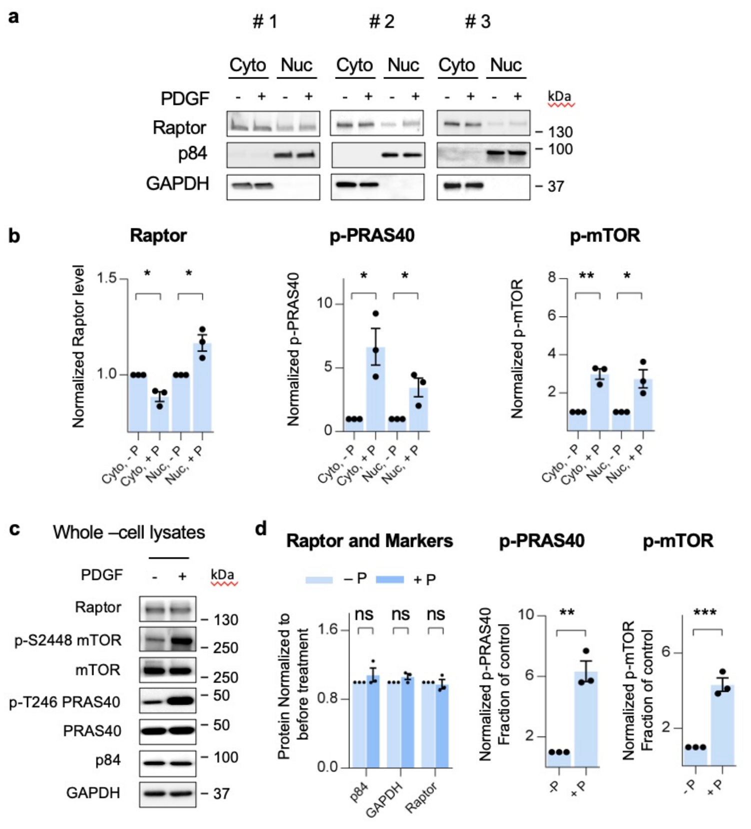

Figure 1.14 Quantification of nuclear translocation and whole cell lysates without or with PDGF stimulation in three independent experiments. a. Three independent fractionation experiments, shown by western blots of cytoplasmic and nuclear fractions from double-starved NIH3T3 cells treated without or with PDGF (50 ng/ml) for 30 min. p84 and GAPDH were used as nuclear and cytoplasmic markers, respectively. **b**. Quantification of changes in relative Raptor protein levels, phosphorylation of PRAS40 and mTOR in cytoplasmic and nuclear fractions between nontreated and treated samples. The levels of the target proteins were normalized to each respective control (GAPDH for cytoplasmic fractions and p84 for nuclear fraction), and the changes between non-treated and treated samples were compared by setting the pre-stimulation condition as 1. Data are representative of three experiments. Values are means ± s.e.m. P value was determined by unpaired two-tailed t-test. For comparison of Raptor protein levels, Cyto, -P vs. Cyto, +P, *, p=0.011; Nuc, -P vs. Nuc, +P, *, p=0.017. For comparison of p-PRAS40, Cyto, -P vs. Cyto, +P, *, p=0.017; Nuc, -P vs. Nuc, +P, *, p=0.028. For comparison of p-mTOR, Cyto, -P vs. Cyto, +P, *, p=0.002; Nuc, -P vs. Nuc, +P, *, p=0.022. **c**. Western blot analysis of the whole-cell lysates of double-starved NIH3T3 cells treated without or with PDGF (50 ng/ml) for 30 min. **d**. Quantification of relative Raptor, GAPDH, and p84 protein levels, phosphorylation of PRAS40 and mTOR in (**c**) after normalizing to the corresponding untreated conditions. Data are representative of three experiments. Values are means ± s.e.m. P value was determined by unpaired two-tailed t-test. p84, ns, not significant, p=0.018; GAPDH, ns, not significant, p=0.30; Raptor, ns, not significant, p=0.70; p-PRAS40, **, p=0.0014; p-mTOR, ***, p=0.0007.

accumulation of mCherry-NLS in the nucleus (**Figure 1.12c**), suggesting this treatment is sufficient to inhibit the nuclear import of protein tagged with an NLS. As shown in **Figure 1.13a** and **1.13b**, pretreatment with IPZ abolished the PDGF-induced nuclear translocation of Raptor in serum and amino acid starved NIH3T3 cells, suggesting that Raptor nuclear translocation is mediated by Ran/importin pathway.

We further examined whether Raptor nuclear translocation specifically depends on the nuclear Akt activity. Akt inhibition by the small molecule inhibitor MK2206 decreased the PDGF-induced nuclear Raptor translocation (**Figure 1.12d, e**). Furthermore, as shown in **Figure 1.13d**, the PDGF-induced increase in the nuc/cyto ratio of Raptor immunofluorescence signal was blocked in cells expressing nuclear targeted Akt-STOPS (H2A-Akt-STOPS), but not in cells expressing nuclear targeted mCherry (H2A-mChe), indicating that this process is dependent on nuclear Akt activity.

Akt is known to phosphorylate Ser58 of the Ran GTPase binding protein 3 (RanBP3) to facilitate the Ran GTPase-mediated nuclear import (Yoon et al., 2008). Given the nuclear localization of RanBP3 (**Figure 1.12f**), we hypothesized that Akt-mediated RanBP3 phosphorylation primarily occurs in the nucleus and that nuclear Akt activity is important for regulating RanBP3. To test this idea, NIH3T3 cells were transiently transfected with nuclear-targeted Akt-STOPS (Akt-STOPS-NLS), double-starved and stimulated with PDGF, and the phosphorylation of RanBP3 at Ser58 was examined. Although transfection efficiency limited the effect of Akt-STOPS-NLS across the entire cell population, Akt-STOPS-NLS led to a 49 ± 6% decrease in RanBP3 phosphorylation (**Figure 1.13e**). These data suggest that nuclear Akt activity mediates phosphorylation of RanBP3, which may contribute to nuclear translocation of Raptor.

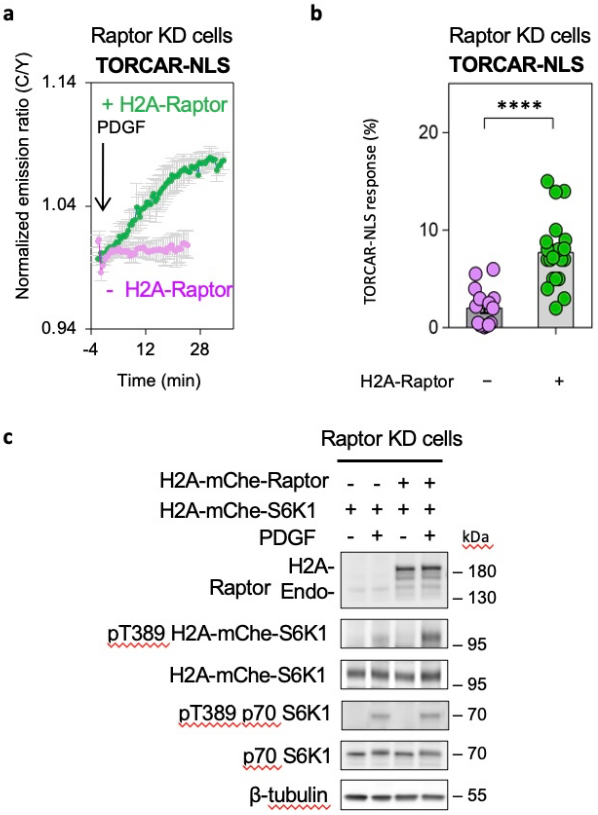

Figure 1.15 Expressing nuclear-targeted Raptor rescues nuclear mTORC1 activity. a. Average time courses of normalized emission ratio (Cyan/Yellow) in double-starved Raptor knockdown NIH3T3 cells expressing nuclear targeted TORCAR (TORCAR-NLS) stimulated with 50 ng/ml of PDGF without (magenta trace, n = 15 cells) or with expression of H2A-Raptor (green trace, n = 23 cells). Curves are representative of and pooled from 4 and 3 experiments, respectively. **b**. Responses of TORCAR-NLS in PDGF-treated double-starved Raptor knockdown NIH3T3 cells without (n = 15 cells from 4 experiments) or with H2A-Raptor expression (n = 23 cells from 3 experiments). All data are individual response with bar graph showing mean ± s.e.m. P value was determined by unpaired two-tailed student's t-test with Welch's correction. ****, $p=1 \times 10^{-6}$. **c**. Western blot analysis of double-starved Raptor knockdown NIH3T3 cells expressing H2A-mChe-S6K1 with or without expression of H2A-Raptor treated with PDGF (50 ng/ml) for 30 min. Representative of three independent experiments.

Nuclear localized Raptor potentiates nuclear TORCAR response and results in nuclear mTORC1 activity in the absence of growth factor stimulation

Our data suggest that growth factor-induced nuclear translocation of Raptor may be important for the increase in nuclear mTORC1 activity. We next examined the effect of localizing Raptor to the nucleus. We first utilized the Raptor shRNA-knockdown NIH3T3 cells and expressed a nuclear-localized Raptor (H2A-Raptor) and examined its effect on nuclear TORCAR response. Expression of H2A-Raptor rescued the PDGF-induced response of TORCAR-NLS in double-starved Raptor knockdown cells (2.0 ± 0.5% vs 7.7 ± 0.8%, n = 15 and 23, ***, $p<0.0005$, **Figure 1.15a, b**). In contrast, overexpression of nuclear Raptor had no effect on cytosolic TORCAR (TORCAR-NES, **Figure 1.16a**) in Raptor knockdown NIH3T3 cells (0.9 ± 0.2% vs 1.9 ± 0.5%, n = 11 and 7, ns, **Figure 1.16b, c**), while cytosolic TORCAR is clearly functional in wildtype NIH3T3 cells (**Figure 1.16d, e**). These data are consistent with the 2.8 ± 0.2 fold increase in PDGF-induced phosphorylation of nuclear localized H2A-S6K1 in the presence of nuclear Raptor (H2A-Raptor) in Raptor knockdown cells compared to that in the absence of nuclear Raptor (**Figure 1.15c**). These results suggest that nuclear localization of Raptor is necessary for rescuing nuclear mTORC1 activity in Raptor knockdown cells.

We next examined how nuclear localized Raptor affects the basal and stimulated nuclear mTORC1 activities in wildtype cells. To directly evaluate basal nuclear mTORC1 activity, we treated resting/unstimulated TORCAR-NLS-expressing cells with the mTOR inhibitor, Torin1, and quantified the resulting decrease in the TORCAR-NLS cyan-over-yellow emission ratio. This technique is widely used to characterize basal pathway activation for other kinases such as PKA

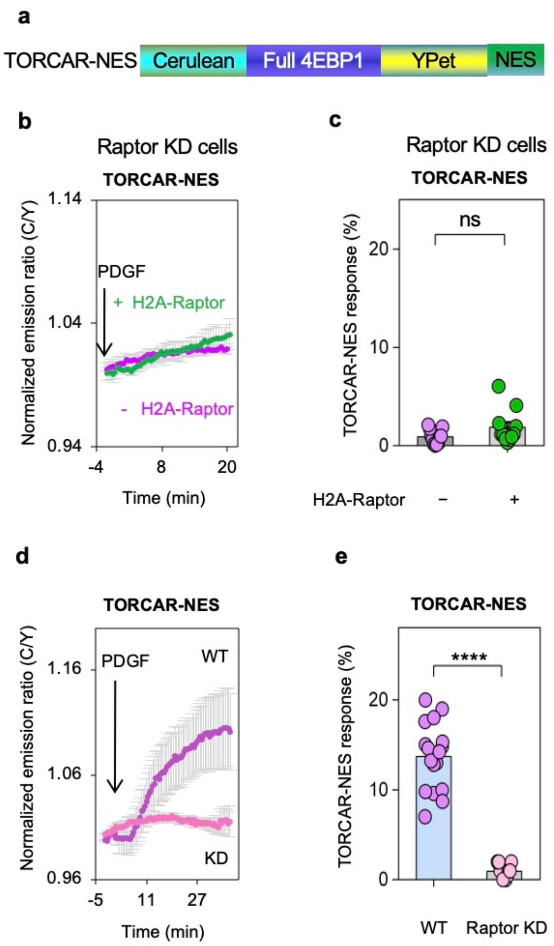

Figure 1.16 Nuclear localized Raptor does not affect cytosolic mTORC1 activity. a. Domain structure of cytosolic TORCAR (TORCAR-NES). **b**. Average time courses of normalized emission ratio (Cyan/Yellow) in double-starved Raptor knockdown NIH3T3 cells expressing cytosol targeted TORCAR (TORCAR-NES) stimulated with 50 ng/ml of PDGF without (magenta trace, n = 11 cells from 4 experiments) or with expression of H2A-Raptor (green trace, n = 11 cells from 3 experiments). Error bar represents mean ± s.e.m. **c**. Responses of TORCAR-NES in PDGF-treated double-starved Raptor knockdown NIH3T3 cells with (n = 11 cells from 3 experiments) or without H2A-Raptor expression (n = 11 cells from 4 experiments). Error bar represents mean ± s.e.m. P value was determined by unpaired two-tailed student's t-test with Welch's correction. ns, not significant, p=0.1. **d**. Average time courses of normalized emission ratio (Cyan/Yellow) in double-starved wildtype (WT, purple trace, n = 17 cells from 3 experiments) or Raptor knockdown (KD, light pink trace, n = 11 cells from 3 experiments) NIH3T3 cells expressing cytosol-targeted TORCAR (TORCAR-NES) stimulated with 50 ng/ml of PDGF. **e**. Responses of TORCAR-NES in PDGF-treated double-starved wildtype (n = 17 cells from 3 experiments) or Raptor knockdown NIH3T3 cells (n = 11 cells from 3 experiments). Error bar represents mean ± s.e.m. P value was determined by unpaired two-tailed student's t-test with Welch's correction. ****, $p=7 \times 10^{-11}$.

(Depry et al., 2011) and PKC (Baffi et al., 2019; Callender et al., 2018; Gallegos et al., 2006). As shown in **Figure 1.17a** and **1.17b**, Torin1 induced a larger decrease in TORCAR-NLS C/Y ratio in cells expressing nuclear Raptor than in cells without expressing nuclear Raptor (6.6 ± 0.6% vs 3.1 ± 0.3%, n = 16 and 22, respectively, ****, p<0.0001), and this decrease is further enhanced (7.3 ± 0.3% and 4.6 ± 0.4%, n = 22 and 26 for cells with and without expressing H2A-Raptor, respectively, ****, p<0.0001) by shRNA knockdown of PRAS40 (**Figure 1.17c**), a negative mTORC1 regulator and Akt substrate(Kovacina et al., 2003; Sancak et al., 2007). On the other hand, tethering Raptor to the nucleus resulted in reduced amplitude of PDGF-induced nuclear TORCAR response (7.3 ± 0.8 vs 4.8 ± 0.8, n = 9 and 11, *, p<0.05), which is further reduced in PRAS40 knockdown cells (4.5 ± 0.6% vs. 1.5 ± 0.4, n = 11 and 11, ***, p<0.0005, **Figure 1.17d** and **1.17e**). Taken together, these results suggest the basal nuclear mTORC1 activity in wildtype cells is low, and localizing additional Raptor to the nucleus increases the basal activity of nuclear mTORC1, suggesting that localization of Raptor to the nucleus itself can result in nuclear mTORC1 activity in the absence of growth factor stimulation. Furthermore, these results suggest that PRAS40, which is phosphorylated in the nucleus by Akt upon PDGF stimulation (Figure **1.13c** and **Figure 1.17f**), also contributes to the PDGF-induced increase in nuclear mTORC1 activity.

Nuclear Akt-STOPS suppresses pol III transcription

mTORC1 has been shown to play an important role in regulating synthesis of tRNA and 5S rRNA by RNA polymerase (pol) III (Shor et al., 2010; Tsang et al., 2011). mTOR was found at tRNA and 5S rRNA genes in the nucleus (Shor et al., 2010; Tsang et al., 2011), where mTOR associates with TFIIIC, a transcription factor that binds to pol III promoters. Maf1, a repressor that

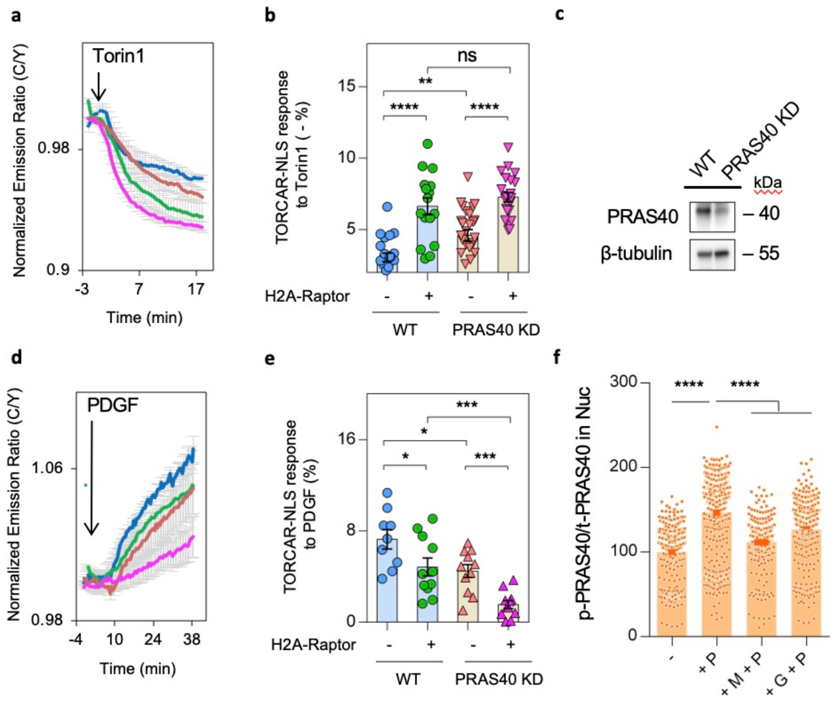

Figure 1.17 Nuclear TORCAR response is influenced by nuclear localized Raptor and PRAS40. a. Torin 1-induced responses in serum-starved NIH3T3 cells or PRAS40 knockdown (KD) NIH3T3 cells expressing nuclear targeted TORCAR (TORCAR-NLS) without (Blue, n = 22 WT cells, 7 experiments; Red, n = 26 KD cells, 5 experiments) or with H2A-Raptor co-expression (Green, n = 16 WT cells, 5 experiments; Pink, n = 22 KD cells, 7 experiments). **b**. Basal activities indicated by Torin 1-induced decreases (-%) in **a**. Error bar represents mean ± s.e.m. Unpaired two-tailed student's t-test. WT vs. WT+H2A-Raptor, ****, $p=2x10^{-6}$ (with Welch's correction); KD vs. KD+H2A-Raptor, ****, $p=8x10^{-6}$; WT vs. KD, **, $p=5x10^{-3}$; WT+H2A-Raptor vs. KD+H2A-Raptor, ns, not significant, p=0.3. **c.** shRNA-mediated knockdown of PRAS40 in NIH3T3 cells. n = three experiments. Full blots are shown in Supplementary Figure 13. **d**. PDGF-induced responses in serum-starved WT cells or PRAS40 KD cells expressing TORCAR-NLS without (Blue, n = 9 WT cells, 3 experiments; Red, n = 11 KD cells, 5 experiments) or with H2A-Raptor co-expression (Green, n = 11 WT cells, 3 experiments; Pink, n = 11 KD cells, 3 experiments). **e.** PDGF-induced Responses - in **c**. Error bar represents mean ± s.e.m. Unpaired two-tailed student's t-test. WT vs. WT+H2A-Raptor, *, $p=5x10^{-3}$; KD vs. KD+H2A-Raptor, ***, $p=3x10^{-4}$; WT vs. KD, *, $p=1x10^{-2}$; WT+H2A-Raptor vs. KD+H2A-Raptor, **, $p=2x10^{-3}$ (with Welch's correction). **f.** Quantification of immunostaining of mean nuclear p-T246 PRAS40 intensity/total PRAS40 intensity ratio (p-PRAS40/PRAS40 in Nuc) per cell. Double-starved NIH3T3 cells without treatment (-), 30 min following PDGF stimulation (+P), and pretreatment with 1 μM MK-2206 (+M+P) or GDC-0068 (+G+P) for 10 min followed by 30 min treatment with PDGF were co-stained with p-T246 and total PRAS40 antibodies. n = 415, 499, 280, 366 cells. Data are pooled from three experiments. Error bar represents mean ± s.e.m. One-way ANOVA with Tukey's test. -P vs. +P, ****, $p=3x10^{-130}$; +P vs. +M+P, ****, $p=3x10^{-65}$; +P vs. +G+P, ****, $p=3x10^{-26}$.

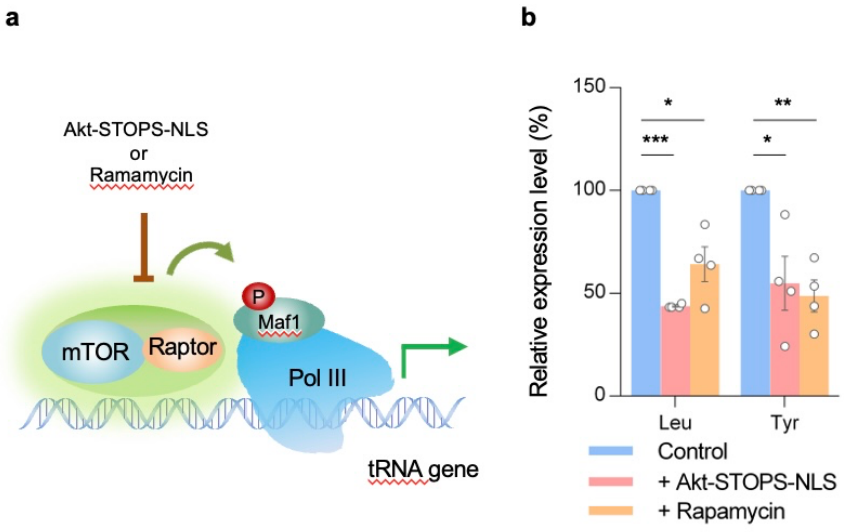

Figure 1.18 Nuclear Akt-STOPS suppresses pol III transcription. a. A model depicting phosphorylation of Maf1 by mTORC1 inactivates Maf1 as a repressor of RNA polymerase III (pol III), leading to upregulated transcription of tRNA. **b**. Akt-STOPS-NLS suppresses mTORC1-mediated Pol III transcription. Quantification of Leu tRNA and Tyr tRNA levels by real time qPCR analysis. Actin was used as normalization control. Data indicate mean values of four independent experiments and error bars refer to standard error between experiments. Statistical analyses were performed using two-way ANOVA followed by Dunnet's multiple comparisons tests. For comparison of relative expression level of Leu tRNA, Control vs. Akt-STOPS-NLS, ****, $p=3 \times 10^{-5}$; Control vs. Rapamycin, **, $p=2 \times 10^{-3}$. For comparison of relative expression level of Tyr tRNA, Control vs. Akt-STOPS-NLS, ***, $p=3 \times 10^{-4}$; Control vs. Rapamycin, ***, $p=1 \times 10^{-4}$.

binds and inhibits pol III, was shown to be phosphorylated in an mTOR-dependent manner at serine 75, a site that is important for its function as a transcriptional repressor. These results led to the model proposing that mTORC1 phosphorylates Maf1 at the promoters, relieving its repression on pol III-dependent transcription of tRNA and 5S rRNA (**Figure 1.18a**) (Kantidakis et al., 2010). To test whether nuclear mTORC1 activity regulates pol III-dependent transcription, we examined the effect of nuclear Akt-STOPS on pol III-dependent transcription of tRNAs. We compared the expression of pre-tRNA^{Leu} and pre-tRNA^{Tyr} in NIH3T3 cells expressing Akt-STOPS-NLS. The presence of Akt-STOPS-NLS down-regulated pol III transcripts tRNA^{Leu} and tRNA^{Tyr} by 2.3- and 1.8-fold, respectively, in agreement with the inhibition of transcription by rapamycin treatment (**Figure 1.18b**). This data suggests Akt-STOPS-NLS negatively regulates the pol III transcription apparatus, consistent with a positive role of nuclear mTORC1 in regulating pol III-mediated transcription.

Discussion

The kinase complex mTORC1 serves as a central signaling node to transduce diverse signal inputs that control cell growth and metabolism. The intricate spatial regulation of mTORC1 allows downstream signaling to be specific and efficient. As the best characterized site for mTORC1 function, the lysosomal surface has been suggested to be a cellular location where growth factors and nutrient signals converge. An intriguing question is whether mTORC1 activity exists at other subcellular sites to exert broader functional control of downstream effectors. In this study, we used a genetically encoded FRET-based biosensor, in combination with an exogenous nuclear-targeted mTORC1 substrate S6K1, to provide clear evidence that mTORC1 activity is present in the nucleus where it can be stimulated by growth factors and insulin.

Given the critical regulation of mTORC1 by Akt downstream of growth factor signaling, we developed Akt-STOPS to perturb the Akt signaling in a location-specific manner. Previously, a location-specific Akt inhibitor, PKBi, was developed based on kinase trapping by a designed pseudosubstrate of Akt (Maiuri et al., 2010). Using a similar approach, but taking advantage of strong inhibitory effects by a kinase substrate compared to a pseudosubstrate, we developed AMPK inhibitor peptide (AIP) using the consensus substrate peptide for AMPK (Miyamoto et al., 2015). Prompted by these studies, we designed Akt-STOPS to buffer Akt activity towards endogenous substrates. These genetically encodable peptide inhibitors (GEPIs), either in pseudosubstrate- or substrate-competitive manner, usually exhibit IC_{50} in high μM range (Henriques et al., 2013; Miyamoto et al., 2015) in *vitro*, in comparison with small molecule inhibitors with IC_{50} in low μM or even nM range, to inhibit the activity of kinases-of-interest. However, these genetically encoded peptide inhibitors can achieve effective inhibition in cells and offer a unique advantage as they can be targeted to specific subcellular locations, membrane microdomains, or multi-protein complexes (Miyamoto et al., 2015), allowing the perturbation of the cellular enzyme activities with high spatial precision.

In this study, by using Akt-STOPS, we found nuclear mTORC1 activity is dependent on nuclear Akt activity upon growth factor stimulation but not amino acid surrogate stimulation. Our findings further suggest a model where nuclear Akt facilitates the nuclear translocation of Raptor (Figure 1.20). Raptor is a critical and defining component of the mTORC1 complex and binds several mTORC1 substrates to the TOR signaling (TOS) motif (Nojima et al., 2003; Schalm et al., 2003). In response to amino acids, Raptor binds to Rag GTPases to localize mTOR to the lysosomal surface (Anandapadamanaban et al., 2019; Rogala et al., 2019; Sancak et al., 2008). Our

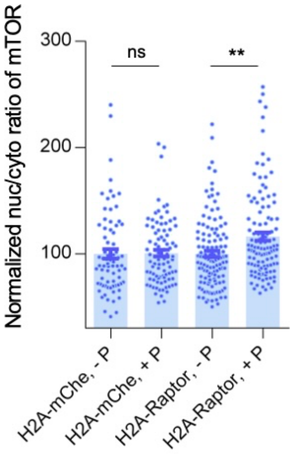

Figure 1.19 Expression of nuclear Raptor slightly increases nuclear distribution of mTOR. Quantification of mean nuclear intensity/mean cytosol intensity ratio (Nuc/Cyto ratio) of mTOR immunostaining per cell. Double-starved NIH3T3 cells expressing H2A-mCherry or H2A-Raptor without treatment (-P) or were treated with 50 ng/ml of PDGF for 30 min (+ P). n = 76, 90, 124, 117 cells. n = three experiments. All data are mean ± s.e.m. P value was determined by unpaired two-tailed student's t-test with Welch's correction. H2A-mChe, - PDGF vs. H2A-mChe, + PDGF, ns, not significant, p=0.9; H2A-Raptor, - PDGF vs. H2A-Raptor, + PDGF, **, p=1 x 10^{-3}.

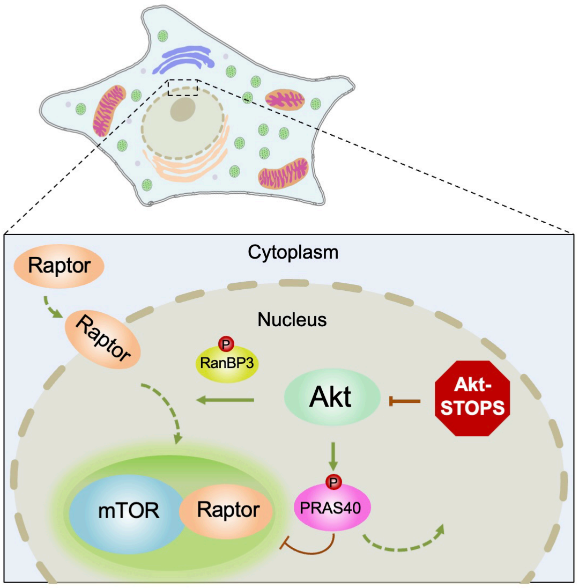

Figure 1.20 A model showing the regulation of nuclear mTORC1 by Akt. Nuclear Akt enhances the nuclear translocation of Raptor through phosphorylation of RanBP3 and relieves the negative regulation of PRAS40 on mTORC1 through phosphorylation of PRAS40. As a result, mTORC1 activity increases upon growth factor stimulation. Nuclear Akt-STOPS selectively suppresses the nuclear Akt activity, thereby reducing nuclear mTORC1 activity.

data showed that localizing exogenous Raptor to the nucleus results in nuclear mTORC1 activity in the absence of growth factor stimulation. An attractive model would be that in the presence of growth factor, Raptor translocates into the nucleus and allows mTORC1 to assemble in the nucleus, leading to an increase in nuclear mTORC1 activity. Interestingly, expression of nuclear Raptor slightly increased the nuclear distribution of mTOR upon growth factor stimulation (**Figure 1.19**), whereas no significant changes in mTOR nuclear localization was observed in wildtype cells following stimulation. Additional regulatory mechanisms may involve PRAS40, the negative regulator of mTORC1 (Kovacina et al., 2003; Sancak et al., 2007), which can be phosphorylated by Akt to relieve its inhibition, further enhancing nuclear mTORC1 activity. Indeed, we showed that PRAS40 knockdown in cells expressing nuclear localized Raptor significantly increased basal mTORC1 activity and diminished the PDGF-stimulated activity (**Figure 1.17a, b, d, e**), suggesting that Akt-mediated suppression of PRAS40-inhibition of mTORC1 provides an additional mechanism for growth factor dependent regulation of nuclear mTORC1 activity. On the other hand, the direct and essential activator for mTORC1, Rheb GTPase, has been suggested to localize in the nucleus (Menon et al., 2014), where relatively low levels of nuclear TSC2, the only well-established regulator and GAP of Rheb, is present. Thus, nuclear translocation of Raptor and phosphorylation of PRAS40, both regulated by Akt, are two major mechanisms that potentially regulate nuclear mTORC1 (**Figure 1.20**).

These findings provide the basis for future work to identify nuclear-specific mTORC1 substrates and elucidate the functions of nuclear mTORC1. Nuclear mTORC1 signaling has been suggested to promote transcription of metabolic genes (Cunningham et al., 2007; Kantidakis et al., 2010; Laplante and Sabatini, 2013). For example, mTORC1 was shown to interact with the transcription factor yin-yang 1 (YY1) at promoter sites of the genes encoding PPARc coactivator-

1 (PGC1a) and cytochrome c, and inhibition of mTORC1 by rapamycin resulted in a failure of YY1 to interact with and be coactivated by PGC-1a (Cunningham et al., 2007). While we show in this study that nuclear Akt-STOPS suppresses pol III transcription, suggesting nuclear mTORC1 regulates pol III transcriptional activity, additional roles of nuclear mTORC1 and its nuclear specific substrates have yet to be uncovered and identified. Diversity in the regulation of different pools of mTORC1 could lead to specificity in functional controls and also provide opportunities for selective targeting.

Chapter 1, in full, is a reformatted reprint of the material as it appears in Zhou, X., Zhong, Y., Molinar-Inglis, O., Kunkel, M.T., Chen, M., Sun, T., Zhang, J., Shyy, J.Y.-J., Trejo, J., Newton, A.C., Zhang, J. (2020). Location-specific inhibition of Akt reveals regulation of mTORC1 activity in the nucleus. *Nat Commun* 11, 6088. The dissertation author was the primary investigator and author of this work.

References

Ali, S. M. & Sabatini, D. M. 2005. Structure of S6 kinase 1 determines whether raptor-mTOR or rictor-mTOR phosphorylates its hydrophobic motif site. *J Biol Chem,* 280(20)**,** pp 19445-8.

Anandapadamanaban, M., Masson, G. R., Perisic, O., Berndt, A., Kaufman, J., Johnson, C. M., Santhanam, B., Rogala, K. B., Sabatini, D. M. & Williams, R. L. 2019. Architecture of human Rag GTPase heterodimers and their complex with mTORC1. *Science,* 366(6462)**,** pp 203-210.

Ananthanarayanan, B., Fosbrink, M., Rahdar, M. & Zhang, J. 2007. Live-cell molecular analysis of Akt activation reveals roles for activation loop phosphorylation. *J Biol Chem,* 282(50)**,** pp 36634-41.

Arosio, P., Knowles, T. P. & Linse, S. 2015. On the lag phase in amyloid fibril formation. *Phys Chem Chem Phys,* 17(12)**,** pp 7606-18.

Baffi, T. R., Van, A. N., Zhao, W., Mills, G. B. & Newton, A. C. 2019. Protein Kinase C Quality Control by Phosphatase PHLPP1 Unveils Loss-of-Function Mechanism in Cancer. *Mol Cell,* 74(2)**,** pp 378-392 e5.

Bayle, J. H., Grimley, J. S., Stankunas, K., Gestwicki, J. E., Wandless, T. J. & Crabtree, G. R. 2006. Rapamycin analogs with differential binding specificity permit orthogonal control of protein activity. *Chem Biol,* 13(1)**,** pp 99-107.

Benvegnu, S., Mateo, M. I., Palomer, E., Jurado-Arjona, J. & Dotti, C. G. 2017. Aging Triggers Cytoplasmic Depletion and Nuclear Translocation of the E3 Ligase Mahogunin: A Function for Ubiquitin in Neuronal Survival. *Mol Cell,* 66(3)**,** pp 358-372 e7.

Bernardi, R., Guernah, I., Jin, D., Grisendi, S., Alimonti, A., Teruya-Feldstein, J., Cordon-Cardo, C., Simon, M. C., Rafii, S. & Pandolfi, P. P. 2006. PML inhibits HIF-1alpha translation and neoangiogenesis through repression of mTOR. *Nature,* 442(7104)**,** pp 779-85.

Betz, C. & Hall, M. N. 2013. Where is mTOR and what is it doing there? *J Cell Biol,* 203(4)**,** pp 563-74.

Bunemann, M., Frank, M. & Lohse, M. J. 2003. Gi protein activation in intact cells involves subunit rearrangement rather than dissociation. *Proc Natl Acad Sci U S A,* 100(26)**,** pp 16077-82.

Callender, J. A., Yang, Y., Lorden, G., Stephenson, N. L., Jones, A. C., Brognard, J. & Newton, A. C. 2018. Protein kinase Calpha gain-of-function variant in Alzheimer's disease displays enhanced catalysis by a mechanism that evades down-regulation. *Proc Natl Acad Sci U S A,* 115(24)**,** pp E5497-E5505.

Carpenter, A. E., Jones, T. R., Lamprecht, M. R., Clarke, C., Kang, I. H., Friman, O., Guertin, D. A., Chang, J. H., Lindquist, R. A., Moffat, J., Golland, P. & Sabatini, D. M. 2006. CellProfiler: image analysis software for identifying and quantifying cell phenotypes. *Genome Biol,* 7(10)**,** pp R100.

Clister, T., Greenwald, E. C., Baillie, G. S. & Zhang, J. 2019. AKAP95 Organizes a Nuclear Microdomain to Control Local cAMP for Regulating Nuclear PKA. *Cell Chem Biol,* 26(6)**,** pp 885-891 e4.

Copp, J., Manning, G. & Hunter, T. 2009. TORC-specific phosphorylation of mammalian target of rapamycin (mTOR): phospho-Ser2481 is a marker for intact mTOR signaling complex 2. *Cancer Res,* 69(5)**,** pp 1821-7.

Cunningham, J. T., Rodgers, J. T., Arlow, D. H., Vazquez, F., Mootha, V. K. & Puigserver, P. 2007. mTOR controls mitochondrial oxidative function through a YY1-PGC-1alpha transcriptional complex. *Nature,* 450(7170)**,** pp 736-40.

Demetriades, C., Doumpas, N. & Teleman, A. A. 2014. Regulation of TORC1 in Response to Amino Acid Starvation via Lysosomal Recruitment of TSC2. *Cell,* 156(4)**,** pp 786-99.

Depry, C., Allen, M. D. & Zhang, J. 2011. Visualization of PKA activity in plasma membrane microdomains. *Mol Biosyst,* 7(1)**,** pp 52-8.

Dibble, C. C. & Cantley, L. C. 2015. Regulation of mTORC1 by PI3K signaling. *Trends Cell Biol,* 25(9)**,** pp 545-55.

Dibble, C. C. & Manning, B. D. 2013. Signal integration by mTORC1 coordinates nutrient input with biosynthetic output. *Nat Cell Biol,* 15(6)**,** pp 555-64.

Gallegos, L. L., Kunkel, M. T. & Newton, A. C. 2006. Targeting protein kinase C activity reporter to discrete intracellular regions reveals spatiotemporal differences in agonist-dependent signaling. *J Biol Chem,* 281(41)**,** pp 30947-56.

Gao, X., Lowry, P. R., Zhou, X., Depry, C., Wei, Z., Wong, G. W. & Zhang, J. 2011. PI3K/Akt signaling requires spatial compartmentalization in plasma membrane microdomains. *Proc Natl Acad Sci U S A,* 108(35)**,** pp 14509-14.

Hara, K., Maruki, Y., Long, X., Yoshino, K., Oshiro, N., Hidayat, S., Tokunaga, C., Avruch, J. & Yonezawa, K. 2002. Raptor, a binding partner of target of rapamycin (TOR), mediates TOR action. *Cell,* 110(2)**,** pp 177-89.

Havel, J. J., Li, Z., Cheng, D., Peng, J. & Fu, H. 2015. Nuclear PRAS40 couples the Akt/mTORC1 signaling axis to the RPL11-HDM2-p53 nucleolar stress response pathway. *Oncogene,* 34(12)**,** pp 1487-98.

Henriques, S. T., Thorstholm, L., Huang, Y. H., Getz, J. A., Daugherty, P. S. & Craik, D. J. 2013. A novel quantitative kinase assay using bacterial surface display and flow cytometry. *PLoS One,* 8(11)**,** pp e80474.

Inoki, K., Li, Y., Zhu, T., Wu, J. & Guan, K. L. 2002. TSC2 is phosphorylated and inhibited by Akt and suppresses mTOR signalling. *Nat Cell Biol,* 4(9)**,** pp 648-57.

Jewell, J. L. & Guan, K. L. 2013. Nutrient signaling to mTOR and cell growth. *Trends Biochem Sci,* 38(5)**,** pp 233-42.

Kantidakis, T., Ramsbottom, B. A., Birch, J. L., Dowding, S. N. & White, R. J. 2010. mTOR associates with TFIIIC, is found at tRNA and 5S rRNA genes, and targets their repressor Maf1. *Proc Natl Acad Sci U S A,* 107(26)**,** pp 11823-8.

Kazyken, D., Kaz, Y., Kiyan, V., Zhylkibayev, A. A., Chen, C. H., Agarwal, N. K. & Sarbassov dos, D. 2014. The nuclear import of ribosomal proteins is regulated by mTOR. *Oncotarget,* 5(20)**,** pp 9577-93.

Keranen, L. M. & Newton, A. C. 1997. Ca2+ differentially regulates conventional protein kinase Cs' membrane interaction and activation. *J Biol Chem,* 272(41)**,** pp 25959-67.

Kim, D. H., Sarbassov, D. D., Ali, S. M., King, J. E., Latek, R. R., Erdjument-Bromage, H., Tempst, P. & Sabatini, D. M. 2002. mTOR interacts with raptor to form a nutrient-sensitive complex that signals to the cell growth machinery. *Cell,* 110(2)**,** pp 163-75.

Kim, D. H., Sarbassov, D. D., Ali, S. M., Latek, R. R., Guntur, K. V., Erdjument-Bromage, H., Tempst, P. & Sabatini, D. M. 2003. GbetaL, a positive regulator of the rapamycin-sensitive pathway required for the nutrient-sensitive interaction between raptor and mTOR. *Mol Cell,* 11(4)**,** pp 895-904.

Kim, J. & Guan, K. L. 2019. mTOR as a central hub of nutrient signalling and cell growth. *Nat Cell Biol,* 21(1)**,** pp 63-71.

Kovacina, K. S., Park, G. Y., Bae, S. S., Guzzetta, A. W., Schaefer, E., Birnbaum, M. J. & Roth, R. A. 2003. Identification of a proline-rich Akt substrate as a 14-3-3 binding partner. *J Biol Chem,* 278(12)**,** pp 10189-94.

Laplante, M. & Sabatini, D. M. 2013. Regulation of mTORC1 and its impact on gene expression at a glance. *J Cell Sci,* 126(Pt 8)**,** pp 1713-9.

Liberles, S. D., Diver, S. T., Austin, D. J. & Schreiber, S. L. 1997. Inducible gene expression and protein translocation using nontoxic ligands identified by a mammalian three-hybrid screen. *Proc Natl Acad Sci U S A,* 94(15)**,** pp 7825-30.

Maiuri, T., Ho, J. & Stambolic, V. 2010. Regulation of adipocyte differentiation by distinct subcellular pools of protein kinase B (PKB/Akt). *J Biol Chem,* 285(20)**,** pp 15038-47.

Mata-Cabana, A., Sin, O., Seinstra, R. I. & Nollen, E. A. A. 2018. Nuclear/Cytoplasmic Fractionation of Proteins from Caenorhabditis elegans. *Bio Protoc,* 8(20)**,** pp.

Menon, S., Dibble, C. C., Talbott, G., Hoxhaj, G., Valvezan, A. J., Takahashi, H., Cantley, L. C. & Manning, B. D. 2014. Spatial Control of the TSC Complex Integrates Insulin and Nutrient Regulation of mTORC1 at the Lysosome. *Cell,* 156(4)**,** pp 771-85.

Merthan, L., Haller, A., Thal, D. R., von Einem, B. & von Arnim, C. A. F. 2019. The role of PTB domain containing adaptor proteins on PICALM-mediated APP endocytosis and localization. *Biochem J,* 476(14)**,** pp 2093-2109.

Miller, C. J., Lou, H. J., Simpson, C., van de Kooij, B., Ha, B. H., Fisher, O. S., Pirman, N. L., Boggon, T. J., Rinehart, J., Yaffe, M. B., Linding, R. & Turk, B. E. 2019. Comprehensive profiling of the STE20 kinase family defines features essential for selective substrate targeting and signaling output. *PLoS Biol,* 17(3)**,** pp e2006540.

Miyamoto, T., Rho, E., Sample, V., Akano, H., Magari, M., Ueno, T., Gorshkov, K., Chen, M., Tokumitsu, H., Zhang, J. & Inoue, T. 2015. Compartmentalized AMPK signaling illuminated by genetically encoded molecular sensors and actuators. *Cell Rep,* 11(4)**,** pp 657-70.

Nojima, H., Tokunaga, C., Eguchi, S., Oshiro, N., Hidayat, S., Yoshino, K., Hara, K., Tanaka, N., Avruch, J. & Yonezawa, K. 2003. The mammalian target of rapamycin (mTOR) partner, raptor, binds the mTOR substrates p70 S6 kinase and 4E-BP1 through their TOR signaling (TOS) motif. *J Biol Chem,* 278(18)**,** pp 15461-4.

Ramiscal, R. R., Parish, I. A., Lee-Young, R. S., Babon, J. J., Blagih, J., Pratama, A., Martin, J., Hawley, N., Cappello, J. Y., Nieto, P. F., Ellyard, J. I., Kershaw, N. J., Sweet, R. A., Goodnow, C. C., Jones, R. G., Febbraio, M. A., Vinuesa, C. G. & Athanasopoulos, V. 2015. Attenuation of AMPK signaling by ROQUIN promotes T follicular helper cell formation. *Elife,* 4(

Rogala, K. B., Gu, X., Kedir, J. F., Abu-Remaileh, M., Bianchi, L. F., Bottino, A. M. S., Dueholm, R., Niehaus, A., Overwijn, D., Fils, A. P., Zhou, S. X., Leary, D., Laqtom, N. N., Brignole, E. J. & Sabatini, D. M. 2019. Structural basis for the docking of mTORC1 on the lysosomal surface. *Science,* 366(6464)**,** pp 468-475.

Rosner, M. & Hengstschlager, M. 2008. Cytoplasmic and nuclear distribution of the protein complexes mTORC1 and mTORC2: rapamycin triggers dephosphorylation and delocalization of the mTORC2 components rictor and sin1. *Hum Mol Genet,* 17(19)**,** pp 2934-48.

Rosner, M. & Hengstschlager, M. 2011. mTOR protein localization is cell cycle-regulated. *Cell Cycle,* 10(20)**,** pp 3608-10.

Rosner, M. & Hengstschlager, M. 2012. Detection of cytoplasmic and nuclear functions of mTOR by fractionation. *Methods Mol Biol,* 821(105-24.

Ryu, H., Chung, M., Dobrzynski, M., Fey, D., Blum, Y., Lee, S. S., Peter, M., Kholodenko, B. N., Jeon, N. L. & Pertz, O. 2015. Frequency modulation of ERK activation dynamics rewires cell fate. *Mol Syst Biol,* 11(11)**,** pp 838.

Sample, V., DiPilato, L. M., Yang, J. H., Ni, Q., Saucerman, J. J. & Zhang, J. 2012. Regulation of nuclear PKA revealed by spatiotemporal manipulation of cyclic AMP. *Nat Chem Biol,* 8(4)**,** pp 375-82.

Sancak, Y., Peterson, T. R., Shaul, Y. D., Lindquist, R. A., Thoreen, C. C., Bar-Peled, L. & Sabatini, D. M. 2008. The Rag GTPases bind raptor and mediate amino acid signaling to mTORC1. *Science,* 320(5882)**,** pp 1496-501.

Sancak, Y., Thoreen, C. C., Peterson, T. R., Lindquist, R. A., Kang, S. A., Spooner, E., Carr, S. A. & Sabatini, D. M. 2007. PRAS40 is an insulin-regulated inhibitor of the mTORC1 protein kinase. *Mol Cell,* 25(6)**,** pp 903-15.

Saxton, R. A. & Sabatini, D. M. 2017. mTOR Signaling in Growth, Metabolism, and Disease. *Cell,* 168(6)**,** pp 960-976.

Schalm, S. S., Fingar, D. C., Sabatini, D. M. & Blenis, J. 2003. TOS motif-mediated raptor binding regulates 4E-BP1 multisite phosphorylation and function. *Curr Biol,* 13(10)**,** pp 797-806.

Shor, B., Wu, J., Shakey, Q., Toral-Barza, L., Shi, C., Follettie, M. & Yu, K. 2010. Requirement of the mTOR kinase for the regulation of Maf1 phosphorylation and control of RNA polymerase III-dependent transcription in cancer cells. *J Biol Chem,* 285(20)**,** pp 15380-92.

Soderholm, J. F., Bird, S. L., Kalab, P., Sampathkumar, Y., Hasegawa, K., Uehara-Bingen, M., Weis, K. & Heald, R. 2011. Importazole, a small molecule inhibitor of the transport receptor importin-beta. *ACS Chem Biol,* 6(7)**,** pp 700-8.

Thoreen, C. C., Kang, S. A., Chang, J. W., Liu, Q., Zhang, J., Gao, Y., Reichling, L. J., Sim, T., Sabatini, D. M. & Gray, N. S. 2009. An ATP-competitive mammalian target of rapamycin inhibitor reveals rapamycin-resistant functions of mTORC1. *J Biol Chem,* 284(12)**,** pp 8023-32.

Torrini, C., Cubero, R. J., Dirkx, E., Braga, L., Ali, H., Prosdocimo, G., Gutierrez, M. I., Collesi, C., Licastro, D., Zentilin, L., Mano, M., Zacchigna, S., Vendruscolo, M., Marsili, M., Samal, A. & Giacca, M. 2019. Common Regulatory Pathways Mediate Activity of MicroRNAs Inducing Cardiomyocyte Proliferation. *Cell Rep,* 27(9)**,** pp 2759-2771 e5.

Tsang, C. K., Liu, H. & Zheng, X. F. 2011. mTOR binds to the promoters of RNA polymerase I- and III-transcribed genes. *Cell Cycle,* 9(5)**,** pp 953-7.

Wagstaff, K. M., Sivakumaran, H., Heaton, S. M., Harrich, D. & Jans, D. A. 2012. Ivermectin is a specific inhibitor of importin alpha/beta-mediated nuclear import able to inhibit replication of HIV-1 and dengue virus. *Biochem J,* 443(3)**,** pp 851-6.

Wan, R., Wu, J., Ouyang, M., Lei, L., Wei, J., Peng, Q., Harrison, R., Wu, Y., Cheng, B., Li, K., Zhu, C., Tang, L., Wang, Y. & Lu, S. 2019. Biophysical basis underlying dynamic Lck activation visualized by ZapLck FRET biosensor. *Sci Adv,* 5(6)**,** pp eaau2001.

Wan, W., You, Z., Xu, Y., Zhou, L., Guan, Z., Peng, C., Wong, C. C. L., Su, H., Zhou, T., Xia, H. & Liu, W. 2017. mTORC1 Phosphorylates Acetyltransferase p300 to Regulate Autophagy and Lipogenesis. *Mol Cell,* 68(2)**,** pp 323-335 e6.

Yang, T. T., Yu, R. Y., Agadir, A., Gao, G. J., Campos-Gonzalez, R., Tournier, C. & Chow, C. W. 2008. Integration of protein kinases mTOR and extracellular signal-regulated kinase 5 in regulating nucleocytoplasmic localization of NFATc4. *Mol Cell Biol,* 28(10)**,** pp 3489-501.

Yoon, S. O., Shin, S., Liu, Y., Ballif, B. A., Woo, M. S., Gygi, S. P. & Blenis, J. 2008. Ran-binding protein 3 phosphorylation links the Ras and PI3-kinase pathways to nucleocytoplasmic transport. *Mol Cell,* 29(3)**,** pp 362-75.

Zhou, X., Clister, T. L., Lowry, P. R., Seldin, M. M., Wong, G. W. & Zhang, J. 2015a. Dynamic Visualization of mTORC1 Activity in Living Cells. *Cell Rep,* 10(10)**,** pp 1767-1777.

Zhou, X., Clister, T. L., Lowry, P. R., Seldin, M. M., Wong, G. W. & Zhang, J. 2015b. Dynamic Visualization of mTORC1 Activity in Living Cells. *Cell Rep*.

Zoncu, R., Bar-Peled, L., Efeyan, A., Wang, S., Sancak, Y. & Sabatini, D. M. 2011. mTORC1 senses lysosomal amino acids through an inside-out mechanism that requires the vacuolar H(+)-ATPase. *Science,* 334(6056)**,** pp 678-83.

Chapter 2

Rheb Regulates Nuclear mTORC1 Activity Independent of Farnesylation

Introduction

The mechanistic target of rapamycin complex 1 (mTORC1) is a key signaling complex that consists of the catalytic kinase mTOR and numerous associated components, including the mTORC1 defining component Raptor. mTORC1 plays a central role in regulating many fundamental cellular processes, such as nutrient sensing, metabolism, macromolecule synthesis, proliferation, and autophagy. mTORC1 signaling pathway is widely implicated in pathological conditions such as cancer and type 2 diabetes (Laplante and Sabatini, 2012). In a canonical model, mTORC1 is activated by the small GTPase Rheb at the lysosomal surface in response to either amino acid or growth factor stimulation (Kim and Guan, 2019; Liu and Sabatini, 2020).

Rheb is a small GTPase and its activity is determined by nucleotide binding state (Tabancay et al., 2003; Long et al., 2005). The active GTP-bound form of Rheb interacts with mTORC1 and allosterically turns on mTOR kinase activity (Yang et al., 2017a). It is well established that Rheb is essential for canonical mTORC1 activation. The nucleotide binding state of Rheb is regulated by the Tuberous Sclerosis Complex 2 (TSC2), a tumor suppressor and a GTPase activating protein (GAP) towards Rheb. TSC2 facilitates hydrolysis of the bound GTP to GDP, thus inactivating Rheb (Inoki et al., 2003; Tee et al., 2003). Like many other small GTPases, Rheb undergoes post-translational modifications at its C-terminus where a CAAX motif marks it for modification by a farnesyl group, which has been shown to regulate the membrane association of Rheb (Clark et al., 1997; Takahashi et al., 2005; Hanker et al., 2010). Rheb has been reported to be present on the lysosomal surface, where mTORC1 and TSC also reside (Demetriades et al., 2014; Menon et al., 2014). In response to growth factor stimulation, the active upstream kinase Akt phosphorylates TSC2 (Inoki et al., 2002; Manning et al., 2002) and triggers its disassociation from the lysosomal surface, thus relieving the inhibition of Rheb and leading to eventual mTORC1 activation on the lysosome by active Rheb (Menon et al., 2014) (Figure S1A).

In addition to the canonical lysosomal pool of mTORC1, mTORC1 components were also found to be present in the nucleus although the presence of mTORC1 activity was under debate (Kim and Chen, 2000; Bernardi et al., 2006; Havel et al., 2015; Kantidakis et al., 2010; Wan et al., 2017; Zhang et al., 2002; Rosner and Hengstschläger, 2012). We recently discovered nuclear mTORC1 activity in living cells, which can be induced by platelet-derived growth factor (PDGF) or leucine-O-methyl ester, an amino acid surrogate, in NIH3T3 cells or by insulin in 3T3L1 adipocytes (Zhou et al., 2015, 2020). This discovery was enabled by the development of a genetically encoded mTORC1 activity reporter (TORCAR). Briefly, the mTORC1 substrate 4EBP1 is sandwiched between a pair of cyan and yellow fluorescent proteins that can undergo fluorescence resonance energy transfer (FRET). Phosphorylation of 4EBP1 within TORCAR by mTORC1 induces a conformational change, leading to an increase in the cyan/yellow emission ratio, which serves as a readout for increased mTORC1 kinase activity. Using TORCAR variant targeted to the nucleus, we detected nuclear mTORC1 activity in response to growth factor stimulation (Zhou et al., 2015). This activity was shown to be dependent on nuclear Akt activity, which promotes Raptor translocation into the nucleus and phosphorylates PRAS40 to relieve its inhibition on mTORC1, leading to an increase in nuclear mTORC1 activity (Zhou et al., 2020) (Figure S1A). While nuclear mTORC1 is under this noncanonical regulation by nuclear Akt, whether other factors in the canonical mTORC1 pathway play a role in modulating nuclear mTORC1 activity is unclear. In particular, does Rheb regulate nuclear mTORC1 activity, given that it is a direct and essential activator of mTORC1? How does a lysosomally localized GTPase regulate a nuclear complex? Related to the latter question, emerging evidence suggests that Rheb also localizes to other cellular compartments in addition to the lysosome (Hao et al., 2018; Angarola and Ferguson, 2019, 2020). However, the functional roles of these subcellular pools of Rheb in mTORC1 signaling have not been defined.

In this study, we focused on examining whether the canonical TSC/Rheb axis is conserved in the nucleus to regulate nuclear mTORC1 activity. We found that although there is no evidence for the presence of nuclear TSC2, active Rheb is present in the nucleus and required for nuclear mTORC1 activity. We further showed that lipid modification of Rheb is not required for regulating nuclear mTORC1 activity and lysosomal tethering of farnesylation-deficient Rheb enables mTORC1 signaling. In summary, the present study reveals the mechanisms that specifically regulate nuclear mTORC1 activity and provides new insights into both the canonical and noncanonical regulation of mTORC1 by an important small GTPase, Rheb.

Methods

Reagents and Drug Treatment

PDGF (P3201) was purchased from Sigma and was used at 50 ng/mL to stimulate starved cells. Rapamycin (R-5000) was purchased from LC Labs and was used at 100 nM for 30 min pretreatment before imaging experiments were performed. FTI-277 was purchased from ApexBio (B5842) and used at 5 µM for overnight treatment. DMSO was purchased from Sigma (D2650) and used as vehicle. Doxycycline was purchased from Clontech (631311) and supplemented in medium at a final concentration of 100 ng/mL to induce gene expression.

Constructs and Cloning

mTORC1 activity reporter (TORCAR) and its targeted versions (TORCAR-NES and TORCAR-NLS) were previously described (Zhou et al., 2020). The shRNA sequence targeting mouse Rheb (TRCN0000075605) and TSC2 (TRCN0000306245) were obtained from The RNAi Consortium shRNA Library. Primers containing the sense and anti-sense shRNA sequences were designed (Eton Bioscience, Inc.) to amplify a lentivirus shRNA transfer plasmid obtained from Addgene (#21339). The resulting PCR products were purified and Gibson assembled into pLKO.shRheb. Similarly, the pcDNA3-mCherry expressing vector was assembled by amplifying fragments from pcDNA3-Akt-STOPS (Zhou et al., 2020). To construct the pcDNA3-mCherry-TSC2 plasmid, pcDNA3-mCherry construct was used to amplify fragments to serve as backbone portions, and pcDNA3-Flag-TSC2 (Addgene #14129) was used to amplify TSC2. The resulting PCR fragments were purified and Gibson assembled to generate pcDNA3-mCherry-TSC2. The pcDNA3-mCherry-TSC2-AA was constructed using a strategy similar to the one used to construct pcDNA3-mCherry-TSC2 using fragments amplified from pcDNA-Flag-TSC2-AA (Addgene #14131). The pcDNA3-mCherry-TSC2-AA-3Q was generated by designing primers covering TSC2 1595-1597 (KRR) to change the sequence to QQQ and fragments with mutations were Gibson assembled. The nuclearly targeted version of these constructs were generated similarly. mCherry-tagged Rheb constructs were Gibson assembled from a human myc-Rheb plasmid (provided by the Kun-Liang Guan Lab), and pcDNA3-mCherry-Rheb was used as the backbone for Gibson assembly to generate pcDNA3-mCherry-Rheb-C181S and pcDNA3-mCherry-Rheb-*Δ*5A mutants using primers with mutation or deletion. pcDNA3-mCherry-Rheb-C181S was cut with BamHI/EcoRI to get mCherry-Rheb-C181S and Lyso-TORCAR (Zhou et al., 2015) was cut with BamHI/EcoRI to get the backbone with the lysosome targeting sequence. The fragments were ligated using T4 ligase to generate pcDNA3-Lyso-mCh-Rheb-C181S. pcDNA-mCherry-Rheb, pcDNA-mCherry-Rheb-C181S and pcDNA-Lyso-mCherry-Rheb-181S were subcloned into a doxycycline inducible lentiviral expressing vector (Addgene #27565) using Gibson assembly, yielding pLenti-TetOn-mCherry-Rheb, pLenti-TetOn-mCherry-Rheb-C181S and pLenti-TetOn-Lyso-mCherry-Rheb-C181S. In these pLenti-TetOn constructs, mutations (ACtTAtTCaATcGAc) were made from Rheb 217-231 (ACATACTCCATAGAT) within the shRNA targeting sequences for Rheb to be resistant to shRNA silencing when Rheb knockdown cells were reconstituted with these exogenously expressed Rheb mutants.

Cell Culture, Transfection and Starvation

NIH3T3 cells (CRL-1658, ATCC) were cultured in Dulbecco's modified Eagle's medium (DMEM, 11885, Gibco) supplemented with 10% calf serum (30-2030, ATCC) and 1% penicillin-streptomycin (Sigma-Aldrich). Cells were routinely tested for mycoplasma contamination and found negative. For transfection, cells were transfected with PolyJet Transfection Reagent (SL100688, SignaGen Laboratories) according to the manufacturer's instructions and incubated in serum-free DMEM overnight (serum starvation). The next day, cells were incubated for 2 hours in modified Hank's balanced salt solution (1×HBSS with 2 g/l glucose, pH 7.4, made from 10× HBSS (14065, GIBCO)) at 37°C (referred to as "double starvation") before live cell imaging or immunoblotting. Cal27, HeLa and Cos7 cells were cultured in DMEM supplemented with 10% fetal bovine serum and penicillin-streptomycin. PLC/PRF/5 cells and 3T3L1 adipocytes were obtained from the Feng lab and the Saltiel lab at UC San Diego respectively to perform experiments.

Lentivirus Production and Stable Cell Lines Generation

Lentivirus was packaged in HEK293T cells. Specifically, HEK293T cells were co-transfected with corresponding lentiviral transfer plasmids + psPAX2 + pMD2.G using PolyJet. After 48hr the supernatant was collected, filtered with a 0.45 μm syringe filter and added to NIH3T3 cells in 35 mm dishes. Polybrene Transfection Reagent (TR-1003-G, Millipore) was supplemented to improve the transduction. After 48 hours, cells were passed in fresh growth medium containing puromycin (2 μg/mL) to select transduced cells for at least one week. Cells were maintained in selection medium and passed for related experiments. For doxycycline inducible cell lines, wild type or Rheb knockdown NIH3T3 cells were co-transduced with lentivirus expressing rtTA transcription factor and doxycycline inducible TetOn expressing vectors. Cells were then maintained in growth medium containing puromycin (2 μg/mL) and blasticidin (2.2 μM) and passaged for related experiments.

Nuclear Fractionation

Nuclear fractionation was done as previously reported (Suzuki et al., 2010). Briefly, two 10cm dishes of NIH3T3 fibroblasts were cultured to 80% confluence. Cells were then washed with cold PBS, collected and resuspended in 0.1% NP-40 (492016, Millipore Sigma) followed by short centrifugation. The supernatant was collected as cytosolic fraction and the pellet was washed and collected as nuclear fraction. The same proportion of samples from each fraction was used for immunoblotting analysis.

Immunoblotting

Cells were washed with ice-cold PBS and then lysed in RIPA lysis buffer containing protease inhibitor cocktail, 1 mM PMSF, 1 mM Na_3VO_4, 1 mM NaF, and 25 nM calyculin A. Total cell lysates were incubated on ice for 30 min and then centrifuged at 15,000g at 4°C for 20 min. Equal amounts of total protein were separated via 4-15% SDS-PAGE and transferred to PVDF membranes. The membranes were blocked with TBS containing 0.1% Tween-20 and 5% bovine serum albumin and then incubated with primary antibodies overnight at 4°C. The next day, membranes were washed, incubated with the appropriate horseradish peroxidase-conjugated secondary antibodies, and were developed using horseradish peroxidase-based chemiluminescent substrate (34579 and 34076, Thermo Fisher Scientific). The following primary antibodies were used for immunoblotting: p-S6K1 (T389) (#9205), S6K1 (#9202), TSC2 (#3612) and tubulin (#2146) antibodies from Cell Signaling Technology, Rheb antibody from Abnova (H00006009-M01), p84 (GTX70220) antibody from GeneTex. Horseradish peroxidase-labeled goat anti-rabbit (PI31460) or anti-mouse (PI31430) secondary antibodies were purchased from Pierce.

Immunofluorescence Imaging

For immunofluorescence, upon reaching ~80% confluency in 6-well plates (353046, Corning) containing glass coverslips (12-541A, Fisher Brand), cells were washed 3 times with PBS and fixed with 4% paraformaldehyde in PBS (15710S, Electron Microscopy Sciences) for 25 min at room temperature. Cells were then washed 3 times with PBS and permeabilized with PBS containing 0.1% Triton X-100 for 25 min at room temperature. Following 1-hour incubation in blocking buffer (PBS containing 0.1% Triton X-100 and 5% BSA) at room temperature, coverslips were incubated overnight at 4ºC in primary antibody diluted in blocking buffer. Following three 5-min washes in PBS, coverslips were incubated for 1 hour at room temperature in the dark in secondary antibody (anti-rabbit Alexa Fluor 488, A11006) at 1:1000 dilution in blocking buffer. Following three 5-min washes with PBS, coverslips were mounted in Prolong Glass antifade Mountant with NucBlue (P36981, Invitrogen). Coverslips were dried and kept in -20°C before images were taken. Primary antibodies used were anti-Rheb (H00006009-M01) from Abnova, and anti-TSC1 (#6935) and anti-TSC2 (#4308) from Cell Signaling Technology. Confocal images for both green (488 nm ex) and blue (405 nm ex) channels were acquired by a Leica SP8 microscope with 60x oil objective (1.40 NA) or 40x oil objective (1.30 NA) in Lightning Deconvolution mode. For each coverslip, the middle slice was obtained and multiple images were taken for each experimental condition from different biological samples. Images were analyzed using CellProfiler software (Broad Institute). Briefly, the green channel was used to segment the cell and the mean intensity was measured for each cell as the whole cell signal. The blue channel was used as nuclear marker to segment the nuclear region, and the nuclear mean intensity in the green channel was measured as nuclear signal. Line scan was drawn in ImageJ software (NIH) and the intensity along the line was measured.

Live-cell Imaging

For live cell imaging, cells were plated onto sterile glass-bottomed 35-mm dishes (D35-14-1.5-N, CellVis) and grown to 40% confluency at 37°C with 5% CO_2. Cells were transfected, double starved, and washed once with HBSS and imaged in the dark at room temperature. Images were acquired on a Zeiss Axio Observer Z1 microscope equipped with a 40x/1.3NA objective (Carl Zeiss), Prime95B sCMOS camera (Photometrics) and a motorized stage (Carl Zeiss). The microscope was controlled by MATLAB (Mathworks) and μmanager (Micro-Manager, an open-source microscope imaging software) -based MATScope imaging suite (Github:

https://github.com/jinzhanglab-ucsd/MatScopeSuite). CFP images were acquired using ET420/20x excitation filter with a T4551pxt dichroic and AT470/40m emission filter. YFP images were acquired using ET495/10x excitation filter with a T5151p dichroic and ET535/25m emission filter. The C/Y FRET images were acquired using ET420/20x excitation filter with T4551pxt dichroic and ET535/25m emission filter. mCherry imaging was performed using HQ568/55x excitation filter with a Q600LPxr dichroic mirror and HQ653/95m emission filter. Exposure times were 50-500 ms, and images were taken every 30 s or 1 min. Imaging data were analyzed using MATLAB scripts developed within the lab. Specifically, fluorescence images were background-corrected and regions of interest (ROI) were manually selected. For TORCAR-NES and TORCAR-NLS, ROIs were within the cytosolic or nuclear regions, respectively. For TORCAR, when whole cell responses were measured (Figures 2.1C-2.1D), individual cells were selected as the ROIs; and when the cytosolic response of TORCAR was examined (Figures 2.8B-22.8C), ROIs were within the cytosolic regions and data was labeled as “Cytosolic regions”. The cyan/yellow FRET emission ratio was calculated for each ROI on each frame of the image series. The ratio was normalized to the time point before addition of PDGF (t = 0 min). For lysosomal colocalization experiments, lysosomes were visualized in live cells using LysoTracker Green DND-26 (L7526, Invitrogen). Briefly, before images were taken under the microscope, LysoTracker Green was added to the medium and incubated with cells for 30 min, then cells were washed twice in HBSS imaging buffer. LysoTracker Green were visualized using 488 nm excitation under the microscope.

Statistical Analysis

The data were analyzed using GraphPad Prism 9. Immunofluorescence data were obtained from two biological replicates, and all other data were obtained from at least three independent biological replicates. Unless otherwise noted, unpaired two-tailed t-test was used for two-group comparison and one-way ANOVA with Dunnett's multiple comparisons test were used for multi-group comparisons. **** indicates a p-value<0.0001; *** indicates a p-value between 0.0001 to 0.001; ** indicates a p-value between 0.001 to 0.01; * indicates a p-value between 0.01 to 0.05; ns, p>0.05, not significant. N numbers, as indicated in figures, legends and the main text, represent the number of cells. Shaded areas in average curves indicate standard error of the mean (SEM). Violin plots and box plots show the upper and lower adjacent value, interquartile range and the median.

Results

Rheb is present in the nucleus and required for nuclear mTORC1 activity

To determine whether Rheb is required for nuclear mTORC1 activity, we generated a Rheb knockdown cell line using NIH3T3 cells infected with lentivirus carrying shRNA targeting Rheb mRNA. The protein level of Rheb was efficiently reduced, as evaluated by western blotting (**Figure 2.1B**). As expected, Rheb knockdown significantly reduced PDGF-induced phosphorylation of mTORC1 substrate, S6K1 at Thr389 (Saitoh et al., 2002; Hay and Sonenberg, 2004) (**Figure 2.1B**). Consistent with these data, the mTORC1 activity reporter TORCAR showed a diminished cyan/yellow (C/Y) emission ratio change in response to PDGF stimulation in Rheb knockdown cells (2.2 ± 0.6 %, n = 34) compared with wild type cells (10.0 ± 0.5 %, n = 32), on par with the response in Raptor knockdown cells (3.7 ± 0.5 %, n = 12), suggesting that Rheb is required for cellular mTORC1 activity (**Figure 2.1C-D**). To examine the impact of knocking down

Figure 2.1 Rheb knockdown abolished mTORC1 activity in response to PDGF. (A) A model showing the growth factor stimulated activation of the lysosomal and nuclear mTORC1. Whether the TSC/Rheb axis exists in the nucleus to regulate mTORC1 is not clear. (B) Western blotting data to show that Rheb protein level was reduced in Rheb knockdown stable NIH3T3 cells. Wild type (WT) and Rheb knockdown (shRheb) cells were double starved and stimulated with 50 ng/mL PDGF for 30 min or were unstimulated. Phosphorylation of mTORC1 substrate S6K1 at Thr389 (T389) was examined. Data are representative from three independent experiments. (C-D) Representative averaged time course traces (C) and summary (D) of PDGF-induced maximum responses of TORCAR in double starved NIH3T3 cells. Blue, wild type cells (WT, N = 29 cells from 4 independent experiments); yellow, Rheb knockdown cells (shRheb, N = 25 cells from 3 independent experiments); green, Raptor knockdown cells (shRaptor, N = 20 cells from 3 independent experiments). Shaded areas indicate standard error of the mean (SEM). Box plots show the upper and lower adjacent values, interquartile range and the median. One-way ANOVA with Dunnett's multiple comparisons is used. ****, $p < 0.0001$. (E) Quantification of the whole cell immunofluorescence staining of Rheb in wild type (WT) or Rheb knockdown (shRheb) NIH3T3 cells. Control experiments were done by leaving out the primary antibody ((-) anti-Rheb). Intensities were normalized to the maximum intensity. Violin plots show the upper and lower adjacent values, interquartile range and the median. One-way ANOVA with Dunnett's multiple comparisons is used. ****, $p < 0.0001$. Blue, wild type cells, (+) anti-Rheb (N = 64 cells); yellow, Rheb knockdown cells, (+) anti-Rheb (N = 51 cells); green, wild type cells, (-) anti-Rheb (N = 66 cells); orange, Rheb knockdown cells, (-) anti-Rheb (N = 42 cells). Data are representative from two independent experiments. (F) Nuclear fractionation experiment examining the presence of Rheb in the nuclei in NIH3T3 cells. Same proportions of cytosolic (Cyto) and nuclear (Nuc) fractions corresponding to the same amount of whole cell lysate (WCL) were loaded and an extra lane was loaded with doubled amount of the nuclear fraction (2x load). β-tubulin and p84 served as cytosolic marker and nuclear marker, respectively. Data are representative of three independent experiments.

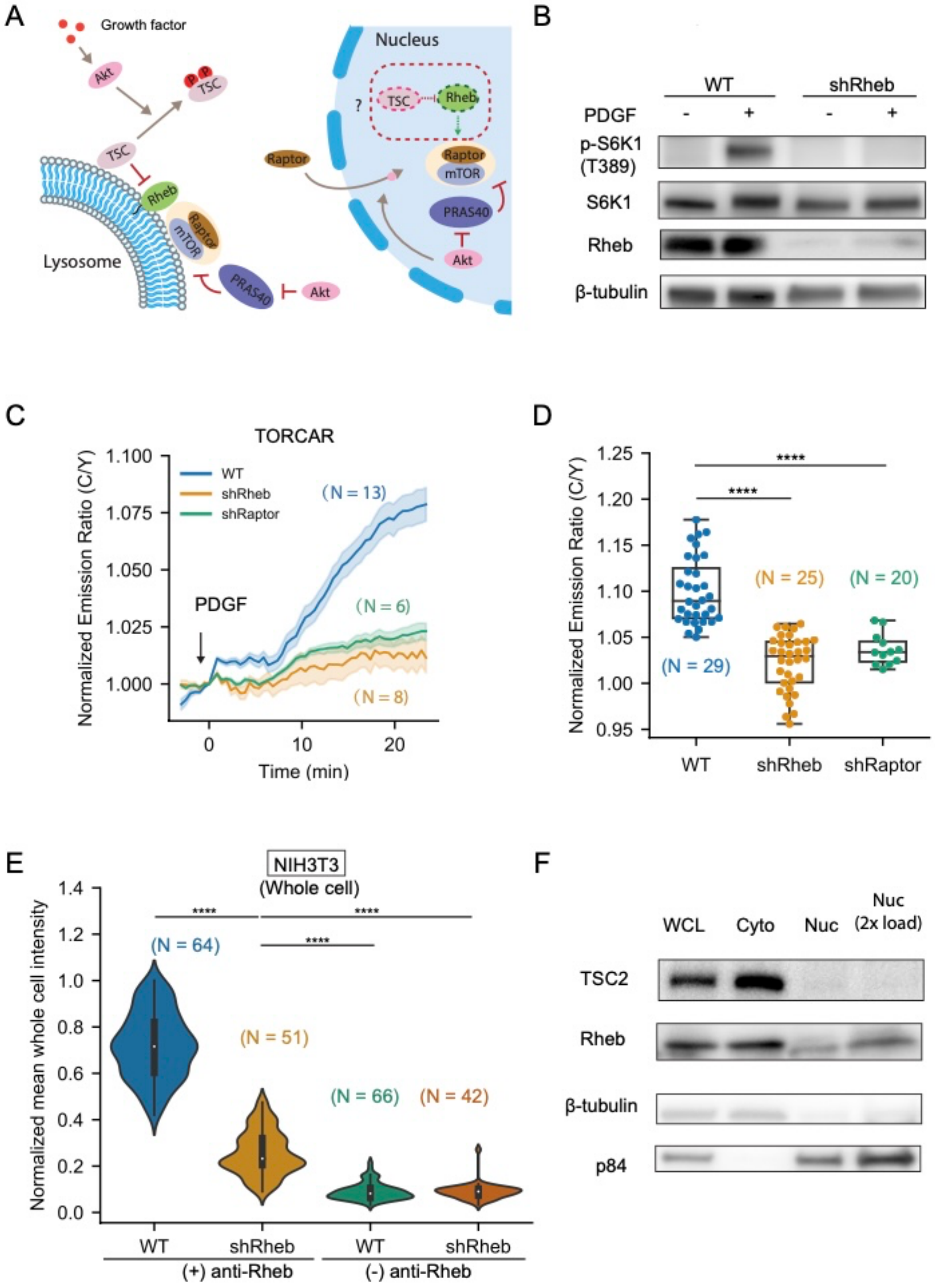
A
Growth factor
Akt
P P
TSC
TSC
Rheb
Raptor
mTOR
Lysosome
PRAS40
Akt
Nucleus
?
TSC
Rheb
Raptor
Raptor
mTOR
PRAS40
Akt
B
WT
shRheb
PDGF
- + - +
p-S6K1 (T389)
S6K1
Rheb
β-tubulin
C
TORCAR
Normalized Emission Ratio (C/Y)
1.100
1.075
1.050
1.025
1.000
WT
shRheb
shRaptor
(N = 13)
(N = 6)
(N = 8)
PDGF
0
10
20
Time (min)
D
Normalized Emission Ratio (C/Y)
1.25
1.20
1.15
1.10
1.05
1.00
0.95
****
****
(N = 29)
(N = 25)
(N = 20)
WT
shRheb
shRaptor
E
NIH3T3
(Whole cell)
Normalized mean whole cell intensity
1.4
1.2
1.0
0.8
0.6
0.4
0.2
0.0
****
****
****
(N = 64)
(N = 51)
(N = 66)
(N = 42)
WT
shRheb
WT
shRheb
(+) anti-Rheb
(-) anti-Rheb
F
WCL
Cyto
Nuc
Nuc (2x load)
TSC2
Rheb
β-tubulin
p84

Rheb on nuclear mTORC1 activity, we expressed the mTORC1 biosensor targeted to the nucleus via a nuclear localization sequence (NLS) (TORCAR-NLS) (Zhou et al., 2015) in both wild type and Rheb knockdown cells and stimulated the cells with PDGF. Rheb knockdown cells showed a minimal emission ratio change upon PDGF stimulation (0.5 ± 0.5 %, n = 25) (**Figure 2.2A-B**). As a control, wild type cells responded to PDGF stimulation with a 6.9 ± 0.4 % increase in C/Y emission ratio (n = 29), which was abolished by pretreatment with rapamycin, an mTORC1 specific inhibitor (**Figure 2.2A-B**). These results suggest an essential role of Rheb for nuclear mTORC1 activity.

Rheb activates lysosomal mTORC1 via co-localization and interaction with mTORC1 (Kim and Guan, 2019; Liu and Sabatini, 2020). We hypothesized that Rheb is also present in the nucleus for activation of nuclear mTORC1. To examine whether endogenous Rheb is present in the nucleus, we probed the distribution of Rheb with an antibody previously validated for immunofluorescence (Menon et al., 2014). As shown in Figure 1C, although the primary localization of Rheb was found to be outside of the nucleus with the majority concentrated in the perinuclear region, a small amount of Rheb was clearly present in the nucleus (**Figure 2.2C** and **Figure 2.3**), which was consistent with previous findings (Menon et al., 2014). The signal was specific to Rheb because knockdown of Rheb significantly reduced the immunofluorescence signal throughout the cell (**Figure 2.1E** and **Figure 2.3**) and essentially abolished the nuclear signal, as shown by the quantifications and line scans across the nuclear region (**Figure 2.2D-E**). To further examine the presence of nuclear Rheb, we performed nuclear fractionation experiments using a published protocol (Suzuki et al., 2010) and found that a small portion of Rheb was present in the nuclear fraction (**Figure 2.1F**). These data show that Rheb is present in the nucleus in NIH3T3

Figure 2.2 Rheb is present in the nucleus and required for nuclear mTORC1 activation. (A-B) Representative averaged time course traces (A) and summary (B) of PDGF-induced maximum responses of TORCAR-NLS, a nuclearly targeted mTORC1 activity reporter, in double starved NIH3T3 cells. Blue, wild type cells (WT, N = 29 cells from 3 independent experiments); yellow, Rheb knockdown cells (shRheb, N = 25 cells from 3 independent experiments); green, wild type cells with rapamycin pretreatment (100 nM for 30 min) (Rapamycin, N = 20 cells from 3 independent experiments). Shaded areas indicate standard error of the mean (SEM). Box plots show the upper and lower adjacent values, interquartile range and the median. One-way ANOVA with Dunnett's multiple comparisons is used. ****, $p < 0.0001$. (C) Representative confocal immunofluorescence images of wild type (WT) NIH3T3 cells and Rheb knockdown (shRheb) cells from two independent experiments. Staining for Rheb is done with a validated antibody (anti-Rheb) and is shown in green and staining for nucleus is shown in blue. Scale bar = 10 μm. (D) Quantification of the nuclear signals in (C). Intensities were normalized to the maximum intensity. Control experiments were done by leaving out the primary antibody ((-) anti-Rheb) for wild type (WT) and Rheb knockdown (shRheb) cells respectively. Violin plots show the upper and lower adjacent values, interquartile range and the median. One-way ANOVA with Dunnett's multiple comparisons is used. ****, $p < 0.0001$. Blue, wild type cells, (+) anti-Rheb (N = 101 cells); yellow, Rheb knockdown cells, (+) anti-Rheb (N = 97 cells); green, wild type cells, (-) anti-Rheb (N = 66 cells); orange, Rheb knockdown cells, (-) anti-Rheb (N = 40 cells). Data are representative from two independent experiments. (E) Line scan shown in (C). A line was drawn across the nuclear region of the cell. Intensities along the line in the green channel were measured and shown as relative arbitrary units (AU).

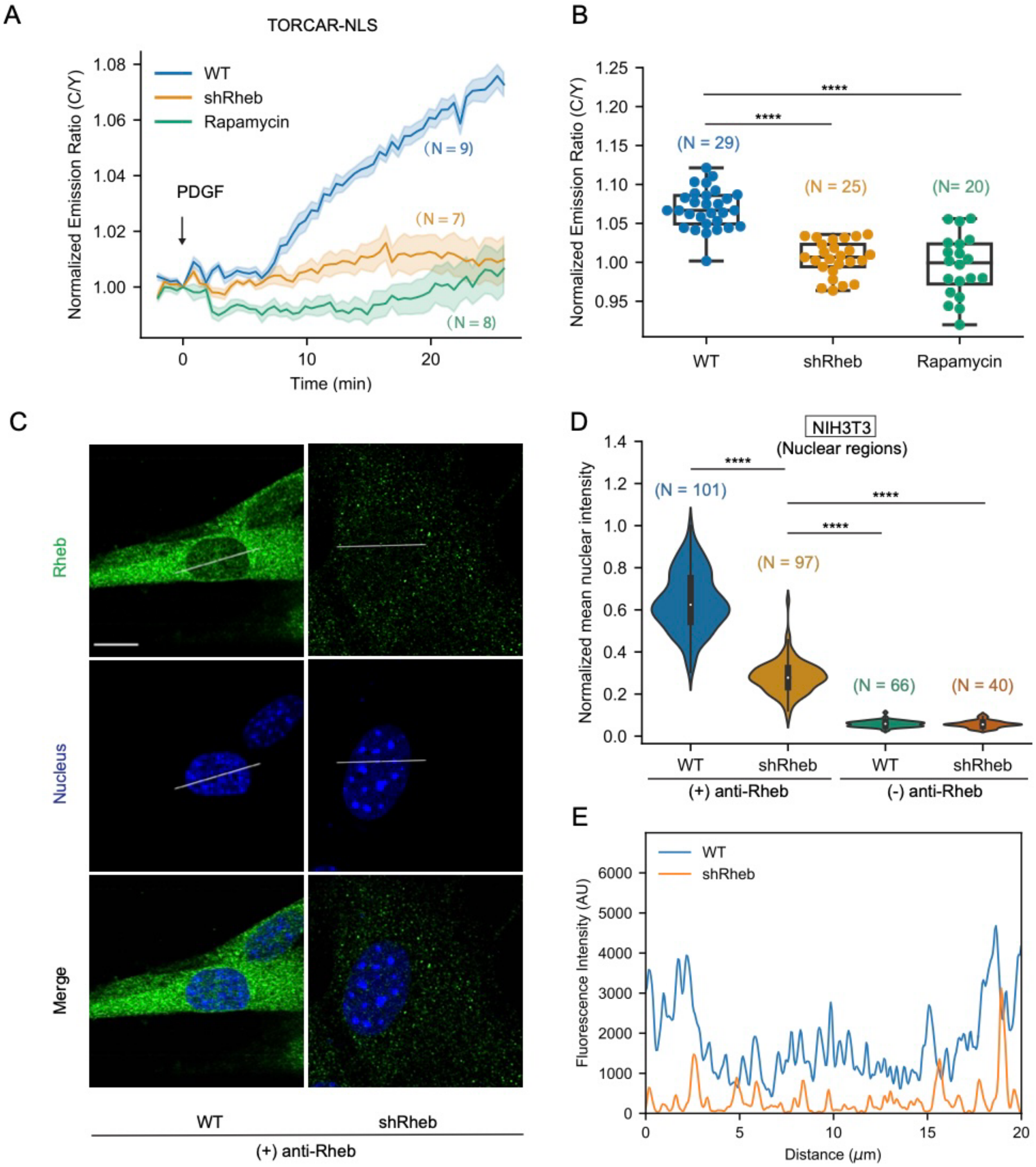
A
TORCAR-NLS
WT
shRheb
Rapamycin
PDGF
(N = 9)
(N = 7)
(N = 8)
Normalized Emission Ratio (C/Y)
1.08
1.06
1.04
1.02
1.00
Time (min)
0
10
20
B
(N = 29)
(N = 25)
(N= 20)
****
****
Normalized Emission Ratio (C/Y)
1.25
1.20
1.15
1.10
1.05
1.00
0.95
WT
shRheb
Rapamycin
C
Rheb
Nucleus
Merge
WT
shRheb
(+) anti-Rheb
D
NIH3T3
(Nuclear regions)
(N = 101)
(N = 97)
(N = 66)
(N = 40)
****
****
****
Normalized mean nuclear intensity
1.4
1.2
1.0
0.8
0.6
0.4
0.2
0.0
WT
shRheb
WT
shRheb
(+) anti-Rheb
(-) anti-Rheb
E
WT
shRheb
Fluorescence Intensity (AU)
6000
5000
4000
3000
2000
1000
0
Distance (μm)
0
5
10
15
20

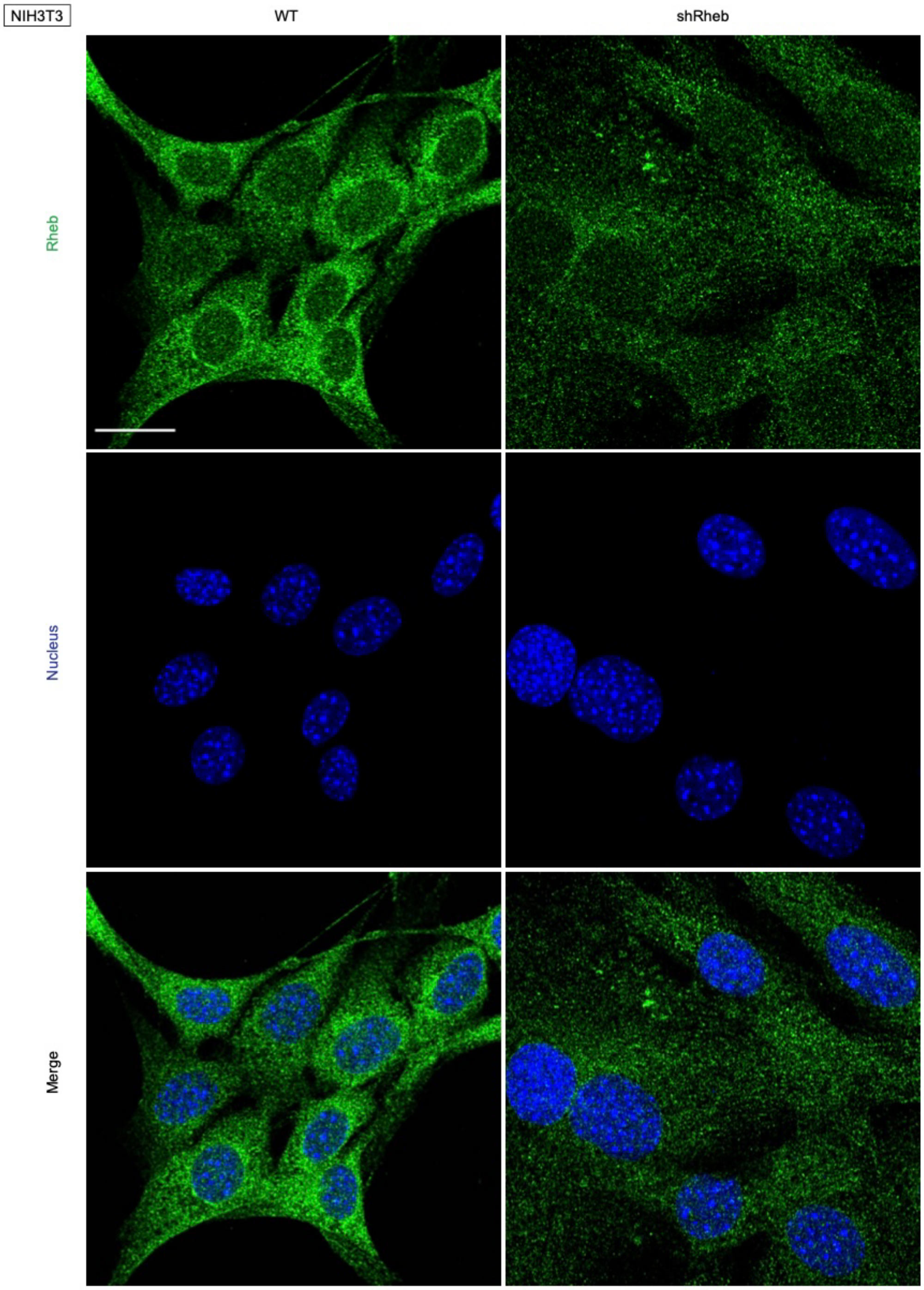

Figure 2.3 Rheb knockdown reduced the nuclear Rheb immunofluorescence signals in NIH3T3 cells. Representative confocal images from two independent experiments showing immunofluorescence staining of wild type and Rheb knockdown NIH3T3 cells. Rheb staining is shown in green and nucleus is shown in blue. Scale bar = 20 µm.

cells. To test the presence of nuclear Rheb in other cell types, we performed immunofluorescence analysis to probe Rheb distribution in Cal27, a human oral squamous carcinoma cell line (Wang et al., 2019). Similar to what we observed in NIH3T3 cells, significant signals were found in the nuclei of Cal27 cells and were sensitive to Rheb knockdown (**Figure 2.4A-C**). In addition, Rheb signals were also observed in the nuclear regions of other cell lines, including HeLa, Cos7, PLC/PRF/5, a human hepatoma cell line (Huo et al., 2019), and 3T3L1 adipocytes (**Figure 2.5**), suggesting Rheb is present in the nucleus of a variety of cell types.

Nuclear mTORC1 activity is suppressed by exogenously expressed nuclear TSC2

In the canonical activation of lysosomal mTORC1, TSC2 plays an important role in growth factor-induced activation of Rheb, which in turn activates mTORC1. As a Rheb GAP, TSC2 is localized to the lysosomal surface at the basal state (Demetriades et al., 2016), keeping Rheb in the inactive, GDP-bound form by stimulating GTP hydrolysis to GDP. Growth factor stimulated Akt phosphorylates TSC2 on two key residues, Ser939 and Thr1462, leading to its dissociation from the lysosome, and thereby relieving Rheb inhibition and leading to lysosomal mTORC1 activation (Inoki et al., 2002; Manning et al., 2002; Menon et al., 2014). However, numerous studies have shown TSC2 is not present in the nucleus (Menon et al., 2014; Demetriades et al., 2014, 2016; Ferlazzo et al., 2017; Prentzell et al., 2021), suggesting that nuclear Rheb, unlike its lysosomal counterpart, is not under the typical Akt-TSC2-mediated control.

To further examine the distribution of endogenous TSC2, we performed immunofluorescence experiments in NIH3T3 cells and found that the specific signal that was sensitive to TSC2 knockdown was only present in the cytosolic regions (**Figure 2.6A-C**). To

Figure 2.4 Rheb knockdown reduced the nuclear Rheb immunofluorescence signals in Cal27 cells. (A) Representative confocal images from two independent experiments showing Rheb immunofluorescence staining in wild type (WT) and Rheb knockdown (shRheb) Cal27 cells. Rheb staining is shown in green and nucleus is shown in blue. Scale bar = 20 µm. (B) Quantification of the nuclear signals in (A). Intensities were normalized to the maximum intensity. Control experiments were done by leaving out the primary antibody ((-) anti-Rheb) for wild type (WT) and Rheb knockdown (shRheb) cells respectively. Violin plots show the upper and lower adjacent values, interquartile range and the median. One-way ANOVA with Dunnett's multiple comparisons is used. ****, $p < 0.0001$. Blue, wild type cells, (+) anti-Rheb (N = 280 cells); yellow, Rheb knockdown cells, (+) anti-Rheb (N = 234 cells); green, wild type cells, (-) anti-Rheb (N = 93 cells); orange, Rheb knockdown cells, (-) anti-Rheb (N = 94 cells). Data are representative from two independent experiments. (C) Western blotting to examine Rheb protein level in wild type (WT) and Rheb knockdown (shRheb) Cal27 cells. β-tubulin served as loading control. Quantification is done with five independent blots and unpaired t-test is used. *, $p < 0.05$.

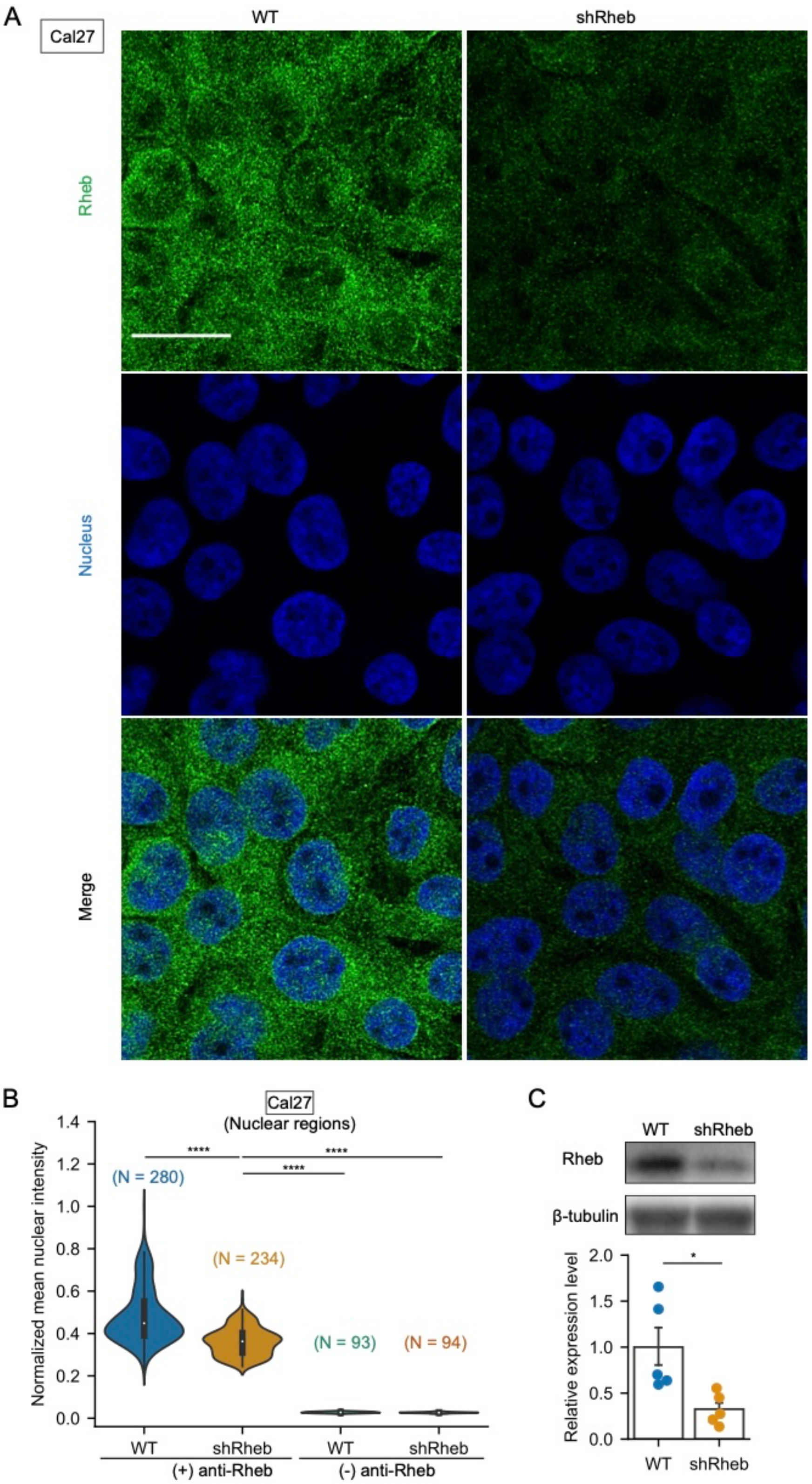
A
Cal27
WT
shRheb
Rheb
Nucleus
Merge
B
Cal27
(Nuclear regions)
Normalized mean nuclear intensity
1.4
1.2
1.0
0.8
0.6
0.4
0.2
0.0
****
****
****
(N = 280)
(N = 234)
(N = 93)
(N = 94)
WT
shRheb
WT
shRheb
(+) anti-Rheb
(-) anti-Rheb
C
WT
shRheb
Rheb
β-tubulin
Relative expression level
2.0
1.5
1.0
0.5
0.0
*
WT
shRheb

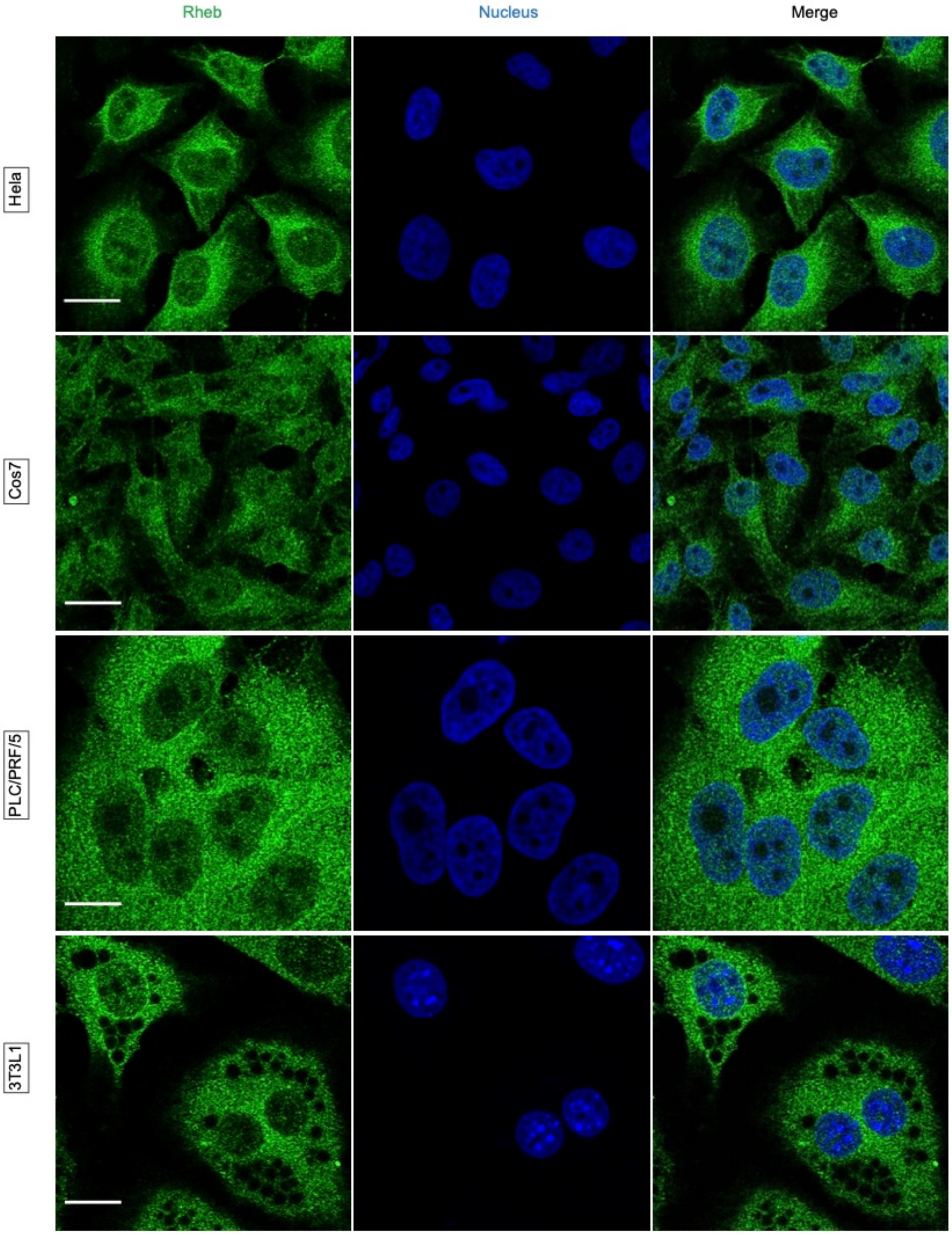

Figure 2.5 Nuclear Rheb is present in a variety of cell lines. Representative immunofluorescence images of Rheb staining in various cell lines including Hela, Cos7, PLC/PRF/5 hepatoma cells and 3T3L1 adipocytes. Data are representative from two independent experiments. Rheb staining is shown in green and nucleus is shown in blue. Scale bars = 20 µm.

Figure 2.6 TSC2 is minimally present in the nucleus in NIH3T3 cells. (A) Representative confocal images from two independent experiments showing TSC2 immunofluorescence staining in wild type (WT) and TSC2 knockdown (shTSC2) NIH3T3 cells. TSC2 staining is shown in green and nucleus is shown in blue. Scale bar = 20 μm. (B) Quantification of the whole cell signals and nuclear signals in (A). Intensities were normalized to the maximum intensity. Control experiments were done by leaving out the primary antibody ((-) anti-TSC2) for wild type and TSC2 knockdown cells respectively. Violin plots show the upper and lower adjacent values, interquartile range and the median. One-way ANOVA with Dunnett's multiple comparisons is used. ****, $p < 0.0001$; ns, not significant. Blue, wild type cells, (+) anti-TSC2 ($N = 26$ cells for whole cell and $N = 26$ cells for nuclear regions); yellow, TSC2 knockdown cells, (+) anti-TSC2 ($N = 16$ cells for whole cell and $N = 15$ cells for nuclear regions); green, wild type cells, (-) anti-TSC2 ($N = 20$ cells for whole cell and $N = 23$ cells for nuclear regions); orange, TSC2 knockdown cells, (-) anti-TSC2 ($N = 22$ cells for whole cell and $N = 22$ cells for nuclear regions). Data are representative from two independent experiments. (C) Western blotting to examine TSC2 protein level in wild type (WT) and TSC2 knockdown (shTSC2) NIH3T3 cells. β-tubulin served as loading control. Data are representative of three independent experiments.

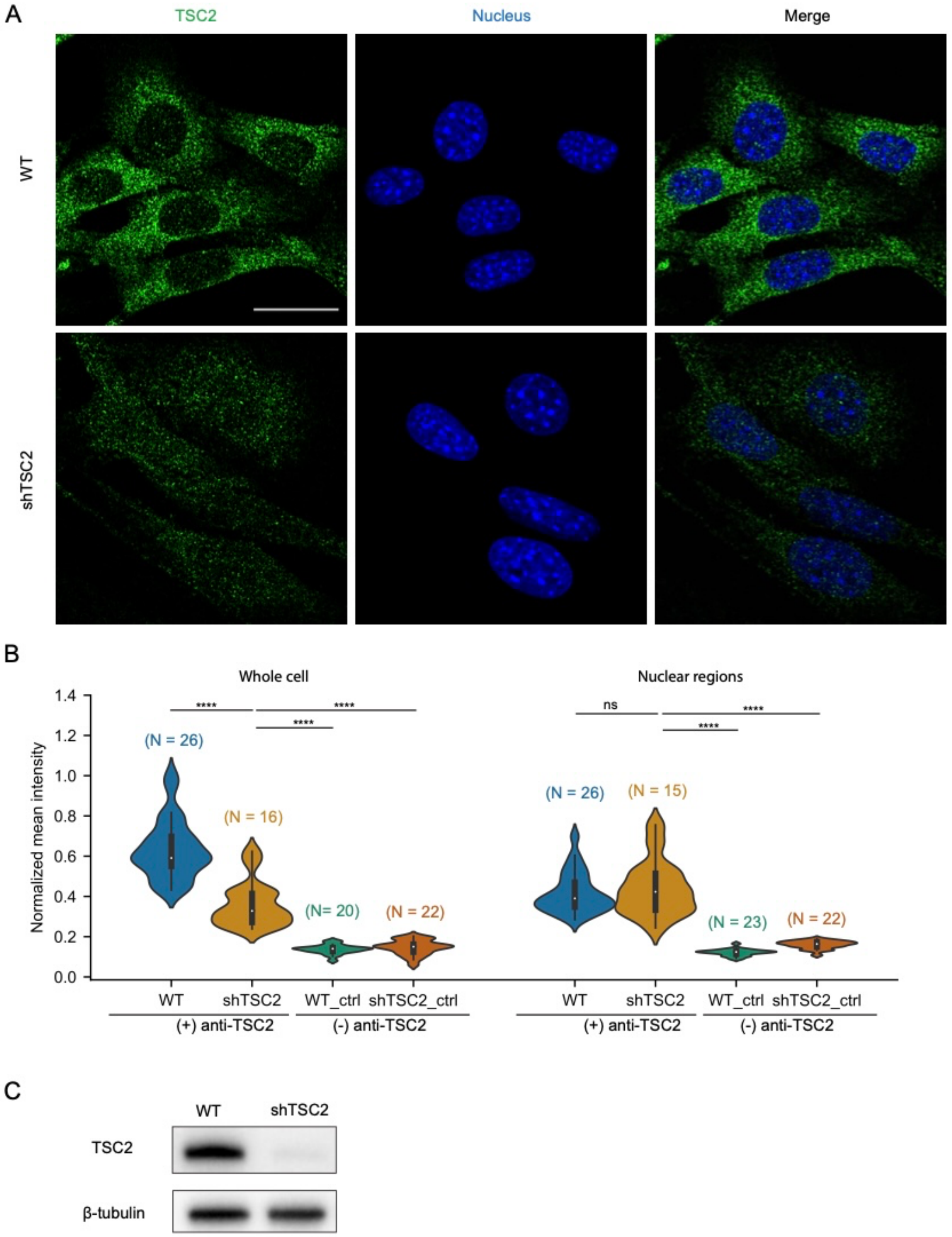
A
TSC2
Nucleus
Merge
WT
shTSC2
B
Whole cell
Nuclear regions
Normalized mean intensity
1.4
1.2
1.0
0.8
0.6
0.4
0.2
0.0
****
****
****
ns
****
****
(N = 26)
(N = 16)
(N= 20)
(N = 22)
(N = 26)
(N = 15)
(N = 23)
(N = 22)
WT
shTSC2
WT_ctrl
shTSC2_ctrl
(+) anti-TSC2
(-) anti-TSC2
WT
shTSC2
WT_ctrl
shTSC2_ctrl
(+) anti-TSC2
(-) anti-TSC2
C
WT
shTSC2
TSC2
β-tubulin

further support these results, we also performed nuclear fractionation and found that TSC2 was absent in the nuclear fraction in contrast to Rheb (**Figure 2.1F**). Taken together, these data support that although mTORC1 activator Rheb is present in the nucleus, the negative regulator TSC2 is unlikely to be present in the nucleus, suggesting that nuclear Rheb is not under Akt-TSC2-mediated control.

No guanine nucleotide exchange factor (GEF) has been identified for Rheb. In the absence of a GEF, it is thought that a relatively low nucleotide binding affinity allows Rheb to spontaneously exchange GDP for GTP to become active (Li et al., 2004). Given that the critical negative regulator TSC2 is absent from the nucleus, we hypothesized that spontaneous activity allows nuclear Rheb to regulate nuclear mTORC1 activity. Because of the small amount of Rheb in the nucleus and the challenges associated with pulldown assays using subcellular fractions, we tested this idea by using a synthetic biology approach. We reasoned that if active GTP bound Rheb is involved in regulating nuclear mTORC1, exogenously expressing nuclearly targeted TSC2 would inhibit Rheb through its GAP activity, thus inhibiting nuclear mTORC1 activity. To test this idea, we focused on several variants of TSC2, including the wide type TSC2, a TSC2-AA variant in which the two critical Akt phosphorylation sites, Ser939 and Thr1462, are mutated to Alanine to eliminate Akt-mediated negative control but retains GAP activity to Rheb (Manning et al., 2002; Menon et al., 2014), and a TSC2-AA-3Q mutant that has no GAP activity (Li et al., 2004) (**Figure 2.7A**). Because TSC1 forms a stable complex with TSC2 and prevents ubiquitin-mediated TSC2 degradation (Chong-Kopera et al., 2006), we first asked how the overexpression and nuclear targeting of TSC2 affect TSC1. By using immunofluorescence, we found that overexpressing nuclear TSC2 (TSC2-NLS) not only increased the level of TSC1 in the whole cell,

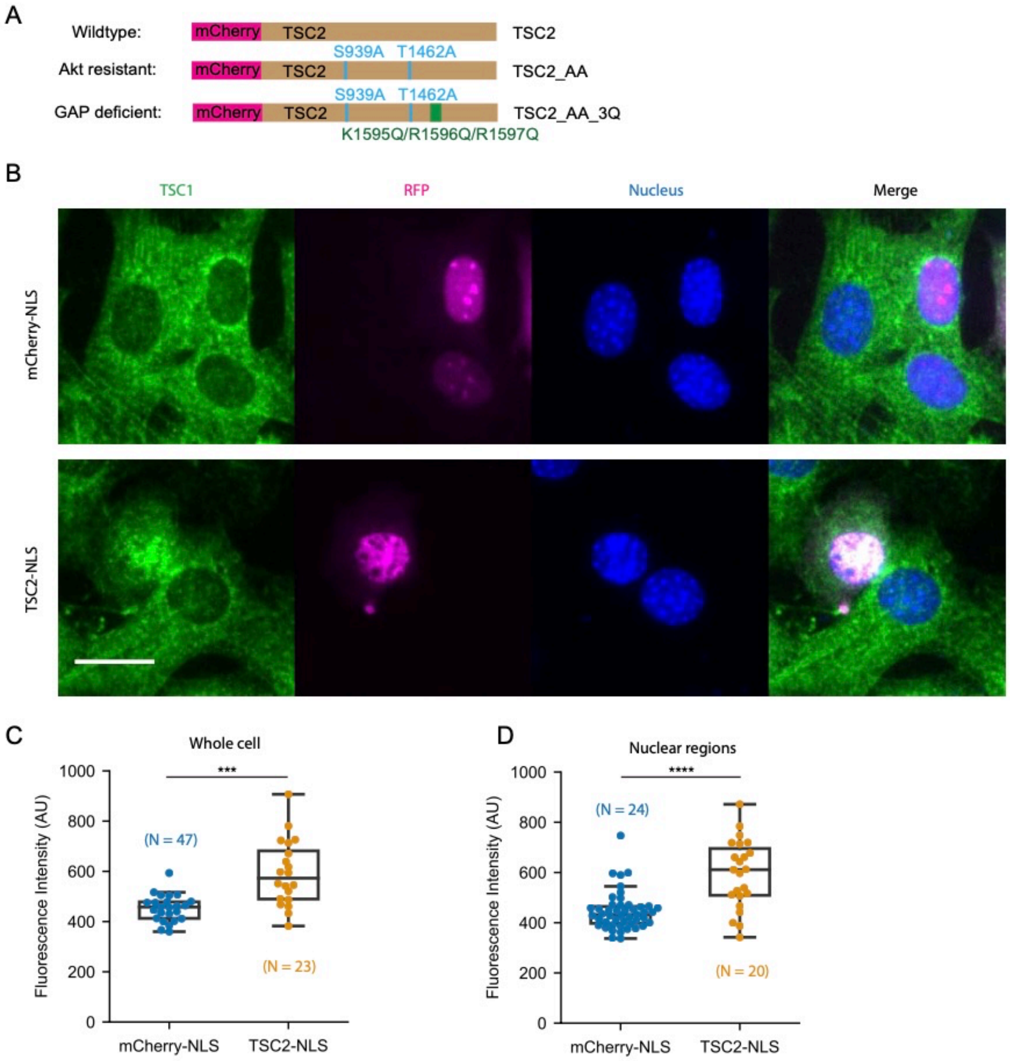

Figure 2.7 Exogenously expressed nuclear TSC2 recruits TSC1 into the nucleus. (A) Schematics of different TSC2 constructs tagged with mCherry. Two Akt phosphorylation sites in wild type TSC2 were mutated to Ala to generate unphosphorylatable mCherry-TSC2-AA. Three residues from 1595-1597 (KRR) were mutated to Gln (QQQ) to generate GAP-deficient mCherry-TSC2-AA-3Q. (B) Representative immunofluorescence images from three independent experiments showing TSC1 staining in NIH3T3 cells overexpressing mCherry-tagged nuclear TSC2 (TSC2-NLS) or nuclear mCherry (mCherry-NLS). TSC1 staining is shown in green, mCherry is labeled as "RFP" and shown in magenta, and nucleus is shown in blue. Scale bar = 10 µm. (C-D) Quantification of the whole cell signals (C) and nuclear signals (D) in (B). Fluorescence intensities were shown as arbitrary units (AU). Box plots show the upper and lower adjacent values, interquartile range and the median. Unpaired t-test is used. ***, $p < 0.001$; ****, $p < 0.0001$. Blue, cells overexpressing mCherry-NLS (N = 47 cells for whole cell and N = 24 cells for nuclear regions); yellow, cells overexpressing TSC2-NLS (N = 23 for whole cell and N = 20 cells for nuclear regions). Data are representative from three independent experiments.

but also significantly increased TSC1 level in the nucleus (**Figure 2.7C-D**), suggesting that exogenously overexpressed nuclear TSC2 may recruit TSC1 to preserve the integrity of the TSC complex in the nucleus.

Next, we tested the capability of these TSC2 variants to suppress mTORC1 activity. When co-expressed with TORCAR, wild type TSC2 showed exclusively cytoplasmic localization, whereas TSC2-AA mutant showed partial lysosomal localization (**Figure 2.8A** and **Figure 2.9A**), which is in line with previous reports (Menon et al., 2014). We stimulated these NIH3T3 cells with PDGF and quantified PDGF-induced response of TORCAR in the cytosolic regions. As shown in Figure 2B and 2C, co-expression of wild type TSC2 did not affect the cytosolic response of TORCAR (7.8 ± 0.5 %, n = 35) in comparison with the mCherry control (8.3 ± 0.7 %, n = 27), while co-expression of TSC2-AA significantly suppressed the cytosolic response of TORCAR (4.2 ± 0.4 %, n = 32). Notably, this suppression was dependent on the GAP activity of TSC2, as TSC2-AA-3Q failed to inhibit cytosolic mTORC1 activity (**Figure 2.9B-D**). These data suggest that GAP activity towards Rheb could inhibit mTORC1 activity (in the case of TSC2-AA), whereas Akt-mediated phosphorylation of TSC2 could abolish the inhibitory effect of overexpressed TSC2 (in the case of TSC2 wild type). As unphosphorylatable TSC2-AA is resistant to Akt-mediated phosphorylation and lysosomal dissociation, it remains on the lysosome as a strong dominant negative regulator to inhibit lysosomal Rheb and mTORC1 activity, regardless of active Akt (**Figure 2.8D**).

To test our hypothesis that active Rheb in the nucleus is involved in regulating nuclear mTORC1 activity, we expressed the nuclear targeted version of TSC2 and its variants and examined nuclear mTORC1 activity by TORCAR-NLS. Both TSC2-NLS and the reporter showed

Figure 2.8 Growth factor induced nuclear mTORC1 activity is suppressed by overexpressing TSC2 in the nucleus. (A) Representative fluorescence images from three independent experiments showing the localization of overexpressed constructs in NIH3T3 cells. Fluorescence of mCherry, mCherry-TSC2 and mCherry-TSC2-AA mutant are shown as "RFP". "CFP" shows fluorescence of TORCAR. Scale bar = 10 µm. (B-C) Representative averaged time course traces (B) and summary (C) of PDGF-induced maximum responses of TORCAR in the cytosolic regions of double starved NIH3T3 cells. Co-expressed constructs: mCherry (blue, N = 27 cells from 3 independent experiments); mCherry-TSC2 (yellow, N = 35 cells from 3 independent experiments); mCherry-TSC2-AA (green, N = 32 cells from 3 independent experiments). Shaded areas indicate standard error of the mean (SEM). Box plots show the upper and lower adjacent values, interquartile range and the median. One-way ANOVA with Dunnett's multiple comparisons is used. ****, $p < 0.0001$; ns, not significant. (D) Model depicting lysosomal TSC-dependent spatial regulation of mTORC1 activation. TSC2 inhibits farnesylated Rheb on the lysosome, preventing the activation of lysosomal mTORC1. Akt-mediated phosphorylation of TSC2 results in its dissociation from the lysosome, thereby unleashing Rheb to activate mTORC1. Unphosphorylatable TSC2 remains on the lysosome to continue suppressing mTORC1 activation. (E) Representative fluorescence images from three independent experiments showing the localization of overexpressed nuclearly targeted constructs in NIH3T3 cells. Fluorescence of mCherry-NLS, mCherry-TSC2-NLS and mCherry-TSC2-AA-NLS mutant are shown as "RFP". "CFP" shows the fluorescence of TORCAR-NLS. Scale bar = 10 µm. (F-G) Representative averaged time course traces (F) and summary (G) of PDGF-induced maximum responses of TORCAR-NLS in double starved NIH3T3 cells. Co-expressed constructs: mCherry-NLS (blue, N = 20 cells from 3 independent experiments); mCherry-TSC2-NLS (yellow, N = 23 cells from 3 independent experiments); mCherry-TSC2-AA-NLS (green, N = 26 cells from 3 independent experiments). Shaded areas indicate standard error of the mean (SEM). Box plots show the upper and lower adjacent values, interquartile range and the median. One-way ANOVA with Dunnett's multiple comparisons is used. *, $p < 0.05$; ****, $p < 0.0001$; ns, not significant. (H) Model depicting the inhibition of nuclear mTORC1 activity by overexpressed nuclear TSC2. In the absence of the spatial regulation in (D), exogenously overexpressed nuclear TSC2 can suppress Rheb regardless of its phosphorylation status.

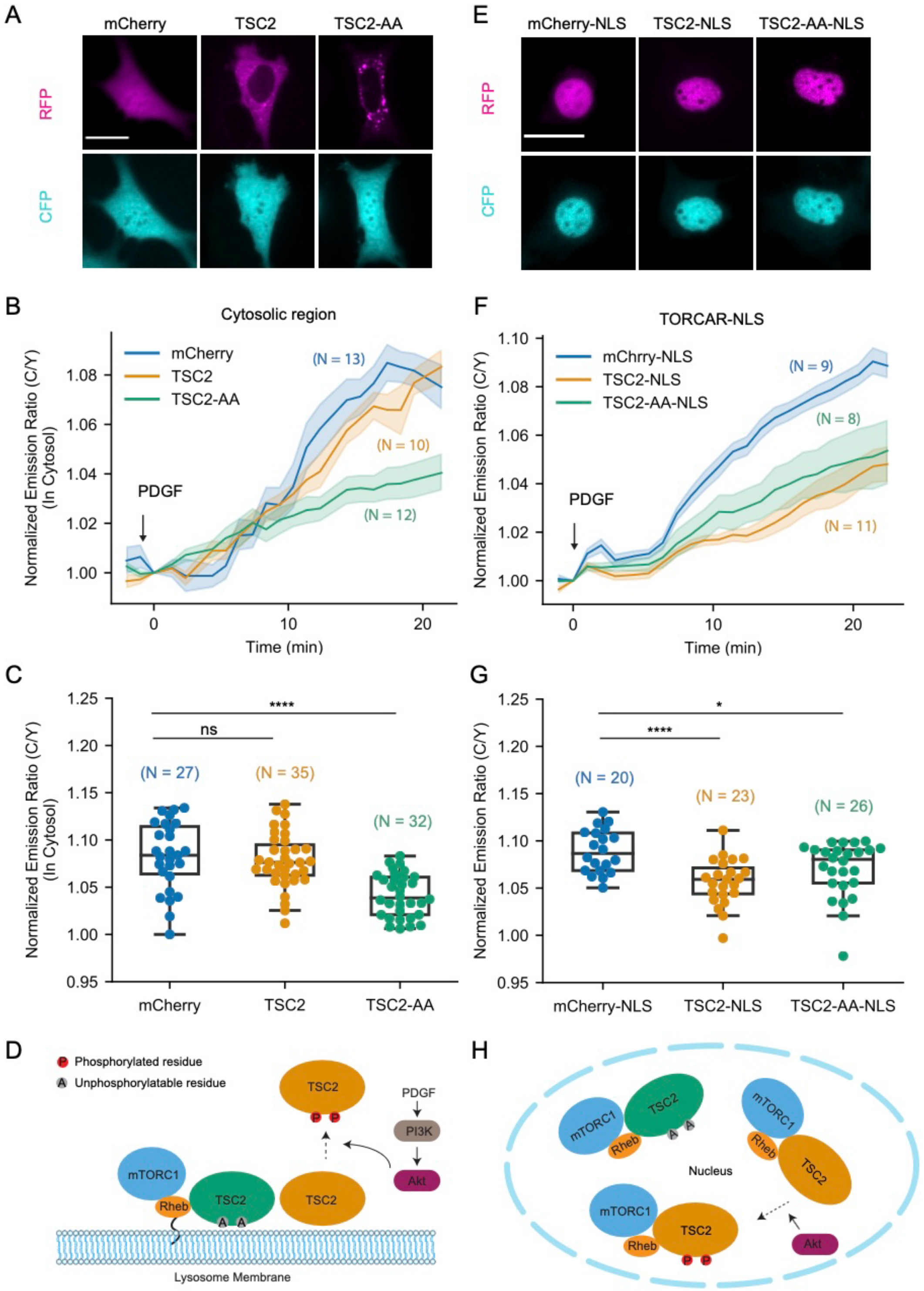
A
mCherry
TSC2
TSC2-AA
RFP
CFP
E
mCherry-NLS
TSC2-NLS
TSC2-AA-NLS
RFP
CFP
B
Cytosolic region
Normalized Emission Ratio (C/Y) (In Cytosol)
mCherry
TSC2
TSC2-AA
(N = 13)
(N = 10)
(N = 12)
PDGF
1.08
1.06
1.04
1.02
1.00
0
10
20
Time (min)
F
TORCAR-NLS
Normalized Emission Ratio (C/Y)
mChrry-NLS
TSC2-NLS
TSC2-AA-NLS
(N = 9)
(N = 8)
(N = 11)
PDGF
1.10
1.08
1.06
1.04
1.02
1.00
0
10
20
Time (min)
C
Normalized Emission Ratio (C/Y) (In Cytosol)
****
ns
(N = 27)
(N = 35)
(N = 32)
1.25
1.20
1.15
1.10
1.05
1.00
0.95
mCherry
TSC2
TSC2-AA
G
Normalized Emission Ratio (C/Y)
*
****
(N = 20)
(N = 23)
(N = 26)
1.25
1.20
1.15
1.10
1.05
1.00
0.95
mCherry-NLS
TSC2-NLS
TSC2-AA-NLS
D
P Phosphorylated residue
A Unphosphorylatable residue
TSC2
PDGF
PI3K
Akt
mTORC1
Rheb
TSC2
A A
TSC2
P P
Lysosome Membrane
H
mTORC1
Rheb
TSC2
A A
mTORC1
Rheb
TSC2
Nucleus
mTORC1
Rheb
TSC2
P P
Akt

Figure 2.9 GAP activity of TSC2 is required to suppress mTORC1 activity. (A) Representative images showing that TSC2-AA partially colocalizes with a lysosomal marker, LysoTracker. mCherry-tagged TSC2 or TSC2-AA mutant were overexpressed in NIH3T3 cells. LysoTracker is shown in green and mCherry is labeled "RFP" and shown in magenta. Data are representative of three independent experiments. Scale bar = 10 μm. (B) Representative fluorescence images from three independent experiments showing the localization of overexpressed constructs in NIH3T3 cells. RFP channel: mCherry and mCherry-TSC2-AA-3Q mutant. CFP channel: TORCAR-NES. Scale bar = 10 μm. (C-D) Representative averaged time course traces (D) and summary (E) of PDGF-induced maximum responses of TORCAR-NES in double starved NIH3T3 cells. Co-expressed constructs: mCherry (blue, N = 35 cells from 3 independent experiments); mCherry-TSC2-AA-3Q (yellow, N = 36 cells from 3 independent experiments). Shaded areas indicate standard error of the mean (SEM). Box plots show the upper and lower adjacent values, interquartile range and the median. Unpaired t-test is used. ns, not significant. (E) Representative fluorescence images from three independent experiments showing the localization of overexpressed nuclearly targeted constructs in NIH3T3 cells. RFP channel: mCherry-NLS and mCherry-TSC2-AA-3Q-NLS mutant. CFP channel: TORCAR-NLS. Scale bar = 10 μm. (F-G) Representative averaged time course traces (G) and summary (H) of PDGF-induced maximum responses of TORCAR-NLS in double starved NIH3T3 cells. Co-expressed constructs: mCherry-NLS (blue, N = 32 cells from 3 independent experiments); mCherry-TSC2-AA-3Q-NLS (yellow, N = 31 cells from 3 independent experiments). Shaded areas indicate standard error of the mean (SEM). Box plots show the upper and lower adjacent values, interquartile range and the median. Unpaired t-test is used. ns, not significant.

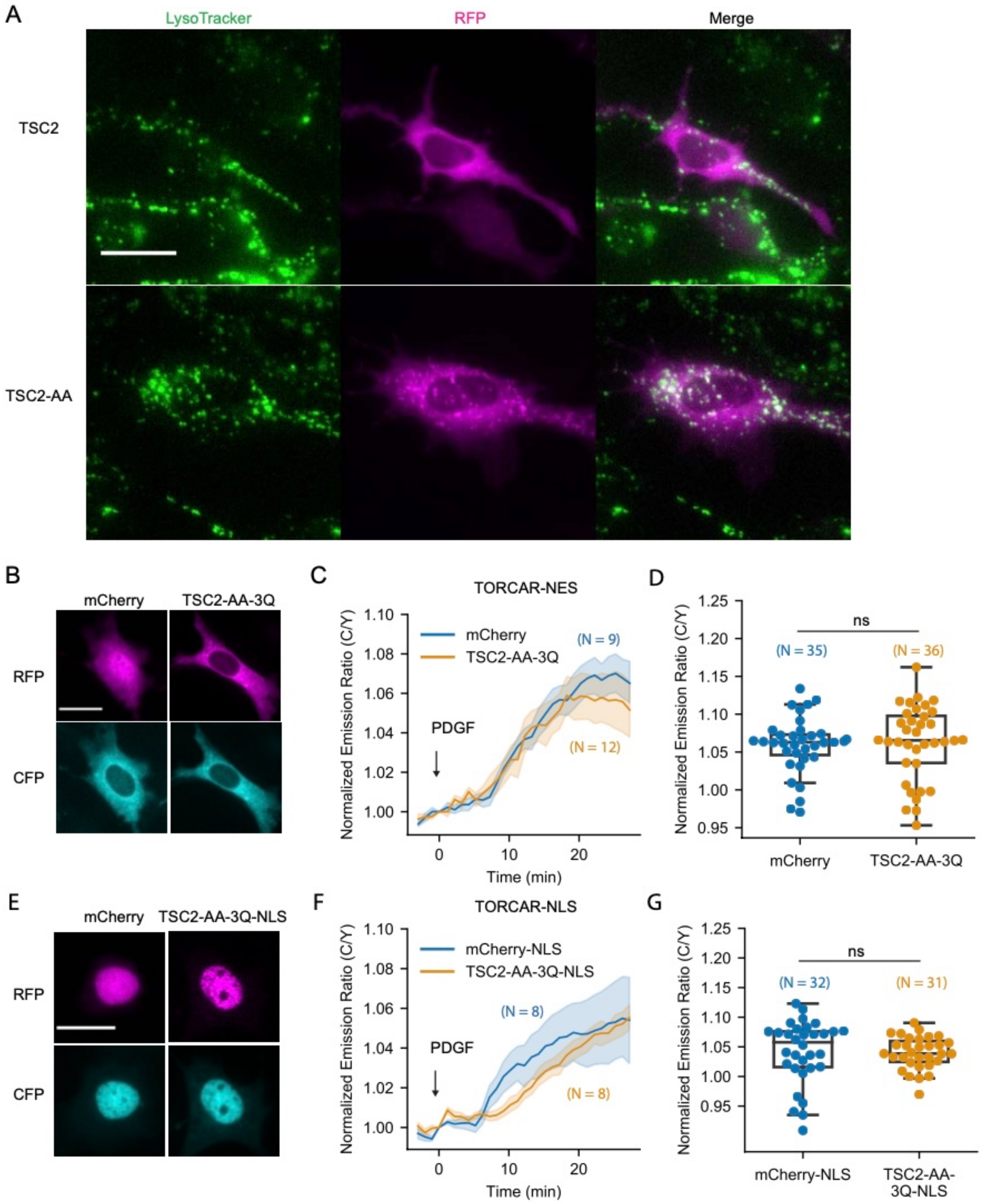
A
LysoTracker
RFP
Merge
TSC2
TSC2-AA
B
mCherry
TSC2-AA-3Q
RFP
CFP
C
TORCAR-NES
Normalized Emission Ratio (C/Y)
1.10
1.08
1.06
1.04
1.02
1.00
mCherry
TSC2-AA-3Q
(N = 9)
PDGF
(N = 12)
0
10
20
Time (min)
D
Normalized Emission Ratio (C/Y)
1.25
1.20
1.15
1.10
1.05
1.00
0.95
ns
(N = 35)
(N = 36)
mCherry
TSC2-AA-3Q
E
mCherry
TSC2-AA-3Q-NLS
RFP
CFP
F
TORCAR-NLS
Normalized Emission Ratio (C/Y)
1.10
1.08
1.06
1.04
1.02
1.00
mCherry-NLS
TSC2-AA-3Q-NLS
(N = 8)
PDGF
(N = 8)
0
10
20
Time (min)
G
Normalized Emission Ratio (C/Y)
1.25
1.20
1.15
1.10
1.05
1.00
0.95
ns
(N = 32)
(N = 31)
mCherry-NLS
TSC2-AA-3Q-NLS

appropriate nuclear localization (**Figure 2.8E** and **Figure 2.9E**). In cells stimulated with PDGF, co-expression of both TSC2-NLS and TSC2-AA-NLS significantly reduced TORCAR-NLS response compared to the control group expressing mCherry-NLS (**Figure 2.8F-G**; mCherry-NLS: 8.9 ± 0.5 %, n = 20; TSC2-NLS: 5.7 ± 0.5 %, n = 23; TSC2-AA-NLS: 7.0 ± 0.6 %, n = 26). The GAP deficient mutant TSC2-AA-3Q-NLS was not able to inhibit nuclear mTORC1 activity (Figure 2.9E-G), suggesting that inhibition of nuclear mTORC1 by nuclear targeted TSC2 is dependent on its GAP activity towards Rheb. Notably, wild type TSC2 showed distinct behaviors in the cytosol and in the nucleus (**Figure 2.8C** and **G**). Indeed, given that the regulation of TSC2 by Akt is achieved via phosphorylation-induced dissociation from the lysosomal surface and that this spatially controlled negative regulation of TSC2 is unlikely to occur in the nucleus, both wild type and unphosphorylatable TSC2 can exert their GAP activity towards Rheb to suppress nuclear mTORC1 activity (**Figure 2.8H**). These data suggest that active Rheb is involved in stimulating nuclear mTORC1 activity.

Farnesylation of Rheb is not required for nuclear mTORC1 activity

Like other Ras family proteins, Rheb possesses a hypervariable region at its C-terminus, ending with the sequence CSVM, which conforms to the CAAX motif that undergoes farnesylation at the cysteine residue (Clark et al., 1997). The weak and transient membrane interaction enabled by C-terminal farnesylation is thought to be important for both subcellular localization of Rheb and Rheb-mediated lysosomal mTORC1 activation (Hanker et al., 2010; Angarola and Ferguson, 2020). We asked whether this farnesylation is also critical for nuclear Rheb to activate nuclear mTORC1. To test this, we used the selective farnesyltransferase inhibitor FTI-277 to inhibit Rheb

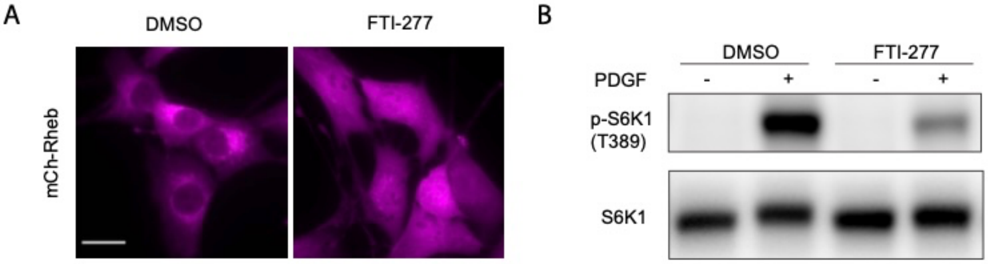

Figure 2.10 Farnesyltransferase inhibitor FTI-277 disrupted membrane association of Rheb and inhibited S6K1 phosphorylation. (A) mCherry-Rheb expression was induced by 100 ng/mL doxycycline in Rheb knockdown NIH3T3 cells with stable reconstitution of mCherry-Rheb. Cells were treated with DMSO or 5 µM FTI-277 overnight and Rheb localization was assessed by live cell imaging. Scale bar = 10 µm. Images are representative from three independent experiments. (B) Western blotting analysis to show FTI-277 inhibits PDGF-induced S6K1 phosphorylation. Wild type (WT) NIH3T3 cells were treated with DMSO or 5 µM FTI-277 overnight, double starved and stimulated with 50 ng/mL PDGF or were unstimulated. Phosphorylation of mTORC1 substrate S6K1 at Thr389 (T389) was examined. Data are representative from three independent experiments.

farnesylation (Hanker et al., 2010). Using NIH3T3 cells stably expressing mCherry-tagged Rheb, we showed that while DMSO treated cells showed perinuclear localization of Rheb (**Figure 2.10A**), similar to what was observed for endogenous Rheb (**Figure 2.2C**), cells treated with FTI-277 showed diffusive Rheb localization (**Figure 2.10A**), suggesting that FTI-277 treatment efficiently disrupted Rheb localization. We then evaluated the effect of the farnesyltransferase inhibitor on PDGF-induced phosphorylation of mTORC1 substrate in wild type NIH3T3 cells. Consistent with previous reports (Basso et al., 2005; Hanker et al., 2010), FTI-277 treatment significantly reduced S6K1 phosphorylation (**Figure 2.10B**). To examine the effect of the farnesyltransferase inhibitor on compartmentalized mTORC1 activity, we expressed TORCAR in the cytosol and nucleus by tagging a nuclear export signal (NES) and an NLS, respectively, and quantified PDGF-induced mTORC1 activity at subcellular locations in the presence or absence of the farnesyltransferase inhibitor. As expected, FTI-277 significantly reduced the cytosolic TORCAR (TORCAR-NES) response to PDGF (**Figure 2.11A-B**, 7.4 ± 0.5 %, n = 32) compared with the DMSO group (**Figure 2.11A-B**, 9.9 ± 0.6 %, n = 23), indicating that farnesylation is essential for canonical mTORC1 activation, as shown in previous studies (Hanker et al., 2010). In stark contrast, FTI-277 treatment did not affect the response of nuclear TORCAR (**Figure 2.11C-D**; DMSO: 5.5 ± 0.6 %, n = 32; FTI-277: 5.2 ± 0.8 %, n = 17), suggesting that nuclear mTORC1 activity does not require farnesylation of Rheb.

Farnesylation-deficient Rheb differentially rescued mTORC1 activity within subcellular compartments

To further investigate the role of Rheb farnesylation in regulating mTORC1 signaling, we

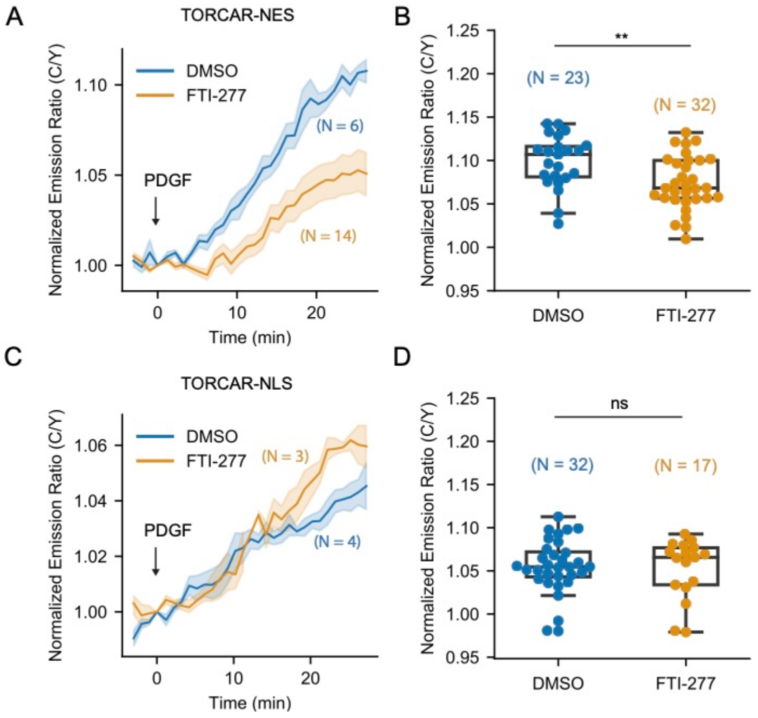

Figure 2.11 Farnesyltransferase inhibitor FTI-277 did not affect nuclear mTOR1 activity. (A-B) Representative averaged time course traces (A) and summary (B) of PDGF-induced maximum responses of TORCAR-NES, a cytoplasm-targeted mTORC1 activity reporter, in double starved NIH3T3 cells treated with DMSO (blue, N = 23 from 4 independent experiments) or farnesyltransferase inhibitor FTI-277 at 5 µM overnight (yellow, N = 32 from 4 independent experiments). Shaded areas indicate standard error of the mean (SEM). Box plots show the upper and lower adjacent values, interquartile range and the median. Unpaired t-test is used. **, $p < 0.01$. (C-D) Representative averaged time course traces (C) and summary (D) of PDGF-induced maximum responses of TORCAR-NLS in double starved NIH3T3 cells treated with DMSO (blue, N = 32 from 4 independent experiments) or farnesyltransferase inhibitor FTI-277 at 5 µM overnight (yellow, N = 17 from 3 independent experiments). Shaded areas indicate standard error of the mean (SEM). Box plots show the upper and lower adjacent values, interquartile range and the median. Unpaired t-test is used. ns, not significant.

took advantage of a farnesylation-deficient Rheb mutant, C181S, in which the cysteine in the CAAX motif is mutated to a serine (Jiang and Vogt, 2008) and reconstituted Rheb knockdown cells with wild type Rheb, Rheb-C181S, and Rheb-*Δ*5A, an inactive form of Rheb which lacks five amino acid residues (amino acids 38-42) and is unable to bind nucleotide (Inoki et al., 2003) (**Figure 2.12A**). We first examined the localization of these Rheb mutants by tagging them with mCherry fluorescent protein (**Figure 2.12B**). Wild type Rheb and Rheb-*Δ*5A showed similar localization to endogenously or stably expressed Rheb (Figures 1C and S8A). The farnesylation-deficient Rheb-C181S showed no indication of membrane association, reminiscent of the effect caused by farnesyltransferase inhibitor treatment (**Figure 2.10A**). In fact, Rheb-C181S showed accumulation in the nucleus (**Figure 2.12B**), consistent with the previous reports (Jiang and Vogt, 2008; Hanker et al., 2010). We then examined cytosolic mTORC1 activity by cytosol-localized TORCAR-NES (**Figure 2.12C**) in these cells. As a control, Rheb knockdown abolished the response of the cytosolic TORCAR (1.0 ± 0.4 %, n = 47), which can be partially rescued by expressing wild type Rheb (7.0 ± 0.6 %, n = 44). On the other hand, Rheb-C181S (1.1 ± 0.4 %, n = 44) and Rheb-*Δ*5A (1.9 ± 0.7 %, n = 28) failed to rescue cytosolic TORCAR responses in Rheb knockdown cells, indicating that both farnesylation and nucleotide binding are important for Rheb to positively regulate cytosolic mTORC1 activity.

Although farnesylation of Rheb is known to be important for mTORC1 activity, it is not clear whether the farnesyl group itself or farnesylation-enabled membrane association of Rheb is critical for mTORC1 activation. To distinguish these mechanisms, we used the lysosomal-associated membrane protein 1 (LAMP1)-derived sequence (Zhou et al., 2015) to target Rheb-C181S to the lysosomal membrane and test if lysosomal targeting without farnesylation can rescue the cytosolic

Figure 2.12 Farnesylation-deficient Rheb had different effects on rescuing subcellular mTORC1 activity. (A) Schematics of different Rheb constructs tagged with mCherry. Cys at 181 in the CAAX motif was mutated to Ser to generate C181S, a farnesylation-deficient Rheb mutant. Amino acids 38-42 from the switch I were deleted to generate Rheb-*Δ*5A, an inactive form that is unable to bind nucleotide. (B) Representative images of overexpressed mCherry-Rheb constructs in NIH3T3 cells from three independent experiments. Scale bar = 10 µm. (C-D) Representative averaged time course traces (C) and summary (D) of PDGF-induced maximum responses of TORCAR-NES in double starved NIH3T3 cells. Blue, wild type cells (WT, N = 25 from 3 independent experiments); yellow, Rheb knockdown cells (shRheb + None, N = 47 cells from 5 independent experiments); green, Rheb knockdown cells transfected with wild type mCherry-Rheb-WT (shRheb + Rheb-WT, N = 44 cells from 4 independent experiments); orange, Rheb knockdown cells transfected with mCherry-Rheb-C181S (shRheb + Rheb-C181S, N = 44 cells from 4 independent experiments); pink, Rheb knockdown cells transfected with mCherry-Rheb-*Δ*5A (shRheb + Rheb-*Δ*5A, N = 28 cells from 3 independent experiments). Shaded areas indicate standard error of the mean (SEM). Box plot shows the upper and lower adjacent values, interquartile range and the median. One-way ANOVA with Dunnett's multiple comparisons is used. ****, $p < 0.0001$; ns, not significant. (E-F) Representative averaged time course traces (E) and summary (F) of PDGF-induced maximum responses of TORCAR-NLS in double starved NIH3T3 cells. Blue, wild type cells (WT, N = 29 from 3 independent experiments); yellow, Rheb knockdown cells (shRheb + None, N = 54 cells from 5 independent experiments); green, Rheb knockdown cells transfected with wild type mCherry-Rheb-WT (shRheb + Rheb-WT, N = 42 cells from 4 independent experiments); orange, Rheb knockdown cells transfected with mCherry-Rheb-C181S (shRheb + Rheb-C181S, N = 84 cells from 4 independent experiments); pink, Rheb knockdown cells transfected with mCherry-Rheb-*Δ*5A (shRheb + Rheb-*Δ*5A, N = 43 cells from 3 independent experiments). Shaded areas indicate standard error of the mean (SEM). Box plots show the upper and lower adjacent values, interquartile range and the median. One-way ANOVA with Dunnett's multiple comparisons is used. ****, $p < 0.0001$; ns, not significant. (G) Model showing that active Rheb in the nucleus is critical for activating nuclear mTORC1, in addition to the previously reported Akt-mediated nuclear translocation of Raptor and phosphorylation of PRAS40.

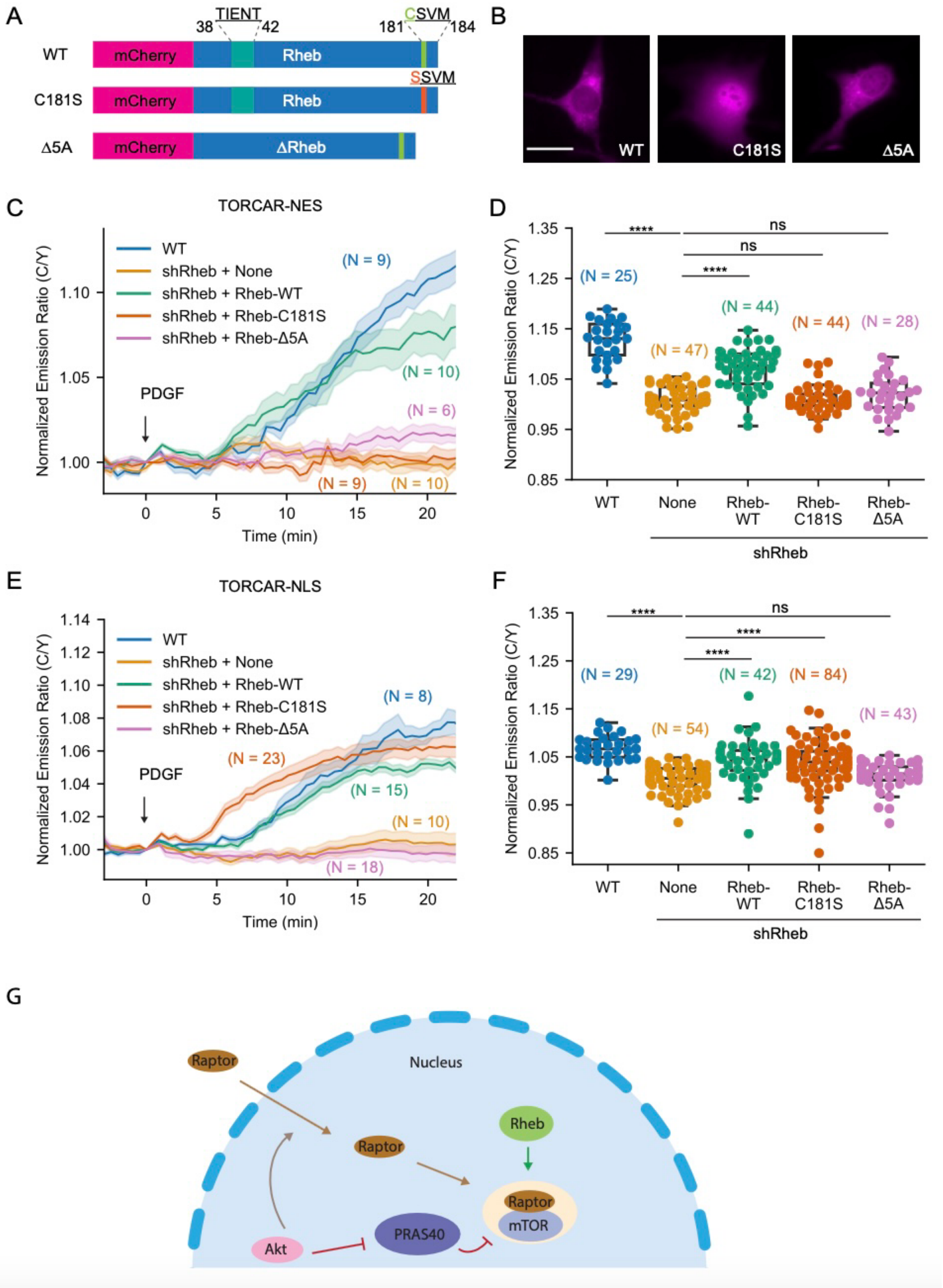
A
TIENT
38
42
CSVM
181
184
WT
mCherry
Rheb
SSVM
C181S
mCherry
Rheb
Δ5A
mCherry
ΔRheb
B
WT
C181S
Δ5A
C
TORCAR-NES
Normalized Emission Ratio (C/Y)
WT
shRheb + None
shRheb + Rheb-WT
shRheb + Rheb-C181S
shRheb + Rheb-Δ5A
(N = 9)
(N = 10)
(N = 6)
(N = 9)
(N = 10)
PDGF
Time (min)
D
Normalized Emission Ratio (C/Y)
****
ns
ns
****
(N = 25)
(N = 47)
(N = 44)
(N = 44)
(N = 28)
WT
None
Rheb-WT
Rheb-C181S
Rheb-Δ5A
shRheb
E
TORCAR-NLS
Normalized Emission Ratio (C/Y)
WT
shRheb + None
shRheb + Rheb-WT
shRheb + Rheb-C181S
shRheb + Rheb-Δ5A
(N = 8)
(N = 23)
(N = 15)
(N = 10)
(N = 18)
PDGF
Time (min)
F
Normalized Emission Ratio (C/Y)
****
ns
****
****
(N = 29)
(N = 54)
(N = 42)
(N = 84)
(N = 43)
WT
None
Rheb-WT
Rheb-C181S
Rheb-Δ5A
shRheb
G
Nucleus
Raptor
Raptor
Rheb
Raptor
mTOR
PRAS40
Akt

Figure 2.13 Lysosomal tethering of farnesylation-deficient Rheb enabled cytosolic mTORC1 activity. (A) Summary of PDGF-induced maximum responses of TORCAR-NES in double starved Rheb knockdown (shRheb) cells transfected with different Rheb constructs. Rheb knockdown cells with no Rheb reconstitution served as a negative control (None, blue, N = 16 cells from 3 independent experiments); Rheb knockdown cells expressing wild type Rheb (Rheb-WT, yellow, N = 25 cells from 3 independent experiments); Rheb knockdown cells expressing lysosomally targeted Rheb-C181S (Lyso-Rheb-C181S, green, N = 44 cells from 6 independent experiments); Rheb knockdown cells expressing Rheb-C181S (Rheb-C181S, orange, N = 41 cells from 6 independent experiments). Box plots show the upper and lower adjacent values, interquartile range and the median. One-way ANOVA with Bonferroni's multiple comparisons is used. *, $p < 0.05$; **, $p < 0.01$; ns, not significant. (B) Representative fluorescence images from three independent experiments showing the localization of different Rheb constructs in Rheb knockdown cells stably expressing wild type mCherry-Rheb (WT), mCherry-Rheb-C181S (C181S) and Lyso-mCherry-Rheb-C181S (Lyso-Rheb-C181S). Lyso-Rheb-C181S showed partial colocalization with LysoTracker, the lysosome marker. Scale bar = 10 μm. (C) Western blotting to assess the role of Rheb membrane association in mTORC1 activity. Cells in (B) were induced with 100 ng/mL doxycycline, double starved and stimulated with 50 ng/mL PDGF for 30 min or were unstimulated. Phosphorylation of mTORC1 substrate S6K1 at Thr389 (T389) was examined. Data are representative from three independent experiments. (D-E) Representative averaged time course traces (D) and summary (E) of PDGF-induced maximum responses of TORCAR-NES in double starved NIH3T3 cells overexpressing Lyso-Rheb-C181S and treated with DMSO (blue, N = 43 cells from 3 independent experiments) or farnesyltransferase inhibitor FTI-277 at 5 μM overnight (yellow, N = 43 cells from 3 independent experiments). Shaded areas indicate standard error of the mean (SEM). Box plots show the upper and lower adjacent values, interquartile range and the median. Unpaired t-test is used. ns, not significant. (F) Representative images from three independent experiments showing that the localization of lysosomally targeted Lyso-Rheb-C181S was not affected by FTI-277 treatment in a Lyso-Rheb-C181S stable line. Cells were treated with DMSO or 5 μM FTI-277 overnight and Lyso-Rheb-C181S localization was assessed by live cell imaging. LysoTracker is shown in green and Lyso-Rheb-C181S is shown in magenta. (G) Western blotting analysis to show Lyso-Rheb-C181S rescued mTORC1 activity in the presence of FTI-277. Wild type (WT) NIH3T3 cells or NIH3T3 cells stably expressing Lyso-Rheb-C181S were treated with DMSO or 5 μM FTI-277 overnight, double starved and stimulated with 50 ng/mL PDGF or were unstimulated. Phosphorylation of mTORC1 substrate S6K1 at Thr389 (T389) was examined. Data are representative from three independent experiments.

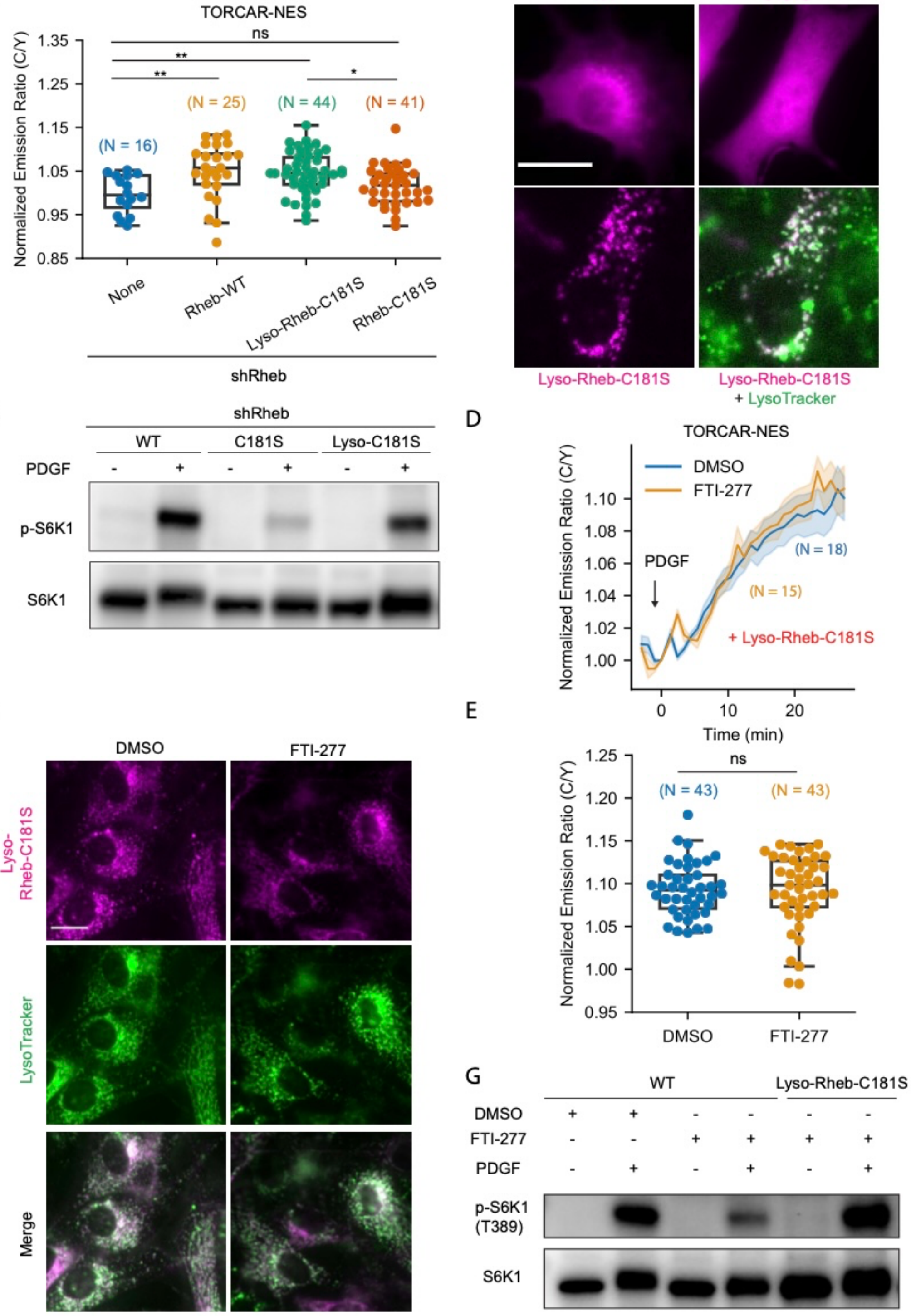
A
TORCAR-NES
Normalized Emission Ratio (C/Y)
1.35
1.25
1.15
1.05
0.95
0.85
ns
**
**
*
(N = 16)
(N = 25)
(N = 44)
(N = 41)
None
Rheb-WT
Lyso-Rheb-C181S
Rheb-C181S
shRheb
B
WT
C181S
Lyso-Rheb-C181S
Lyso-Rheb-C181S
+ LysoTracker
C
shRheb
WT
C181S
Lyso-C181S
PDGF
-
+
-
+
-
+
p-S6K1
S6K1
D
TORCAR-NES
Normalized Emission Ratio (C/Y)
DMSO
FTI-277
1.10
1.08
1.06
1.04
1.02
1.00
PDGF
(N = 18)
(N = 15)
+ Lyso-Rheb-C181S
0
10
20
Time (min)
F
DMSO
FTI-277
Lyso-Rheb-C181S
LysoTracker
Merge
E
Normalized Emission Ratio (C/Y)
1.25
1.20
1.15
1.10
1.05
1.00
0.95
ns
(N = 43)
(N = 43)
DMSO
FTI-277
G
WT
Lyso-Rheb-C181S
DMSO
+
+
-
-
-
-
FTI-277
-
-
+
+
+
+
PDGF
-
+
-
+
-
+
p-S6K1
(T389)
S6K1

TORCAR response in Rheb knockdown cells (**Figure 2.13A-B**). Interestingly, while the Rheb knockdown cells did not respond to PDGF stimulation (0.0 ± 1.1 %, n = 16), localizing Rheb-C181S mutant to the lysosomal membrane can partially rescue the cytosolic TORCAR response (Lyso-Rheb-C181S: 4.6 ± 0.7 %, n = 44). Lysosomal targeting is critical for this activity as the untargeted Rheb-C181S was not able to rescue the cytosolic TORCAR response (1.7 ± 0.7 %, n = 41). Similar results were also observed in western blotting experiments examining S6K1 phosphorylation using Rheb knockdown cells stably reconstituted with Rheb mutants (Figure S9C). To further validate this finding and examine the role of farnesylation, we tested whether Lyso-Rheb-C181S could rescue cytosolic TORCAR response in cells treated with farnesyltransferase inhibitor. Indeed, in cells overexpressing Lyso-Rheb-C181S, FTI-277 was not able to inhibit cytosolic TORCAR response (**Figure 2.13D-F**. DMSO: 8.9 ± 0.6 %, n = 43; FTI-277: 9.2 ± 0.7 %, n = 43). Furthermore, in cells stably expressing Lyso-Rheb-C181S, FTI-277 treatment did not lead to a reduction of PDGF-induced phosphorylation of S6K1 (**Figure 2.13G**). These data support that farnesylation itself is not required for Rheb to activate mTORC1 but the lysosomal membrane association enabled by farnesylation is essential for Rheb to activate the canonical mTORC1 pathway. Thus, non-farnesylated Rheb should be capable of interacting with and allosterically activating mTORC1, which can occur on the lysosomal surface or in the nucleus.

To further test this hypothesis, we examined if farnesylation-deficient Rheb could rescue nuclear mTORC1 activity. Consistent with previous results, knockdown of Rheb abolished nuclear TORCAR response (0.3 ± 0.4 %, n = 54) compared to wild type cells (6.9 ± 0.5 %, n = 29) (**Figure 2.12E-F**). Overexpressing wild type Rheb rescued nuclear TORCAR response to a level that is comparable to wild type cells (4.3 ± 0.7 %, n = 42) (**Figure 2.12E-F**). Strikingly, Rheb-C181S rescued a significant amount nuclear mTORC1 activity (3.7 ± 0.5 %, n = 84). As a negative control, Rheb-*Δ*5A failed to rescue nuclear TORCAR response (1.2 ± 0.4 %, n = 43). These data support that Rheb regulates mTORC1 in the nucleus independent of its farnesylation and that farnesylation regulates the localization of Rheb, not its capability to stimulate mTORC1 activity.

Discussion

As a small GTPase, the activity of Rheb is determined by its nucleotide binding status. Wild type Rheb was shown to have high basal GTP binding, and yet no GEF has been identified for Rheb. Thus, a relatively low nucleotide affinity may allow Rheb to spontaneously exchange GDP for GTP to become active, given that the cellular concentration of GTP is 10-fold higher than GDP (Traut, 1994). TSC2 acts as a GAP for Rheb and colocalizes with Rheb on the lysosomal surface to keep Rheb in its GDP form to suppress the canonical mTORC1 activity, but how TSC2 is targeted to the lysosomal surface is less clear. It was reported that TSC2 directly interacts with lysosomally localized Rheb. However, only a small pool of Rheb is localized to lysosomes (Angarola and Ferguson, 2020), suggesting that there might be other factors mediating lysosomal localization of TSC2. Recent work showed that G3BPs play an important role in tethering TSC2 to lysosomes (Prentzell et al., 2021). Whether the phosphorylation of TSC2 affects its interaction with G3BPs and thus its lysosomal association requires further investigation.

Upon growth factor stimulation, active Akt phosphorylates TSC2, promoting its disassociation from the lysosomal surface and allowing Rheb to activate mTORC1 on the lysosomal surface (**Figure 2.1A**). Using live cell imaging, we showed that overexpression of the unphosphorylatable TSC2, but not wild type TSC2, suppressed the cytosolic response of TORCAR (**Figure 2.8B-C**), supporting the lysosome-dependent spatial regulation of TSC2 as a mechanism to regulate lysosomal mTORC1 signaling. In contrast, wild type TSC2 strongly inhibited the nuclear targeted TORCAR response (**Figure 2.8F-G**), despite the presence of nuclear Akt activity (Zhou et al., 2020). These data suggest that colocalization of TSC2 and Rheb is a prerequisite for the inhibitory effect of TSC2 on Rheb and imply that Akt-mediated phosphorylation of TSC2 disrupts its colocalization with Rheb on the lysosomal surface. Molecularly, it has been reported that phosphorylated TSC2 binds to 14-3-3 in the cytosol (Cai et al., 2006), which may prevent its binding to the lysosomal surface. On the other hand, in the nucleus, phosphorylated exogenous TSC2 cannot be spatially re-positioned or restricted by 14-3-3, and can therefore freely bind to Rheb to inhibit nuclear mTORC1 activity. In fact, the absence of endogenous nuclear TSC2 allows nuclear Rheb to be in an active "standby" status, which could allow for faster nuclear mTORC1 response to external signals (**Figure 2.12G**). It is also possible that nuclear Rheb is controlled by other mechanisms of regulation, such as other nuclear GAPs or E3 ligases (Martin et al., 2014; Ge et al., 2020), which requires future investigation.

Rheb undergoes farnesylation to achieve weak membrane association. In line with previous studies (Hanker et al., 2010), we also found that farnesylation is essential for Rheb to localize to membrane compartments and important for mTORC1 signaling since the farnesyltransferase inhibitor disrupted Rheb membrane localization as well as S6K1 phosphorylation (**Figure 2.10A-B**). Significantly, our genetically encoded biosensor (TORCAR) allowed us to reveal the differential effects of abolishing farnesylation on subcellular mTORC1 activities. In contrast to canonical mTORC1 regulation, we found that the farnesyltransferase inhibitor did not affect nuclear mTORC1 activity (**Figure 2.11C-D**) and the farnesylation-deficient Rheb-C181S could stimulate nuclear mTORC1 (**Figure 2.12E-F**). Farnesyltransferase and other enzymes responsible for Rheb farnesylation have been proposed as drug targets for cancers, but the effects of farnesyltransferase inhibitors were less satisfying than anticipated (Wang et al., 2017; Yang et al., 2017b; Mullard, 2021). Given that nuclear mTORC1 does not require farnesylated Rheb, it is possible that nuclear mTORC1 activity is spared from effects of farnesyltransferase inhibitors. It would be very interesting to test the roles of subcellular pools of mTORC1 in mediating drug toxicity and resistance in the context of various diseases.

As a signaling hub, mTORC1 senses a variety of cues to regulate a broad range of biological processes, yet with high specificity and efficacy. This is likely to be achieved through the spatial compartmentalization of the signaling pathway (Mehta and Zhang, 2021; Zhang et al., 2021). Nuclear mTORC1 has been suggested to directly regulate transcription, such as those mediated by Pol III (Michels et al., 2010; Shor et al., 2010). Further investigation is needed to identify the substrates and the functions of nuclear mTORC1, which could benefit from the targeted TSC2 mutants developed in this study, given that TSC2-NLS specifically inhibits nuclear mTORC1 activity (**Figure 2.8**).

In summary, we clarified the role of Rheb farnesylation in mTORC1 signaling, provided new insights into the regulation of nuclear mTORC1 and developed tools for selectively perturbing subcellular pools of mTORC1 activity for functional dissection. Understanding the precise mechanisms and functions of subcellular mTORC1 signaling should provide us with the opportunity to target subcellular mTORC1 activity as a potential therapeutic strategy.

Chapter 2, in full, has been accepted for publication of the material as it will appear in Zhong, Y., Zhou, X., Guan, KL., Zhang, J. Rheb Regulates Nuclear mTORC1 Activity Independent of Farnesylation. *Cell Chemical Biology*. The dissertation author was the primary investigator and author of this work.

References

Angarola, B., Ferguson, S.M., 2019. Weak membrane interactions allow Rheb to activate mTORC1 signaling without major lysosome enrichment. Mol. Biol. Cell 30, 2750–2760.

Angarola, B., Ferguson, S.M., 2020. Coordination of Rheb lysosomal membrane interactions with mTORC1 activation. F1000Res. 9.

Basso, A.D., Mirza, A., Liu, G., Long, B.J., Bishop, W.R., Kirschmeier, P., 2005. The farnesyl transferase inhibitor (FTI) SCH66336 (lonafarnib) inhibits Rheb farnesylation and mTOR signaling. Role in FTI enhancement of taxane and tamoxifen anti-tumor activity. J. Biol. Chem. 280, 31101–31108.

Bernardi, R., Guernah, I., Jin, D., Grisendi, S., Alimonti, A., Teruya-Feldstein, J., Cordon-Cardo, C., Simon, M.C., Rafii, S., Pandolfi, P.P., 2006. PML inhibits HIF-1alpha translation and neoangiogenesis through repression of mTOR. Nature 442, 779–785.

Cai, S.-L., Tee, A.R., Short, J.D., Bergeron, J.M., Kim, J., Shen, J., Guo, R., Johnson, C.L., Kiguchi, K., Walker, C.L., 2006. Activity of TSC2 is inhibited by AKT-mediated phosphorylation and membrane partitioning. J. Cell Biol. 173, 279–289.

Chong-Kopera, H., Inoki, K., Li, Y., Zhu, T., Garcia-Gonzalo, F.R., Rosa, J.L., Guan, K.-L., 2006. TSC1 stabilizes TSC2 by inhibiting the interaction between TSC2 and the HERC1 ubiquitin ligase. J. Biol. Chem. 281, 8313–8316.

Clark, G.J., Kinch, M.S., Rogers-Graham, K., Sebti, S.M., Hamilton, A.D., Der, C.J., 1997. The Ras-related protein Rheb is farnesylated and antagonizes Ras signaling and transformation. J. Biol. Chem. 272, 10608–10615.

Demetriades, C., Doumpas, N., Teleman, A.A., 2014. Regulation of TORC1 in response to amino acid starvation via lysosomal recruitment of TSC2. Cell 156, 786–799.

Demetriades, C., Plescher, M., Teleman, A.A., 2016. Lysosomal recruitment of TSC2 is a universal response to cellular stress. Nat. Commun. 7, 10662.

Ferlazzo, M.L., Bach-Tobdji, M.K.E., Djerad, A., Sonzogni, L., Devic, C., Granzotto, A., Bodgi, L., Bachelet, J.-T., Djefal-Kerrar, A., Hennequin, C., Foray, N., 2017. Radiobiological Characterization of Tuberous Sclerosis: a Delay in the Nucleo-Shuttling of ATM May Be Responsible for Radiosensitivity. Mol. Neurobiol. 55, 1–11.

Ge, M.-K., Zhang, N., Xia, L., Zhang, C., Dong, S.-S., Li, Z.-M., Ji, Y., Zheng, M.-H., Sun, J., Chen, G.-Q., Shen, S.-M., 2020. FBXO22 degrades nuclear PTEN to promote tumorigenesis. Nat. Commun. 11, 1720.

Hanker, A.B., Mitin, N., Wilder, R.S., Henske, E.P., Tamanoi, F., Cox, A.D., Der, C.J., 2010. Differential requirement of CAAX-mediated posttranslational processing for Rheb localization and signaling. Oncogene 29, 380–391.

Hao, F., Kondo, K., Itoh, T., Ikari, S., Nada, S., Okada, M., Noda, T., 2018. Rheb localized on the Golgi membrane activates lysosome-localized mTORC1 at the Golgi-lysosome contact site. J. Cell Sci. 131.

Havel, J.J., Li, Z., Cheng, D., Peng, J., Fu, H., 2015. Nuclear PRAS40 couples the Akt/mTORC1 signaling axis to the RPL11-HDM2-p53 nucleolar stress response pathway. Oncogene 34, 1487–1498.

Hay, N., Sonenberg, N., 2004. Upstream and downstream of mTOR. Genes Dev. 18, 1926–1945.

Huo, Y., Chen, W.S., Lee, J., Feng, G.-S., Newton, I.G., 2019. Stress conditions induced by locoregional therapies stimulate enrichment and proliferation of liver cancer stem cells. J Vasc Interv Radiol.

Inoki, K., Li, Y., Xu, T., Guan, K.-L., 2003. Rheb GTPase is a direct target of TSC2 GAP activity and regulates mTOR signaling. Genes Dev. 17, 1829–1834.

Inoki, K., Li, Y., Zhu, T., Wu, J., Guan, K.-L., 2002. TSC2 is phosphorylated and inhibited by Akt and suppresses mTOR signalling. Nat. Cell Biol. 4, 648–657.

Jiang, H., Vogt, P.K., 2008. Constitutively active Rheb induces oncogenic transformation. Oncogene 27, 5729–5740.

Kantidakis, T., Ramsbottom, B.A., Birch, J.L., Dowding, S.N., White, R.J., 2010. mTOR associates with TFIIIC, is found at tRNA and 5S rRNA genes, and targets their repressor Maf1. Proc. Natl. Acad. Sci. USA 107, 11823–11828.

Kim, J., Guan, K.-L., 2019. mTOR as a central hub of nutrient signalling and cell growth. Nat. Cell Biol. 21, 63–71.

Kim, J.E., Chen, J., 2000. Cytoplasmic-nuclear shuttling of FKBP12-rapamycin-associated protein is involved in rapamycin-sensitive signaling and translation initiation. Proc. Natl. Acad. Sci. USA 97, 14340–14345.

Laplante, M., Sabatini, D.M., 2012. mTOR signaling in growth control and disease. Cell 149, 274–293.

Li, Y., Inoki, K., Guan, K.-L., 2004. Biochemical and functional characterizations of small GTPase Rheb and TSC2 GAP activity. Mol. Cell. Biol. 24, 7965–7975.

Liu, G.Y., Sabatini, D.M., 2020. mTOR at the nexus of nutrition, growth, ageing and disease. Nat. Rev. Mol. Cell Biol. 21, 183–203.

Long, X., Lin, Y., Ortiz-Vega, S., Yonezawa, K., Avruch, J., 2005. Rheb binds and regulates the mTOR kinase. Curr. Biol. 15, 702–713.

Manning, B.D., Tee, A.R., Logsdon, M.N., Blenis, J., Cantley, L.C., 2002. Identification of the tuberous sclerosis complex-2 tumor suppressor gene product tuberin as a target of the phosphoinositide 3-kinase/akt pathway. Mol. Cell 10, 151–162.

Martin, T.D., Chen, X.-W., Kaplan, R.E.W., Saltiel, A.R., Walker, C.L., Reiner, D.J., Der, C.J., 2014. Ral and Rheb GTPase activating proteins integrate mTOR and GTPase signaling in aging, autophagy, and tumor cell invasion. Mol. Cell 53, 209–220.

Mehta, S., Zhang, J., 2021. Biochemical Activity Architectures Visualized-Using Genetically Encoded Fluorescent Biosensors to Map the Spatial Boundaries of Signaling Compartments. Acc. Chem. Res. 54, 2409–2420.

Menon, S., Dibble, C.C., Talbott, G., Hoxhaj, G., Valvezan, A.J., Takahashi, H., Cantley, L.C., Manning, B.D., 2014. Spatial control of the TSC complex integrates insulin and nutrient regulation of mTORC1 at the lysosome. Cell 156, 771–785.

Michels, A.A., Robitaille, A.M., Buczynski-Ruchonnet, D., Hodroj, W., Reina, J.H., Hall, M.N., Hernandez, N., 2010. mTORC1 directly phosphorylates and regulates human MAF1. Mol. Cell. Biol. 30, 3749–3757.

Mullard, A., 2021. The FDA approves a first farnesyltransferase inhibitor. Nat. Rev. Drug Discov. 20, 8.

Prentzell, M.T., Rehbein, U., Cadena Sandoval, M., De Meulemeester, A.-S., Baumeister, R., Brohée, L., Berdel, B., Bockwoldt, M., Carroll, B., Chowdhury, S.R., von Deimling, A., Demetriades, C., Figlia, G., Genomics England Research Consortium, de Araujo, M.E.G., Heberle, A.M., Heiland, I., Holzwarth, B., Huber, L.A., Jaworski, J., Kedra, M., Kern, K., Kopach, A., Korolchuk, V.I., van 't Land-Kuper, I., Macias, M., Nellist, M., Palm, W., Pusch, S., Ramos Pittol, J.M., Reil, M., Reintjes, A., Reuter, F., Sampson, J.R., Scheldeman, C., Siekierska, A., Stefan, E., Teleman, A.A., Thomas, L.E., Torres-Quesada, O., Trump, S., West, H.D., de Witte, P., Woltering, S., Yordanov, T.E., Zmorzynska, J., Opitz, C.A., Thedieck, K., 2021. G3BPs tether the TSC complex to lysosomes and suppress mTORC1 signaling. Cell 184, 655–674.e27.

Rosner, M., Hengstschläger, M., 2012. Detection of cytoplasmic and nuclear functions of mTOR by fractionation. Methods Mol. Biol. 821, 105–124.

Saitoh, M., Pullen, N., Brennan, P., Cantrell, D., Dennis, P.B., Thomas, G., 2002. Regulation of an activated S6 kinase 1 variant reveals a novel mammalian target of rapamycin phosphorylation site. J. Biol. Chem. 277, 20104–20112.

Shor, B., Wu, J., Shakey, Q., Toral-Barza, L., Shi, C., Follettie, M., Yu, K., 2010. Requirement of the mTOR kinase for the regulation of Maf1 phosphorylation and control of RNA polymerase III-dependent transcription in cancer cells. J. Biol. Chem. 285, 15380–15392.

Suzuki, K., Bose, P., Leong-Quong, R.Y., Fujita, D.J., Riabowol, K., 2010. REAP: A two minute cell fractionation method. BMC Res. Notes 3, 294.

Tabancay, A.P., Gau, C.-L., Machado, I.M.P., Uhlmann, E.J., Gutmann, D.H., Guo, L., Tamanoi, F., 2003. Identification of dominant negative mutants of Rheb GTPase and their use to implicate the involvement of human Rheb in the activation of p70S6K. J. Biol. Chem. 278, 39921–39930.

Takahashi, K., Nakagawa, M., Young, S.G., Yamanaka, S., 2005. Differential membrane localization of ERas and Rheb, two Ras-related proteins involved in the phosphatidylinositol 3-kinase/mTOR pathway. J. Biol. Chem. 280, 32768–32774.

Tee, A.R., Manning, B.D., Roux, P.P., Cantley, L.C., Blenis, J., 2003. Tuberous sclerosis complex gene products, Tuberin and Hamartin, control mTOR signaling by acting as a GTPase-activating protein complex toward Rheb. Curr. Biol. 13, 1259–1268.

Traut, T.W., 1994. Physiological concentrations of purines and pyrimidines. Mol. Cell. Biochem. 140, 1–22.

Wan, W., You, Z., Xu, Y., Zhou, L., Guan, Z., Peng, C., Wong, C.C.L., Su, H., Zhou, T., Xia, H., Liu, W., 2017. mTORC1 Phosphorylates Acetyltransferase p300 to Regulate Autophagy and Lipogenesis. Mol. Cell 68, 323–335.e6.

Wang, J., Yao, X., Huang, J., 2017. New tricks for human farnesyltransferase inhibitor: cancer and beyond. Medchemcomm 8, 841–854.

Wang, Z., Feng, X., Molinolo, A.A., Martin, D., Vitale-Cross, L., Nohata, N., Ando, M., Wahba, A., Amornphimoltham, P., Wu, X., Gilardi, M., Allevato, M., Wu, V., Steffen, D.J., Tofilon, P., Sonenberg, N., Califano, J., Chen, Q., Lippman, S.M., Gutkind, J.S., 2019. 4E-BP1 Is a Tumor Suppressor Protein Reactivated by mTOR Inhibition in Head and Neck Cancer. Cancer Res. 79, 1438–1450.

Yang, H., Jiang, X., Li, B., Yang, H.J., Miller, M., Yang, A., Dhar, A., Pavletich, N.P., 2017. Mechanisms of mTORC1 activation by RHEB and inhibition by PRAS40. Nature 552, 368–373.

Yang, W.S., Yeo, S.-G., Yang, S., Kim, K.-H., Yoo, B.C., Cho, J.Y., 2017. Isoprenyl carboxyl methyltransferase inhibitors: a brief review including recent patents. Amino Acids 49, 1469–1485.

Zhang, J.-F., Mehta, S., Zhang, J., 2021. Signaling microdomains in the spotlight: visualizing compartmentalized signaling using genetically encoded fluorescent biosensors. Annu. Rev. Pharmacol. Toxicol. 61, 587–608.

Zhang, X., Shu, L., Hosoi, H., Murti, K.G., Houghton, P.J., 2002. Predominant nuclear localization of mammalian target of rapamycin in normal and malignant cells in culture. J. Biol. Chem. 277, 28127–28134.

Zhou, X., Clister, T.L., Lowry, P.R., Seldin, M.M., Wong, G.W., Zhang, J., 2015. Dynamic Visualization of mTORC1 Activity in Living Cells. Cell Rep. 10, 1767–1777.

Zhou, X., Zhong, Y., Molinar-Inglis, O., Kunkel, M.T., Chen, M., Sun, T., Zhang, Jiao, Shyy, J.Y.-J., Trejo, J., Newton, A.C., Zhang, Jin, 2020. Location-specific inhibition of Akt reveals regulation of mTORC1 activity in the nucleus. Nat. Commun. 11, 6088.

Chapter 3

Genetically targetable mTORC1 inhibitor reveals differential transcriptional control by subcellular mTORC1

Introduction

Rapamycin, the bacterium-produced macrolide, leads to the discovery of the mechanistic target of rapamycin (mTOR), a key signaling component involved in regulating a number of cellular processes and the mediator of the potent immunosuppressive and antiproliferative effects of Rapamycin (Sabatini, 2017). mTOR forms two distinct complexes in cells, mTORC1 and mTORC2. Among these, mTORC1 plays an essential role in sensing upstream signals including growth factors and amino acids, and regulating downstream cellular processes ranging from macromolecule biosynthesis and metabolism to cell growth and proliferation (Saxton and Sabatini, 2017).

To achieve signaling specificity and efficiency, mTORC1 signaling is spatially compartmentalized. Activation of mTORC1 by amino acids and growth factors on the lysosome has been extensively studied. Amino acid signals promote the guanine-nucleotide exchange factor (GEF) activity of Ragulator towards Rag GTPases, which recruit mTORC1 to the lysosomal membrane, where the mTORC1 activator Rheb also resides (Sancak et al., 2010). Growth factor activates Akt which phosphorylates TSC2 of the Tuberous Sclerosis Complex (TSC), leading to the disassociation of TSC from the lysosomal membrane and relieving the inhibition of TSC towards Rheb (Cai et al., 2006; Inoki et al., 2002; Manning et al., 2002; Menon et al., 2014). Besides the canonical lysosomal mTORC1 activation, we recently discovered the growth factor stimulated nuclear mTORC1 activity using a genetically encoded fluorescent mTORC1 activity reporter (TORCAR) (Zhou et al., 2015). The noncanonical nuclear mTORC1 activity is dependent on the nuclear Akt activity, which promotes nuclear translocation of Raptor, the mTORC1 defining component, and phosphorylates PRAS40, a negative mTORC1 regulatory protein, to relieve its inhibition on nuclear mTORC1 activity (Zhou et al., 2020). Although it is known that mTORC1 controls numerous cellular functions such as promoting protein synthesis by phosphorylating ribosomal S6 kinase 1 (S6K1) and eIF4E-binding protein 1 (4EBP1) (Nandagopal and Roux, 2015), and inhibiting autophagy via phosphorylating ULK1 (Kim et al., 2011), it remains unclear how subcellular pools of mTORC1 contribute to the different functions.

To understand the specific functions regulated by distinct pools of mTORC1, there is an urgent need to develop molecular tools that can be used to perturb subcellular mTORC1 activity in a location-specific manner. The ATP competitive inhibitors of mTOR, including Torin1 (Liu et al., 2010) and INK128 (Feldman et al., 2009), indistinguishably inhibit both mTORC1 and mTORC2. mTORC1 specific inhibitors based on rapamycin, including rapalogs (Lamming et al., 2013) and the newly developed rapalink (Rodrik-Outmezguine et al., 2016), could not target specific pools of mTORC1 given the diffusible property of small molecules. Current genetic perturbations of the regulatory network, including knockdown of mTORC1 component Raptor (Sancak et al., 2007) and mTORC1 activator Rheb (Angarola and Ferguson, 2019), also globally suppressed mTORC1 activity. Thus, new approaches are needed to develop an mTORC1 specific and targetable inhibitor to examine the functions of specific subcellular pools of mTORC1.

In this study, we reported a genetically **t**argetable and **e**ncodable **r**epressor to **min**imize **a**ctivity of m**TOR**C1 (TerminaTOR), which potently inhibits cellular mTORC1 activity. Using TerminaTOR targeted to different compartments, we achieved specific inhibition of canonical lysosomal mTORC1 activity and noncanonical nuclear mTORC1 activity. We performed comparative transcriptome profiling on NIH3T3 fibroblasts expressing TerminaTOR targeted to different subcellular compartments, and uncovered transcriptional programs that are specifically regulated by the nuclear mTORC1.

Methods

Reagents and Drug Treatment

PDGF (P3201) was purchased from Sigma and was used at 50 ng/mL to stimulate starved cells. Torin1 was purchased from TOCRIS (#4247) and used at 1 μM for 30 min pretreatment before imaging experiments were performed. H89 was used at 10 μM for 10 min pretreatment. Gö 6983 was used at 1 μM for 10 min pretreatment. GDC-0068 was purchased from APExBIO (RG7440) and was used at 1 μM for 30 min pretreatment. DMSO was purchased from Sigma (D2650) and used as vehicle. Doxycycline was purchased from Clontech (631311) and supplemented in medium at a final concentration of 100 ng/mL to induce gene expression.

Constructs and Cloning

mTORC1 activity reporter (TORCAR) and its targeted versions (TORCAR-NES, Lyso-TORCAR and TORCAR-NLS) were previously described (Zhou et al., 2020). PRAS40 sequence was obtained from Addgene (#86758) and primers were designed (Eton Bioscience, Inc.) to generate different truncated fragments using PCR. Similarly, backbone fragments were amplified from pcDNA3-mCherry plasmid. PRAS40 fragments and backbone fragments were Gibson assembled to generate different mCherry-tagged PRAS40 fragments, including pcDNA3-mCherry-114-245. Mutations in pcDNA-mCherry-114-245 were generated similarly by Gibson assembly using fragments amplified with primers containing desired mutation, giving rise to pcDNA3-mCherry-114-245A (Cyto-TerminaTOR). pcDNA3-Cyto-TerminaTOR was cut with BamHI/EcoRI to get TerminaTOR fragment and Lyso-TORCAR (Zhou et al., 2015) was cut with BamHI/EcoRI to get the backbone with the lysosome targeting sequence. The fragments were ligated using T4 ligase to generate pcDNA3-Lyso-TerminaTOR. To generate Nuc-TerminaTOR, NES mutations were first introduced to generate pcDNA3-TerminaTOR (NES mutant), which was cut with BamHI/EcoRI get TerminaTOR (NES mutant) fragment. Backbone containing H2A was also cut with BamHI/EcoRI. Fragments were ligated using T4 ligase to generate pcDNA-Nuc-TerminaTOR. To generate lentiviral transfer plasmids, fragments from pcDNA were amplified and assembled with backbone fragments amplified from a lentiviral plasmid (Addgene #17452). pcDNA-Cyto-TerminaTOR, pcDNA-Lyso-TerminaTOR and pcDNA-Nuc-TerminaTOR were subcloned into a doxycycline inducible lentiviral expressing vector (Addgene #27565) using Gibson assembly, yielding pLenti-TetOn-Cyto-TerminaTOR, pLenti-TetOn-Lyso-TerminaTOR and pLenti-TetOn-Nuc-TerminaTOR.

Cell Culture, Transfection and Starvation

NIH3T3 cells (CRL-1658, ATCC) were cultured in Dulbecco's modified Eagle's medium (DMEM, 11885, Gibco) supplemented with 10% calf serum (30-2030, ATCC) and 1% penicillin-streptomycin (Sigma-Aldrich). Cells were routinely tested for mycoplasma contamination and found negative. For transfection, cells were transfected with PolyJet Transfection Reagent (SL100688, SignaGen Laboratories) according to the manufacturer's instructions and incubated in serum-free DMEM overnight (serum starvation). The next day, cells were incubated for 2 hours in modified Hank's balanced salt solution (1×HBSS with 2 g/l glucose, pH 7.4, made from 10× HBSS (14065, GIBCO)) at 37°C (referred to as "double starvation") before live cell imaging.

Lentivirus Production and Stable Cell Lines Generation

Lentivirus was packaged in HEK293T cells. Specifically, HEK293T cells were co-transfected with corresponding lentiviral transfer plasmids + psPAX2 + pMD2.G using PolyJet. After 48hr the supernatant was collected, filtered with a 0.45 µm syringe filter and added to NIH3T3 cells in 35 mm dishes. Polybrene Transfection Reagent (TR-1003-G, Millipore) was supplemented to improve the transduction. After 48 hours, cells were passed in fresh growth medium containing puromycin (2 µg/mL) to select transduced cells for at least one week. Cells were maintained in selection medium and passed for related experiments. For doxycycline inducible cell lines, NIH3T3 cells were co-transduced with lentivirus expressing rtTA transcription factor and doxycycline inducible TetOn expressing vectors. Cells were then maintained in growth medium containing puromycin (2 µg/mL) and blasticidin (2.2 µM) and passaged for related experiments.

Immunoblotting

Cells were washed with ice-cold PBS and then lysed in RIPA lysis buffer containing protease inhibitor cocktail, 1 mM PMSF, 1 mM Na3VO4, 1 mM NaF, and 25 nM calyculin A. Total cell lysates were incubated on ice for 30 min and then centrifuged at 15,000g at 4°C for 20 min. Equal amounts of total protein were separated via 4-15% SDS-PAGE and transferred to PVDF membranes. The membranes were blocked with TBS containing 0.1% Tween-20 and 5% bovine serum albumin and then incubated with primary antibodies overnight at 4°C. The next day, membranes were washed, incubated with the appropriate horseradish peroxidase-conjugated secondary antibodies, and were developed using horseradish peroxidase-based chemiluminescent substrate (34579 and 34076, Thermo Fisher Scientific). The following primary antibodies were used for immunoblotting: p-S6K1 (T389) (#9205) and S6K1 (#9202) antibodies from Cell Signaling Technology and anti-6x His tag antibody from ThermoFisher Scientific (#MA1-21315-HRP). Horseradish peroxidase-labeled goat anti-rabbit (PI31460) or anti-mouse (PI31430) secondary antibodies were purchased from Pierce.

Live-cell Imaging

For live cell imaging, cells were plated onto sterile glass-bottomed 35-mm dishes (D35-14-1.5-N, CellVis) and grown to 40% confluency at 37°C with 5% CO2. Cells were transfected, double starved or not starved, and washed once with HBSS and imaged in the dark at room temperature. Images were acquired on a Zeiss Axio Observer Z1 microscope equipped with a 40x/1.3NA objective (Carl Zeiss), Prime95B sCMOS camera (Photometrics) and a motorized stage (Carl Zeiss). The microscope was controlled by MATLAB (Mathworks) and μmanager (Micro-Manager, an open-source microscope imaging software) -based MATScope imaging suite (Github: https://github.com/jinzhanglab-ucsd/MatScopeSuite). CFP images were acquired using ET420/20x excitation filter with a T4551pxt dichroic and AT470/40m emission filter. YFP images were acquired using ET495/10x excitation filter with a T5151p dichroic and ET535/25m emission filter. The C/Y FRET images were acquired using ET420/20x excitation filter with T4551pxt dichroic and ET535/25m emission filter. mCherry imaging was performed using HQ568/55x excitation filter with a Q600LPxr dichroic mirror and HQ653/95m emission filter. EGFP was imaged using an or ET480/30x excitation filter with a T505dcxr dichroic, and ET535/50m emission filter. Exposure times were 50-500 ms, and images were taken every 30 s or 1 min. Imaging data were analyzed using MATLAB scripts developed within the lab. Specifically, fluorescence images were background-corrected and regions of interest (ROI) were manually selected. The cyan/yellow FRET emission ratio was calculated for each ROI on each frame of the image series. The ratio was normalized to the time point before addition of PDGF (t = 0 min).

mRNA Sequencing and Analyses

Stable NIH3T3 cells were cultured in growth medium supplemented with doxycycline at the final concentration of 100 ng/mL and incubated for overnight to induce TerminaTOR expression or mCherry expression as control. DMSO or Torin1 was added to the medium at the final concentration of 1 μM for overnight. Total RNA was extracted using Direct-zol RNA Miniprep kits (R2051, Zymo Research) from triplicated samples from each group and send to RNA sequencing (Novogene, NovaSeq 6000 PE150). All samples passed quality control and sequencing data were analyzed using open-source software project, Galaxy. Differential expressed gene (DEG) analyses were carried out by open-source software R (DESeq2 package) and gene set enrichment analyses (GSEA) were done by open-source GSEA software (UC San Diego and Broad Institute).

Statistical Analysis

The data were analyzed using GraphPad Prism 9. Immunofluorescence data were obtained from two biological replicates, and all other data were obtained from at least three independent biological replicates. Unless otherwise noted, unpaired two-tailed t-test was used for two-group comparison and one-way ANOVA with Dunnett's multiple comparisons test were used for multi-group comparisons. **** indicates a p-value<0.0001; *** indicates a p-value between 0.0001 to 0.001; ** indicates a p-value between 0.001 to 0.01; * indicates a p-value between 0.01 to 0.05; ns, p>0.05, not significant. N numbers, as indicated in figures, legends and the main text, represent the number of cells. Shaded areas in average curves indicate standard error of the mean (SEM). Violin plots and box plots show the upper and lower adjacent value, interquartile range and the median.

Results

Development of a specific, genetically encodable mTORC1 inhibitor

In order to develop a genetically encodable kinase inhibitor (GEKI) for mTORC1, we utilized the endogenous mTORC1 negative regulator, PRAS40, which interacts with mTORC1 via three key motifs: TOR signaling (TOS) motif, β-strand and α-helix (Yang et al., 2017). All three motifs are reported to play important roles for the inhibitory effect on mTORC1 activity (**Figure 3.1A**). Owing to this multisite-binding mode, PRAS40 showed a higher binding affinity to mTORC1 than endogenous mTORC1 substrates, such as 4EBP1 and S6K1 (Yang et al., 2017). We reasoned that if overexpressed in cells, peptide fragments containing the three key motifs would competitively binds to mTORC1, preventing mTORC1 from binding and phosphorylating endogenous mTORC1 substrates. Choosing PRAS40 as the peptide template has several advantages. First, as an endogenous mTORC1 inhibitory protein, it potently inhibits mTORC1 activity (Sancak et al., 2007) and the specificity is ensured by the multiple interacting motifs with mTORC1 (Yang et al., 2017); second, PRAS40 is a relatively small protein and small-size mTORC1 GEKIs can be derived from it; third, limited regulatory residues can be engineered to generate GEKIs that are free from other signaling controls. To test this idea and minimize the PRAS40-based fragment sequence, we first made a panel of truncated versions of PRAS40 (**Figure 3.1B**), including fragments that contain all three key motifs and some variants that lack

Figure 3.1 Development of PRAS40-based mTORC1 inhibitor. (A). A domain structure of TORCAR and a scheme depicting the interactions between PRAS40 and mTORC1. Three motifs in PRAS40 mediates the interactions: TOS motif interacts with Raptor, β-strand interacts with mLST8 (an mTORC1 component), and α-helix interacts with mTOR. S183 is an mTORC1 phosphorylation site and T246 is an Akt phosphorylation site. (B). Left, domain structures of PRAS40-based fragments. Middle, mTORC1 activity was examined in NIH3T3 cells stably expressing TORCAR. Cells were transfected, double starved, pretreated with Torin1 or not pretreated, and stimulated with 50 ng/mL PDGF. Normalized emission ratio at 30 min was calculated for each experiment and compared. When compared with control cells (9.0 ± 0.7 %, n = 25, ref. 1, significance was marked by † or NS), Torin1 (0 ± 0.2 %, n = 30) and full length PRAS40 inhibited the response (1.0 ± 0.9 %, n = 21). mCherry control (10.0 ± 0.9 %, n = 24) had no impact on TORCAR response. Compared with mCherry control (ref. 2, significance was marked by * or n.s.), all PRAS40-based fragments except 153-245 (7.0 ± 0.7 %, n = 22), showed reduced TORCAR responses (1-232: 2.0 ± 1.3 %, n = 21; 114-256: 1.0 ± 0.6 %, n = 20; 114-256AA: 0 ± 0.7 %, n = 31; 114-245: 0 ± 1.0 %, n = 18; 114-245A: 0 ± 0.5 %, n = 18; 153-245A: 5.0 ± 0.8 %, n = 20; 172-245: 2.0 ± 1.2 %, n = 21; 172-245A: 3.0 ± 1.1 %, n = 21). n indicates cell numbers analyzed in each experiment. Data are representative from three independent experiments. Violin plots show the upper and lower adjacent values, interquartile range and the median. One-way ANOVA with Dunnett's multiple comparisons is used. ††††, $p < 0.0001$; ****, $p < 0.0001$; **, $p < 0.01$; NS and n.s., not significant. Right, averaged time course traces of each experiment. Horizontal axis represents time in min and vertical axis represents normalized emission ration in percentage (%). Shaded areas indicate standard error of the mean (SEM). (C). Western blotting to show fragment 114-245 and 114-245A were able to block mTORC1 activity. Wild type NIH3T3 cells or cells stably expressing mCherry, 114-245 and 114-245A (all constructs have His tag) were double starved and stimulated with 50 ng/mL PDGF or unstimulated. Phosphorylation of mTORC1 substrate S6K1 at Thr389 (T389) was examined. Arrow indicates the position of 114-245 and 114-245A bands. Data are representative from three independent experiments.

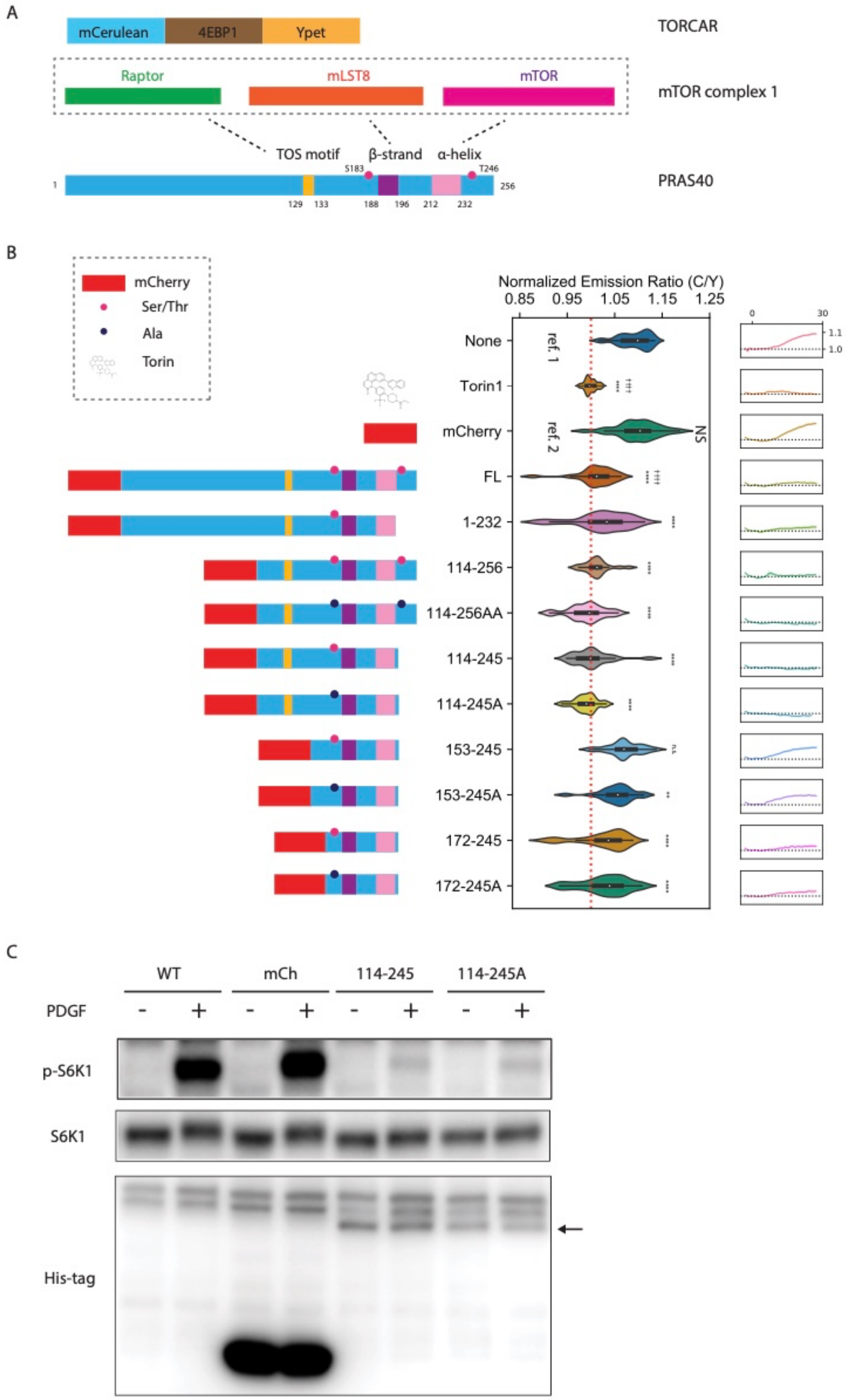
A
mCerulean
4EBP1
Ypet
TORCAR
Raptor
mLST8
mTOR
mTOR complex 1
TOS motif
β-strand
α-helix
S183
T246
PRAS40
1
129
133
188
196
212
232
256
B
mCherry
Ser/Thr
Ala
Torin
Normalized Emission Ratio (C/Y)
0.85
0.95
1.05
1.15
1.25
None
Torin1
mCherry
FL
1-232
114-256
114-256AA
114-245
114-245A
153-245
153-245A
172-245
172-245A
ref. 1
ref. 2
NS
n.s.
0
30
1.1
1.0
C
WT
mCh
114-245
114-245A
PDGF
-
+
-
+
-
+
-
+
p-S6K1
S6K1
His-tag

the TOS motif. We also mutated the two key regulatory residues, Ser183 and Thr246, to Ala to eliminate endogenous regulation that could dampen the inhibitory effect on mTORC1 activity (Wiza et al., 2012). These PRAS40-based fragments were all tagged with mCherry fluorescent protein and coexpressed in NIH3T3 cells stably expressing the mTORC1 activity reporter (TORCAR) (Zhou et al., 2015). These cells were starved and stimulated with PDGF and the mTORC1 activity were measured by TORCAR emission ratio change (**Figure 3.1B**). We found that the full length PRAS40 strongly inhibited TORCAR responses (1.0 ± 0.9 %, n = 21), to a similar extent as Torin 1 (0 ± 0.2 %, n = 30), compared with positive control cells not expressing PRAS40 fragments (9.0 ± 0.7 %, n = 25) or expressing mCherry control (10.0 ± 0.9 %, n = 24). Importantly, all PRAS40-based fragments, except 153-245 (7.0 ± 0.7 %, n = 22), showed reduced TORCAR responses, though the extent of suppression varied (1-232: 2.0 ± 1.3 %, n = 21; 114-256: 1.0 ± 0.6 %, n = 20; 114-256AA: 0 ± 0.7 %, n = 31; 114-245: 0 ± 1.0 %, n = 18; 114-245A: 0 ± 0.5 %, n = 18; 153-245A: 5.0 ± 0.8 %, n = 20; 172-245: 2.0 ± 1.2 %, n = 21; 172-245A: 3.0 ± 1.1 %, n = 21). Fragment 1-232 that lacks all residues after the α-helix showed reduced inhibitory effect on TORCAR response (2.0 ± 1.3 %, n = 21), indicating that residues after the α-helix may function as a scaffold that allows PRAS40 to interact with mTORC1 via the α-helix. Interestingly, fragments lacking the TOS motif (153-245, 153-245A, 172-245 and 172-245A) also showed less inhibitory effect on TORCAR responses but are still capable of suppressing TORCAR response. The essentiality of TOS motif of PRAS40 to inhibit mTORC1 activity was under debate from earlier studies (Hsu et al., 2011; Yang et al., 2017). Our data suggested TOS motif of PRAS40 is not required its inhibitory activity but can further enhance the suppression of mTORC1 activity. Among the PRAS40-based fragments, four truncated fragments that contain all three key motifs (114-256, 114-256AA, 114-245 and 114-245A) showed inhibitory effect on TORCAR responses similar to that of full length PRAS40 or the torin1-treated group. These data showed that fragments derived from PRAS40 containing three key motifs could serve as GEKI that targets mTORC1 activity. To further validate the inhibition on mTORC1 activity, we chose two fragments, 114-245 and 114-245A, and stably expressed them in NIH3T3 cells. We examined the phosphorylation of S6K1, one of the mTORC1 substrates, in response to PDGF stimulation. Consistent with the TORCAR results, we found while PDGF induced strong S6K1 phosphorylation in control cells and cells expressing mCherry, S6K1 phosphorylation was abolished in cells expressing 114-245 or 114-245A (**Figure 3.1C**). The expression level of both 114-245 and 114-245A were obviously lower than mCherry control (**Figure 3.1C**), suggesting these peptide fragments were potent in inhibiting mTORC1.

Next, to test the specificity of these fragments, we examined the effect of overexpressing 114-245 or 114-245A on several essential signaling hubs, PKA, PKC and Akt, by using fluorescent biosensors, AKAR4 (Clister et al., 2019), CKAR2 (Ross et al., 2018) and AktAR2 (Zhou et al., 2015) to measuring PKA, PKC and Akt activities respectively. We found in control HEK293T cells or cells overexpressing mCherry, Forskolin/IBMX (Fsk/IBMX) could stimulate PKA activity to a maximum level (None: 33.2 ± 1.6 %, n = 24; mCherry: 33.5 ± 1.0 %, n = 23), which could be significantly suppressed by PKA inhibitor H89 (5.0 ± 0.4 %, n = 21). Cells overexpressing either 114-245 or 114-245A showed similar responses to Fsk/IBMX stimulation (114-245: 34.8 ± 1.5 %, n = 20; 114-245A: 32.4 ± 1.3 %, n = 19) (**Figure 3.2A-B**), suggesting neither inhibits PKA activity. In Hela cells, we found overexpressing 114-245 (25.3 ±1.5 %, n = 28) or 114-245A (21.8 ± 1.6 %, n = 26) did not affect phorbol myristate acetate (PMA) -induced CKAR2 responses compared to control cells (23.3 ± 0.8 %, n = 39) or cells expressing mCherry (23.5 ± 1.1 %, n = 28), while PKC

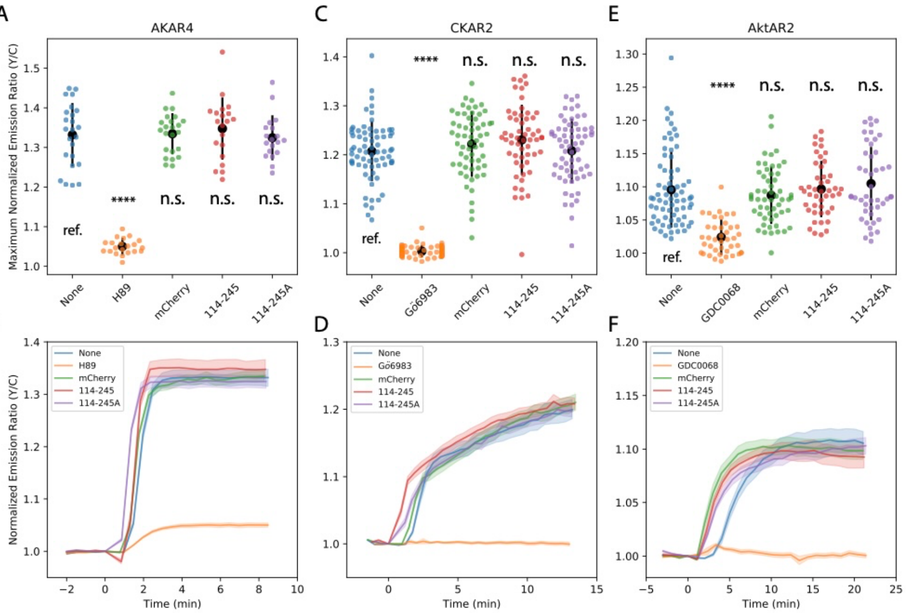

Figure 3.2 Characterization of the specificity of PRAS40-based mTORC1 inhibitor. (A-B). Summary (A) and averaged time course traces (B) of forsklin/IBMX-induced maximum responses of AKAR4 in HEK293T cells. Control cells were not transfected (None, 33.2 ± 1.6 %, n = 24). Negative control was pretreated with 10 µM H89 for 10 min (5.0 ± 0.4 %, n = 21). Co-expressed constructs: mCherry (33.5 ± 1.0 %, n = 23); 114-245 (34.8 ± 1.5 %, n = 20); 114-245A (32.4 ± 1.3 %, n = 19). n indicates cell numbers analyzed in each experiment. Data are representative from three independent experiments. (C-D). Summary (C) and averaged time course traces (D) of PMA-induced maximum responses of CKAR2 in HEK293T cells. Control cells were not transfected (None, 23.3 ± 0.8 %, n = 39). Negative control was pretreated with 1 µM Gö 6983 for 10 min (0.5 ± 0.1 %, n = 39). Co-expressed constructs: mCherry (23.5 ± 1.1 %, n = 28); 114-245 (25.3 ±1.5 %, n = 28); 114-245A (21.8 ± 1.6 %, n = 26). n indicates cell numbers analyzed in each experiment. Data are representative from three independent experiments. (E-F). Summary (E) and averaged time course traces (F) of PDGF-induced maximum responses of AktAR2 in NIH3T3 cells. Control cells were not transfected (None, 9.6 ± 0.7 %, n = 70 cells from 4 independent experiments). Negative control was pretreated with 10 µM GDC-0068 for 10 min (2.4 ± 0.4 %, n = 41 cells from 3 independent experiments). Co-expressed constructs: mCherry (8.7 ± 0.6 %, n = 55 cells from 3 independent experiments); 114-245 (9.7 ± 0.6, n = 45 cells from 3 independent experiments); 114-245A (10.5 ± 0.8 %, n = 45 cells from 3 independent experiments). Shaded areas indicate standard error of the mean (SEM). Line range in swarm plots show average and the upper and lower adjacent values. One-way ANOVA with Dunnett's multiple comparisons is used. ****, $p < 0.0001$; ns, not significant.

inhibitor Gö6983 strongly inhibited PKC activity (0.5 ± 0.1 %, n = 39) (**Figure 3.2C-D**). These data suggest that overexpressing these truncated PRAS40-based fragments does not interfere with the other major signaling pathways than mTORC1 pathway. Akt is a critical upstream regulator of mTORC1 pathway, we did not observe any significant inhibition of PDGF-induced Akt activity in NIH3T3 cell overexpressing 114-245 or 114-245A (114-245: 9.7 ± 0.6, n = 45; 114-245A: 10.5 ± 0.8 %, n = 45) comparing to controls (None: 9.6 ± 0.7 %, n = 70; mCherry: 8.7 ± 0.6 %, n = 55) (**Figure 3.2E-F**), suggesting that these fragments directly target mTORC1 activity rather than suppress upstream positive regulator. An advantage of a GEKI is that it can be targeted to subcellular compartments. Thus, we chose one fragment, 114-245A and named it TerminaTOR, which stands for targetable and encodable repressor to minimize activity of mTORC1.

Lysosomally targeted TerminaTOR inhibited mTORC1 activity at lysosomes and induced autophagy under nutrient rich conditions

As shown by the mCherry fluorescence, the untargeted TerminaTOR was mainly localized to the cytosol (**Figure 3.3A**), as it contains a strong native nuclear exporting sequence (NES) from PRAS40 (Wiza et al., 2013), thereby serving as a cytosol-localized TerminaTOR (Cyto-TerminaTOR). We found Cyto-TerminaTOR significantly suppressed PDGF-induced cytosolic mTORC1 activity in NIH3T3 cells (Ctrl: 10.9 ± 0.7 %, n = 29; Cyto-TerminaTOR: 0.5 ± 0.7 %, n = 34), examined by coexpressing TORCAR-NES, a cytosol localized TORCAR (Zhou et al., 2020). To verify the ability of TerminTOR to inhibit mTORC1 activity at more confined subcellular locations, we targeted TerminaTOR to the lysosome since lysosome is a well-established compartment where amino acid and growth factor signals converge to activate the canonical

Figure 3.3 Lyso-TerminaTOR inhibited lysosomal mTORC1 activity and induced autophagy. (A). Left, representative fluorescent images of TORCAR-NES and Cyto-TerminaTOR. Right, summary of PDGF-induced maximum responses of TORCAR-NES in NIH3T3 cells. Cells were transfected, double starved and stimulated with 50 ng/mL PDGF. Control cells were not transfected (Ctrl, 10.9 ± 0.7 %, n = 29 cells from 3 independent experiments). Cells expressing Cyto-TerminaTOR showed reduced response (Cyto-Ter, 0.5 ± 0.7 %, n = 34 cells from 3 independent experiments). (B). Left, representative fluorescent images of Lyso-TORCAR and Lyso-TerminaTOR. Right, summary of PDGF-induced maximum responses of Lyso-TORCAR in NIH3T3 cells. Cells were transfected, double starved and stimulated with 50 ng/mL PDGF. Control cells were not transfected (Ctrl, 5.0 ± 1.0 %, n = 15 cells from 3 independent experiments). Cells expressing Lyso-TerminaTOR showed reduced response (Lyso-Ter, 0.5 ± 0.5 %, n = 25 cells from 3 independent experiments). (C). Left, representative fluorescent images of TORCAR-NES and Lyso-TerminaTOR. Right, summary of PDGF-induced maximum responses of TORCAR-NES in NIH3T3 cells. Cells were transfected, double starved and stimulated with 50 ng/mL PDGF. Control cells were transfected with H2A-mCherry (Ctrl, 9.7 ± 1.0 %, n = 21 cells from 2 independent experiments). Cells expressing Lyso-TerminaTOR showed reduced response (Lyso-Ter, 0 ± 0.5 %, n = 60 cells from 5 independent experiments). (D). Left, representative fluorescent images of TORCAR-NLS and Lyso-TerminaTOR. Right, summary of PDGF-induced maximum responses of TORCAR-NES in NIH3T3 cells. Cells were transfected, double starved and stimulated with 50 ng/mL PDGF. Control cells were transfected with H2A-mCherry (Ctrl, 5.7 ± 0.5 %, n = 53 cells from 4 independent experiments). Cells expressing Lyso-TerminaTOR showed reduced response (Lyso-Ter, 0.3 ± 0.8 %, n = 29 cells from 2 independent experiments). (E). Summary of PDGF-induced maximum responses of TORCAR-NLS in stable NIH3T3 cells that can be induced to express Lyso-TerminaTOR. Cells were transfected, double starved and stimulated with 50 ng/mL PDGF. Doxycycline was added (+ Dox) to the medium to induce Lyso-TerminaTOR expression or not added (- Dox). Stable expression of Lyso-TerminaTOR did not affect TORCAR-NLS responses (– Dox: 3.1 ± 0.6 %, n = 43 cells from 3 independent experiments; + Dox: 4.3 ± 0.5 %, n = 39 cells from 3 independent experiments). (F). Left, representative fluorescent images of GFP-LC3 in NIH3T3 cells under growth conditions (No starve) or serum starvation conditions (Starve). Right, puncta numbers per cell were counted for each cell in two conditions (No starve: 6 ± 2 per cell; starve: 16 ± 2 per cell). Data are representative from three independent experiments. Box plots show the upper and lower adjacent values, interquartile range and the median. Student t-tests are used. ****, $p < 0.0001$; ***, $p < 0.001$; **, $p < 0.01$; n.s., not significant.

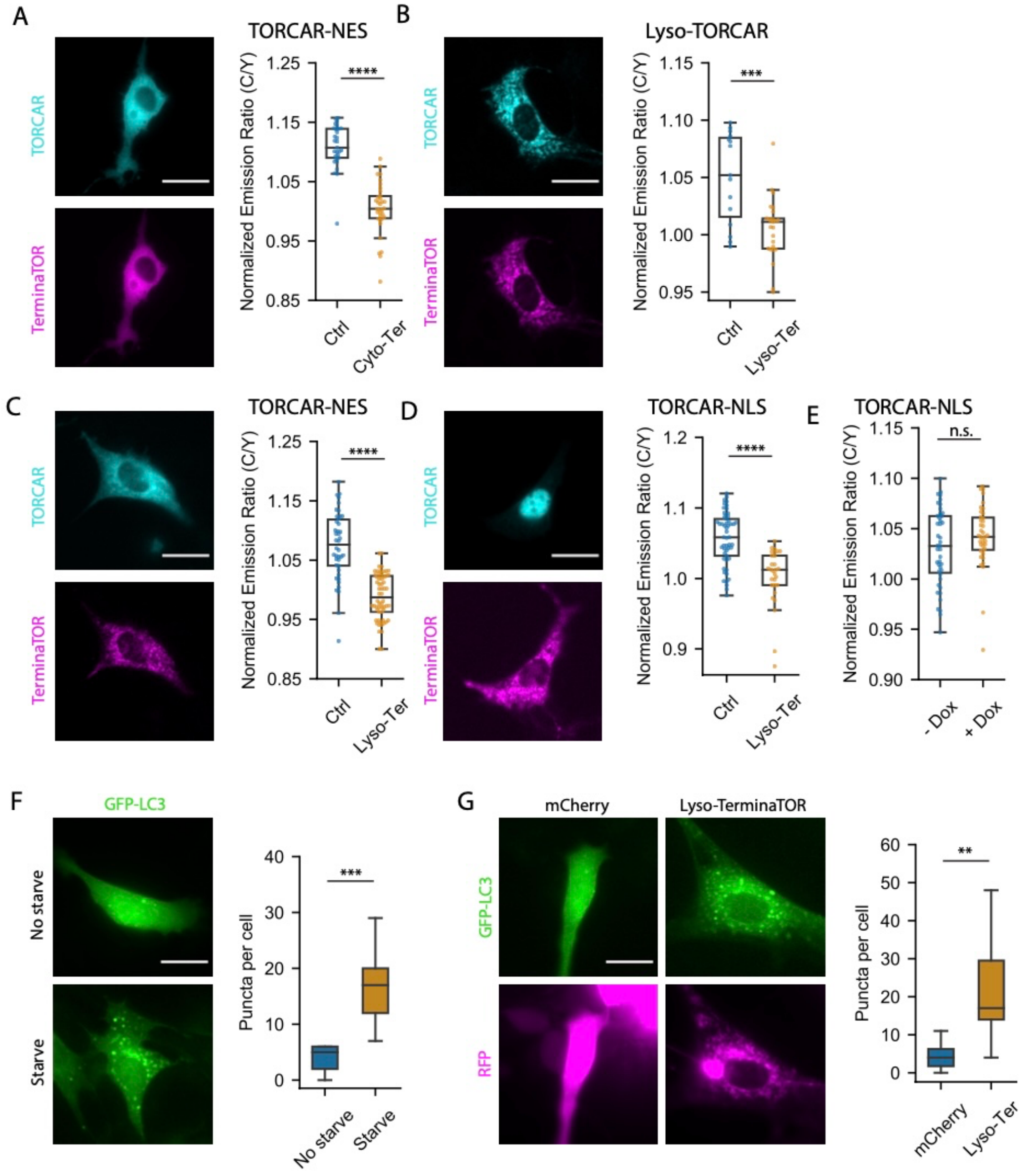
A
TORCAR
TerminaTOR
TORCAR-NES
Normalized Emission Ratio (C/Y)
1.25
1.15
1.05
0.95
0.85
****
Ctrl
Cyto-Ter
B
TORCAR
TerminaTOR
Lyso-TORCAR
Normalized Emission Ratio (C/Y)
1.15
1.10
1.05
1.00
0.95
***
Ctrl
Lyso-Ter
C
TORCAR
TerminaTOR
TORCAR-NES
Normalized Emission Ratio (C/Y)
1.25
1.15
1.05
0.95
0.85
****
Ctrl
Lyso-Ter
D
TORCAR
TerminaTOR
TORCAR-NLS
Normalized Emission Ratio (C/Y)
1.2
1.1
1.0
0.9
****
Ctrl
Lyso-Ter
E
TORCAR-NLS
Normalized Emission Ratio (C/Y)
1.15
1.10
1.05
1.00
0.95
0.90
n.s.
- Dox
+ Dox
F
GFP-LC3
No starve
Starve
Puncta per cell
40
30
20
10
0
***
No starve
Starve
G
mCherry
Lyso-TerminaTOR
GFP-LC3
RFP
Puncta per cell
60
50
40
30
20
10
0
**
mCherry
Lyso-Ter

mTORC1 (Liu and Sabatini, 2020). Lysosome-localized TerminaTOR (Lyso-TerminaTOR) was made by fusing TerminaTOR with a lysosomal associated membrane protein 1 (LAMP) -derived sequence (Zhou et al., 2015). Lyso-TerminaTOR significantly inhibited lysosomal mTORC1 activity (Ctrl: 5.0 ± 1.0 %, n = 15; Lyso-TerminaTOR: 0.5 ± 0.5 %, n = 25), as examined by Lyso-TORCAR, a lysosomally targeted TORCAR (Zhou et al., 2015) (**Figure 3.3B**), supporting our idea that TerminaTOR can be targeted to suppress subcellular mTORC1 activity.

To verify the local inhibition on mTORC1 by Lyso-TerminaTOR, we examined mTORC1 activity at other subcellular compartments in NIH3T3 cells expressing Lyso-TerminaTOR. We observed that cytosolic mTORC1 activity were inhibited by Lyso-TerminaTOR expression (**Figure 3.3C**. Ctrl: 9.7 ± 1.0 %, n = 21; Lyso-TerminaTOR: 0 ± 0.5 %, n = 60), which might be due to the rapid exchange between lysosomal membranes and the cytosol. To our surprise, we found Lyso-TerminaTOR also inhibited nuclear mTORC1 activity (**Figure 3.3D.** Ctrl: 5.7 ± 0.5 %, n = 53; Lyso-TerminaTOR: 0.3 ± 0.8 %, n = 29), examined by TORCAR-NLS, a nuclearly localized TORCAR (Zhou et al., 2015). We surmised that overexpression of Lyso-TerminaTOR may result in mislocalized protein (Mikuni et al., 2016), which led to inhibition at undesired locations due to its potent inhibitory effect. To overcome this caveat, we constructed stable NIH3T3 cells that can be induced to express Lyso-TerminaTOR by doxycycline. Using more controllable expression system, we found induction of Lyso-TerminaTOR expression in NIH3T3 cells did not affect nuclear TORCAR response to PDGF stimulation (**Figure 3.3E**. – Dox: 3.1 ± 0.6 %, n = 43; + Dox: 4.3 ± 0.5 %, n = 39). These data suggest that TerminaTOR can be targeted to specifically inhibit lysosomal mTORC1 activity.

One critical functional role of mTORC1 is inhibiting autophagy (Kim et al., 2011; Martina et al., 2012), but whether this is carried out by lysosomal pool of mTORC1 is unknown. We sought to examine this question by Lyso-TerminaTOR. We utilized a green fluorescent protein (GFP) - tagged microtubule-associated protein 1A/1B-light chain 3 (LC3) (GFP-LC3), an autophagy marker, which forms puncta during autophagy (Ding and Hong, 2020). Consistent with previous report, exogenously expressed GFP-LC3 formed punctate structure in NIH3T3 cells under serum starvation condition (**Figure 3.3F**. No starve: 6 ± 2 per cell; starve: 16 ± 2 per cell) which induces autophagy. In cells that were not starved but stably expressing Lyso-TerminaTOR, we also observed increased number of GFP-LC3 positive puncta compared with control (**Figure 3.3G**. mCherry: 4 ± 1 per cell; Lyso-TerminaTOR: 22 ± 3 per cell), suggesting Lyso-TerminaTOR can inhibit the basal mTORC1 activity as well as its function at the lysosome under the physiological conditions.

Location-specific inhibition of nuclear mTORC1 reveals gene expression regulated by nuclear mTORC1

mTORC1 is known to impact gene transcription through modulating the translation or nuclear translocation of an important set of master transcription factors, including sterol regulatory element binding protein (SREBP), transcription factor EB (TFEB) and peroxisome proliferator-activated receptor γ (PPARγ) (Laplante and Sabatini, 2013). The control on protein translation and the phosphorylation of cytosolic transcription factors are likely achieved by mTORC1 outside the nucleus. On the other hand, nuclear mTORC1 could directly interact and phosphorylate some of the transcriptional regulators that are present in the nucleus. Indeed, emerging studies suggest mTORC1 plays a crucial role in the nucleus by physically interacting with transcription factors or modulating activity of epigenetic modifiers via phosphorylation (Audet-Walsh et al., 2017; Cunningham et al., 2007; Laribee, 2018; Wan et al., 2017). Therefore, we hypothesized that nuclear mTORC1 regulates distinct transcriptional programs. The ability of TerminaTOR to inhibit mTORC1 activity in a location-specific manner makes it a valuable tool to examine this hypothesis.

We first generated a nuclearly targeted TerminaTOR using the histone protein H2A tag, a nuclear exclusive protein, to reduce mislocalization due to overexpression. In order to counteract the strong NES in native PRAS40 sequence, we also mutated two Leu residues (L225 and L227) in the NES to Ala (Wiza et al., 2013) to achieve stringent confinement to the nucleus, giving rise to a nuclearly targeted TerminaTOR (Nuc-TerminaTOR). Next, we examined the effects of Nuc-TerminaTOR on the PDGF-induced nuclear mTORC1 activity using TORCAR targeted to the nucleus in NIH3T3 cells. We found that Nuc-TerminaTOR exclusively localized to nucleus and significantly inhibited nuclear mTORC1 activity (**Figure 3.4A**. Ctrl: 5.7 ± 0.5 %, n = 53; Nuc-TerminaTOR: 1.7 ± 0.4 %, n = 35). In contrast, we found Nuc-TerminaTOR did not affect cytosolic (**Figure 3.4B**. Ctrl: 9.7 ± 1.0 %, n = 21; Nuc-TerminaTOR: 7.4 ± 0.9 %, n = 42) or lysosomal mTORC1 activity (**Figure 3.4C.** Ctrl: 4.2 ± 0.7 %, n = 24; 4.6 ± 0.6 %, n = 37). These results demonstrate that Nuc-TerminaTOR is capable of specifically inhibiting noncanonical nuclear mTORC1 activity.

To examine the gene transcription regulated by nuclear mTORC1, we used NIH3T3 stable cells that can be induced by doxycycline to express mCherry, Cyto-TerminaTOR or Nuc-TerminTOR, and did mRNA sequencing using total RNA collected from four different groups of samples, including mCherry expressing cells treated with DMSO or Torin1, and Cyto-TerminaTOR or Nuc-TerminaTOR expressing cells treated with DMSO (**Figure 3.5A**). We analyzed the differentially expressed genes (DEGs) that are affected by Torin1, Cyto-TerminaTOR

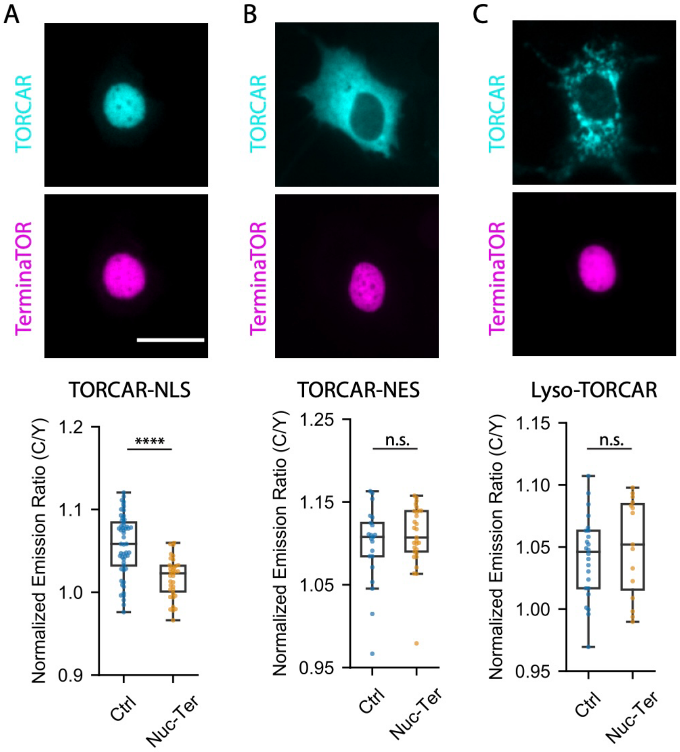

Figure 3.4 Nuc-TerminaTOR specifically inhibited nuclear mTORC1 activity. (A). Upper, representative fluorescent images of TORCAR-NLS and Nuc-TerminaTOR. Lower, summary of PDGF-induced maximum responses of TORCAR-NLS in NIH3T3 cells. Cells were transfected, double starved and stimulated with 50 ng/mL PDGF. Control cells were transfected with H2A-mCherry (Ctrl, 5.7 ± 0.5 %, n = 53 cells from 4 independent experiments). Cells expressing Nuc-TerminaTOR showed reduced response (Nuc-Ter, 1.7 ± 0.4 %, n = 35 cells from 4 independent experiments). (B). Upper, representative fluorescent images of TORCAR-NES and Nuc-TerminaTOR. Lower, summary of PDGF-induced maximum responses of TORCAR-NES in NIH3T3 cells. Cells were transfected, double starved and stimulated with 50 ng/mL PDGF. Control cells were transfected with H2A-mCherry (9.7 ± 1.0 %, n = 21 cells from 2 independent experiments). Cells expressing Nuc-TerminaTOR did not affect responses (Nuc-Ter, 7.4 ± 0.9 %, n = 42 cells from 3 independent experiments). (C). Upper, representative fluorescent images of Lyso-TORCAR and Nuc-TerminaTOR. Lower, summary of PDGF-induced maximum responses of Lyso-TORCAR in NIH3T3 cells. Cells were transfected, double starved and stimulated with 50 ng/mL PDGF. Control cells were transfected with H2A-mCherry (4.2 ± 0.7 %, n = 24 cells from 4 independent experiments). Cells expressing Nuc-TerminaTOR did not affect responses (Nuc-Ter, 4.6 ± 0.6 %, n = 37 cells from 3 independent experiments). Box plots show the upper and lower adjacent values, interquartile range and the median. Student t-tests are used. ****, $p < 0.0001$; n.s., not significant.

and Nuc-TerminaTOR, respectively, by making pair-wise comparison with the mCherry expressing, DMSO-treated control group (Ctrl) (**Figure 3.5B**). In the Cyto-TerminaTOR vs Ctrl comparison group, there were 648 DEGs, with 376 genes up-regulated and 272 genes down-regulated; in the Nuc-TerminaTOR vs Ctrl comparison group, 1951 DEGs were identified, with 998 genes up-regulated and 953 genes down-regulated. These data indicate that nuclear mTORC1 may have boarder impact on the transcriptional regulation than the cytosolic mTORC1. In the Torin1 vs Ctrl comparison, there were 2956 DEGs, of which 1605 DEGs were not overlapping with DEGs from the other two comparisons, most likely representing gene transcription regulated by mTORC2 which is supposed to be inhibited by Torin1 but not by TerminaTOR. There were also 1351 DEGs that overlap with the other two comparisons, which covers 81.6 % and 58.4 % of DEGs affected by Cyto-TerminaTOR and Nuc-TerminaTOR, respectively, suggesting TerminaTOR can efficiently suppress mTORC1 activity. The Venn diagram also showed 822 genes that were sensitive to mTORC1 inhibition induced by Torin1 and Nuc-TerminaTOR but not affected by Cyto-TerminaTOR, suggesting nuclear mTORC1 may have unique functions than canonical mTORC1.

In order to determine the functions of the nuclear mTORC1, we performed gene set enrichment analysis (GSEA) on the sequencing results from each comparison above. When global mTORC1 activity was suppressed by Torin1, gene expression in 17 hallmark pathways were down-regulated (**Figure 3.5C**), among which mTORC1 signaling ranked first (data not shown), in accordance with that Torin1 treatment strongly inhibited cellular mTORC1 activity. When nuclear mTORC1 activity is inhibited by Nuc-TerminaTOR, GSEA only identified 7 down-regulated hallmark pathways, and 5 out of 7 also were also observed when global mTORC1 was inhibited.

Figure 3.5 Differential gene transcription by nuclear and cytosolic mTORC1. (A). Experimental design for RNA sequencing. Stable NIH3T3 cells were cultured in growth medium supplemented with doxycycline and incubated for overnight to induce Cyto-TerminaTOR, Nuc-TerminaTOR and mCherry (Ctrl group and Torin1 group) expression as control. Torin1 was added to the medium for overnight and DMSO was added as vehicle. Total RNA was extracted from triplicated samples from each group and send to RNA sequencing. (B). Overview of differential expressed genes (DEGs) from Torin1 treated, Cyto-TerminaTOR expressing and Nuc-TerminaTOR expressing groups comparing to control (Ctrl) group. Veen diagram in the center shows the overlapping DEGs from three different comparisons. Numbers of up-regulated and down-regulated genes are displayed in the veen diagram around the corner corresponding each comparison. (C). Veen Diagram showing the overlapping of down-regulated pathways by Torin1, Cyto-TerminaTOR and Nuc-TerminaTOR. Three pathways are uniquely down-regulated by Nuc-TerminaTOR. (D). Veen Diagram showing the overlapping of up-regulated pathways by Torin1, Cyto-TerminaTOR and Nuc-TerminaTOR. (E). Three pathways uniquely down-regulated by Nuc-TerminaTOR are E2F targets, G2M checkpoint and Oxidative phosphorylation pathways. (F). Nuc-TermiaTOR impairs oral squamous cell carcinoma (OSCC) cell growth. OSCC stably expressing H2A-mCherry or Nuc-TerminaTOR were seeded at the same density and were collected and counted at 72 hr time point. Cell numbers were normalized to the seeding density. (G). Pathways that are affected by Cyto-TerminaTOR and Nuc-TerminaTOR. Horizontal axis shows the normalized enrichment score. Four pathways in the middle were oppositely regulated by Cyto-TerminaTOR and Nuc-TerminTOR. (H). Example of differentially impacted genes in glycolysis pathway by Cyto-TerminaTOR and Nuc-TerminaTOR. Percentage change was calculated by (fold change – control)/control. Positive value means up-regulated and negative value means down-regulated.

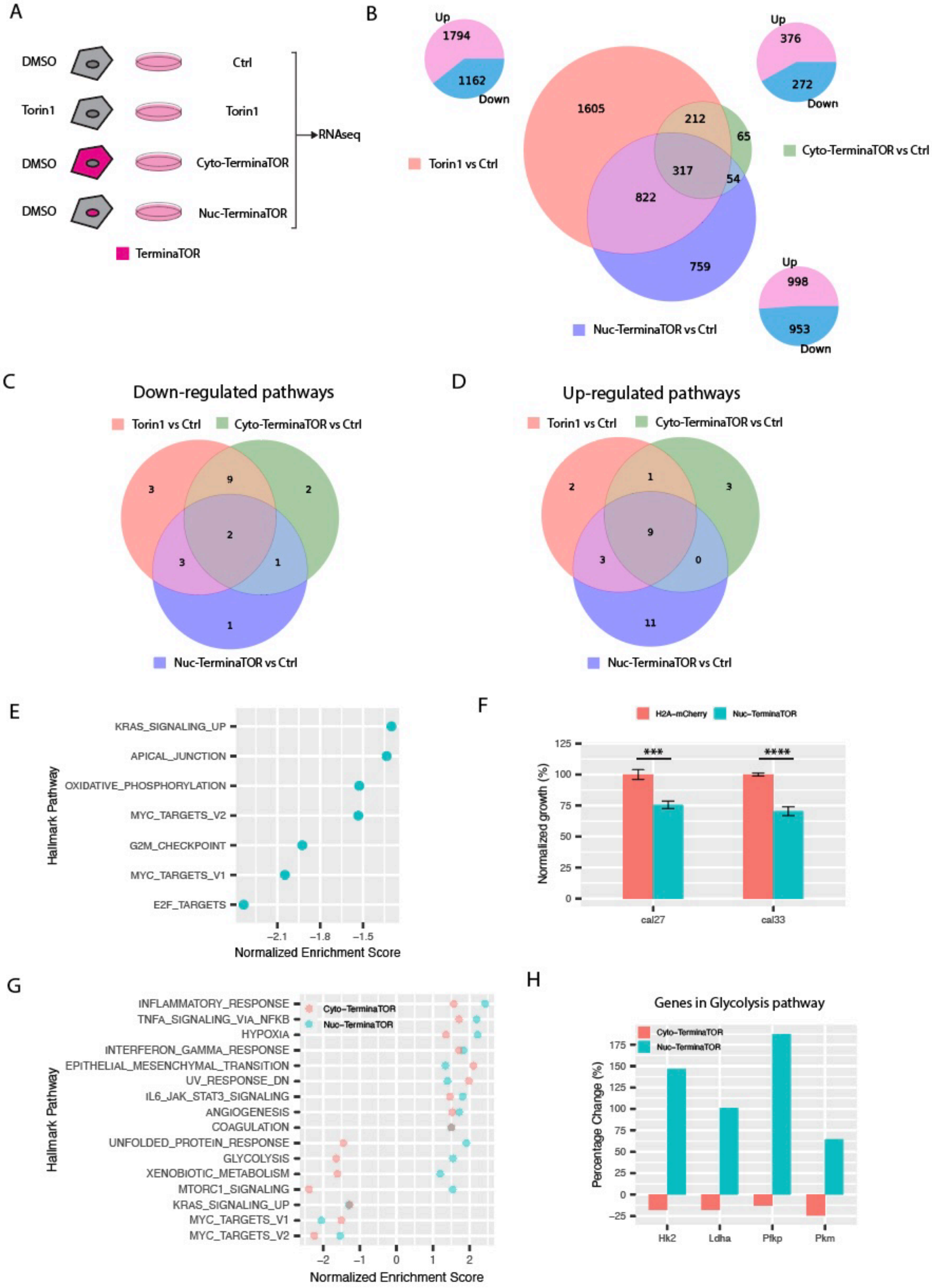
A
DMSO
Torin1
DMSO
DMSO
Ctrl
Torin1
Cyto-TerminaTOR
Nuc-TerminaTOR
RNAseq
TerminaTOR
B
Up
1794
1162
Down
Torin1 vs Ctrl
1605
212
65
317
54
822
759
Up
376
272
Down
Cyto-TerminaTOR vs Ctrl
Up
998
953
Down
Nuc-TerminaTOR vs Ctrl
C
Down-regulated pathways
Torin1 vs Ctrl
Cyto-TerminaTOR vs Ctrl
3
9
2
2
3
1
1
Nuc-TerminaTOR vs Ctrl
D
Up-regulated pathways
Torin1 vs Ctrl
Cyto-TerminaTOR vs Ctrl
2
1
3
9
3
0
11
Nuc-TerminaTOR vs Ctrl
E
KRAS_SIGNALING_UP
APICAL_JUNCTION
OXIDATIVE_PHOSPHORYLATION
MYC_TARGETS_V2
G2M_CHECKPOINT
MYC_TARGETS_V1
E2F_TARGETS
Hallmark Pathway
−2.1
−1.8
−1.5
Normalized Enrichment Score
F
H2A-mCherry
Nuc-TerminaTOR
125
100
75
50
25
0
Normalized growth (%)
***
****
cal27
cal33
G
INFLAMMATORY_RESPONSE
TNFA_SIGNALING_VIA_NFKB
HYPOXIA
INTERFERON_GAMMA_RESPONSE
EPITHELIAL_MESENCHYMAL_TRANSITION
UV_RESPONSE_DN
IL6_JAK_STAT3_SIGNALING
ANGIOGENESIS
COAGULATION
UNFOLDED_PROTEIN_RESPONSE
GLYCOLYSIS
XENOBIOTIC_METABOLISM
MTORC1_SIGNALING
KRAS_SIGNALING_UP
MYC_TARGETS_V1
MYC_TARGETS_V2
Cyto-TerminaTOR
Nuc-TerminaTOR
Hallmark Pathway
−2
−1
0
1
2
Normalized Enrichment Score
H
Genes in Glycolysis pathway
Cyto-TerminaTOR
Nuc-TerminaTOR
175
150
125
100
75
50
25
0
−25
Percentage Change (%)
Hk2
Ldha
Pfkp
Pkm

Similarly, when cytosolic mTORC1 was inhibited, 14 hallmark pathways were down-regulated and 11 out of 14 pathways were also down-regulated with global mTORC1 inhibition (**Figure 3.5C**). To further understand the nuclear mTORC1 regulated functions, we also examined the up-regulated pathways (**Figure 3.5D**). 23 pathways were found to be up-regulated in case of nuclear mTORC1 inhibition and only 13 for cytosolic mTORC1 inhibition, suggesting the differences in functions between nuclear and cytosolic mTORC1. We looked further into the specific down-regulated pathways, we found three distinctive pathways that are specifically down-regulated only in the case of nuclear mTORC1 inhibition and Torin1 treatment, including E2F targets pathway and G2M checkpoint pathway (**Figure 3.5E**). E2F and G2M checkpoint are two large families of proteins, including various transcription factors, that regulate cell cycle and both have been linked to mTORC1 signaling (Hsieh et al., 2018; Real et al., 2011). This result suggests nuclear mTORC1 could regulate cell cycle independent of cytosolic mTORC1 activity, thus, we hypothesized that nuclear mTORC1 could regulate cell growth. To test our hypothesis, we examined if Nuc-TerminaTOR could affect the growth of oral squamous cell carcinoma (OSCC) cells, in which mTORC1 pathway is frequently activated and confers resistance to treatment (Wang et al., 2014). We found that expressing Nuc-TerminaTOR in two OSCC cell lines, Cal27 and Cal33 (Wang et al., 2019), significantly reduced the cell growth compared to cells expressing mCherry control (**Figure 3.5F**), supporting that nuclear mTORC1 can regulate cell growth independent of cytosolic mTORC1, possibly via cell cycle related transcriptional control.

By comparing the up-regulated pathways by nuclear and cytosolic mTORC1, we surprisingly found four pathways that were oppositely regulated (**Figure 3.5G**). Genes in glycolysis pathway, unfolded protein response pathway and xenobiotic metabolism pathway were up-regulated in case of nuclear mTORC1 inhibition, but were down-regulated enriched in case of cytosolic mTORC1 inhibition. We looked into the specific genes in the glycolysis pathway and found several genes encoding key enzymes in glycolysis, including hexokinase 2 (Hk2), lactate dehydrogenase A (Ldha), phosphofructokinase, platelet (Pfkp) and pyruvate kinase M1/2 (Pkm), were up-regulated in case of nuclear mTORC1 inhibition and down-regulated by cytosolic mTORC1 inhibition (**Figure 3.5H**). These data suggest nuclear mTORC1 may differentially regulate cellular processes compared with the canonical mTORC1. Interestingly, the genes in the mTORC1 signaling pathway itself is also differentially regulated by nuclear mTORC1 and cytosolic mTORC1 (**Figure 3.5G**), suggesting a possibility that nuclear mTORC1 has distinct roles in regulating transcription and may counteract the functions of cytosolic mTORC1.

Discussion

The master regulator, mTORC1, acts as a nexus point, integrating cues from nutrients and growth factors to control cellular metabolism and growth (Laplante and Sabatini, 2012). Signaling compartmentation for mTORC1 has been proposed but only until recently was mTORC1 activity observed in subcellular compartments via fluorescent biosensors (Zhou et al., 2015). Conventional methods to block mTORC1 activity, such as pharmacological inhibitors and genetic perturbations, are incapable of specifically targeting subcellular mTORC1 activity. We used a synthetic biology approach to generate targetable tools to dissect the regulation and functions of subcellular mTORC1. Previously, we developed AktSTOPS, which allowed us to determine that nuclear mTORC1 can be directly regulated by nuclear Akt (Zhou et al., 2020). AktSTOPS was shown to suppress nuclear mTORC1 activity (Zhou et al., 2020), in a manner dependent on nuclear Akt, which is also a master regulator of various cellular processes (Manning and Toker, 2017). Compared with AktSTOPS, TerminaTOR specifically and directly inhibits mTORC1, In addition, it is free of endogenous regulation as the regulatory sites are removed via truncation or mutation. We showed TerminaTOR could be targeted to subcellular compartment to suppress local mTORC1 activity (**Figure 3.3, 3.4**), although stringent targeting strategies may be required to achieve location-specific inhibition (**Figure 3.4A**), since mislocalization of a small amount of TerminaTOR could result in off-site inhibition due to its potent inhibitory effect on mTORC1 (**Figure 3.1C**). We found that using stable cell line that has inducible expressing system could reduce mislocalized exogenously expressed protein (**Figure 3.3E**) to achieve location-specific mTORC1 inhibition.

It is well established that canonical mTORC1 activation occurs on the lysosomal membrane, though the interconnections between different pools of mTORC1 are unclear. Earlier studies showed that mTORC1 could propagates to other compartments after its activation on the lysosome (Manifava et al., 2016), but our results showed that lysosomal and nuclear mTORC1 activities are independently regulated, as inhibiting mTORC1 at one site did not affect mTORC1 at the other site (**Figure 3.3E, 3.4C**). As mTORC1 activation was shown to occur at different subcellular locations, including Golgi and mitochondria (de la Cruz López et al., 2019; Hao et al., 2018), it would be interesting to use targeted TerminaTOR to elucidate the interplays between these subcellular pools of mTORC1.

Although we discovered noncanonical regulation of mTORC1 by nuclear Akt and Rheb (Zhou et al., 2020), the functions of nuclear mTORC1 were unclear. Nuclearly targeted TerminaTOR can specifically inhibit nuclear mTORC1 activity, which permits the examination of nuclear mTORC1 functions. mTORC1 is known to regulate gene transcription, but how much the nuclear mTORC1 contributes to transcriptional regulation remains unknown. By comparing the differentially expressed genes (DEGs) in cells expressing Nuc-TerminaTOR and Cyto-

TerminaTOR, we found that a subpopulation of genes from E2F and G2M checkpoint pathways are specifically regulated by nuclear mTORC1(**Figure 3.5E**). Gene set enrichment analysis (GSEA) reveals that nuclear mTORC1 can exhibit synergistic and antagonistic effect on the same pathway compared to canonical mTORC1 (**Figure 3.5G**), in accordance with the idea that nuclear and canonical mTORC1 can be independently regulated. We also found that certain genes encoding key enzymes in glycolysis pathway were oppositely regulated by nuclear (down-regulation) and cytosolic (up-regulation) mTORC1 (**Figure 3.5H**). High rate of glycolysis has been widely observed in many tumor cells and mTORC1 inhibitors have shown effect on glycolysis-dependent tumor cell growth (Ganapathy-Kanniappan and Geschwind, 2013; Li et al., 2015). Given the complex roles of subcellular pools of mTORC1 on cell cycle and glycolysis pathways, a precise-tuning but not a sledgehammer approach is necessary to target mTORC1 therapeutically.

Nuclear mTORC1 might regulate gene transcription by directly binding to the promoters or by phosphorylating transcription factors (Laribee, 2018). Previous studies using chromatin-immunoprecipitation (ChIP) found mTOR associated with pol III-transcribed genes and mTORC1 was also reported to phosphorylate proteins that regulate gene transcription, such as Maf1 (Shor et al., 2010), p300 (Wan et al., 2017) and TFEB (Martina et al., 2012). TerminaTOR developed in this study, could allow researchers to identify mTORC1 substrates at specific locations, which will provide further insights into the functions of mTORC1 at different compartments.

Chapter 3, in full, is currently being prepared for submission for publication of the material. Zhong, Y., Zhou, X., Sahan A., Gutkind, JS., Zhang, J. Genetically targetable mTORC1 inhibitor reveals differential transcriptional control by subcellular mTORC1. The dissertation author was

the primary investigator and author of this work.

References

Angarola, B., and Ferguson, S.M. (2019). Weak membrane interactions allow Rheb to activate mTORC1 signaling without major lysosome enrichment. Mol. Biol. Cell *30*, 2750–2760.

Audet-Walsh, É., Dufour, C.R., Yee, T., Zouanat, F.Z., Yan, M., Kalloghlian, G., Vernier, M., Caron, M., Bourque, G., Scarlata, E., et al. (2017). Nuclear mTOR acts as a transcriptional integrator of the androgen signaling pathway in prostate cancer. Genes Dev. *31*, 1228–1242.

Cai, S.-L., Tee, A.R., Short, J.D., Bergeron, J.M., Kim, J., Shen, J., Guo, R., Johnson, C.L., Kiguchi, K., and Walker, C.L. (2006). Activity of TSC2 is inhibited by AKT-mediated phosphorylation and membrane partitioning. J. Cell Biol. *173*, 279–289.

Clister, T., Greenwald, E.C., Baillie, G.S., and Zhang, J. (2019). AKAP95 Organizes a Nuclear Microdomain to Control Local cAMP for Regulating Nuclear PKA. Cell Chem. Biol. *26*, 885–891.e4.

de la Cruz López, K.G., Toledo Guzmán, M.E., Sánchez, E.O., and García Carrancá, A. (2019). mTORC1 as a Regulator of Mitochondrial Functions and a Therapeutic Target in Cancer. Front. Oncol. *9*, 1373.

Cunningham, J.T., Rodgers, J.T., Arlow, D.H., Vazquez, F., Mootha, V.K., and Puigserver, P. (2007). mTOR controls mitochondrial oxidative function through a YY1-PGC-1alpha transcriptional complex. Nature *450*, 736–740.

Ding, S., and Hong, Y. (2020). The fluorescence toolbox for visualizing autophagy. Chem. Soc. Rev.

Feldman, M.E., Apsel, B., Uotila, A., Loewith, R., Knight, Z.A., Ruggero, D., and Shokat, K.M. (2009). Active-site inhibitors of mTOR target rapamycin-resistant outputs of mTORC1 and mTORC2. PLoS Biol. *7*, e38.

Ganapathy-Kanniappan, S., and Geschwind, J.-F.H. (2013). Tumor glycolysis as a target for cancer therapy: progress and prospects. Mol. Cancer *12*, 152.

Hao, F., Kondo, K., Itoh, T., Ikari, S., Nada, S., Okada, M., and Noda, T. (2018). Rheb localized on the Golgi membrane activates lysosome-localized mTORC1 at the Golgi-lysosome contact site. J. Cell Sci. *131*.

Hsieh, H.-J., Zhang, W., Lin, S.-H., Yang, W.-H., Wang, J.-Z., Shen, J., Zhang, Y., Lu, Y., Wang, H., Yu, J., et al. (2018). Systems biology approach reveals a link between mTORC1 and G2/M DNA damage checkpoint recovery. Nat. Commun. *9*, 3982.

Hsu, P.P., Kang, S.A., Rameseder, J., Zhang, Y., Ottina, K.A., Lim, D., Peterson, T.R., Choi, Y., Gray, N.S., Yaffe, M.B., et al. (2011). The mTOR-regulated phosphoproteome reveals a mechanism of mTORC1-mediated inhibition of growth factor signaling. Science *332*, 1317–1322.

Inoki, K., Li, Y., Zhu, T., Wu, J., and Guan, K.-L. (2002). TSC2 is phosphorylated and inhibited by Akt and suppresses mTOR signalling. Nat. Cell Biol. *4*, 648–657.

Kim, J., Kundu, M., Viollet, B., and Guan, K.-L. (2011). AMPK and mTOR regulate autophagy through direct phosphorylation of Ulk1. Nat. Cell Biol. *13*, 132–141.

Lamming, D.W., Ye, L., Sabatini, D.M., and Baur, J.A. (2013). Rapalogs and mTOR inhibitors as anti-aging therapeutics. J. Clin. Invest. *123*, 980–989.

Laplante, M., and Sabatini, D.M. (2012). mTOR signaling in growth control and disease. Cell *149*, 274–293.

Laplante, M., and Sabatini, D.M. (2013). Regulation of mTORC1 and its impact on gene expression at a glance. J. Cell Sci. *126*, 1713–1719.

Laribee, R.N. (2018). Transcriptional and epigenetic regulation by the mechanistic target of rapamycin complex 1 pathway. J. Mol. Biol. *430*, 4874–4890.

Li, X.-B., Gu, J.-D., and Zhou, Q.-H. (2015). Review of aerobic glycolysis and its key enzymes - new targets for lung cancer therapy. Thorac Cancer *6*, 17–24.

Liu, G.Y., and Sabatini, D.M. (2020). mTOR at the nexus of nutrition, growth, ageing and disease. Nat. Rev. Mol. Cell Biol. *21*, 183–203.

Liu, Q., Chang, J.W., Wang, J., Kang, S.A., Thoreen, C.C., Markhard, A., Hur, W., Zhang, J., Sim, T., Sabatini, D.M., et al. (2010). Discovery of 1-(4-(4-propionylpiperazin-1-yl)-3-(trifluoromethyl)phenyl)-9-(quinolin-3-yl)benzo[h][1,6]naphthyridin-2(1H)-one as a highly potent, selective mammalian target of rapamycin (mTOR) inhibitor for the treatment of cancer. J. Med. Chem. *53*, 7146–7155.

Manifava, M., Smith, M., Rotondo, S., Walker, S., Niewczas, I., Zoncu, R., Clark, J., and Ktistakis, N.T. (2016). Dynamics of mTORC1 activation in response to amino acids. Elife *5*.

Manning, B.D., and Toker, A. (2017). AKT/PKB signaling: navigating the network. Cell *169*, 381–405.

Manning, B.D., Tee, A.R., Logsdon, M.N., Blenis, J., and Cantley, L.C. (2002). Identification of the tuberous sclerosis complex-2 tumor suppressor gene product tuberin as a target of the phosphoinositide 3-kinase/akt pathway. Mol. Cell *10*, 151–162.

Martina, J.A., Chen, Y., Gucek, M., and Puertollano, R. (2012). MTORC1 functions as a transcriptional regulator of autophagy by preventing nuclear transport of TFEB. Autophagy *8*, 903–914.

Menon, S., Dibble, C.C., Talbott, G., Hoxhaj, G., Valvezan, A.J., Takahashi, H., Cantley, L.C., and Manning, B.D. (2014). Spatial control of the TSC complex integrates insulin and nutrient regulation of mTORC1 at the lysosome. Cell *156*, 771–785.

Mikuni, T., Nishiyama, J., Sun, Y., Kamasawa, N., and Yasuda, R. (2016). High-Throughput, High-Resolution Mapping of Protein Localization in Mammalian Brain by In Vivo Genome Editing. Cell *165*, 1803–1817.

Nandagopal, N., and Roux, P.P. (2015). Regulation of global and specific mRNA translation by the mTOR signaling pathway. Translation (Austin) *3*, e983402.

Real, S., Meo-Evoli, N., Espada, L., and Tauler, A. (2011). E2F1 regulates cellular growth by mTORC1 signaling. PLoS One *6*, e16163.

Rodrik-Outmezguine, V.S., Okaniwa, M., Yao, Z., Novotny, C.J., McWhirter, C., Banaji, A., Won, H., Wong, W., Berger, M., de Stanchina, E., et al. (2016). Overcoming mTOR resistance mutations with a new-generation mTOR inhibitor. Nature *534*, 272–276.

Ross, B.L., Tenner, B., Markwardt, M.L., Zviman, A., Shi, G., Kerr, J.P., Snell, N.E., McFarland, J.J., Mauban, J.R., Ward, C.W., et al. (2018). Single-color, ratiometric biosensors for detecting signaling activities in live cells. Elife *7*.

Sabatini, D.M. (2017). Twenty-five years of mTOR: Uncovering the link from nutrients to growth. Proc. Natl. Acad. Sci. USA *114*, 11818–11825.

Sancak, Y., Thoreen, C.C., Peterson, T.R., Lindquist, R.A., Kang, S.A., Spooner, E., Carr, S.A., and Sabatini, D.M. (2007). PRAS40 is an insulin-regulated inhibitor of the mTORC1 protein kinase. Mol. Cell *25*, 903–915.

Sancak, Y., Bar-Peled, L., Zoncu, R., Markhard, A.L., Nada, S., and Sabatini, D.M. (2010). Ragulator-Rag complex targets mTORC1 to the lysosomal surface and is necessary for its activation by amino acids. Cell *141*, 290–303.

Saxton, R.A., and Sabatini, D.M. (2017). mTOR Signaling in Growth, Metabolism, and Disease. Cell *168*, 960–976.

Shor, B., Wu, J., Shakey, Q., Toral-Barza, L., Shi, C., Follettie, M., and Yu, K. (2010). Requirement of the mTOR kinase for the regulation of Maf1 phosphorylation and control of RNA polymerase III-dependent transcription in cancer cells. J. Biol. Chem. *285*, 15380–15392.

Wan, W., You, Z., Xu, Y., Zhou, L., Guan, Z., Peng, C., Wong, C.C.L., Su, H., Zhou, T., Xia, H., et al. (2017). mTORC1 Phosphorylates Acetyltransferase p300 to Regulate Autophagy and Lipogenesis. Mol. Cell *68*, 323–335.e6.

Wang, Z., Martin, D., Molinolo, A.A., Patel, V., Iglesias-Bartolome, R., Degese, M.S., Vitale-Cross, L., Chen, Q., and Gutkind, J.S. (2014). mTOR co-targeting in cetuximab resistance in head and neck cancers harboring PIK3CA and RAS mutations. J. Natl. Cancer Inst. *106*.

Wang, Z., Feng, X., Molinolo, A.A., Martin, D., Vitale-Cross, L., Nohata, N., Ando, M., Wahba, A., Amornphimoltham, P., Wu, X., et al. (2019). 4E-BP1 Is a Tumor Suppressor Protein Reactivated by mTOR Inhibition in Head and Neck Cancer. Cancer Res. *79*, 1438–1450.

Wiza, C., Nascimento, E.B.M., and Ouwens, D.M. (2012). Role of PRAS40 in Akt and mTOR signaling in health and disease. Am. J. Physiol. Endocrinol. Metab. *302*, E1453-60.

Wiza, C., Nascimento, E.B.M., Linssen, M.M.L., Carlotti, F., Herzfeld de Wiza, D., van der Zon, G.C.M., Maassen, J.A., Diamant, M., Guigas, B., and Ouwens, D.M. (2013). Proline-rich Akt substrate of 40-kDa contains a nuclear export signal. Cell Signal. *25*, 1762–1768.

Yang, H., Jiang, X., Li, B., Yang, H.J., Miller, M., Yang, A., Dhar, A., and Pavletich, N.P. (2017). Mechanisms of mTORC1 activation by RHEB and inhibition by PRAS40. Nature *552*, 368–373.

Zhou, X., Clister, T.L., Lowry, P.R., Seldin, M.M., Wong, G.W., and Zhang, J. (2015). Dynamic Visualization of mTORC1 Activity in Living Cells. Cell Rep. *10*, 1767–1777.

Zhou, X., Zhong, Y., Molinar-Inglis, O., Kunkel, M.T., Chen, M., Sun, T., Zhang, J., Shyy, J.Y.-J., Trejo, J., Newton, A.C., et al. (2020). Location-specific inhibition of Akt reveals regulation of mTORC1 activity in the nucleus. Nat. Commun. *11*, 6088.

Conclusion

The main goal of these studies presented here is to understand the undefined mTORC1 activity at subcellular compartments, including its mechanisms of regulation and functions. mTORC1 activity at different subcellular regions is able to be monitored by genetically encoded fluorescent biosensors, which can be targeted to specific compartments via well-established targeting sequences. mTORC1 activities were found at the plasma membrane, lysosomes, cytosol and nucleus in a manner dependent on the stimulus. Nuclear mTORC1 activity can be stimulated by both growth factors and amino acids, and growth factor-stimulated nuclear mTORC1 activity showed similar kinetics as that of cytosolic mTORC1 activity, suggesting it is less likely that nuclear mTORC1 is originated from activated mTORC1 in the cytosol which could translocate into the nucleus. Thus, a model of nuclear mTORC1 activation independent of cytosolic mTORC1 is possible.

The first sub-aim of the dissertation is to examine if the same group of proteins are present in the nucleus to regulate nuclear mTORC1 activity. To achieve this goal, a molecular tool named AktSTOPS was developed to specifically inhibit nuclear mTORC1. We showed that nuclear Akt is required for nuclear mTORC1 activity. Growth factors activate mTORC1 through Akt in two ways, phosphorylating TSC2 to release inhibition on Rheb-dependent mTORC1 activation, or phosphorylating PRAS40 to release direct inhibition of mTORC1 by PRAS40. Upon careful biochemical assays, Akt and Rheb were found to be present in the nucleus besides other mTORC1 components, however, no clues of TSC2 were found in the nucleus, suggesting nuclear Akt might regulate nuclear mTORC1 in a noncanonical manner. Further experiments suggest that nuclear Akt stimulates nuclear mTORC1 activity by phosphorylating RanBP, a protein that facilitates small GTPase Ran-dependent protein translocation into the nucleus. By this way, nuclear Akt promotes the nuclear translocation of Raptor, the mTORC1 defining component, getting ready to form a complex with mTOR. On the other hand, nuclear Akt can phosphorylate PRAS40 and induce the dissociation of PRAS40 from mTORC1. Consistently, a small population of Rheb that might have been escaped from farnesylation in the cytosol localizes in the nucleus and is active due to the absence of its GAP, TSC2. The newly formed mTORC1 complex is ready to be activated by the active Rheb in the nucleus. The “standby” status of nuclear mTORC1 may enables fast response to growth factor stimulation to an extent on par with cytosolic mTORC1.

The second sub-aim of the dissertation was to examine the functional roles of nuclear mTORC1. In order to specifically perturb subcellular pools of mTORC1, a genetically targetable mTORC1 inhibitor, TerminaTOR, was developed and characterized. TerminaTOR exhibited potent inhibition on endogenous mTORC1 activity and can be localized to subcellular compartments to achieve local inhibition. mTORC1 is known to regulate very broad functions through phosphorylating a wide range of effector proteins, including those that translocate into nucleus after being phosphorylated. Native nuclear mTORC1 exists in an environment full of regulators of gene transcription, and is very like to interact with and phosphorylate these regulators, thus could play an important and distinct role in regulating gene transcription. By comparing cells with cytosolic mTORC1 inhibition and nuclear mTORC1 inhibition, we showed that a set of genes were specifically regulated by nuclear mTORC1. Functionally, nuclear mTORC1 could differentially regulate specific pathways compared with cytosolic mTORC1. Notably, the top ranked pathways that are differentially regulated by nuclear and cytosolic mTORC1 are connected to cellular metabolism, a process that is often reprogrammed in cancer cells. Nuclear mTORC1 might play essential roles in regulating cancer cell survival. How does nuclear mTORC1 achieve the distinct regulation in gene transcription? Apparently, identifying the corresponding substrates in the nucleus should be of high priority in order to understand the mechanisms by which nuclear mTORC1 regulates a specific set of genes. TerminaTOR developed in the dissertation can serve as a valuable tool to identify nuclear mTORC1 substrates.

The research presented in the dissertation elucidated a noncanonical mechanism that regulates growth factor-induced nuclear mTORC1 activity. It also shed light on the distinct role of nuclear mTORC1 in regulating gene transcription. This work improved our understanding of the compartmentalization of mTORC1 signaling, which in the future could be utilized in precision medicine.